Variabilité Holocène des poussières atmosphériques et du mercure dans l'hémisphère Sud

Chuxian Li

Université Fédérale
Toulouse Midi-Pyrénées

THÈSE

En vue de l'obtention du

DOCTORAT DE L'UNIVERSITÉ DE TOULOUSE

Délivré par l'Université Toulouse 3 - Paul Sabatier

Présentée et soutenue par

Chuxian LI

Le 17 septembre 2019

Variabilité Holocène des poussières atmosphériques et du mercure dans l'hémisphère Sud

---

Ecole doctorale : **SDU2E - Sciences de l'Univers, de l'Environnement et de l'Espace**

Spécialité : **Surfaces et interfaces continentales, Hydrologie**

Unité de recherche :
ECOLAB - Laboratoire d'Ecologie Fonctionnelle et Environnement

Thèse dirigée par
François De Vleeschouwer et Jeroen SONKE

Jury
M. Dominic Hodgson, Rapporteur
M. Jiubin Chen, Rapporteur
Mme Mattielli Nadine, Examinatrice
M. Gaël Le Roux, Examinateur
Mme Catherine Jeandel, Invitée
M. De Vleeschouwer François, Directeur de thèse
M. Sonke Jeroen, co-Directeur de thèse

Abstract

The Southern westerly winds (SWW) play an important role in regulating Southern Ocean carbon budget by enhancing the absorbance of atmospheric CO_2 or resurfacing deep ocean carbon. Changes in SWW intensity are thought to determine whether Southern Ocean acts as a net CO_2 sink or source, thereby affecting atmospheric CO_2 concentration and then global climate. SWW also affect Southern Hemisphere (SH) dust trajectory and mercury biogeochemical cycling, which in turn can be used to trace SWW dynamics. Less is known about the past SWW variabilities and historical mercury cycle. The aim of this PhD study is to improve our understanding of the SWW trend and mercury deposition in the Holocene at remote SH sites by using geochemical and isotopic proxies in peat archives. We investigated Amsterdam Island (AMS) peat record coupled with three other peatlands in the SH mid latitudes as long-term archives of atmospheric dust and/or mercury deposition. At the northern edge of SWW and free from anthropogenic disturbance, AMS is a key site to study SWW dynamics. We find that during the Holocene, dust and mercury deposition at AMS oscillated on millennial time scales. Mercury isotope signatures, which are sensitive to rainfall inputs, indicate that high dust, high mercury events correspond to low rainfall. We suggest that these events were caused by a poleward shift of the SWW at AMS. The peat mercury records also inform on recent, human perturbation of the natural mercury cycle in the SH. We find however that the 4-fold anthropogenic mercury enrichment we observe in the SH since 1450AD, is smaller than the 16-fold enrichment in the northern hemisphere. These scientific contributions should help improve global climate models and international environmental policy under the Minamata convention on mercury.

Résumé

Les vents de sud-ouest (VSO) de l'hémisphère sud (HS) régularisent les cycles biogéochimiques du carbone de l'océan Austral en augmentant l'absorption du CO_2 atmosphérique ou en faisant remonter les éléments nutritifs et le carbone des profondeurs de l'océan. Les changements d'intensité des VSO déterminent si l'océan Austral agit comme un puits ou une source nette de CO_2, affectant ainsi la concentration de CO_2 atmosphérique et donc le climat. Les VSO régularisent également la trajectoire des poussières dans l'HS et le cycle biogéochimique du mercure, ces deux paramètres pouvant donc être utilisés en retour pour suivre la dynamique des VSO. Or, les variabilités des VSO passées et sur le cycle historique du mercure sont mal connus. L'objectif de cette étude doctorale est d'améliorer la compréhension de la dynamique des VSO et du Hg atmosphérique d'abord dans un contexte de variabilité climatique naturelle puis sur une période affectée par le changement global en HS. Nous avons étudié l'enregistrement de la tourbe de l'île d'Amsterdam (AMS) ainsi que de trois autres tourbières situéesaux latitudes moyennes de l'SH, comme archives à long terme de la poussière atmosphérique et/ou du dépôt de mercure. A la limite nord des VSO et libre de perturbation anthropique, AMS est un site clé pour l'étude de la dynamique des VSO. Nous avons révélé qu'au cours de l'holocène, les dépôts de poussières et de Hg à AMS ont oscillé sur des échelles de temps millénaires. Les signatures isotopiques du Hg, sensibles aux précipitations, indiquent que des épisodes de fortes concentrations de poussières et de Hg correspondent à de faibles précipitations. Nous suggérons que ces événements ont été causés par un transfert polaire du VSO à AMS. Les dépôts de Hg reconstruits montrent également que le quadruplement du Hg anthropique observé dans l'HS depuis 1450 reste inférieur à l'enrichissement dans l'hémisphère nord, multiplié par 16 pendant la même période. Ces contributions scientifiques permettront d'améliorer les modèles climatiques et la politique environnementale internationale dans le cadre de la convention de Minamata sur le Hg.

Extended abstract

The Southern westerly winds (SWW) are one of the main Southern Hemisphere (SH) climatic features, which regulate the Southern ocean carbon sink, mercury (Hg) biogeochemical cycles and dust trajectories from Southern South America, Southern Africa and Australia. Changes in SWW intensity are thought to determine whether Southern Ocean acts as a sink or source of CO_2, therefore affecting atmospheric CO_2 concentration and then global climate. Less is known about the long-term SWW variabilities, which hampers a thoroughful assessment on the relationship between SWW dynamics and atmospheric CO_2. Atmospheric dust deposition to mid-latitude SH records information of SWW dynamics. Atmospheric Hg mainly exists as gaseous elemental Hg (Hg^0, >95%), which has a long atmospheric lifetime (months), allowing its hemispheric dispersion before deposition to the Earth's surface, including remote areas. Hg has seven stable isotopes that fractionate both mass dependently (MDF) and mass independently (MIF) during source mixing and Hg transformation. Hg even-isotope MIF (reported as $\Delta^{200}Hg$) is conservative in the Earth's surface environment, with distinct signatures in different Hg deposition end-members (rainfall Hg^{II} and gaseous Hg^0). This gives an insight to investigate the SH mid-latitude Hg rainfall Hg^{II} deposition and subsequently the principal climate driver, SWW. Hg is a toxic element. The extent of anthropogenic Hg enrichment in the SH relative to the natural background period (<1450AD, before large-scale Spanish mining) remains unclear.

This PhD research focuses on the SWW variabilities in the Holocene and historical Hg deposition by studying the time-series variations of two atmospheric proxies, dust and Hg, both of which can derive from natural and anthropogenic emissions. Natural peat deposits can be used as archives of past atmospheric dust and Hg deposition. Peat bogs are exclusively fed by atmospheric input and therefore ideal atmospheric recorders. We principally use a peat bog profile from Amsterdam Island (AMS) as a main historical archive, coupled with three other bogs from the Falkland Islands (Islas Malvinas), and Tierra del Fuego (Argentina). AMS, located at the northern edge of SWW, is sensitive to the change in wind intensity.

In this thesis, Chapter 1 estabilishes a robust chronology for the AMS peat core and shows distal dust input to AMS peatland. Chapter 2 quantifies the amount of dust input to AMS peat from different potential sources and shows oscillated SWW at the northern edge of the wind belts in the Holocene. Chapter 3 attemps to develop a new SWW proxy by using mercury

isotopes. Chapter 4 focuses on historical mercury deposition, which highlights that atmospheric background Hg levels in the NH and SH are different.

AMS recent peat chronology is established by the ^{210}Pb Constant Rate of Supply (CRS) model, which is validated by peaks of artificial radionuclides (^{137}Cs and ^{241}Am) that are related to nuclear weapon tests. The AMS ^{210}Pb flux results coupled with an updated global ^{210}Pb data compilation show that an important quantity of continental dust is deposited over this island (Chapter 1). Using REE and Nd isotope mass balance calculations, we find Southern South America as a dominant atmospheric dust contributor (~45%) to AMS over the past 6.6 kyr. Local AMS dust sources contribute 40%, while Southern Africa contributes the remaining 15% (Chapter 2). Two mineral dust flux minima occur during 6.2-4.9 cal. kyr BP and 3.9-2.7 cal. kyr BP, interpreted as periods with equatorward-shifted and/or strengthened SWW at its northern edge. These interpretations are based on higher wind speeds leading to removal of distal dust on the way to AMS, by turbulence and enhanced wet deposition. We find that AMS peat Δ^{200}Hg, a proxy for rainfall Hg, covaries with low dust and low Hg deposition and is in agreement with the dust-based SWW variability (Chapter 3). Our results, therefore, give the first insight to use Hg isotopes as a climatic rainfall paleoproxy.

Recent peat layers show larger, 1.0‰, Δ^{199}Hg variability from mid-19th to mid-20th centuries that could reflect changes in the isotopic composition of the SH atmospheric Hg pool in response to growing industrial emissions and/or changes in Hg photochemistry (Chapter 3). Our study also shows a doubling of the Southern African dust contribution to AMS in the last 100 years relative to the long past (Chapter 2). This recent shift in dust provenance is not accompanied by enhanced dust deposition at AMS. We therefore suggest that land degradation, agriculture and dryer climate conditions in Southern Africa have led to enhanced dust mobilization in the last 100 years.

Four SH peat Hg profiles have contributed to the under-represented SH Hg dataset, showing a x3 increase in atmospheric Hg deposition since pre-industrial times (1450-1880AD). After reviewing 18 other SH sediment and 3 peat core, and updating the NH historical Hg peat and sediment database, we find that the all-time Hg increase (from pre-1450AD to 20th century) is x16 in the NH and x4 in the SH (Chapter 4). We attribute this difference to a combination of lower anthropogenic Hg emissions in the SH, and higher marine SH Hg emissions, supported by x2 higher natural background Hg accumulation in the SH peat. Our findings suggest that background Hg levels in both hemispheres are different and should be taken into account in international Hg assessment reports and environmental policy objectives.

Résumé étendu

Les vents du Sud-Ouest (VSO) sont l'une des principales caractéristiques climatiques de L'hémisphère Sud (HS). Ils régulent le puits de carbone de l'océan Austral, les précipitations et les trajectoires de poussières des latitudes moyennes du Sud de l'Amérique du Sud, de l'Afrique australe et de l'Australie. Les dépôts de poussières atmosphériques sur les continents et les îles de l'HS incorporent à leur tour des informations sur la dynamique des VSO. Le mercure atmosphérique existe principalement sous forme de Hg élémentaire gazeux (Hg^0,> 95%), d'une durée de vie suffisamment longue (6-12 mois) dans l'atmosphère pour permettre sa dispersion hémisphérique avant son dépôt à la surface terrestre, y compris dans des régions éloignées. L'ampleur de l'enrichissement anthropique en Hg dans l'HS par rapport à la période naturelle de référence reste incertaine (<1450AD, avant l'extraction minière à grande échelle en Espagne). Le Hg est caractérisé par sept isotopes stables dont les masses fractionnent de façon dépendante (MDF) et indépendante (MIF) lors des transformations du Hg. Le MIF du Hg à isotopes pairs (rapporté par Δ^{200}Hg), qui résulte de réactions photochimiques en haute atmosphère, présente des signatures distinctes selon le mode de dépôt (précipitations Hg^{II} et Hg^0 gazeux). Les dépôts de tourbe peuvent être utilisés comme archives des dépôts de poussières atmosphériques et du mercure (Hg) au cours de l'Holocène.

Cette thèse de doctorat porte sur les variations de deux variables atmosphériques au cours de l'Holocène et dans l'Hemisphéère Sud: les poussières et le Hg, pouvant toutes deux provenir d'émissions naturelles et anthropiques. Les tourbières sont exclusivement alimentées par les apports atmosphériques et sont donc des enregistreurs atmosphériques idéaux. Nous avons principalement étudié un profil de tourbière bien daté de 6.6 kyr de l'île d'Amsterdam (AMS, Océan Indien, extrémité nord-ouest de VSO), ainsi que de trois tourbières des îles Malouines et de Terre de Feu (Argentine).

Nos résultats de ^{210}Pb à AMS, associés à une compilation de données ^{210}Pb globale actualisée, montrent qu'une quantité importante de poussières continentales se dépose sur cette île (Chapter 1). En utilisant les calculs du bilan de masse à partir des données des terres rares (REE) et des isotopes du Nd, nous trouvons que l'Amérique du Sud contribue pour environ 45% à ces dépôts de poussière atmosphérique sur l'AMS au cours des derniers 6,6 kyr (Chapter 2). La contribution de l'Afrique Australe s'élève à 15%, tandis que les sources de poussières

locales d'AMS représentent 40%. Deux périodes de flux minimal de poussières minérales sont enregistrées entre 6.2 et 4.9 kyr BP et 3.9-2.7 cal. kyr BP, et interprétées comme des périodes de mouvement équatorial et/ou de renforcement des VSO à leur limite nord. Ces interprétations sont basées sur des vitesses de vent plus élevées conduisant à l'élimination de la poussière distale sur son trajet menant à AMS, par turbulence et augmentation du dépôt humide. Nous constatons que le Δ^{200}Hg (témoin de dépôt humides du Hg) enregistré à dans la tourbe de AMS correspond à un faible dépôt de poussières et de Hg (Chapter 3). Ceci est en accord avec la variabilité des VSO basée sur les poussières. Nos résultats offrent donc un premier aperçu de l'utilisation des isotopes du Hg en tant que paléoproxy des précipitations climatiques. Notre étude montre un doublement de la contribution de la poussière d'Afrique Australe à AMS au cours des 100 dernières années. Cette augmentation récente ne s'accompagne pas d'un accroissement du dépôt de poussière global. Nous suggérons donc que la dégradation des sols, l'agriculture et les conditions climatiques plus sèches en Afrique Australe ont conduit à une augmentation de la taille des zones sources mobilité accrue de la poussière.

Les profils de Hg des quatre tourbières de cette étude contribuent à la base de données globale du mercure en apportant un nombre conséquent de nouvelles données pour l'HS. Nos données montrent un triplement des dépôts atmosphériques de Hg depuis l'ère préindustrielle (1450-1880AD). Après avoir examiné 18 sondages sédimentaires et 5 de tourbe de l'HS, et mis à jour la base de données historique de l'HN, nous pouvons montrer que l'augmentation absolue du Hg (d'avant 1450AD au 20ème siècle) est d'un facteur 16 dans l'HN et 4 dans l'HS (Chapter 4). Nous attribuons cette différence à une combinaison d'émissions anthropiques de Hg plus faibles dans le SH, et d'émissions marines de Hg plus élevées dans le SH, soutenues par une accumulation de Hg de fond naturel x2 plus élevée dans la tourbe du SH. Nos conclusions suggèrent que les niveaux atmosphériques de Hg dans les deux hémisphères sont différents et doivent être pris en compte dans les rapports internationaux d'évaluation du Hg et la politique environnementale internationale en appuie de la Conventions de Minamata sur le Hg.

Acknowledgements

Looking back for the past four years, I am so grateful for what I have had and who I have met. I am just lucky, lucky to have two excellent supervisors, an amazing mentor, two great committee members, two good teams and many nice friends! My PhD life is, awesome!

Before I started my PhD life, a little bird told me that it was more difficult to have nice supervisors than to win a lottery. When I met François and Jeroen, I knew I hit the jackpot. Both of them are brilliant and patient. They are often there to supervise me in lab work, presentation, scientific writing and of course how to conduct good scientific research. In the first half of my PhD, I mainly stayed in Ecolab and worked with François. Apart from academic teaching in science, Francois also shows me how to enjoy life. When we travelled together to Poland, Argentina, Chile, China and Spain for field trips and conferences, he never stopped exploring the local cuisine when we finished work. François is also an excellent cook, from which I have benefited a lot in the first two years of my PhD! Once François told me, "Take it seriously for science, but take it easy for life." I think I will never forget about it.

I moved my office to GET to work with Jeroen when François was on secondment to Argentina last year. I still remember the frequency that I went to knock at the door of Jeroen's office for discussions on my work (at least 4 times per week). Jeroen is a super busy researcher with plenty of scientific and administrative responsibility. But he always spares his time for me, helping me better understand how science works and guiding me to think about science in a different but exciting way. For example, the first draft of my abstract to *ICMGP 2019* was pale and boring. It was Jeoren's suggestions and comments that inspired me to improve it to a very interesting version. In addition, Jeoren's way of expression is always straight to the point and enlightening. The discussions with him can always give me deeper insights about my work and other science. Both Jeroen and François are easy going and open minded. It is so comfortable and exciting to work with them!

So far, I have known some part of French culture pretty well, especially about the wine, fromage and magret de canard. Most of my French knowledge are gained from Catherine and her family (Hugo, Jane and Rémi). Catherine is my mentor for life and science. She is the best mentor I have ever had by far. When I think about Catherine at this moment, the song "*You raise me up*" just come to my mind. There are countless times that my soul was weary during my PhD period and Catherine was always there for me, giving me courage and love, like a parent. "She is so wise, intelligent and kind", said my parents after they met in my hometown

in Guangdong province, China. I cannot agree more. I have openly and secretly learned so many things from her. For example, she always respects people regardless of their backgrounds. I have seen so many times that she helped refugees and uneducated persons to make a better life. She is very good at conducting public science, such as, *le train du climat*. To do public science is part of my future projects. I think I have gained some inspirations and ideas from her these years.

The luckiest thing during my PhD life is that I have lived with Catherine and her family in a super cozy house since my arrival in France four years ago. They keep teaching me French all the time, especially Rémi, who speaks French so elegantly. One of the most exciting and interesting things to live in this house is that they cook various type of cuisine every day, which is absolutely delicious. Like Francois, Hugo and Catherine are also fantastic cooks. Hugo can not only make the dishes excellent in taste but also in looks. Jane excels in making desserts, especially chocolate cake and Tiramisu! It is a shame that I still don't know how to cook good French cuisine because I always prefer washing the dishes than cooking. But I guess I will follow the family's recipes during my post-doc. All these good times with the family support me to work efficiently for my research in science.

I have travelled to many countries for conferences and meetings by far. One fourths of the trips are funded by Gaël Le Roux, the head of BIZ team in Ecolab. Gaël is very smart and contributes a lot to improve my PhD study. He often guides me to think in a global scale in research. I had no clue how he was capable of possessing a global view of various scientific fields even including the ones out of his specialized areas, until we attended the conference *SIL 2018* in Nanjing, China together. I found out that he liked attending the keynote talks from different disciplines. He told me that those big names who gave keynotes would always give you an expert's view from a different field, from which we could learn many other sciences. What a good point! Gael is like an unofficial supervisor to me because of his great efforts on my work.

When I just arrived in France, my French was quite bad since I had only learned it for 40 days in China. In Ecolab, especially in the Clean Room, most of the experiment guidelines are presented in French. But I don't think I have a bad time working in Ecolab, mainly because of Marie-Jo, the technician with whom I work with a lot. She only speaks French but she is so patient with me and tries to explain to me all the requirements related to experiments in a clear way, even though I could not understand her instantly. I still remember one French phrase I

said often at the beginning when we worked together, "*Répétez, SVP, Marie-Jo*". She is so nice and often brings me one of my favorite cookies from Corsica.

It is always nice to have peer colleagues to discuss our research freely. I am lucky to have Max to discuss Hg and Clemens to talk about dust during my PhD. Both of them are very nice and smart. Max has spent much time with me on my Hg experiments and data analysis when Jeroen was not there. He also shared with me lots of his comments on the classical and new published Hg papers, which made me realize that we should hold a critical view for science even though we were just PhD students. With Clemens, I can always have fun on the discussions about the Clean Room, field trips and peat dust studies etc.

Sometimes the French administrative paper works can drive me crazy because they are cumbersome and time-consuming. What makes it more difficult is that I have to do it in French. But with Annick, the secretary of Ecolab, those administrative work became much easier. She is patient and always smiling, which make it really pleasant to work with her! This is the same to Franck Gilbert (head of Ecolab), Mme Soucail (head of Doctoral School), and Mme Cathala and Sheila Artigau (secretaries of doctoral school). There are two other persons related to the paper works I would like to thank, Cecile and Cyril. Both of them are Gestionnaire Financiers, who work so efficiently for the mission orders and refunds. With all these managers in the lab and doctoral school, I have saved a lot of precious time from administrative work to focus on my study.

I think I should stop blablabla here, just like Jeroen's suggestion for my study --"*try to make it concise*". Ok. Here I would like to show my gratitude to those who helped me a lot for the field work and logistic support: Svante Björck, Bart Klink and Elisabeth Michel, Alain Quivoron and Hubert Launay, Nina Marchand, Cédric Marteau, Olivier Magand and Isabelle Jouvie, Jan-Berend Stuut, Andorea, Coronato; Ramiro López and Verónica Pancotto. To those who aided me for the analysis: David Baqué, Camille Duquenoy, Aurélie Marquet, Jérôme Chmeleff, Stéphanie Mounic, Virginie Payre, Frédéric Julien, Laure Laffont, Martin Jiskra, Jean-Yves Charcosset, and Corinne Pautot. To the Liberian at OMP who helped me access many valuable literatures and books: Williams Ebrayat. To the lab informaticians: Hugues Alexandre, Julien Correge and Yann. To other administrative staff: Régine, Vincent and Christelle. To my co-authors and those who helped improve my papers: Pieter van Beek, Marc Souhaut, Nathalie Van der Putten, Natalia Piotrowska, Nadine Mattielli, Mathieu Benoit, Giles F.S. Wiggs, Stephen J. Roberts, Tim Daley, Roland Gehrels, Dmitri Mauquoy, Dominic Hodgson.

Many thanks to my lovely friends for backing me up during my PhD: Lulu, Tengteng, Hengjun, Xi, Bea, Marina, Paty, Alvaro, Gaël L.C., Laura, Hongmei, Yi, Roxeland, Vivian, Steve A., Dee A., Xinda, Thomas, Marilen, Pila, Laure G., Alex. To those who gave me a lot of fun: Theo, Amine B, Amine Z, Anom, Steve P, Clement, Columba, Pankya, Sophia H, Francesco, Alpha, Phillipe, Anne, Maritxu, Marine, Eva R., Anne P., Jean-luc P., Anna-Belle, Nicolas, Xiaojun, Wei, Xu, Buyun, Xin, Le, Ariane, Simon, Benjamin, Sabine, Jeremy, Eva, Clarisse, Diana, Juan, Amina, Roman, Thierry, David P., Cristina, Segolene, Sophia, Fausto, Joelle, Merlin, Anatole, Johana, Christelle L., Jean, Felix, Camille, Jessica, Arua, Romulo, Natalia, Dmitri, and Stefan.

A big Thank-you to *Chinese Scholarship Council* which funded my four years' PhD study. Many thanks for Prof. Dominic Hodgson and Prof. Jiubin Chen as my thesis reviewers. Their nice and constructive comments give me the green light to defense on 17th Sep, 2019.

Finally, I would like to extend my gratitude to my beloved Family, who is always there to support me. I really appreciate that Dad and Mom have taught us to be grateful and cherish what we have had since we were little. My adorable two brothers, sister (Weiheng, Ruoxian and Zhengheng) and sister-in-law (Huaxian) share the responsibility to take care of the whole family and always support each other. Because of them, I do not have to worry anything about the household and can focus on my study. I am, so lucky, to have a wonderful family.

Words are beyond my gratitude to all the persons mentioned above. Why not use some champagne? You are all warmly welcomed to my defense pot in the afternoon of 17th September 2019 at 14 Avenue Berlin, Toulouse.

2019-9-1

Contents

List of abbreviations

^{137}Cs	Cesium isotope with an atom mass of 137
^{14}C	Carbon isotope with an atom mass of 14
^{210}Pb	Lead isotope with an atom mass of 210
^{222}Rn	Radon isotope with an atom mass of 222
^{241}Am	Americium isotope with an atom mass of 241
AD	Anno Domini
AFS	Atomic Fluorescence Spectroscopy
AMS	Amsterdam Island
AND	Andorra
AUS	Australia
BC	Before Christ
BP	Before Present (1950AD)
CRS	Constant Rate of Supply
CV	Cold Vapor
DMA	Direct Mercury Analyzer
$EF_{alltime}$	Mercury Accumulation Rate Enrichment Factor from Background periods (pre-1450AD) to 20th century. The periods are defined based on a compilation of global data set.
$EF_{p/b}$	Mercury Accumulation Rate Enrichment Factor from Background periods (pre-1450AD) to Pre-industrial times (1450-1880AD). The periods are defined based on a compilation of global data set.
EF_{preind}	Mercury Accumulation Rate Enrichment Factor from Pre-industrial times (1450AD-1880AD) to 20th century. The periods are defined based on a compilation of global data set.
εNd	Epsilon Neodymium
GEM	Gaseous Elemental Mercury (Hg^0)
GOM	Gaseous oxidized mercury
HAR	Harberton
Hg	Mercury
HgAR	Mercury Accumulation Rate

ICP-OES	Inductively Coupled Plasma-Optical Emission Spectrometry
MC-ICPMS	Multi Collector-Inductively Coupled Mass Spectrometry
MDF	Mass Dependent Fractionation
MIF	Mass-Independent Fractionation
NH	Northern Hemisphere
PCA	Principal Component Analysis
PHg	Paticulate-Bound Mercury
PP	Primary Productivity
Q-ICPMS	Quadruple Inductively Coupled Mass Spectrometry
REE	Rare Earth Element
SAF	Southern Africa
SCB	San Carlos Bog (from the Falkland Islands, Islas Malvinas)
SH	Southern Hemisphere
SSA	Southern South America
SWW	Southern Westerly Winds
TIMS	Thermal Ionization Mass Spectrometry

General introduction

1. Southern Hemisphere atmospheric circulations

More than ¼ of the CO_2 released from anthropogenic activities is absorbed by the global oceans, which substanstially slows down the rate of climate change (Sabine et al., 2004). The capacity of oceans to absorb CO_2 depends on the main processes of sequestration of carbon at the ocean surface (e.g., diffusion and biological carbon pump) and the subsequent transport from surface to the deep ocean and sediments. Conversely, oceans can also emit CO_2 to the atmosphere from deep ocean by the processes, such as, upwelling and outgassing. The balance between these two sets of processes determines whether oceans act as a net source or sink of CO_2. The Southern Hemisphere (SH) consists of 81% ocean areas, marking the importance of ocean circulation on SH biogeochemistry, ecology and climate. Ocean currents, which convey ocean carbon, are principally driven by atmospheric circulations (Munk and Palmen, 1951). Atmospheric circulations are key control factors of SH climate in the past (Menviel et al., 2018; Saunders et al., 2018), the present (Ogawa and Spengler, 2019) and the future (Swart and Fyfe, 2012; Bell et al., 2019).

One of the main SH atmospheric circulation features is the easterly winds within its corresponding Hadley cell (0-30°S, Hadley, 1735), which controls the spatial distribution of both the tropical rainfall and atmospheric meridional heat transport (Donohoe et al., 2013). The tropical rainfall maximum area, named intertropical convergence zone (ITCZ, Figure 1), lies in the near-equatorial trough and constitutes the ascending branch of the Hadley circulation (Waliser and Gautier, 1993). The ITCZ is formed by the encounter of maritime moist-hot air and continental dry-hot air, leading to high convection, cloudiness and precipitation within the trade wind zone. The ITCZ plays an important role in regulating the atmospheric energy balance by releasing heat during convection and via the planetary albedo by increasing cloud formation (Waliser and Gautier, 1993). The migration and structure of the ITCZ depend on the seasons and the interhemispheric thermal gradient (Donohoe et al., 2013). ITCZ dynamics can affect the shifts in the eddy-driven westerlies and subsequently the global warming in the context of anthropogenic climate change (Ceppi et al., 2013).

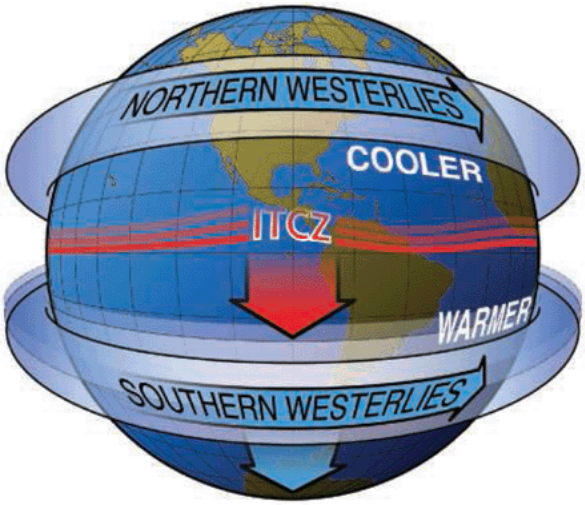

Figure 1. Positions of Intertropical Convergence Zone (ITCZ) and Southern Westerly Winds (SWW) (Toggweiler, 2009).

Another important SH climate features is the southern westerly winds (SWW), which prevail between 30 and 60°S with its core belt at ca. 50 - 55°S (Saunders et al., 2018, Figure 2). The position and intensity of SWW vary seasonally due to changes in the sea surface temperature. During the austral winter, SWW shift equatorward and expand, while during the austral summer, SWW move poleward and contract. The SWW dynamics regulate Southern Ocean carbon sink, SH mid-latitude climate, and Southern African, Australian and Southern American aeolian dust trajectories. The displacement of SWW affects the volume of precipitation in SH mid-latitude (e.g., Central Chile, Jenny et al., 2003). SWW are the main driving force of the Antarctica Circumpolar Current - the world's largest current flowing from the west to the east, connecting the Atlantic, Indian and Pacific oceans. SWW can transport the surface waters to the northern side of the wind belt, leading to upwelling to the south of the wind stress maximum (resurfacing waters from 2-3 km deep) and downwelling to the north (Rintoul, 2010). SWW can also carry dust over long distance from continental sources to remote sites (e.g., Antarctic, Gili et al., 2017).

The Southern Ocean south of 30°S, accounts for approximately 43% of the global oceanic uptake of anthropogenic CO_2 over the historical period (Frölicher et al., 2013). By resurfacing more deep ocean carbon or enhancing more CO_2 sequestration at the ocean surface, changes in the SWW intensity through time are thought to determine whether the Southern Ocean acts as a net source, or sink, of CO_2 (Menviel et al., 2018; Landschützer et al., 2015; Hodgson and Sime, 2010; Toggweiler and Russell, 2008; Thompson and Solomon, 2006; Hodgson, personal communication). This affects atmospheric CO_2 concentration and then global climate.

Some models and observations have suggested that the capacity of Southern Ocean to absorb CO_2 has weakened under the scenario of increased atmospheric CO_2 and strengthened

SWW (Le Quéré et al., 2007; Saunders et al., 2018). In this scenario, SWW enhance ocean mixing drawing deep waters with high concentrations of dissolved inorganic carbon to the surface, limiting its capacity to obsorb atmospheric CO_2 (Hodgson and Sime, 2010). This means that Southern Ocean may no longer function as a net sink of CO_2. As a result, there might be a higher level of stabilization of atmospheric CO_2 (Le Quéré et al., 2007), which will enhance global warming. In contast, observations coupled with biogeochemistry models have indicated a strengthened Southern Ocean CO_2 sinks since 2002 resulting from an increased zonal asymmetry in SH atmospheric circulation (Landschützer et al., 2015). Similarly, a model study suggests that poleward-intensified SWW have strengthened the Southern Ocean carbon sink (Russell et al., 2006). Poleward-intensified SWW are suggested to reduce oceanic stratification and allow Southern Ocean to remove anthropogenic CO_2 from the atmosphere (Russell et al., 2006).

Paleoclimate science offers a unique opportunity to investigate the SWW dynamics by providing long-term reconstructions of changes in their strength and position. The reconstructions can be achieved by investigating the wind proxies within different natural archives (ice, sediment and peat) in different SH regions. Numerous archive-based studies have attempted to reconstruct past SWW variability in three different sectors (northern edge with ~35-45°S, core section at ~50-55°S and southern edge below-55°S). The wind variabilities at the northern edge, the core belt and the southern edge of the SWW can be dependent or independent from one another, which highlights the complexity of the SWW dynamics (e.g., Lamy et al., 2001; 2010; Moreno et al., 2010; Lindvall et al., 2011; Van der Putten et al., 2012; Voigt et al., 2015; Saunders et al., 2018). Even though at similar latitude but different longitude, SWW may be recorded with distinct behaviors. For example, during 3-1 cal. kyr BP, Moreno et al., (2010) suggests a poleward-shifted SWW based on pollen signatures from lake sediment at 41°S in Southern Chile, while Voigt et al., (2015) indicates an equatorward-shifted SWW derived from oxygen isotope composition in marine sediment at 38°S in Western South Atlantic. So far, most field studies related to the past SWW dynamics have been conducted in Southern South America (e.g., Lamy et al., 2010; Xia et al., 2018), Southern Africa (e.g., Humphries et al., 2017; Chase et al., 2017) and Australia (e.g., Shulmeister et al., 2004; Marx et al., 2011). By comparison, less attention has been given to SWW records from oceanic islands (e.g., Amsterdam Island, Diego Ramirez Island, Macquarie Island, Saunders et al., 2018), which have minimal continental complex orographic effects and regional climatic effects (e.g., monsoon climate in Australia), and able to directly record SWW variations.

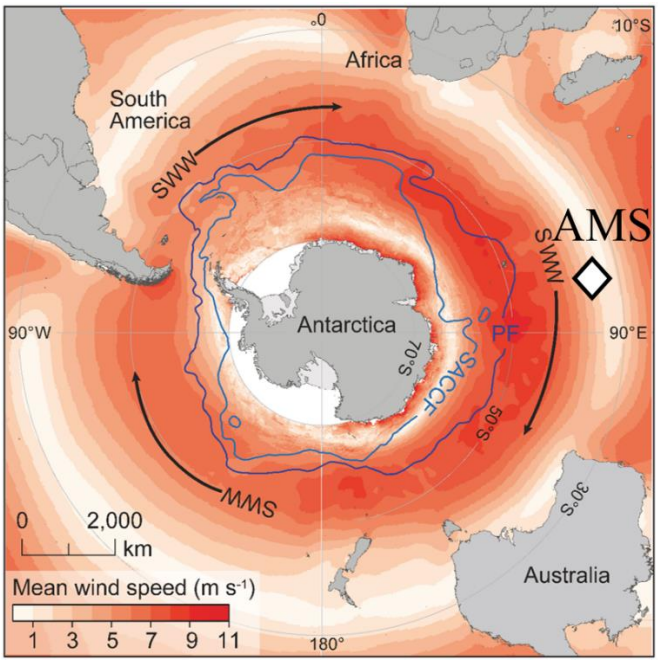

Figure 2. Southern Westerly Winds (SWW) and wind speeds. White diamond is the location of Amsterdam Island (AMS), which is the main study site of this PhD. The core SWW belt is between 50-55°S**.** Arrows show wind direction. (Modified from Saunders et al., 2018)

2. Amsterdam Island peat as an archive of Southern Westerly Winds dynamics

Amsterdam Island (AMS, 55 km^2), is located at the northern edge of SWW and halfway between Southern African continent and Australia (Figure 2). This island is sensitive to the changes in the SWW and free from anthropogenic influence. It is an ideal site to study the past SWW variabilities. Ombrotophic peatlands, archives of atmospheric deposition, are widespread in AMS. Details on AMS see the description on "study site" in Chapter 1, 2 and 3.

2.1 Peatlands as archives of atmospheric deposition

A peatland is an ecosystem characterized by organic soils from the accumulation of decomposed plant materials. The organic matter is produced and deposited at a greater rate than it is decomposed, which leads to the formation of peat. Peat net mass accumulation (g m^{-2} yr^{-1}) is the balance between annual net primary production and annual decomposition, regardless of geographic location (Wieder and Lang, 1983). Peat mass is added at the surface and the material will decay after death. The decomposition processes, which cause the collapse of the peat, mainly occur in aerobic conditions (Clymo, 1984) and above the water table. This part of the peat column is referred as the acrotelm (Ingram, 1978). Below the water table, conditions are anaerobic with low oxygen diffusion in water (Clymo, 1984) and this part of the

profile is referred as the catotelm (Ingram, 1978). In this section, the decay rate of most materials by anaerobic microflora is much lower than that in aerobic conditions.

Peatlands are estimated to occupy 3.5 million km^2, covering 3% of the Earth's land surface (Gorham, 1991; Lappalainen et al., 1996, Figure 3). More than 85% of the peatlands are distributed in the Northern Hemisphere, under cold temperate climates and high humidity, covering Europe, Russia and North America. Only a small proportion of peatlands (<10%) exists in Southern America, Southern Africa, Australia, New Zealand and small oceanic islands in the Southern Hemisphere (e.g., Amsterdam Island, The Falkland Islands (Islas Malvinas)).

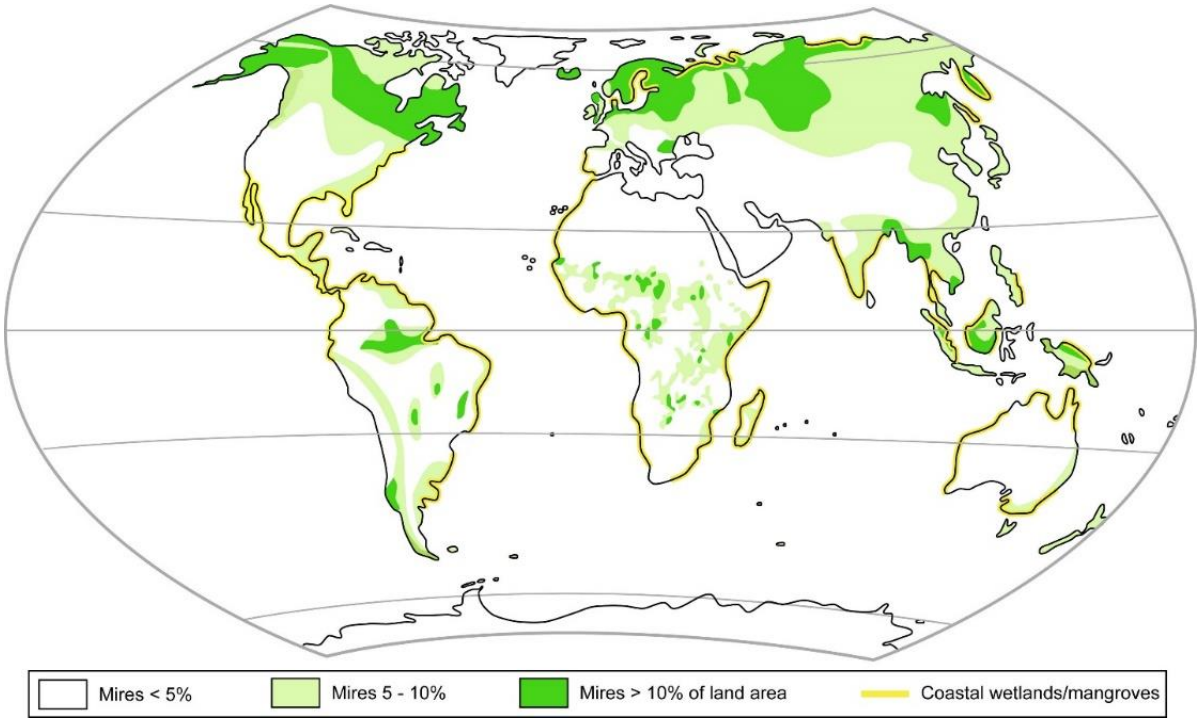

Figure 3. Global Peat Ressources. (Redrawn after Lappalainen 1996).

Peatlands are sensitive to changes in the local hydrological regime and mineral inputs under both climate change and basin geomorphology alternation (e.g., Charman et al., 2009; Mitsch and Gosselink, 2015). Peat cores as environmental archives have the advantages of: 1/ being easy to access due to its worldwide-spread status, especially in the mid-latitudes; 2/ covering Holocene or beyond and 3/ well preserving climatic/atmospheric signals (e.g., macrofossils and chemical elements). Peat cores can be used to reconstruct paleoclimate variability under investigations on multi proxies from biological aspect (e.g., pollen, macrofossils, diatoms and testate amoebae) or from geochemical and isotopic perspectives (e.g., minerogenic input and gas uptake).

Ombrotrophic Peatland, one type of peatlands, exclusively receive nutrients, water and pollutants/chemicals from the atmosphere. They are unique to atmospheric deposition study and have been proven to be reliable archives for particle deposition (e.g., dust, Shotyk et al., 2001; De Vleeschouwer et al.,2014; Kylander et al., 2018) and gas deposition (e.g., Hg^0, Enrico et al., 2016; 2017).

2.2 Reconstructions of peat chronology

Absolute age constraint plays a fundamental role in reconstructing past climate variability in the environmental archives. Methods by radiocarbon dating (conventional ^{14}C and post-bomb ^{14}C) and ^{210}Pb are widely used in peat studies. Radiocarbon (^{14}C) dating method was discovered by W.F. Libby, (1949) 70 years ago, which is one of the most reliable dating approaches for the whole Holocene. ^{14}C is the only radioactive form of three natural carbon isotopes (^{12}C, ^{13}C and ^{14}C), with a half-life of 5730 ± 40 years (Godwin, 1962). ^{14}C constitutes of a tiny amount of total carbon, e.g., ~1.2 * 10^{-10}% in the troposphere (Olsson, 1968). ^{14}C is continuously produced in the lower stratosphere and upper troposphere by the interaction of the secondary neutron flux from cosmic ray with atmospheric ^{14}N (Hua, 2009; Gäggeler, 1995). Once produced, ^{14}C is oxidized to $^{14}CO_2$ and subsequently diffuses throughout the Earth Surface. Terrestrial living organisms can take up CO_2 from the atmosphere, with $^{14}C/C$ ratio similar to that in the atmosphere. Once the organisms die, they stop exchanging the $^{14}CO_2$ with atmosphere. Then $^{14}CO_2$ decays gradually to ^{14}N. Based on the remaining ^{14}C content and the decay rate, one can calculate the time (^{14}C age) when the organism died. Peat is mainly formed by organic matters, rich in C content (Charman, 2002). Macrofossils (e.g., Sphagnum, moss) from the peat are generally selected for ^{14}C dating.

^{210}Pb, a natural radioactive isotope of lead, is a decay product of ^{222}Rn. The decay processes occur in both atmosphere and the soil. The ^{210}Pb faction of atmospheric origin is called "unsupported ^{210}Pb", which is used to reconstruct the recent age by Constant Rate Supply (CRS) and Constant Initial Concentration (CIC). CRS model assumes a constant rate of ^{210}Pb supply irrespective of any variations which may have occurred in the sedimentation rate, while CIC model assumes a constant initial ^{210}Pb concentration regardless of any changes in the sedimentation rate (Appleby and Oldfield, 1978). There are many cases that can lead to invalidity in both CRS and CIC models, such as, mixing of the surficial sediment by physical and biological processes (Appleby, 2001), and Pb mobility during the post-depositional stage. In this case, some independent dating proxies are needed to validate the CRS or CIC models. A widely application of chronomarkers are ^{137}Cs and ^{241}Am, which are mainly produced during

the nuclear test from 1950s to 1960s with peaking at 1963, and during Chernobyl accident at 1983. Ombrotrophic peatlands receive ^{210}Pb fallout by atmospheric deposition. If CIC model is applicable, the unsupported ^{210}Pb concentration in the peat colume must show a monotonic decline with depth (Appleby and Oldfiled, 1983). Considering the organic decay characteristic of peat, the CIC model may be inappropriate for dating peat accumulations (Appleby and Oldfield, 1992; Appleby et al., 1997). Numerous researches have successfully applied CRS models to the peat archives with validation by chronomarkers (e.g., ^{137}Cs and ^{241}Am, Olid et al., 2013) and/or comparison to post-bomb age (e.g., Davis et al., 2018).

Post-bomb ^{14}C is different from the conventional ^{14}C, with the former of anthropogenic origin and the latter from natural source. Post-bomb calibration curves can be applied to the age reconstruction over the last 70 years (Hua et al., 2013). The tropospheric bomb ^{14}C start to rise in the mid-1950s with peaking in the 1960s due to the influences of aboveground nuclear explosions. At mid to high latitudes, the value of peaked bomb ^{14}C at 1963-1964 almost doubles its pre-bomb level (e.g., Levin et al., 1985). The post-bomb era lasts up to very recent time with a decreasing trend of atmospheric ^{14}C since 1964 (Hua et al., 2013). The decreased atmospheric ^{14}C signature results from the cease of the nuclear detonations and exchange between hemispheres. The bomb ^{14}C from nuclear test in the atmosphere will die out at ca. 2030 AD and cannot serve any longer as an age indicator for the periods after 2030.

Age-depth model can be generated with a sequence of ^{14}C dates and/or calibrated calendar ages based on ^{210}Pb or post bomb using classical age modelling (Clam, Blaauw, 2010) or Bayesian methods (Bacon, Blaauw and Christen, 2011). Clam can generate age-depth model in the forms of linear interpolation, linear/polynomial regression and smoothed/cubic splines with calibrated ^{14}C dates (Blauuw, 2010). However, the outliers in the sequence of ^{14}C dates can bias the age model leading to some unrealistic changes in the accumulation rate (Blaauw and Christen, 2005). Bacon is applied to Bayesian statistics and characterized by the assumed constant piecewise accumulation rate. This Bayesian method can be programed with prior knowledge, which allows the researchers adjust the model based on the core conditions. However, the simplified piecewise constant accumulation rate may smooth from a lesser to a greater extent some abrupt change in the deposits. For this case, some additional chronomarkers are needed to better reconstruct the age model, such as, tephra (Vandergoes et al., 2013). Both of Clam and Bacon methods have been widely applied to the global peat study (e.g., Martinez-Cortizas et al., 1999; Marx et al., 2009; Piotrowska et al., 2011; Van der Putten et al., 2015). The choice of methods should be site specific.

3. Wind proxies based on the transport and provenance of dust

There are three main groups of wind proxies that used in archive-based studies: 1/ dust provenance and flux (e.g., Vanneste et al., 2015; 2016); 2/ sea salt aerosol flux (directly through geochemical measurements, and indirectly through diatoms and testate amoebae, e.g., Saunders et al., 2018; Whittle et al., 2018); and 3/ rainfall indicators (inferred from macrofossil, pollen, lake levels, magnetic susceptibility, and isotopes, e.g., Van der Putten et al., 2015; Jenny et al., 2003; Lindvall et al., 2011). Below are the introdutions on dust and its potential as wind proxies.

3.1 Atmospheric dust distribution and transport in the Southern Hemisphere

Atmospheric Dust is one type of primary aerosol, while sea salt is another type (Raynaud et al., 2003; Kohfeld and Tegen, 2007). Primary aerosol originates from the dispersal of fine materials from the continental areas (so called dust) and ocean surface (so called sea salt). To be specific, dust is defined as small particles mostly generated by wind from solid materials in the continental regions. Secondary aerosols result from chemical reactions and condensation of atmospheric gases and vapors, e.g., sulfate aerosol droplets formed by oxidation of gaseous dimethylsulfide emitted from marine biogenic activity (Raynaud et al., 2003).

Dust emission and deposition are sporadic phenomena, especially in areas close to the main dust sources (Jickells and Spokes, 2001). There are four main dust source areas on Earth (Bryant et al., 2007; Engelstaedter and Washington, 2007; Prospero et al., 2002; Vickery et al., 2013; Li et al., 2008): (1) Sahara, Arabian and Gobi deserts in the Northern Hemisphere (NH); (2) Kalahari desert in Southern Africa (SAF); (3) Patagonian desert in Southern South America (SSA), and (4) the Great Artesian basin desert in Australia (AUS, Figure 4). Desert dust emissions from most dust sources have doubled over the 20th century due to anthropogenic activities (Mahowald et al., 2010). The current global dust emission is modelled as 2323 Tg yr^{-1}, with approximately 90% from the NH. AUS shares half of the remaining 10% global dust emission with 120 ± 8.4 Tg yr^{-1}. SSA plays a second important role in the SH annual dust emission with 50 ± 3.0 Tg yr^{-1}, while SAF contributes 34 ± 2.1 Tg yr^{-1} (Li et al., 2008). These three SH continents (SSA, SAF and AUS) partially fall in the SWW. SWW can affect the SH dust emissions and depositions by regulating the wind speed and humidity.

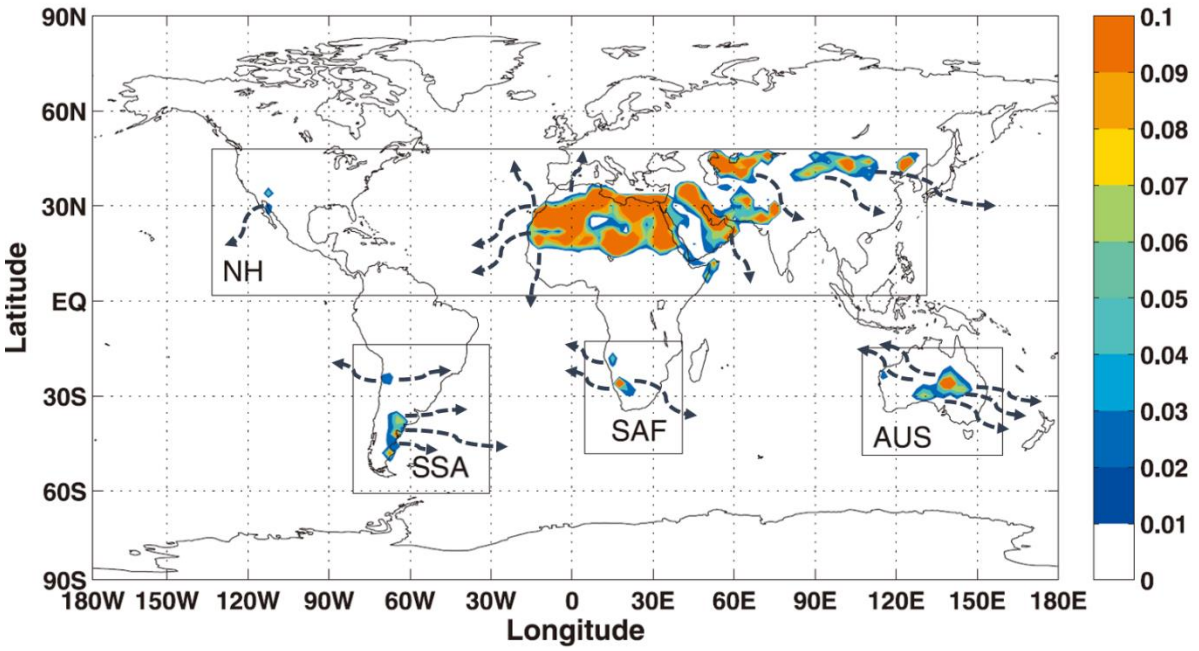

Figure 4. Global distribution of averaged annual dust emission from 1979 to 1998 (kg m^{-2} yr^{-1}). The four main dust sources NH, SSA, SAF and AUS represent Northern Hemisphere, Southern South America. Southern Africa and Australia, respectively. Dark blue dashed arrows represent the main dust trajectories. (Modified from Li et al., 2008)

Atmospheric dust generally goes through three steps in one full cycle: emission, transport and deposition (e.g., Bergametti and Forêt, 2014). Dust generation is a highly complex process that is controlled by multiple environmental factors (e.g., wind, dryness and sparsely-covered vegetation in the soil surface, Mahowald et al., 2005). Dust can be lifted into the atmosphere when high winds pass over the erodible surfaces. When air currents drive the particles along the surface, these particles collide with other solids on the ground, breaking them into smaller pieces, which may easily become airborne and be entrained into the atmosphere (e.g., Van Loon and Duffy, 2017). Wet soil surface and vegetation can stabilize soil dust and limit its mobilization by consuming a proportion of the wind momentum (Mahowald et al., 2005). Thus, an increase in the non-erodible factors can lower the dust availability. Disturbance of the soil surface by anthropogenic activities (e.g., deforestation, agriculture) can facilitate the dust generation, by producing substantial amounts of relatively large particles (tens to hundreds μm diameter) on the soil surface. These large partciles can be "gripped" and transported by the wind (Mahowald et al., 2005). The extra-small particles (i.e., <0.4μm) are not available to wind erosion individually, probably due to agglomeration and adhesive binding with other soil particles (Tegen and Fung, 1994).

When being uplifted into the atmosphere, dust can be transported by prevailing winds over hundreds or even thousands of kilometers to remote locations. Saharan dust is carried over long distances and deposits over Europe (Le Roux et al., 2012; Conceição et al., 2018; Gobbi et al., 2019) and the Caribbean Sea (Groß et al., 2016; Velasco-Merino et al., 2018). Dust from the Gobi desert is transported over the Eastern Pacific Ocean (Tan et al., 2017; Dong et al., 2018). Patagonian dust is transported over thousands of kilometers reaching the west coast of South Africa and Australia (Johnson et al., 2011), the Southern Ocean (Neff and Betler, 2015) and East and West Antarctica (Gili et al., 2016; Delmonte et al., 2017). Australian dust is exported to New Zealand (Brahney et al., 2019) and Antarctica (Sudarchikova et al., 2015; Winton et al., 2016).

The loading of atmospheric mineral dust is controlled by dust sources (e.g., aridity, vegetation cover and geology) and climate (e.g., wind strength and airmass circulation) (Harrison et al., 2001; Marx et al., 2018; De Deckker, 2019). For example, higher surface wind speeds can uplift greater amounts of dust. Increased aridity has the potential to expand source areas and decreased atmospheric water content can reduce the washout of sub-micron aeolian dust (Mahowald et al., 2005). The current human-climate interaction (e.g., global warming), can alter dust mobilization by changing the local vegetation cover (Guan et al., 2016; Brahney et al., 2019), and the size of water bodies (Prospero et al., 2002). To study environmental and climatic variability, geochemical dust signatures can be used as wind proxies by assessing dust flux and origins.

3.2 Identification of dust origins

Reconstructions of dust deposition rates and provenances allow us to identify the changes in the source areas and transport pathway associated with climate variability and/or anthropogenic influence (Marx et al., 2018; De Vleeschouwer et al., 2014; Prospero et al., 2002; De Deckker, 2019). Proxies used for source fingerprint range from physical properties (e.g., grain size), to chemical signatures (e.g., rare earth elements), and to isotope compositions (e.g., Neodymium (Nd), Strontium (Sr), Lead (Pb)). Regardless of its nature (physical, chemical and isotopic signatures), dust serving as a tracer should have three characteristics, 1/ representative for a geographical region; 2/ distinctive for that region respect to other areas; 3/ conservative from the source to the sink (Delmonte, 2003).

Different origins of minerals may have different size distributions, which can enable us to distinguish the dust sources in the deposited archives (Stuut et al., 2002; Weltje and Prins, 2007;

Gaiero et al., 2013). For example, different dust events have specific fingerprints of particle mode (e.g., a median mode of 12-14 μm, Gaiero et al., 2013). Mineral particles over 20 μm are generally assumed to originate from local/regional areas, because they can rarely be transported over long distances (e.g., several thousands of km) (Lancaster, 2013), except some rare cases (>70μm Saharan dust travelling over 1000km, Betzer et al., 1988). Note that grain size distribution method should be carefully applied to natural archives. For example, in peat studies, a pre-treatment procedure of 550°C for the grain-size analysis, may induce the formation of larger-size salt, which can subsequently bias the results. Conservative chemical elements are less prone to be altered during weathering, transport and the preparation procedures for analysis, which can then well preserve the source information. The conservative properties of the chemical elements coupled with well-developed analytical methods allow us to reconstruct dust flux and identify source origins. The chemical-ratio approaches (e.g., Aluminum/Titanium, Lanthanum/Ytterbium) have been broadly applied to climate-related dust studies in ice cores (e.g., Thompson et al., 2002; Bohleber et al., 2018), sediment (e.g., Bertrand et al., 2014; Frugone-Álvarez et al., 2017; Saunders et al., 2018) and peat (e.g., Shotyk et al., 2001; Marx et al., 2014; Von Scheffer et al., 2019). Since the conservative chemical elements do not always have distinct signatures among different sources, it may be not sufficient to only apply chemical approaches to source identification.

Isotope applications have opened a promising avenue to investigate dust provenance. Isotopic signatures of Nd, Sr and Pb are conservative and may have a distinct geological distribution. For example, $^{143}Nd/^{144}Nd$ signature (denoted as εNd, DePaolo and Wasserburg, 1976) has a range of -15 to 2 in Australia (Revel-Rolland et al., 2006; De Deckker, 2019), of -25 to -8 in Southern Africa (Grousset et al., 1992; Delmonte et al., 2004; Wegner et al., 2012; Hahn et al., 2016), and of -10 to -3 in Puna-Altiplano Plateau, -6 to 0 in Central Argentina, and of-1 to 5 in Patagonia from Southern South America (Gili et al., 2017). Since targeted isotopes may be less abundant in samples and easily be interfered by other element/isotopes during analysis, isotopic approaches require careful chemical separation from the matrix and highly sensitive mass spectrometry. No dust tracer can be universally applied to every study. Each work should choose the optimum approaches to investigate the dust origin based on the archive itself, lab environment and budgets.

Combining isotope and element geochemistry are effective in identifying the dust sources and subsequently accessing the environmental changes (Kohfeld and Tegen, 2007; Cheng et al., 2018), provided that some conditions are satisfied (e.g., selecting the optimum tracers and

easily accessing the the signatures of relevant tracers from the potential source areas). Investigation on dust sources using isotope and elment geochemistry identifies Southern South America (Patagonia and Puna-Altipalno Plateau) as the most important dust source supply to Antarctica (Delmonte et al., 2004; Gili et al., 2017), and to the Atlantic sector of the Southern Ocean during glacial periods (Noble et al., 2012). It is found the supply of continental-sourced detritus to the Southern Ocean during the last glacial period (Noble et al., 2012; Franzese et al., 2006), and an enhanced influence of local Antarctic dust to a peripheral area of the East Antarctic ice sheet during interglacial periods (Baccolo et al., 2018). Isotope and element geochemistry have also been applied to identify the past SWW dynamics in Southern South America (Vanneste et al., 2015; 2016), Southern Africa (Humphries et al., 2017), Australia (Marx et al., 2011) and Macquarie Island (Saunders et al., 2018).

4. Wind proxies based on precipitations using mercury stable isotopes

This section will broadly introduce mercury, its isotopes and its potential as a rainfall proxy.

4.1 Global biogeochemical mercury cycle

The word mercury (Hg) is originally derived from Latin '*Hydraryrum*' with the meaning of 'liquid silver'. Compared to silver, Hg, however, can be toxic at low doses in the organic form, methyl-Hg (see section 5, UNEP-GMA, 2018). Hg is the only element which exists in the liquid form at room temperature (melting point, -38.9°C), with a low enthalpy of vaporization (ΔH_{vap}= 59.15 kJ/mol). More than 95% of atmospheric Hg exists as gaseous elemental Hg (Hg^0), while smaller proportions exist as gaseous oxidized Hg (Hg^{II}) and particle-bound Hg (PHg) (Shia et al., 1999; Saiz-Lopez et al., 2018). Atmospheric Hg species can transform from one to another under certain conditions. For example, the presence of halogens under sunlight can oxidize emitted-Hg^0 into Hg^{II}, which finally deposits over the ocean surface in the form of Hg^{II} and/or PHg (Vandal et al., 1993; Fu et al., 2016a; Saiz-Lopez et al., 2018). Conversely, Hg^{II} can be reduced back to Hg^0 by photochemical reactions (Bergquist and Blum, 2007), biotic (Kritee et al., 2007; Demers et al., 2018) and abiotic conditions (Zheng et al., 2018). The speciation of Hg affects its lifespan at the atmosphere, with residence time ranging from days for PHg, to weeks for Hg^{II}, and to months for globally-distributed Hg^0 (Horowitz et al., 2017; Saiz-Lopez et al., 2018). The long residence time of Hg^0 in the troposphere allows it to travel over long distances and deposit to remote areas including Arctic (Korosi et al., 2018), Southern Ocean areas (Angot et al., 2014) and Antarctic (Zaferani et al., 2018).

Hg^0 is emitted naturally by outgassing of the Earth's crust and mantle (e.g., volcanism) as primary release, and by re-emission of geogenically-sourced Hg from soil, vegetation and water bodies (e.g., ocean, Amos et al., 2015). In addition to natural release, Hg^0 has been substantially liberated from geological deposits by human industrial activities, such as mining, refining and energy production (Pirrone et al., 2010; Streets et al., 2017). When entering the aquatic and/or terrestrial environment, Hg from these two sources will have the same fate for the subsequent life cycle.

Atmospheric Hg deposition over Earth's surface occurs by vegetation Hg^0 uptake (dry deposition, Jiskra et al., 2018), Hg^{II} wet and dry deposition (Sprovieri et al., 2017), and Hg^0 gas exchange with aqueous water bodies including the Oceans. A growing amount of evidences have highlighted the role of vegetation as Hg^0 pump (Obrist et al., 2017; Jiskra et al., 2018; Olson et al., 2019). Vegetation cover constitutes 80% of Earth's continental surface (Schulze, 1982) and provides substantial leaf surface area for pollutant exchange (Bush and McInerey, 2015). Previous observational studies have shown that leaf interior is the dominant pathway of Hg accumulation under plant growth period (Rutter et al., 2011). Foliar Hg accumulation rate may be species-dependent (Pokharel and Obrist, 2011; Rutter et al., 2011; Teixeira et al., 2018; Pérez-Rodríguez et al., 2018; Olson et al., 2019). Non-vascular vegetation (e.g., peat) accumulates x3 to x6 times more Hg than vascular vegetation (Olson et al., 2019). Hg sequestration by vegetation is controlled by primary productivity, which is related to climate variability (e.g., temperature, humidity, Gallego-Sala et al., 2018; Wang et al., 2017). Gallego-Sala et al., (2018) suggests longer and warmer growing seasons under global warming will lead to enhanced primary productivity at mid to high latitudes in the future. Increased rainfall can also promote water-limited plant primary productivity (Wang et al., 2017). The influence of climate on plant Hg sequestration can lead to a question: Is it possible to use deposited Hg (e.g., vegetation uptake of Hg^0 and input of rainfall Hg^{II}) as a proxy to reconstruct the prevailing climate?

4.2 Hg isotope signatures in the environment

Mercury has 7 stable isotopes with a relative mass range of 4% with approximate abundances of: ^{196}Hg (0.16%), ^{198}Hg (10%), ^{199}Hg (17%), ^{200}Hg (23%), ^{201}Hg (13%), ^{202}Hg (30%), ^{204}Hg (6.8%) (Blum and Bergquist, 2007). Hg isotope geochemistry studies have been abundantly conducted since the appearance of high-precision analytical equipment (i.e., Multicollector inductively coupled plasma mass spectrometry). Since Hg stable isotopes have a volatile form (Hg^0), redox-active properties and a tendency to form covalent bonds, they can undergo

isotopic fractionation (Bergquist and Blum, 2007). Nearly all incomplete, physico-chemical Hg transformations are accompanied by mass-dependent isotope fractionation (MDF, presented by δ^{202}Hg (‰), see equation 1, XXX represents for the mass of isotope). MDF is the fractionation of isotopes in proportion to the relative difference in the masses. In addition to MDF, Hg isotopes can also undergo mass-independent fractionation (MIF). MIF is the fractionation of isotopes nonlinear to their mass differences. Odd-MIF for odd mass number Hg isotopes is presented by Δ^{199}Hg or Δ^{201}Hg, while even-MIF for even mass number Hg isotopes is presented by Δ^{200}Hg or Δ^{204}Hg (Blum and Berquist, 2007; Young et al., 2002, See equations 2-5).

$$\delta^{XXX}\text{Hg} = \{[(^{XXX}\text{Hg}/^{198}\text{Hg})_{sample}/(^{XXX}\text{Hg}/^{198}\text{Hg})_{SRM3133}]\text{-}1\} \text{ X } 1000 \quad \text{(Eq. 1)}$$

$$\Delta^{199}\text{Hg} = \delta^{199}\text{Hg} - (\delta^{202}\text{Hg X } 0.2520) \quad \text{(Eq. 2)}$$

$$\Delta^{200}\text{Hg} = \delta^{200}\text{Hg} - (\delta^{202}\text{Hg X } 0.5024) \quad \text{(Eq. 3)}$$

$$\Delta^{201}\text{Hg} = \delta^{201}\text{Hg} - (\delta^{202}\text{Hg X } 0.7520) \quad \text{(Eq. 4)}$$

$$\Delta^{204}\text{Hg} = \delta^{204}\text{Hg} - (\delta^{202}\text{Hg X } 1.493) \quad \text{(Eq. 5)}$$

Hg isotope signatures can be used to better constrain on source, transport and transformations of Hg in the environment (e.g., Demers et al., 2018; Sonke, 2011). Two mechanisms relevant to Hg MIF are the magnetic isotope effect (MIE) and the nuclear volume effect (NVE). MIE primarily occurs during photochemical radical pair reactions. Odd-mass isotopes can have high MIF due to its magnetic spin, which can enhance triplet to singlet and singlet to triplet intersystem crossing (Blum, 2012). NVE occurs because nuclear volume and nuclear charge radius do not scale linearly with the number of neutrons. NVE in Hg transformation has not been fully understood. Only a few studies have observed NVE under laboratory environments (Estrade et al., 2009; Zheng and Hintelmann, 2010). Hg isotope mass independent fractionation caused by NVE (< ~0.5 ‰) is found to be smaller than by MIE (> 1‰) (Blum et al., 2014). Hg MIF leads to significant enrichments or depletions of odd mass number Hg isotopes relative to the even ones in environmental Hg pools. Different pathways of Hg transformation can result in different Hg MDF and MIF signatures in the products and reactants. Hg isotopic fractionation can therefore be applied to trace the transformation processes and/or sources. Bergquist and Blum, (2007) found that natural sunlight can lead to photochemical reduction of aqueous Hg species in the presence of organic matter, with a slope of 1.15 ± 0.07 (1σ) in the Δ^{199}Hg/δ^{202}Hg line of produced Hg^0 and residual Hg^{II}, whereas a slope of 2.43 ± 0.10 (1σ) in the Δ^{199}Hg/δ^{202}Hg line of produced Hg^0 and residual methylmercury under photochemical degradation of methylmercury. After a compilation of Hg

isotope study up to 2014, Blum et al., (2014) found different reactions of producing Hg^0 from Hg^{II}/ methylmercury lead to different $\Delta^{199}Hg/\delta^{202}Hg$ signatures, with slopes ranging from -3.5 during photochemical reduction from snow (Sherman et al., 2010), to -0.8 during Xenon lamp reduction with thiol ligands (Zheng and Hintelmann, 2010), to 0.1 during equilibrium evaporation, to 1.2 during aqueous photochemical reduction and to 2.4 during aqueous photochemical demethylation. No odd MIF is found during microbial methylation/reduction/demethylation and Thiol-ligand binding/iron oxide in the absence of sunlight sorption (Kritee et al., 2007; 2009; Rodríguez-González et al., 2009).

The development of Hg isotope tools has enabled us to quantify the Hg depositions from different sources. During a long period (> 30 yrs), wet deposition was thought to be dominate Hg deposition over terrestrial environment and great efforts have been given in studying Hg flux in rainfall (e.g., Sorensen et al., 1994; Bullock et al., 2002; Lindberg et al., 2007; Selin et al., 2008; Prestbo and Gay, 2009; Huang et al., 2012; Sprovieri et al., 2017). Relative to wet deposition, Hg dry deposition (e.g., plant uptake of Hg^0) is difficult to measure, leading to unclear contributions of Hg dry deposition to the Earth's surface. Demers et al., (2013) was the first to apply Hg isotopic values ($\Delta^{199}Hg$ and $\delta^{202}Hg$) from different sources (foliage, underlying mineral soil and rainfall) to reconstruct the Hg sources in forest floor. The authors found that only ~16% of input is from rainfall, which is against the dominant role of Hg wet deposition. The authors attribute the lower Hg wet deposition to a greater throughfall input, assuming that the isotopically unconstrained throughfall has similar Hg isotopic signatures as foliage. Similarly, some other studies also suggest a dominant Hg dry deposition to the boreal forest floor, rather than Hg^{II} precipitation, by Hg isotope MIF and/or MDF mixing calculation (Jiskra et al., 2015; Zheng et al., 2016; Wang et al., 2017). These studies have broadly distinguished the contributions of Hg dry and wet deposition, even though their approach of using $\Delta^{199}Hg$ and/or $\delta^{202}Hg$ is not free from bias. MDF ($\delta^{202}Hg$) can fractionate during the source mixing (e.g., preferential of light isotope uptake by plant) and Hg transformation, while MIF ($\Delta^{199}Hg$) can occur under photochemical reduction. Overall, $\delta^{202}Hg$ and $\Delta^{199}Hg$ might have given unprecise output in source mass balance calculation.

4.3 The potential of Hg stable isotopes as rainfall proxies

MIF of even Hg isotopes (reported as $\Delta^{200}Hg$ and $\Delta^{204}Hg$) is thought to be conservative at the Earth's surface. Even MIF isn't observed in anthropogenic Hg sources, but it is present in precipitation (Gratz et al., 2010; Chen et al., 2012; Demers et al., 2013; Enrico et al., 2016; Obrist et al., 2017) and in ambient atmospheric Hg^0 (Enrico et al., 2016). In general, Hg^0 is

characterized by negative Δ^{200}Hg (-0.06 ± 0.02‰, 1σ, n=71) and positive Δ^{204}Hg (0.07 ± 0.05‰, 1σ, n=32) (Enrico et al., 2016; Gratz et al., 2010; Demers et al., 2013; Obrist et al., 2017; Sherman et al., 2010; Fu et al., 2016a; 2016b). Different from Hg^0, rainfall Hg^{II} is characterized by positive Δ^{200}Hg (0.19 ± 0.13‰, 1σ, n=77) and negative Δ^{204}Hg (-0.16 ± 0.17‰, 1σ, n=17) (Enrico et al., 2016; Gratz et al., 2010; Chen et al., 2012; Demers et al., 2013; Obrist et al., 2017). Observations of Δ^{200}Hg anomalies in rainfall from Canada is explained by upper airmass origin, which undergoes photo-oxidation at the tropopause (Chen et al., 2012). Distinct Δ^{200}Hg signatures between Hg^0 and rainfall enable us to identify different Hg deposition pathways.

Atmospheric mercury deposition to ombrotrophic peatlands mainly occurs in two ways: peat vegetation uptake of Hg^0 and rainfall Hg^{II} input. A recent study has successfully applied Δ^{200}Hg to quantify the contribution of Hg^0 uptake and rainfall Hg input to ombrotrophic peatlands in the NH, and shows that rainfall Hg^{II} input contributes approximately 20% of total Hg deposition to the peat surface in the modern time (Enrico et al., 2016). Rainfall in SH mid-latitudes is regulated by SWW (Jenny et al., 2003). Changes in SWW intensity can shift the rainfall volume and subsequent rainfall Hg^{II} input in the areas that are sensitive to SWW variations. Hg even isotopes can be used as powerful tools in quantifying the SWW-related rainfall Hg^{II} deposition and hence, SWW dynamics. This requires Hg isotopic compositions from historical archives and sources (Hg^0 and rainfall) at local or regional scales.

5. Investigation on anthropogenic Hg deposition and background atmospheric Hg levels

Over the past centuries, Hg has been abundantly transferred to the Earth's surface from geological deposits due to human activities, which has greatly increased the modern atmospheric Hg level (Lindberg et al., 2007; Amos et al., 2015; Streets et al., 2017; Enrico et al., 2017). A cumulative total of 1540 (1060-2800) Gg (gigagrams, 10^9 grams) of Hg is estimated to have been released into the environment by human activities by 2010, of which 73% was released since industrialization (Street et al., 2017). The anthropogenic Hg deposition to the environment can potentially elevate the environmental concentration of methyl-Hg (Sunderland et al, 2018).

Methyl-Hg is a toxin of high concern that can bio-magnify in the food chain. Methyl-Hg can affect human health (e.g., neurotoxicity to fetus and children; cardiovascular problems in adults, Roman et al., 2011). Methyl-Hg is produced from inorganic Hg mainly through microbial activities in aquatic ecosystems (UNEP-GMA, 2018). Methyl-Hg in top predators

(e.g., shark and tuna) is over a million times higher than in the surrounding oceanic water (Lavoie et al., 2013). The consumption of highly methyl-Hg-contaminated products has caused severe poisoning events (e.g., Minamata disease in Japan, Rice problems in Iraq, Harada, 1995; Bakir et al., 1973). Human is exposed to methylmercury mainly by seafood consumption and rice uptake from Hg mining areas (Feng et al., 2007; Zhao et al., 2019). The UNEP Minamata Convention, ratified by 130 countries in 2019, aims at lowering Hg release to the global environment. Over the next decades environmental monitoring of air water and biota will show the effectiveness of the Minamata Convention. Setting global clean up targets requires the knowledge about the levels of anthropogenically-emitted Hg and natural background atmospheric Hg. Unlike anthropogenic sources, Hg emission from natural origins cannot be reduced or controlled (Lindberg et al., 2007).

Hg deposition to the environment has been investigated by direct instrumental measurement (e.g., Brosset, 1981; Iverfeldt, 1991; Sprovieri et al., 2017), and indirect measurements, such as, using historical/environmental archives (e.g., lake sediment and peat cores, Enrico et al., 2016; Biester et al., 2018). Numerous lake sediment cores from remote sites have demonstrated an approximately x3 increase in Hg deposition since pre-industrial times (e.g., Engstrom et al., 1997; Fitzgerald et al., 2005; Drevnick et al., 2010; Kang et al., 2016; Kurz et al., 2019; Pérez-Rodríguez et al., 2019). A growing number of peat core studies have been used to investigate historical trends in Hg deposition (e.g., Norton et al., 1997; Benoit et al., 1998; Martinez-Cortizas et al., 1999; Biester et al., 2002; Shotyk et al., 2003; 2005; Bindler, 2003; Bindler et al., 2004; Steinnes and Sjøbakk, 2005; Givelet et al., 2004; Farmers et al., 2009; Coggins et al., 2006). One decade ago, peat was suggested to be a less reliable historical Hg recorder relative to lake sediment by Biester et al. who reported that pre-industrial HgAR enrichment recorded in sediment and peat disagree by more than a factor 10 (Biester et al., 2007). These authors assumed that ^{210}Pb mobility in peat column had led to inaccurate age reconstructions and subsequent unreliable Hg accumulation rate. Recently, Amos et al. (2015) has reviewed the published peat studies and found a similar x3 Hg enrichment since pre-industrial period (1760-1880AD), by correcting a reference time inconsistency for peat and sediment archives in Biester et al., (2007). Since then, peat has regained the confidence to be used as historical Hg recorder (Li et al., 2016; Enrico et al., 2016; 2017; Guédron et al., 2018; Pérez-Rodríguez et al., 2018a; Gao et al., 2019).

Amos et al., (2015) also found that reconstructed Hg deposition has increased before pre-industrial times (1760AD-1880AD), which shows an approximate x5 enrichment from the

natural background (pre-1550AD). That is, there is an overall x20 enrichment from pre-1550AD to 20th century. These Hg enrichments are mainly obtained based on the Hg records from the NH. Historical Hg deposition in the SH, however, have received much less scrutiny.

Terrestrial vegetation has been proven to be a global Hg^0 pump, which contributes to seasonal changes in Hg^0 in the NH in the past two decades (Jiskra et al., 2018; Obrist et al., 2017). SH with less vegetation cover doesn't display Hg^0 seasonality (Jiskra et al., 2018). SH present-day Hg^0 concentration is 1.0-1.3 ng m^{-3}, which is lower than that in the NH (1.5-1.7 ng m^{-3}) (Slemr et al., 1981; Sprovieri et al., 2016). Some studies suggest that SH atmospheric Hg mainly originates from SH oceanic emission and local/regional input, rather than NH transport (Sprovieri et al., 2016; Horowitz et al., 2017). Other studies suggest that a proportion of Hg in the SH can be transported from the NH by oceanic mixing and convection in the Intertropical Convergence Zone (e.g., Slemr et al., 1981; Fitzgerald et al., 1984; Lamborg et al., 2002). Less anthropogenic Hg emission from 1850 AD to 2010 AD in the SH (240 Gg) is estimated by models compared to NH (890 Gg, Streets et al., 2017). Background Hg^0 concentration of 0.27 ng m^{-3} (pre-1550AD) in the NH is shown in Enrico et al. (2017), which highlights the impact of anthropogenic Hg emission on the NH present-day Hg^0 level (1.5-1.7 ng m^{-3}). No studies have been conducted on the natural background atmospheric Hg in the SH, which highlights the need to investigate the historical Hg level in the SH through ^{14}C-dated long Hg records.

6. Role of atmospheric dust on Hg deposition

Mineral dust itself consists of a minor proportion of Hg (56 ppb, Wedepohl, 1995). Atmospheric dust particles can be carriers for Hg^{II}, leading to the formation of PHg and subsequent deposition over Earth's surface. Enhanced Hg accumulation in coincidence with high dust flux are recorded in SH peat and ice cores during Last Glacial Maximum (Vandal et al., 1993; Baccolo et al., 2018; De Lacerda et al., 2017; Pérez-Rodriguez et al., 2015; 2018b; Jitaru et al., 2009). PHg flux peaks during cold climate are explained by elevated oceanic production (Vandal et al., 1993) or enhanced Hg-enriched dust deposition (Jitaru et al., 2009; De Lacerda et al., 2017). Jitaru et al., (2009) suggest that a significant correlation between deposited dust and Hg during the coldest period results from more oxidized Hg being attached to the abundant atmospheric dust particles and then deposits on snowpack. Cold climate elevates the production of sea-salt-derived halogens, which can enhance the oxidation of Hg^0 (Jitaru et al., 2009). Recent Arctic Hg study also indicates that dissolved Hg in the winter snowpack may originate from natural sources possibly linked to sea spray and atmospheric dust (Agnan et al., 2018). Numerous observation and modelling studies have suggested that

partitioning of Hg species and subsequent deposition can be influenced by temperature, humidity and aerosol loadings (Steffen et al., 2008; 2014; Amos et al., 2012; Song et al., 2015; Pérez-Rodríguez et al., 2018b). Aerosol loadings are also subjected to the climate variability.

In addition to being Hg^{II}-carrier, enhanced atmospheric dust input can also increase the primary productivity (e.g., peat moss, Mullan-Boudreau et al., 2017), leading to more Hg^0 sequestration to the vegetation pool. Anthropogenic activities have greatly increased atmospheric dust loading (Tao et al., 2016; Hooper and Marx, 2018), and Hg deposition (UNEP-GMA, 2018), which might accelerate the interaction between atmospheric dust and Hg.

7. Peat dust and Hg studies in the Southern Hemisphere

Peat dust and Hg studies have been abundantly performed in the Northern Hemisphere. Only a few SH peat dust studies have been conducted in Australia (Marx et al., 2010; 2011; Kylander et al., 2007; Muller et al., 2008a; 2008b), New Zealand (Marx et al., 2009), Southern South America (Vanneste et al., 2015; 2016) and South Africa (Humpries et al., 2017) (Figure 6). Some SH dust records attempt to reconstruct the past SWW dynamics (Marx et al., 2011; Vanneste et al., 2015; Humpries et al., 2017), glacial fluctuation (Vanneste et al., 2016), ENSO variability (Marx et al., 2009), and ITCZ migration (Muller et al., 2008a). Others focus on the development of reliable proxies/methods to fingerprint dust origins (Kylander et al., 2007; Muller et al., 2008b), and the influence of recent human activity (Marx et al., 2010). These records mentioned above mainly focus on local/regional mineral inputs, while cross-continental dust deposition related to large-scale air mass circulation (e.g., SWW) draws less attention.

Fewer studies on peat Hg deposition have been conducted in the Southern Hemisphere (e.g., Biester et al., 2002; Guédron et al., 2018, Figure 5). No Holocene peat Hg isotope research has been reported in the Southern Hemisphere. The biogeochemical cycle of pre-anthropogenic Hg in the Southern Hemisphere remains unclear.

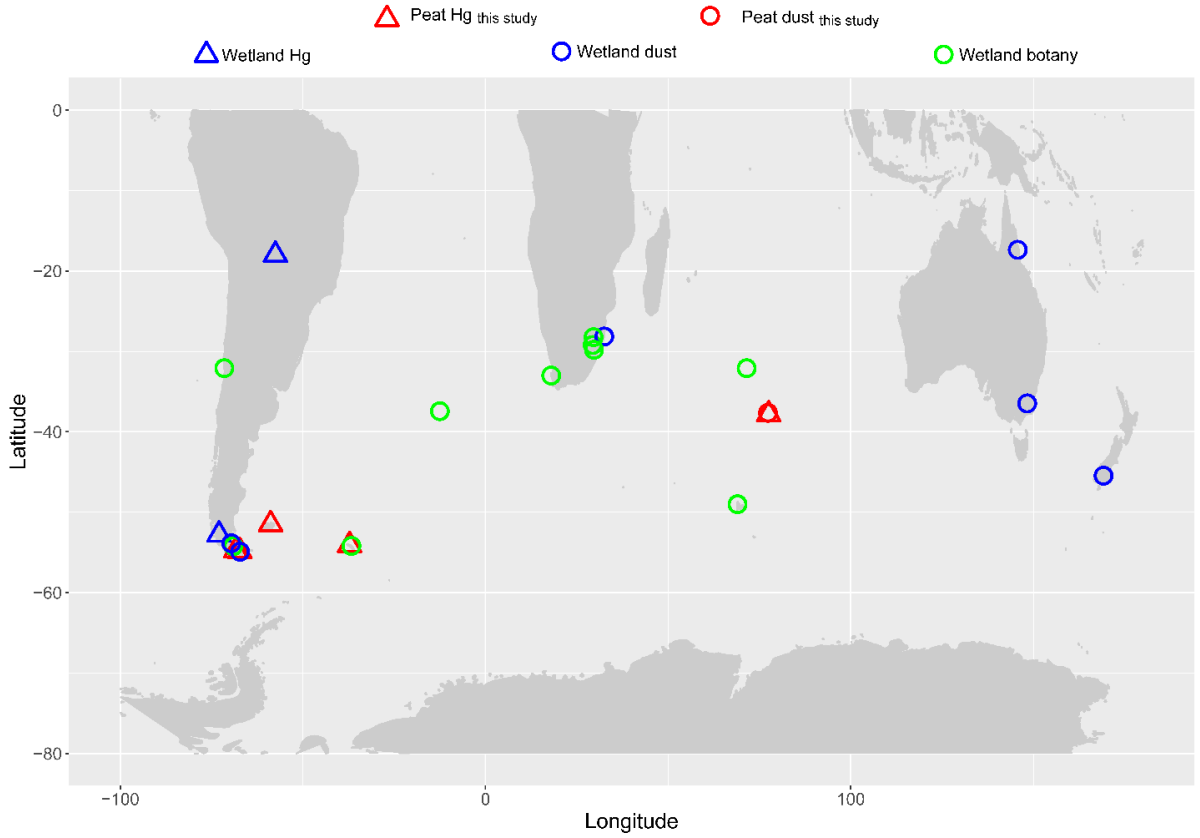

Figure 5. Studies on dust and Hg based on the wetland archives in the Southern Hemisphere. Red triangles and red circles represent peat Hg and dust research in this thesis. Investigations on wetlands include peat, salt marsh and swamp. Blue triangle, blue and green circle represent paleo-studies on wetland Hg, wetland dust and wetland botany, respectively (references see the text). Wetland botany is defined when the studies mainly focus on the botanical proxies interpretation.

8. Objectives of this thesis

The main focuses of this thesis are to investigate the SWW dynamics and hisitorical Hg deposition in the Holocene. To the specific, objectives are to: 1/ reconstruct Holocene SWW dynamics at its northern edge in Indian Ocean sector using dust geochemistry and isotope chemistry; 2/ explore the potential of Hg isotopes to be climatic indicators; and 3/ investigate the natural background (pre-1450AD) Hg level in the SH and access to the present-day global Hg enrichment. Figure 6 shows the research line of this thesis.

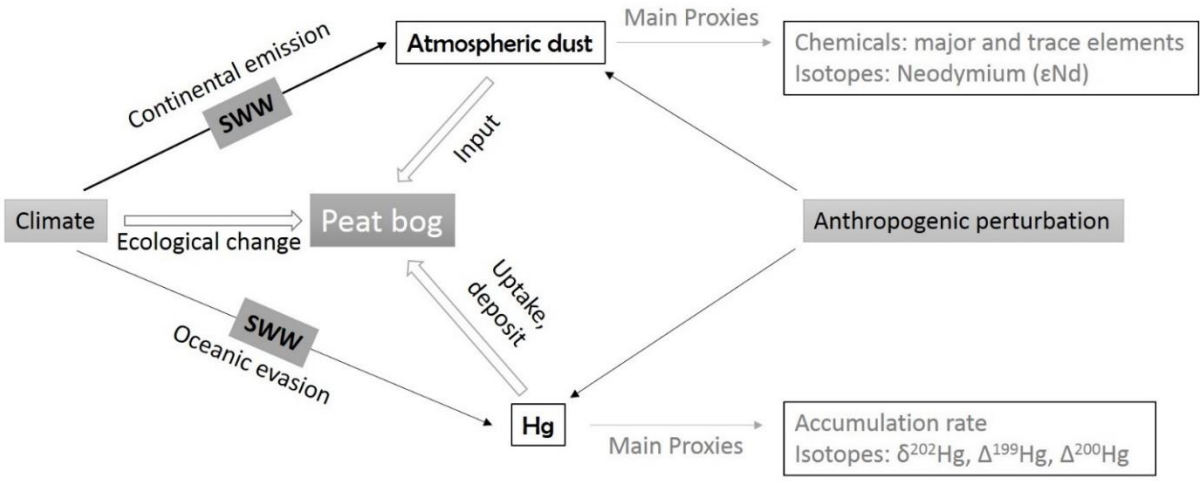

Figure 6. Research line of this thesis. SWW represents for Southern Hemisphere Westerly Winds. Peat bog refers to ombrotrophic peatland.

References:

Agnan, Y., Douglas, T.A., Helmig, D., Hueber, J. and Obrist, D., 2018. Mercury in the Arctic tundra snowpack: temporal and spatial concentration patterns and trace gas exchanges. *The Cryosphere*, *12*(6), pp.1939-1956.

Amos, H.M., Jacob, D.J., Holmes, C.D., Fisher, J.A., Wang, Q., Yantosca, R.M., Corbitt, E.S., Galarneau, E., Rutter, A.P., Gustin, M.S. and Steffen, A., 2012. Gas-particle partitioning of atmospheric Hg (II) and its effect on global mercury deposition. *Atmospheric Chemistry and Physics*, *12*(1), pp.591-603.

Amos, H.M., Sonke, J.E., Obrist, D., Robins, N., Hagan, N., Horowitz, H.M., Mason, R.P., Witt, M., Hedgecock, I.M., Corbitt, E.S. and Sunderland, E.M., 2015. Observational and modeling constraints on global anthropogenic enrichment of mercury. *Environmental science & technology*, *49*(7), pp.4036-4047.

Angot, H., Barret, M., Magand, O., Ramonet, M. and Dommergue, A., 2014. A 2-year record of atmospheric mercury species at a background Southern Hemisphere station on Amsterdam Island. *Atmospheric Chemistry and Physics*, *14*(20), pp.11461-11473.

Appleby, P.G. and Oldfield, F., 1978. The calculation of lead-210 dates assuming a constant rate of supply of unsupported 210Pb to the sediment. *Catena*, *5*(1), pp.1-8.

Appleby, P.G. , Shotyk, W. and Fankhauser, A. 1997: 210Pb age dating of three peat cores in the Jura Mountains, Switzerland. Water, Air & Soil Pollution 100, 223—31.

Appleby, P.G. 2001: Chronostratigraphic techniques in recent sediments. In Last, W.M. and Smol, J.P. , editors, Tracking environmental change using lake sediments volume 1: basin analysis, coring, and chronological techniques. Kluwer Academic, 171—203.

Appleby, P.G. and Oldfield, F., 1992. Applications of lead-210 to sedimentation studies. In *Uranium-series disequilibrium: applications to earth, marine, and environmental sciences. 2. ed*.

Appleby, P.G. and Oldfield, F., 1983. The assessment of 210Pb data from sites with varying sediment accumulation rates. Hydrobiogia, 103, 29-35.

Baccolo, G., Delmonte, B., Albani, S., Baroni, C., Cibin, G., Frezzotti, M., Hampai, D., Marcelli, A., Revel, M., Salvatore, M.C. and Stenni, B., 2018. Regionalization of the atmospheric dust cycle on the periphery of the East Antarctic ice sheet since the last glacial maximum. *Geochemistry, Geophysics, Geosystems*, *19*(9), pp.3540-3554.

Bakir, F., Damluji, S.F., Amin-Zaki, L., Murtadha, M., Khalidi, A., Al-Rawi, N.Y., Tikriti, S., Dhahir, H.I., Clarkson, T.W., Smith, J.C. and Doherty, R.A., 1973. Methylmercury poisoning in Iraq. *Science*, *181*(4096), pp.230-241.

Bell, S.S., Chand, S.S., Tory, K.J., Dowdy, A.J., Turville, C. and Ye, H., 2019. Projections of southern hemisphere tropical cyclone track density using CMIP5 models. *Climate Dynamics*, *52*(9-10), pp.6065-6079.

Benoit, J.M., Gilmour, C.C., Mason, R.P., Riedel, G.S. and Riedel, G.F., 1998. Behavior of mercury in the Patuxent River estuary. *Biogeochemistry*, *40*(2-3), pp.249-265.

Bergametti, G. and Forêt, G., 2014. Dust deposition. In *Mineral Dust* (pp. 179-200). Springer, Dordrecht.

Bergquist, B.A. and Blum, J.D., 2007. Mass-dependent and-independent fractionation of Hg isotopes by photoreduction in aquatic systems. *Science*, *318*(5849), pp.417-420.

Bertrand, S., Daga, R., Bedert, R. and Fontijn, K., 2014. Deposition of the 2011–2012 Cordón Caulle tephra (Chile, 40 S) in lake sediments: Implications for tephrochronology and volcanology. *Journal of Geophysical Research: Earth Surface*, *119*(12), pp.2555-2573.

Betzer, P.R., Carder, K.L., Duce, R.A., Merrill, J.T., Tindale, N.W., Uematsu, M., Costello, D.K., Young, R.W., Feely, R.A., Breland, J.A. and Bernstein, R.E., 1988. Long–range transport of giant mineral aerosol particles. *Nature*, *336*(6199), p.568.

Biester, H., Bindler, R., Martinez-Cortizas, A. and Engstrom, D.R., 2007. Modeling the past atmospheric deposition of mercury using natural archives. *Environmental science & technology*, *41*(14), pp.4851-4860.

Biester, H., Kilian, R., Franzen, C., Woda, C., Mangini, A. and Schöler, H.F., 2002. Elevated mercury accumulation in a peat bog of the Magellanic Moorlands, Chile (53 S)–an anthropogenic signal from the Southern Hemisphere. *Earth and Planetary Science Letters*, *201*(3-4), pp.609-620.

Biester, H., Pérez-Rodríguez, M., Gilfedder, B.S., Martínez Cortizas, A. and Hermanns, Y.M., 2018. Solar irradiance and primary productivity controlled mercury accumulation in sediments of a remote lake in the Southern Hemisphere during the past 4000 years. *Limnology and Oceanography*, *63*(2), pp.540-549.

Bindler, R., 2003. Estimating the natural background atmospheric deposition rate of mercury utilizing ombrotrophic bogs in southern Sweden. *Environmental science & technology*, *37*(1), pp.40-46.

Bindler, R., Klarqvist, M., Klaminder, J. and Förster, J., 2004. Does within-bog spatial variability of mercury and lead constrain reconstructions of absolute deposition rates from

single peat records? The example of Store Mosse, Sweden. *Global Biogeochemical Cycles*, *18*(3).

Blaauw, M., 2010. Methods and code for 'classical'age-modelling of radiocarbon sequences. *quaternary geochronology*, *5*(5), pp.512-518.

Blaauw, M. and Christen, J.A., 2005. Radiocarbon peat chronologies and environmental change. *Journal of the Royal Statistical Society: Series C (Applied Statistics)*, *54*(4), pp.805-816.

Blaauw, M. and Christen, J.A., 2011. Flexible paleoclimate age-depth models using an autoregressive gamma process. *Bayesian analysis*, *6*(3), pp.457-474.

Blum, J.D., 2012. Applications of stable mercury isotopes to biogeochemistry. In *Handbook of Environmental Isotope Geochemistry* (pp. 229-245). Springer, Berlin, Heidelberg.

Blum, J.D., Sherman, L.S. and Johnson, M.W., 2014. Mercury isotopes in earth and environmental sciences. *Annual Review of Earth and Planetary Sciences*, *42*, pp.249-269.

Blum, J.D. and Bergquist, B.A., 2007. Reporting of variations in the natural isotopic composition of mercury. *Analytical and bioanalytical chemistry*, *388*(2), pp.353-359.

Bohleber, P., Erhardt, T., Spaulding, N., Hoffmann, H., Fischer, H. and Mayewski, P., 2018. Temperature and mineral dust variability recorded in two low-accumulation Alpine ice cores over the last millennium. *Climate of the Past*, *14*(1), pp.21-37.

Brahney, J., Ballantyne, A.P., Vandergoes, M., Baisden, T. and Neff, J.C., 2019. Increased Dust Deposition in New Zealand Related to Twentieth Century Australian Land Use. *Journal of Geophysical Research: Biogeosciences*.

Brosset, C., 1981. The mercury cycle. *Water, Air, and Soil Pollution*, *16*(2), pp.253-255.

Bryant, R.G., Bigg, G.R., Mahowald, N.M., Eckardt, F.D. and Ross, S.G., 2007. Dust emission response to climate in southern Africa. Journal of Geophysical Research: Atmospheres 112(D9).

Bullock Jr, O.R. and Brehme, K.A., 2002. Atmospheric mercury simulation using the CMAQ model: formulation description and analysis of wet deposition results. *Atmospheric Environment*, *36*(13), pp.2135-2146.

Bush, R.T. and McInerney, F.A., 2015. Influence of temperature and C4 abundance on n-alkane chain length distributions across the central USA. *Organic Geochemistry*, *79*, pp.65-73.

Ceppi, P., Hwang, Y.T., Liu, X., Frierson, D.M. and Hartmann, D.L., 2013. The relationship between the ITCZ and the Southern Hemispheric eddy-driven jet. *Journal of Geophysical Research: Atmospheres*, *118*(11), pp.5136-5146.

Charman, D.J., Barber, K.E., Blaauw, M., Langdon, P.G., Mauquoy, D., Daley, T.J., Hughes, P.D. and Karofeld, E., 2009. Climate drivers for peatland palaeoclimate records. *Quaternary Science Reviews*, *28*(19-20), pp.1811-1819.

Charman, D., 2002. *Peatlands and environmental change*. John Wiley & Sons Ltd.

Chase, B.M., Chevalier, M., Boom, A. and Carr, A.S., 2017. The dynamic relationship between temperate and tropical circulation systems across South Africa since the Last Glacial Maximum. Quaternary Science Reviews 174, 54-62.

Chen, J., Hintelmann, H., Feng, X. and Dimock, B., 2012. Unusual fractionation of both odd and even mercury isotopes in precipitation from Peterborough, ON, Canada. *Geochimica et Cosmochimica Acta*, *90*, pp.33-46.

Cheng, Z., Weng, C., Steinke, S. and Mohtadi, M., 2018. Anthropogenic modification of vegetated landscapes in southern China from 6,000 years ago. *Nature Geoscience*, *11*(12), p.939.

Clymo, R.S., 1984. The limits to peat bog growth. *Philosophical Transactions of the Royal Society of London. B, Biological Sciences*, *303*(1117), pp.605-654.

Coggins, A.M., Jennings, S.G. and Ebinghaus, R., 2006. Accumulation rates of the heavy metals lead, mercury and cadmium in ombrotrophic peatlands in the west of Ireland. *Atmospheric Environment*, *40*(2), pp.260-278.

Conceição, R., Silva, H.G., Mirão, J., Gostein, M., Fialho, L., Narvarte, L. and Collares-Pereira, M., 2018. Saharan dust transport to Europe and its impact on photovoltaic performance: A case study of soiling in Portugal. *Solar Energy*, *160*, pp.94-102.

Davies, L.J., Appleby, P., Jensen, B.J., Magnan, G., Mullan-Boudreau, G., Noernberg, T., Shannon, B., Shotyk, W., van Bellen, S., Zaccone, C. and Froese, D.G., 2018. High-resolution age modelling of peat bogs from northern Alberta, Canada, using pre-and post-bomb 14C, 210Pb and historical cryptotephra. *Quaternary Geochronology*, *47*, pp.138-162.

De Deckker, P., 2019. An evaluation of Australia as a major source of dust. *Earth-Science Reviews*.

De Lacerda, L.D., Turcq, B., Sifeddine, A. and Cordeiro, R.C., 2017. Mercury accumulation rates in Caço Lake, NE Brazil during the past 20.000 years. *Journal of South American Earth Sciences*, *77*, pp.42-50.

De Vleeschouwer, F., Vanneste, H., Mauquoy, D., Piotrowska, N., Torrejón, F., Roland, T., Stein, A. and Le Roux, G., 2014. Emissions from pre-Hispanic metallurgy in the South American atmosphere. PloS one 9(10), e111315.

Delmonte, B., Basile-Doelsch, I., Petit, J.R., Maggi, V., Revel-Rolland, M., Michard, A., Jagoutz, E. and Grousset, F., 2004. Comparing the Epica and Vostok dust records during the last 220,000 years: stratigraphical correlation and provenance in glacial periods. *Earth-Science Reviews*, *66*(1-2), pp.63-87.

Delmonte, B., 2003. Quaternary variations and origin of continental dust in East antarctica. Glaciology. Università degli studi di Milano-Bicocca. Thesis.

Delmonte, B., Paleari, C.I., Andò, S., Garzanti, E., Andersson, P.S., Petit, J.R., Crosta, X., Narcisi, B., Baroni, C., Salvatore, M.C. and Baccolo, G., 2017. Causes of dust size variability in central East Antarctica (Dome B): Atmospheric transport from expanded South American sources during Marine Isotope Stage 2. *Quaternary Science Reviews*, *168*, pp.55-68.

Demers, J.D., Blum, J.D. and Zak, D.R., 2013. Mercury isotopes in a forested ecosystem: Implications for air-surface exchange dynamics and the global mercury cycle. *Global Biogeochemical Cycles*, *27*(1), pp.222-238.

Demers, J.D., Blum, J.D., Brooks, S.C., Donovan, P.M., Riscassi, A.L., Miller, C.L., Zheng, W. and Gu, B., 2018. Hg isotopes reveal in-stream processing and legacy inputs in East Fork Poplar Creek, Oak Ridge, Tennessee, USA. *Environmental Science: Processes & Impacts*, *20*(4), pp.686-707.

Demers, J.D., Sherman, L.S., Blum, J.D., Marsik, F.J. and Dvonch, J.T., 2015. Coupling atmospheric mercury isotope ratios and meteorology to identify sources of mercury impacting a coastal urban-industrial region near Pensacola, Florida, USA. *Global Biogeochemical Cycles*, *29*(10), pp.1689-1705.

DePaolo, D.J. and Wasserburg, G.J., 1976. Nd isotopic variations and petrogenetic models. *Geophysical Research Letters*, *3*(5), pp.249-252.

Dong, X., Fu, J.S., Huang, K., Lin, N.H., Wang, S.H. and Yang, C.E., 2018. Analysis of the Co-existence of Long-range Transport Biomass Burning and Dust in the Subtropical West Pacific Region. *Scientific reports*, *8*(1), p.8962.

Donohoe, A., Marshall, J., Ferreira, D. and Mcgee, D., 2013. The relationship between ITCZ location and cross-equatorial atmospheric heat transport: From the seasonal cycle to the Last Glacial Maximum. *Journal of Climate*, *26*(11), pp.3597-3618.

Drevnick, P.E., Shinneman, A.L., Lamborg, C.H., Engstrom, D.R., Bothner, M.H. and Oris, J.T., 2010. Mercury Flux to Sediments of Lake Tahoe, California–Nevada. *Water, Air, & Soil Pollution*, *210*(1-4), pp.399-407.

Engelstaedter, S. and Washington, R., 2007. Temporal controls on global dust emissions: The role of surface gustiness. Geophysical Research Letters 34(15).

Engstrom, D.R. and Swain, E.B., 1997. Recent declines in atmospheric mercury deposition in the upper Midwest. *Environmental Science & Technology*, *31*(4), pp.960-967.

Enrico, M., Le Roux, G., Heimbürger, L.E., Van Beek, P., Souhaut, M., Chmeleff, J. and Sonke, J.E., 2017. Holocene atmospheric mercury levels reconstructed from peat bog mercury stable isotopes. *Environmental science & technology*, *51*(11), pp.5899-5906.

Enrico, M., Le Roux, G., Marusczak, N., Heimbürger, L.E., Claustres, A., Fu, X., Sun, R. and Sonke, J.E., 2016. Atmospheric mercury transfer to peat bogs dominated by gaseous elemental mercury dry deposition. *Environmental science & technology*, *50*(5), pp.2405-2412.

Estrade, N., Carignan, J., Sonke, J.E. and Donard, O.F., 2009. Mercury isotope fractionation during liquid–vapor evaporation experiments. *Geochimica et Cosmochimica Acta*, *73*(10), pp.2693-2711.

Farmer, J.G., Anderson, P., Cloy, J.M., Graham, M.C., MacKenzie, A.B. and Cook, G.T., 2009. Historical accumulation rates of mercury in four Scottish ombrotrophic peat bogs over the past 2000 years. *Science of the Total Environment*, *407*(21), pp.5578-5588.

Feng, X., Li, P., Qiu, G., Wang, S., Li, G., Shang, L., Meng, B., Jiang, H., Bai, W., Li, Z. and Fu, X., 2007. Human exposure to methylmercury through rice intake in mercury mining areas, Guizhou Province, China. *Environmental science & technology*, *42*(1), pp.326-332.

Fitzgerald, W.F., Engstrom, D.R., Lamborg, C.H., Tseng, C.M., Balcom, P.H. and Hammerschmidt, C.R., 2005. Modern and historic atmospheric mercury fluxes in northern Alaska: Global sources and Arctic depletion. *Environmental science & technology*, *39*(2), pp.557-568.

Fitzgerald, W.F., Gill, G.A. and Kim, J.P., 1984. An equatorial Pacific Ocean source of atmospheric mercury. *Science*, *224*(4649), pp.597-599.

Franzese, A.M., Hemming, S.R., Goldstein, S.L. and Anderson, R.F., 2006. Reduced Agulhas Leakage during the Last Glacial Maximum inferred from an integrated provenance and flux study. *Earth and Planetary Science Letters*, *250*(1-2), pp.72-88.

Frölicher, T.L., Sarmiento, J.L., Paynter, D.J., Dunne, J.P., Krasting, J.P., Winton, M., 2015. Dominance of the Southern Ocean in Anthropogenic Carbon and Heat Uptake in CMIP5 Models. *Journal of Climate*, 28, 862–886.

Frugone-Álvarez, M., Latorre, C., Giralt, S., Polanco-Martínez, J., Bernárdez, P., Oliva-Urcia, B., Maldonado, A., Carrevedo, M.L., Moreno, A. and Delgado Huertas, A., 2017. A 7000-

year high-resolution lake sediment record from coastal central Chile (Lago Vichuquén, 34° S): implications for past sea level and environmental variability. *Journal of Quaternary Science*, 32(6), 830-844.

Fu, X., Zhu, W., Zhang, H., Sommar, J., Yu, B., Yang, X., Wang, X., Lin, C.J. and Feng, X., 2016a. Depletion of atmospheric gaseous elemental mercury by plant uptake at Mt. Changbai, Northeast China. *Atmospheric Chemistry and Physics*, *16*(20), pp.12861-12873.

Fu, X., Marusczak, N., Heimbürger, L.E., Sauvage, B., Gheusi, F., Prestbo, E.M. and Sonke, J.E., 2016b. Atmospheric mercury speciation dynamics at the high-altitude Pic du Midi Observatory, southern France. *Atmospheric Chemistry and Physics*, *16*(9), p.5623.

Gaiero, D.M., Simonella L., Gassó S., Gili S., Stein A. F., Sosa P., Becchio R., Arce J., and Marelli H., 2013. "Ground/satellite observations and atmospheric modeling of dust storms originating in the high Puna-Altiplano deserts (South America): Implications for the interpretation of paleo-climatic archives." *Journal of Geophysical Research: Atmospheres* 118, no. 9: 3817-3831.

Gäggeler, H.W., 1995. Radioactivity in the atmosphere. Radiochimica Acta 70/71, 345–353.

Gallego-Sala, A.V., Charman, D.J., Brewer, S., Page, S.E., Prentice, I.C., Friedlingstein, P., Moreton, S., Amesbury, M.J., Beilman, D.W., Björck, S. and Blyakharchuk, T., 2018. Latitudinal limits to the predicted increase of the peatland carbon sink with warming. *Nature climate change*, *8*(10), p.907.

Gao, C., Zhang, S., Li, Y., Han, D., Liu, H. and Wang, G., 2019. Holocene mercury accumulation calibrated by peat decomposition in a peat sequence from the Sanjiang Plain, northeast China. *Quaternary International*.

Gili, S., Gaiero, D.M., Goldstein, S.L., Chemale Jr, F., Jweda, J., Kaplan, M.R., Becchio, R.A. and Koester, E., 2017. Glacial/interglacial changes of Southern Hemisphere wind circulation from the geochemistry of South American dust. *Earth and Planetary Science Letters*, *469*, pp.98-109.

Gili, S., Gaiero, D.M., Goldstein, S.L., Chemale Jr, F., Koester, E., Jweda, J., Vallelonga, P. and Kaplan, M.R., 2016. Provenance of dust to Antarctica: A lead isotopic perspective. *Geophysical Research Letters*, *43*(5), pp.2291-2298.

Givelet, N., Roos-Barraclough, F., Goodsite, M.E., Cheburkin, A.K. and Shotyk, W., 2004. Atmospheric mercury accumulation rates between 5900 and 800 calibrated years BP in the High Arctic of Canada recorded by peat hummocks. *Environmental science & technology*, *38*(19), pp.4964-4972.

Gobbi, G.P., Barnaba, F., Di Liberto, L., Bolignano, A., Lucarelli, F., Nava, S., Perrino, C., Pietrodangelo, A., Basart, S., Costabile, F. and Dionisi, D., 2019. An inclusive view of Saharan dust advections to Italy and the Central Mediterranean. *Atmospheric Environment*, *201*, pp.242-256.

Godwin, H., 1962. Half-life of radiocarbon. *Nature*, *195*(4845), pp.984-984.

Gorham, E., 1991. Northern peatlands: role in the carbon cycle and probable responses to climatic warming. *Ecological applications*, *1*(2), pp.182-195.

Gratz, L.E., Keeler, G.J., Blum, J.D. and Sherman, L.S., 2010. Isotopic composition and fractionation of mercury in Great Lakes precipitation and ambient air. *Environmental Science & Technology*, *44*(20), pp.7764-7770.

Groß, S., Gasteiger, J., Freudenthaler, V., Müller, T., Sauer, D., Toledano, C. and Ansmann, A., 2016. Saharan dust contribution to the Caribbean summertime boundary layer–a lidar study during SALTRACE. *Atmospheric Chemistry and Physics*, *16*(18), pp.11535-11546.

Grousset, F.E., Biscaye, P.E., Revel, M., Petit, J.R., Pye, K., Joussaume, S. and Jouzel, J., 1992. Antarctic (Dome C) ice-core dust at 18 ky BP: Isotopic constraints on origins. *Earth and Planetary Science Letters*, *111*(1), pp.175-182.

Guan, X., Huang, J., Zhang, Y., Xie, Y. and Liu, J., 2016. The relationship between anthropogenic dust and population over global semi-arid regions. *Atmospheric Chemistry and Physics*, *16*(8), pp.5159-5169.

Guédron, S., Ledru, M.P., Escobar-Torrez, K., Develle, A.L. and Brisset, E., 2018. Enhanced mercury deposition by Amazonian orographic precipitation: Evidence from high-elevation Holocene records of the Lake Titicaca region (Bolivia). *Palaeogeography, palaeoclimatology, palaeoecology*, *511*, pp.577-587.

Hadley, G., 1735. VI. Concerning the cause of the general trade-winds. *Philosophical Transactions of the Royal Society of London*, *39*(437), pp.58-62.

Hahn, A., Compton, J.S., Meyer-Jacob, C., Kirsten, K.L., Lucasssen, F., Mayo, M.P., Schefuß, E. and Zabel, M., 2016. Holocene paleo-climatic record from the South African Namaqualand mudbelt: A source to sink approach. *Quaternary International*, *404*, pp.121-135.

Harada, M., 1995. Minamata disease: methylmercury poisoning in Japan caused by environmental pollution. *Critical reviews in toxicology*, *25*(1), pp.1-24.

Harrison, S.P., Kohfeld, K.E., Roelandt, C. and Claquin, T., 2001. The role of dust in climate changes today, at the last glacial maximum and in the future. *Earth-Science Reviews*, *54*(1-3), pp.43-80.

Hodgson, D.A. and Sime, L.C., 2010. Palaeoclimate: Southern westerlies and CO2. Nature Geoscience, 3(10):666-667

Hooper, J. and Marx, S., 2018. A global doubling of dust emissions during the Anthropocene? *Global and planetary change*.

Horowitz, H.M., Jacob, D.J., Zhang, Y., Dibble, T.S., Slemr, F., Amos, H.M., Schmidt, J.A., Corbitt, E.S., Marais, E.A. and Sunderland, E.M., 2017. A new mechanism for atmospheric mercury redox chemistry: implications for the global mercury budget. *Atmospheric Chemistry and Physics*, *17*(10), pp.6353-6371.

Hua, Q., 2009. Radiocarbon: A chronological tool for the recent past. Quaternary Geochronology 4, 378–390. https://doi.org/10.1016/j.quageo.2009.03.006

Hua, Q., Barbetti, M. and Rakowski, A.Z., 2013. Atmospheric radiocarbon for the period 1950–2010. *Radiocarbon*, *55*(4), pp.2059-2072.

Huang, J., Kang, S., Zhang, Q., Yan, H., Guo, J., Jenkins, M.G., Zhang, G. and Wang, K., 2012. Wet deposition of mercury at a remote site in the Tibetan Plateau: concentrations, speciation, and fluxes. *Atmospheric Environment*, *62*, pp.540-550.

Humphries, M., Benitez-Nelson, C., Bizimis, M. and Finch, J., 2017. An aeolian sediment reconstruction of regional wind intensity and links to larger scale climate variability since the last deglaciation from the east coast of southern Africa. Global and Planetary Change 156, 59-67.

Ingram, H.A.P., 1978. Soil layers in mires: function and terminology. *Journal of Soil Science*, *29*(2), pp.224-227.

Iverfeldt, Å., 1991. Mercury in forest canopy throughfall water and its relation to atmospheric deposition. *Water Air & Soil Pollution*, *56*(1), pp.553-564.

Jenny, B., Wilhelm, D. and Valero-Garcés, B., 2003. The Southern Westerlies in Central Chile: Holocene precipitation estimates based on a water balance model for Laguna Aculeo (33 50′ S). Climate Dynamics 20(2-3), 269-280.

Jickells, T.D. and Spokes, L.J., 2001. Atmospheric iron inputs to the oceans.

Jiskra, M., Sonke, J.E., Obrist, D., Bieser, J., Ebinghaus, R., Myhre, C.L., Pfaffhuber, K.A., Wängberg, I., Kyllönen, K., Worthy, D. and Martin, L.G., 2018. A vegetation control on seasonal variations in global atmospheric mercury concentrations. *Nature Geoscience*, *11*(4), p.244.

Jiskra, M., Wiederhold, J.G., Skyllberg, U., Kronberg, R.M., Hajdas, I. and Kretzschmar, R., 2015. Mercury deposition and re-emission pathways in boreal forest soils investigated with Hg isotope signatures. *Environmental science & technology*, *49*(12), pp.7188-7196.

Jitaru, P., Gabrielli, P., Marteel, A., Plane, J.M., Planchon, F.A., Gauchard, P.A., Ferrari, C.P., Boutron, C.F., Adams, F.C., Hong, S. and Cescon, P., 2009. Atmospheric depletion of mercury over Antarctica during glacial periods. *Nature Geoscience*, *2*(7), p.505.

Johnson, M.S., Meskhidze, N., Kiliyanpilakkil, V.P. and Gassó, S., 2011. Understanding the transport of Patagonian dust and its influence on marine biological activity in the South Atlantic Ocean. *Atmospheric Chemistry & Physics*, *11*(6).

Kang, S., Huang, J., Wang, F., Zhang, Q., Zhang, Y., Li, C., Wang, L., Chen, P., Sharma, C.M., Li, Q. and Sillanpää, M., 2016. Atmospheric mercury depositional chronology reconstructed from lake sediments and ice core in the Himalayas and Tibetan Plateau. *Environmental science & technology*, *50*(6), pp.2859-2869.

Kohfeld, K.E. and Tegen, I., 2007. Record of mineral aerosols and their role in the Earth system.

Korosi, J.B., Griffiths, K., Smol, J.P. and Blais, J.M., 2018. Trends in historical mercury deposition inferred from lake sediment cores across a climate gradient in the Canadian High Arctic. *Environmental pollution*, *241*, pp.459-467.

Kritee, K., Barkay, T. and Blum, J.D., 2009. Mass dependent stable isotope fractionation of mercury during mer mediated microbial degradation of monomethylmercury. *Geochimica et Cosmochimica Acta*, *73*(5), pp.1285-1296.

Kritee, K., Blum, J.D., Johnson, M.W., Bergquist, B.A. and Barkay, T., 2007. Mercury stable isotope fractionation during reduction of Hg (II) to Hg (0) by mercury resistant microorganisms. *Environmental science & technology*, *41*(6), pp.1889-1895.

Kurz, A.Y., Blum, J.D., Washburn, S.J. and Baskaran, M., 2019. Changes in the mercury isotopic composition of sediments from a remote alpine lake in Wyoming, USA. *Science of The Total Environment*, *669*, pp.973-982.

Kylander, M.E., Martínez-Cortizas, A., Bindler, R., Kaal, J., Sjöström, J.K., Hansson, S.V., Silva-Sánchez, N., Greenwood, S.L., Gallagher, K., Rydberg, J. and Mörth, C.M., 2018. Mineral dust as a driver of carbon accumulation in northern latitudes. *Scientific reports*, *8*(1), p.6876.

Kylander, M.E., Muller, J., Wüst, R.A.J., Gallagher, K., Garcia-Sanchez, R., Coles, B.J. and Weiss, D.J., 2007. Rare earth element and Pb isotope variations in a 52 kyr peat core from Lynch's Crater (NE Queensland, Australia): proxy development and application to paleoclimate in the Southern Hemisphere. *Geochimica et Cosmochimica Acta*, *71*(4), pp.942-960.

Lamborg, C.H., Fitzgerald, W.F., O'Donnell, J. and Torgersen, T., 2002. A non-steady-state compartmental model of global-scale mercury biogeochemistry with interhemispheric atmospheric gradients. *Geochimica et Cosmochimica Acta, 66*(7), pp.1105-1118.

Lamy, F., Hebbeln, D., Röhl, U. and Wefer, G., 2001. Holocene rainfall variability in southern Chile: a marine record of latitudinal shifts of the Southern Westerlies. Earth and Planetary Science Letters 185(3), 369-382.

Lamy, F., Kilian, R., Arz, H.W., Francois, J.-P., Kaiser, J., Prange, M. and Steinke, T., 2010. Holocene changes in the position and intensity of the southern westerly wind belt. Nature Geoscience 3(10), 695.

Lancaster, N., 2013. *Geomorphology of desert dunes*. Routledge.

Landschützer, P., Gruber, N., Haumann, F.A., Rödenbeck, C., Bakker, D.C., Van Heuven, S., Hoppema, M., Metzl, N., Sweeney, C., Takahashi, T. and Tilbrook, B., 2015. The reinvigoration of the Southern Ocean carbon sink. *Science*, *349*(6253), pp.1221-1224.

Lappalainen, E. ed., 1996. *Global peat resources* (Vol. 4, p. 358). Jyskä: International Peat Society.

Lavoie, R.A., Jardine, T.D., Chumchal, M.M., Kidd, K.A. and Campbell, L.M., 2013. Biomagnification of mercury in aquatic food webs: a worldwide meta-analysis. *Environmental science & technology*, *47*(23), pp.13385-13394.

Le Quéré, C., Rödenbeck, C., Buitenhuis, E.T., Conway, T.J., Langenfelds, R., Gomez, A., Labuschagne, C., Ramonet, M., Nakazawa, T., Metzl, N. and Gillett, N., 2007. Saturation of the Southern Ocean CO2 sink due to recent climate change. *Science*, *316*(5832), pp.1735-1738.

Le Roux, G., Fagel, N., De Vleeschouwer, F., Krachler, M., Debaille, V., Stille, P., Mattielli, N., Van Der Knaap, W.O., Van Leeuwen, J.F. and Shotyk, W., 2012. Volcano-and climate-driven changes in atmospheric dust sources and fluxes since the Late Glacial in Central Europe. *Geology*, *40*(4), pp.335-338.

Levin, I., Kromer, B., Schoch-Fischer, H., Bruns, M., Münnich, M., Berdau, D., Vogel, J.C. and Münnich, K.O., 1985. 25 years of tropospheric 14 C observations in central Europe. *Radiocarbon*, *27*(1), pp.1-19.

Li, F., Ginoux, P. and Ramaswamy, V., 2008. Distribution, transport, and deposition of mineral dust in the Southern Ocean and Antarctica: Contribution of major sources. Journal of Geophysical Research: Atmospheres 113(D10).

Li, Y., Ma, C., Zhu, C., Huang, R. and Zheng, C., 2016. Historical anthropogenic contributions to mercury accumulation recorded by a peat core from Dajiuhu montane mire, central China. *Environmental pollution*, *216*, pp.332-339.

Libby, W.F., Anderson, E.C. and Arnold, J.R., 1949. Age determination by radiocarbon content: world-wide assay of natural radiocarbon. *Science*, *109*(2827), pp.227-228.

Lindberg, S., Bullock, R., Ebinghaus, R., Engstrom, D., Feng, X., Fitzgerald, W., Pirrone, N., Prestbo, E. and Seigneur, C., 2007. A synthesis of progress and uncertainties in attributing the sources of mercury in deposition. *Ambio*, pp.19-32.

Lindvall, H., Björck, S., Holmgren, S., Ljung, K., Van der Putten, N. and Porter, C., 2011. A Holocene peat record in the central South Atlantic: an archive of precipitation changes. *GFF*, *133*(3-4), pp.195-206.

Mahowald, N.M., Baker, A.R., Bergametti, G., Brooks, N., Duce, R.A., Jickells, T.D., Kubilay, N., Prospero, J.M. and Tegen, I., 2005. Atmospheric global dust cycle and iron inputs to the ocean. *Global biogeochemical cycles*, *19*(4).

Mahowald, N.M., Kloster, S., Engelstaedter, S., Moore, J.K., Mukhopadhyay, S., McConnell, J.R., Albani, S., Doney, S.C., Bhattacharya, A., Curran, M.A. and Flanner, M.G., 2010. Observed 20th century desert dust variability: impact on climate and biogeochemistry. *Atmospheric Chemistry and Physics*.

Martınez-Cortizas, A., Pontevedra-Pombal, X., Garcıa-Rodeja, E., Novoa-Munoz, J.C. and Shotyk, W., 1999. Mercury in a Spanish peat bog: archive of climate change and atmospheric metal deposition. *Science*, *284*(5416), pp.939-942.

Marx, S.K., Kamber, B.S., McGowan, H.A. and Denholm, J., 2011. Holocene dust deposition rates in Australia's Murray-Darling Basin record the interplay between aridity and the position of the mid-latitude westerlies. *Quaternary Science Reviews*, 30(23-24), 3290-3305.

Marx, S.K., Kamber, B.S., McGowan, H.A. and Zawadzki, A., 2010. Atmospheric pollutants in alpine peat bogs record a detailed chronology of industrial and agricultural development on the Australian continent. *Environmental Pollution*, *158*(5), pp.1615-1628.

Marx, S.K., Kamber, B.S., McGowan, H.A., Petherick, L.M., McTainsh, G.H., Stromsoe, N., Hooper, J.N. and May, J.H., 2018. Palaeo-dust records: A window to understanding past environments. *Global and planetary change*, *165*, pp.13-43.

Marx, S.K., McGowan, H.A., Kamber, B.S., Knight, J.M., Denholm, J. and Zawadzki, A., 2014. Unprecedented wind erosion and perturbation of surface geochemistry marks the

Anthropocene in Australia. *Journal of Geophysical Research: Earth Surface*, *119*(1), pp.45-61.

Marx, S.K., McGowan, H.A. and Kamber, B.S., 2009. Long-range dust transport from eastern Australia: a proxy for Holocene aridity and ENSO-type climate variability. *Earth and Planetary Science Letters*, *282*(1-4), pp.167-177.

Menviel, L., Spence, P., Yu, J., Chamberlain, M.A., Matear, R.J., Meissner, K.J. and England, M.H., 2018. Southern Hemisphere westerlies as a driver of the early deglacial atmospheric CO 2 rise. *Nature communications*, *9*(1), p.2503.

Mitsch, W.J. and Gosselink, J.G., 2015. Wetlands of the world. *Wetlands*, pp.45-110.

Moreno, P.I., Francois, J.P., Moy, C.M. and Villa-Martínez, R., 2010. Covariability of the Southern Westerlies and atmospheric CO2 during the Holocene. *Geology*, *38*(8), pp.727-730.

Mullan-Boudreau, G., Belland, R., Devito, K., Noernberg, T., Pelletier, R. and Shotyk, W., 2017. Sphagnum moss as an indicator of contemporary rates of atmospheric dust deposition in the Athabasca bituminous sands region. *Environmental science & technology*, *51*(13), pp.7422-7431.

Muller, J., Kylander, M., Martinez-Cortizas, A., Wüst, R.A., Weiss, D., Blake, K., Coles, B. and Garcia-Sanchez, R., 2008a. The use of principle component analyses in characterising trace and major elemental distribution in a 55 kyr peat deposit in tropical Australia: implications to paleoclimate. *Geochimica et Cosmochimica Acta*, *72*(2), pp.449-463.

Muller, J., Kylander, M., Wüst, R.A., Weiss, D., Martinez-Cortizas, A., LeGrande, A.N., Jennerjahn, T., Behling, H., Anderson, W.T. and Jacobson, G., 2008b. Possible evidence for wet Heinrich phases in tropical NE Australia: the Lynch's Crater deposit. *Quaternary Science Reviews*, *27*(5-6), pp.468-475.

Munk, W. H. and Palmen, E., 1951. Note on the dynamics of the antarctic circumpolar current. *Tellus*, *3*(1), 53-55.

Neff, P.D. and Bertler, N.A., 2015. Trajectory modeling of modern dust transport to the Southern Ocean and Antarctica. *Journal of Geophysical Research: Atmospheres*, *120*(18), pp.9303-9322.

Noble, T.L., Piotrowski, A.M., Robinson, L.F., McManus, J.F., Hillenbrand, C.D. and Bory, A.J.M., 2012. Greater supply of Patagonian-sourced detritus and transport by the ACC to the Atlantic sector of the Southern Ocean during the last glacial period. *Earth and Planetary Science Letters*, *317*, pp.374-385.

Norton, S.A., Evans, G.C. and Kahl, J.S., 1997. Comparison of Hg and Pb fluxes to hummocks and hollows of ombrotrophic Big Heath Bog and to nearby Sargent Mt. Pond, Maine, USA. *Water, Air, and Soil Pollution*, *100*(3-4), pp.271-286.

Obrist, D., Agnan, Y., Jiskra, M., Olson, C.L., Colegrove, D.P., Hueber, J., Moore, C.W., Sonke, J.E. and Helmig, D., 2017. Tundra uptake of atmospheric elemental mercury drives Arctic mercury pollution. *Nature*, *547*(7662), p.201.

Ogawa, F. and Spengler, T., 2019. Prevailing Surface Wind Direction during Air-Sea Heat Exchange. *Journal of Climate*, (2019).

Olid, C., Garcia-Orellana, J., Masqué, P., Cortizas, A.M., Sanchez-Cabeza, J.A. and Bindler, R., 2013. Improving the 210Pb-chronology of Pb deposition in peat cores from Chao de Lamoso (NW Spain). *Science of the total environment*, *443*, pp.597-607.

Olson, C.L., Jiskra, M., Sonke, J.E. and Obrist, D., 2019. Mercury in tundra vegetation of Alaska: Spatial and temporal dynamics and stable isotope patterns. *Science of the Total Environment*, *660*, pp.1502-1512.

Olsson, I.U., 1968. Modern aspects of radiocarbon datings. *Earth-Science Reviews*, *4*, pp.203-218.

Pérez-Rodríguez, M., Biester, H., Aboal, J.R., Toro, M. and Cortizas, A.M., 2019. Thawing of snow and ice caused extraordinary high and fast mercury fluxes to lake sediments in Antarctica. *Geochimica et Cosmochimica Acta*, *248*, pp.109-122.

Pérez-Rodríguez, M., Horák-Terra, I., Rodríguez-Lado, L., Aboal, J.R. and Martinez Cortizas, A., 2015. Long-term (~ 57 ka) controls on mercury accumulation in the souther hemisphere reconstructed using a peat record from Pinheiro Mire (Minas Gerais, Brazil). *Environmental science & technology*, *49*(3), pp.1356-1364.

Pérez-Rodríguez, M., Silva-Sánchez, N., Kylander, M.E., Bindler, R., Mighall, T.M., Schofield, J.E., Edwards, K.J. and Cortizas, A.M., 2018a. Industrial-era lead and mercury contamination in southern Greenland implicates North American sources. *Science of the Total Environment*, *613*, pp.919-930.

Pérez-Rodríguez, M., Horák-Terra, I., Rodríguez-Lado, L., Aboal, J.R. and Martinez Cortizas, A., 2015. Long-term (~ 57 ka) controls on mercury accumulation in the souther hemisphere reconstructed using a peat record from Pinheiro Mire (Minas Gerais, Brazil). *Environmental science & technology*, *49*(3), pp.1356-1364.

Piotrowska, N., Blaauw, M., Mauquoy, D. and Chambers, F.M., 2011. Constructing deposition chronologies for peat deposits using radiocarbon dating. *Mires and Peat*, *7*(10), pp.1-14.

Pirrone, N., Cinnirella, S., Feng, X., Finkelman, R.B., Friedli, H.R., Leaner, J., Mason, R., Mukherjee, A.B., Stracher, G.B., Streets, D.G. and Telmer, K., 2010. Global mercury emissions to the atmosphere from anthropogenic and natural sources. *Atmospheric Chemistry and Physics*, *10*(13), pp.5951-5964.

Pokharel, A.K. and Obrist, D., 2011. Fate of mercury in tree litter during decomposition. *Biogeosciences*, *8*(9), pp.2507-2521.

Prestbo, E.M. and Gay, D.A., 2009. Wet deposition of mercury in the US and Canada, 1996–2005: Results and analysis of the NADP mercury deposition network (MDN). *Atmospheric Environment*, *43*(27), pp.4223-4233.

Prospero, J.M., Ginoux, P., Torres, O., Nicholson, S.E. and Gill, T.E., 2002. Environmental characterization of global sources of atmospheric soil dust identified with the Nimbus 7 Total Ozone Mapping Spectrometer (TOMS) absorbing aerosol product. *Reviews of Geophysics*, 40(1), 2-1-2-31.

Raynaud, D., Blunier, T., Ono, Y. and Delmas, R.J., 2003. The Late Quaternary history of atmospheric trace gases and aerosols: interactions between climate and biogeochemical cycles. In *Paleoclimate, Global Change and the Future* (pp. 13-31). Springer, Berlin, Heidelberg.

Revel-Rolland, M., De Deckker, P., Delmonte, B., Hesse, P.P., Magee, J.W., Basile-Doelsch, I., Grousset, F. and Bosch, D., 2006. Eastern Australia: A possible source of dust in East Antarctica interglacial ice. *Earth and Planetary Science Letters*, *249*(1-2), pp.1-13.

Rintoul, S.R., 2010. Antarctic circumpolar current. *Elements of Physical Oceanography: A derivative of the Encyclopedia of Ocean Sciences. Academic Press, London*, pp.196-208.

Rodríguez-González, P., Epov, V.N., Bridou, R., Tessier, E., Guyoneaud, R., Monperrus, M. and Amouroux, D., 2009. Species-specific stable isotope fractionation of mercury during Hg (II) methylation by an anaerobic bacteria (Desulfobulbus propionicus) under dark conditions. *Environmental science & technology*, *43*(24), pp.9183-9188.

Roman, H.A., Walsh, T.L., Coull, B.A., Dewailly, É., Guallar, E., Hattis, D., Mariën, K., Schwartz, J., Stern, A.H., Virtanen, J.K. and Rice, G., 2011. Evaluation of the cardiovascular effects of methylmercury exposures: current evidence supports development of a dose–response function for regulatory benefits analysis. *Environmental health perspectives*, *119*(5), pp.607-614.

Russell, J.L., Dixon, K.W., Gnanadesikan, A., Stouffer, R.J. and Toggweiler, J.R., 2006. The Southern Hemisphere westerlies in a warming world: Propping open the door to the deep ocean. *Journal of Climate*, *19*(24), pp.6382-6390.

Rutter, A.P., Schauer, J.J., Shafer, M.M., Creswell, J.E., Olson, M.R., Robinson, M., Collins, R.M., Parman, A.M., Katzman, T.L. and Mallek, J.L., 2011. Dry deposition of gaseous elemental mercury to plants and soils using mercury stable isotopes in a controlled environment. *Atmospheric environment*, *45*(4), pp.848-855.

Sabine, C.L. et al., 2004. The Oceanic Sink for Anthropogenic CO2. Science 305, 367–371. https://doi.org/10.1126/science.1097403

Saiz-Lopez, A., Sitkiewicz, S.P., Roca-Sanjuán, D., Oliva-Enrich, J.M., Dávalos, J.Z., Notario, R., Jiskra, M., Xu, Y., Wang, F., Thackray, C.P. and Sunderland, E.M., 2018. Photoreduction of gaseous oxidized mercury changes global atmospheric mercury speciation, transport and deposition. *Nature communications*, *9*(1), p.4796.

Saunders, K.M., Roberts, S.J., Perren, B., Butz, C., Sime, L., Davies, S., Van Nieuwenhuyze, W., Grosjean, M. and Hodgson, D.A., 2018. Holocene dynamics of the Southern Hemisphere westerly winds and possible links to CO2 outgassing. *Nature geoscience*, *11*, pp.650-655.

Schulze, E.D., 1982. Plant life forms and their carbon, water and nutrient relations. In *Physiological plant ecology II* (pp. 615-676). Springer, Berlin, Heidelberg.

Selin, N.E. and Jacob, D.J., 2008. Seasonal and spatial patterns of mercury wet deposition in the United States: Constraints on the contribution from North American anthropogenic sources. *Atmospheric Environment*, *42*(21), pp.5193-5204.

Sherman, L.S., Blum, J.D., Johnson, K.P., Keeler, G.J., Barres, J.A. and Douglas, T.A., 2010. Mass-independent fractionation of mercury isotopes in Arctic snow driven by sunlight. *Nature Geoscience*, *3*(3), p.173.

Shia, R.L., Seigneur, C., Pai, P., Ko, M. and Sze, N.D., 1999. Global simulation of atmospheric mercury concentrations and deposition fluxes. *Journal of Geophysical Research: Atmospheres*, *104*(D19), pp.23747-23760.

Shotyk, W., Goodsite, M.E., Roos-Barraclough, F., Frei, R., Heinemeier, J., Asmund, G., Lohse, C. and Hansen, T.S., 2003. Anthropogenic contributions to atmospheric Hg, Pb and As accumulation recorded by peat cores from southern Greenland and Denmark dated using the 14C "bomb pulse curve". *Geochimica et Cosmochimica Acta*, *67*(21), pp.3991-4011.

Shotyk, W., Goodsite, M.E., Roos-Barraclough, F., Givelet, N., Le Roux, G., Weiss, D., Cheburkin, A.K., Knudsen, K., Heinemeier, J., van Der Knaap, W.O. and Norton, S.A., 2005. Accumulation rates and predominant atmospheric sources of natural and

anthropogenic Hg and Pb on the Faroe Islands. *Geochimica et Cosmochimica Acta*, *69*(1), pp.1-17.

Shotyk, W., Weiss, D., Kramers, J.D., Frei, R., Cheburkin, A.K., Gloor, M. and Reese, S., 2001. Geochemistry of the peat bog at Etang de la Gruère, Jura Mountains, Switzerland, and its record of atmospheric Pb and lithogenic trace metals (Sc, Ti, Y, Zr, and REE) since 12,370 14C yr BP. *Geochimica et Cosmochimica Acta*, *65*(14), pp.2337-2360.

Shulmeister, J., Goodwin, I., Renwick, J., Harle, K., Armand, L., McGlone, M.S., Cook, E., Dodson, J., Hesse, P.P., Mayewski, P. and Curran, M., 2004. The Southern Hemisphere westerlies in the Australasian sector over the last glacial cycle: a synthesis. *Quaternary International*, *118*, pp.23-53.

Slemr, F., Seiler, W. and Schuster, G., 1981. Latitudinal distribution of mercury over the Atlantic Ocean. *Journal of Geophysical Research: Oceans*, *86*(C2), pp.1159-1166.

Song, S., Selin, N.E., Soerensen, A.L., Angot, H., Artz, R., Brooks, S., Brunke, E.G., Conley, G., Dommergue, A., Ebinghaus, R. and Holsen, T.M., 2015. Top-down constraints on atmospheric mercury emissions and implications for global biogeochemical cycling. *Atmospheric Chemistry and Physics*, *15*(12), pp.7103-7125.

Sonke, J.E., 2011. A global model of mass independent mercury stable isotope fractionation. *Geochimica et Cosmochimica Acta*, *75*(16), pp.4577-4590.

Sorensen, J.A., Glass, G.E. and Schmidt, K.W., 1994. Regional patterns of wet mercury deposition. *Environmental science & technology*, *28*(12), pp.2025-2032.

Sprovieri, F., Pirrone, N., Bencardino, M., D'Amore, F., Angot, H., Barbante, C., Brunke, E.G., Arcega-Cabrera, F., Cairns, W., Comero, S. and Diéguez, M.D.C., 2017. Five-year records of mercury wet deposition flux at GMOS sites in the Northern and Southern hemispheres. *Atmospheric Chemistry and Physics*, *17*(4), pp.2689-2708.

Sprovieri, F., Pirrone, N., Bencardino, M., D'Amore, F., Carbone, F., Cinnirella, S., Mannarino, V., Landis, M., Ebinghaus, R., Weigelt, A. and Brunke, E.G., 2016. Atmospheric mercury concentrations observed at ground-based monitoring sites globally distributed in the framework of the GMOS network. *Atmospheric chemistry and physics*, *16*(18), pp.11915-11935.

Steffen, A., Bottenheim, J., Cole, A., Ebinghaus, R., Lawson, G. and Leaitch, W.R., 2014. Atmospheric mercury speciation and mercury in snow over time at Alert, Canada. *Atmospheric Chemistry and Physics*, *14*(5), pp.2219-2231.

Steffen, A., Douglas, T., Amyot, M., Ariya, P., Aspmo, K., Berg, T., Bottenheim, J., Brooks, S., Cobbett, F., Dastoor, A. and Dommergue, A., 2008. A synthesis of atmospheric

mercury depletion event chemistry in the atmosphere and snow. *Atmospheric Chemistry and Physics*, *8*(6), pp.1445-1482.

Steinnes, E. and Sjøbakk, T.E., 2005. Order-of-magnitude increase of Hg in Norwegian peat profiles since the outset of industrial activity in Europe. *Environmental Pollution*, *137*(2), pp.365-370.

Streets, D.G., Horowitz, H.M., Jacob, D.J., Lu, Z., Levin, L., Ter Schure, A.F. and Sunderland, E.M., 2017. Total mercury released to the environment by human activities. *Environmental science & technology*, *51*(11), pp.5969-5977.

Stuut, J.B.W., Prins, M.A., Schneider, R.R., Weltje, G.J., Jansen, J.F. and Postma, G., 2002. A 300-kyr record of aridity and wind strength in southwestern Africa: inferences from grain-size distributions of sediments on Walvis Ridge, SE Atlantic. *Marine Geology*, *180*(1-4), pp.221-233.

Sudarchikova, N., Mikolajewicz, U., Timmreck, C., O'Donnell, D., Schurgers, G., Sein, D. and Zhang, K., 2015. Modelling of mineral dust for interglacial and glacial climate conditions with a focus on Antarctica. *Climate of the Past*.

Sunderland, E.M., Li, M. and Bullard, K., 2018. Erratum:"Decadal Changes in the Edible Supply of Seafood and Methylmercury Exposure in the United States". *Environmental Health Perspectives*, *126*(2), p.029003.

Swart, N.C. and Fyfe, J.C., 2012. Observed and simulated changes in the Southern Hemisphere surface westerly wind-stress. *Geophysical Research Letters*, *39*(16).

Tan, S.C., Li, J., Che, H., Chen, B. and Wang, H., 2017. Transport of East Asian dust storms to the marginal seas of China and the southern North Pacific in spring 2010. *Atmospheric Environment*, *148*, pp.316-328.

Tao, M., Chen, L., Wang, Z., Wang, J., Tao, J. and Wang, X., 2016. Did the widespread haze pollution over China increase during the last decade? A satellite view from space. *Environmental Research Letters*, *11*(5), p.054019.

Tegen, I. and Fung, I., 1994. Modeling of mineral dust in the atmosphere: Sources, transport, and optical thickness. *Journal of Geophysical Research: Atmospheres*, *99*(D11), pp.22897-22914.

Teixeira, F.B., de Oliveira, A.C., Leão, L.K., Fagundes, N.C., Fernandes, R.M., Fernandes, L.M., da Silva, M.C., Amado, L.L., Sagica, F.E., de Oliveira, E.H. and Crespo-Lopez, M.E., 2018. Exposure to inorganic mercury causes oxidative stress, cell death, and functional deficits in the motor cortex. *Frontiers in Molecular Neuroscience*, *11*.

Thompson, D. W., and Solomon, S., 2002. Interpretation of recent Southern Hemisphere climate change. Science, 296(5569), 895-899.

Thompson, L.G., Mosley-Thompson, E., Davis, M.E., Henderson, K.A., Brecher, H.H., Zagorodnov, V.S., Mashiotta, T.A., Lin, P.N., Mikhalenko, V.N., Hardy, D.R. and Beer, J., 2002. Kilimanjaro ice core records: evidence of Holocene climate change in tropical Africa. *science*, *298*(5593), pp.589-593.

Toggweiler, J.R. and Russell, J., 2008. Ocean circulation in a warming climate. *Nature*, *451*(7176), p.286.

Toggweiler, J.R., 2009. Shifting westerlies. *Science*, *323*(5920), pp.1434-1435.

UNEP-GMA, 2018. United Nations Environment Programme: Global mercury assessment, pp. 1-62.

Van der Putten, N., Mauquoy, D., Verbruggen, C. and Björck, S., 2012. Subantarctic peatlands and their potential as palaeoenvironmental and palaeoclimatic archives. *Quaternary International*, *268*, pp.65-76.

Van der Putten, N., Verbruggen, C., Björck, S., Michel, E., Disnar, J.-R., Chapron, E., Moine, B.N., de Beaulieu, J.-L., 2015. The Last Termination in the South Indian Ocean: A unique terrestrial record from Kerguelen Islands (49°S) situated within the Southern Hemisphere westerly belt. Quaternary Science Reviews 122, 142–157. https://doi.org/10.1016/j.quascirev.2015.05.010

Vandal, G.M., Fitzgerald, W.F., Boutron, C.F. and Candelone, J.P., 1993. Variations in mercury deposition to Antarctica over the past 34,000 years. *Nature*, *362*(6421), p.621.

Vandergoes, M.J., Hogg, A.G., Lowe, D.J., Newnham, R.M., Denton, G.H., Southon, J., Barrell, D.J., Wilson, C.J., McGlone, M.S., Allan, A.S. and Almond, P.C., 2013. A revised age for the Kawakawa/Oruanui tephra, a key marker for the Last Glacial Maximum in New Zealand. *Quaternary Science Reviews*, *74*, pp.195-201.

Van Loon, G.W. and Duffy, S.J., 2017. *Environmental chemistry: a global perspective*. Oxford university press.

Vanneste, H., De Vleeschouwer, F., Bertrand, S., Martínez-Cortizas, A., Vanderstraeten, A., Mattielli, N., Coronato, A., Piotrowska, N., Jeandel, C. and Le Roux, G., 2016. Elevated dust deposition in Tierra del Fuego (Chile) resulting from Neoglacial Darwin Cordillera glacier fluctuations. *Journal of Quaternary Science*, 31(7), 713-722.

Vanneste, H., De Vleeschouwer, F., Martínez-Cortizas, A., Von Scheffer, C., Piotrowska, N., Coronato, A. and Le Roux, G., 2015. Late-glacial elevated dust deposition linked to westerly wind shifts in southern South America. *Scientific reports*, 5, 11670.

Velasco-Merino, C., Mateos, D., Toledano, C., Prospero, J.M., Molinie, J., Euphrasie-Clotilde, L., González, R., Cachorro, V.E., Calle, A. and Frutos, A.M.D., 2018. Impact of long-range transport over the Atlantic Ocean on Saharan dust optical and microphysical properties based on AERONET data. *Atmospheric Chemistry and Physics*, *18*(13), pp.9411-9424.

Vickery, K.J., Eckardt, F.D. and Bryant, R.G., 2013. A sub-basin scale dust plume source frequency inventory for southern Africa, 2005–2008. *Geophysical Research Letters*, 40(19), 5274-5279.

Voigt, I., Chiessi, C.M., Prange, M., Mulitza, S., Groeneveld, J., Varma, V., Henrich, R., 2015. Holocene shifts of the southern westerlies across the South Atlantic: Holocene shifts of Southern Westerlies. *Paleoceanography*, 30, 39–51.

Von Scheffer, C., Lange, A., De Vleeschouwer, F. and Schrautzer, J., 2019. 6200 years of human activities and environmental change in the northern central Alps. *E & G Quaternary Science Journal*, *68*(1), pp.13-28.

Waliser, D.E. and Gautier, C., 1993. A satellite-derived climatology of the ITCZ. *Journal of climate*, *6*(11), pp.2162-2174.

Wang, X., Luo, J., Yin, R., Yuan, W., Lin, C.J., Sommar, J., Feng, X., Wang, H. and Lin, C., 2017. Using mercury isotopes to understand mercury accumulation in the montane forest floor of the Eastern Tibetan Plateau. *Environmental science & technology*, *51*(2), pp.801-809.

Wedepohl, K.H. (1995) The composition of the continental crust. Geochimica et Cosmochimica Acta 59(7), 1217-1232.

Wegner, A., Gabrielli, P., Wilhelms-Dick, D., Ruth, U., Kriews, M., Deckker, P.D., Barbante, C., Cozzi, G., Delmonte, B. and Fischer, H., 2012. Change in dust variability in the Atlantic sector of Antarctica at the end of the last deglaciation. *Climate of the Past*, *8*(1), pp.135-147.

Weltje, G.J. and Prins, M.A., 2007. Genetically meaningful decomposition of grain-size distributions. *Sedimentary Geology*, *202*(3), pp.409-424.

Whittle, A., Amesbury, M.J., Charman, D.J., Hodgson, D.A., Perren, B.B., Roberts, S.J. and Gallego-Sala, A.V., 2019. Salt-enrichment impact on biomass production in a natural population of peatland dwelling Arcellinida and Euglyphida (testate amoebae). *Microbial ecology*, *78*(2), pp.534-538

Wieder, R.K. and Lang, G.E., 1983. Net primary production of the dominant bryophytes in a Sphagnum-dominated wetland in West Virginia. *Bryologist*, pp.280-286.

Winton, V.H.L., Edwards, R., Delmonte, B., Ellis, A., Andersson, P.S., Bowie, A., Bertler, N.A.N., Neff, P. and Tuohy, A., 2016. Multiple sources of soluble atmospheric iron to Antarctic waters. *Global Biogeochemical Cycles*, *30*(3), pp.421-437.

Xia, Z., Yu, Z. and Loisel, J., 2018. Centennial-scale dynamics of the Southern Hemisphere Westerly Winds across the Drake Passage over the past two millennia. *Geology*, *46*(10), pp.855-858.

Young, E.D., Galy, A. and Nagahara, H., 2002. Kinetic and equilibrium mass-dependent isotope fractionation laws in nature and their geochemical and cosmochemical significance. *Geochimica et Cosmochimica Acta*, *66*(6), pp.1095-1104.

Zaferani, S., Pérez-Rodríguez, M. and Biester, H., 2018. Diatom ooze—A large marine mercury sink. *Science*, *361*(6404), pp.797-800.

Zhao, H., Yan, H., Zhang, L., Sun, G., Li, P. and Feng, X., 2019. Mercury contents in rice and potential health risks across China. *Environment international*, *126*, pp.406-412.

Zheng, W. and Hintelmann, H., 2010. Nuclear field shift effect in isotope fractionation of mercury during abiotic reduction in the absence of light. *The Journal of Physical Chemistry A*, *114*(12), pp.4238-4245.

Zheng, W., Demers, J.D., Lu, X., Bergquist, B.A., Anbar, A.D., Blum, J.D. and Gu, B., 2018. Mercury Stable Isotope Fractionation during Abiotic Dark Oxidation in the Presence of Thiols and Natural Organic Matter. *Environmental science & technology*.

Zheng, W., Obrist, D., Weis, D. and Bergquist, B.A., 2016. Mercury isotope compositions across North American forests. *Global Biogeochemical Cycles*, *30*(10), pp.1475-1492.

Method

Table 1. Brief introduction of the methods used in this PhD. See single chapters for further details.

Items	Analytical equipement /tool	Location	People involved	Number of samples	Reference	Presented in Chapter
Peat coring	Russian corer; Wardenaar corer	Amsterdam Island; Falkland Islands (*Islas Malvinas*); Harberton and Andorra (Tierra del Fuego, Argentina)	EcoLab team and collaborators	6 cores	[1, 2, 3]	1, 2, 3, 4
Peat sub-samping	Band saw (slicing)	*Ecolab*, Toulouse, France	EcoLab BIZ team and collaborators including **C. Li**	700	[3, 4]	1, 2, 3, 4
Peat acid-digestion	Teflon savillex	*Ecolab*, Toulouse, France	**C. Li**; M. Tavella; F. De Vleeschouwer; G. Le Roux	150		2
^{210}Pb, ^{137}Cs and ^{241}Am preparation and measurement	Germanium Detector (Gamma-ray)	LAFARA underground laboratory, Ferrières, France	P. Van Beek; M. Souhaut; **C. Li**; M. Tavella;	15	[5]	1
^{14}C measurements on selected macrofossil samples	Accelerator Mass Spectrometry	Silesian University of Technology, Poland (GdA code); Plateforme Nationale, France (LMC14 code)	N. Piotrowska; N. Van der Putten; D. Mauquoy	60	[6, 7, 8]	2, 3, 4
Major elements	Inductively Coupled Plasma-Optical Emission Spectrometry	Ecolab, Toulouse, France	**C. Li** D. Baqué; M. Tavella; F. De Vleeschouwer; J. Sonke	120		2
Major and trace elements	Quadruple Inductively Coupled Mass Spectrometry	Observatoire Midi-Pyrenees, Toulouse, France	**C. Li**; M. Tavella; F. De Vleeschouwer; G. Le Roux ; J. Sonke	160		2
Nd isotopes	Thermal Ionization Mass Spectrometry	Observatoire Midi-Pyrenees, Toulouse, France	**C. Li**; C. Jeandel; M. Benoit; S. Mounic ; J. Prunier ; F. De Vleeschouwer	60		2
Hg concentration in Solid	Direct Mercury Analyzer	Observatoire Midi-Pyrenees, Toulouse, France	**C. Li**; J. Sonke	500		3, 4
Hg isotope extraction	Oven (Combustion and acid trapping)	Observatoire Midi-Pyrenees, Toulouse, France	**C. Li**; J. Sonke; M. Enrico	60	[9]	4
Hg concentration in Solution	Cold vapor atomic fluorescence spectroscopy	Observatoire Midi-Pyrenees, Toulouse, France	**C. Li**; J. Sonke	60		4
Hg isotope analysis	Multi Collector-Inductively Coupled Mass Spectrometry	Observatoire Midi-Pyrenees, Toulouse, France	**C. Li**; J. Sonke; M. Enrico	60		4

Table 2. Principal element/isotope information from Certified Standard Materials (CRMs) used in this PhD. Informative provisional values are reported in italic and under brackets, respectively. (Mean ± standard deviation; 2σ for Hg isotopes, 1σ otherwise). All measured values without CRMs information are in agreement with previously reported values (see references). See single chapters for further details.

Element/ Isotopes	**Materials**	**Numbers of analysis**	**measured values**	**Certified value**
Lanthanum (La, µg g^{-1})	SRM 1515 (Apple leave)	n=4	20.7±0.8	*20*
	SRM 1947 (Peach leave)	n=3	8.3±0.4	*9*
	NJV 942 (*Sphagnum* peat)	n=4	0.87±0.09	0.84±0.03 (n=8), [ref 10]
	NJV 941 (Carex/sedge peat)	n=8	0.7±0.06	
	WQB-1 (sediment)	n=3	46±2	*37.9*
	LKSD-3 (sediment)	n=4	50±1	(52)
Cerium (Ce, µg g^{-1})	SRM 1515	n=4	3.0±0.1	*3*
	SRM 1947	n=3	9±0.4	*10*
	NJV 942	n=4	1.65±0.17	
	NJV 941	n=8	1.49±0.13	
	WQB-1	n=3	96±2	*77.6*
	LKSD-3	n=4	99±3	(90)
Praseodynium (Pr, µg g^{-1})	SRM 1515	n=4	4.1±0.2	4.1±0.4 (n=3), [ref 11]
	SRM 1947	n=3	1.7±0.1	1.6±0.1 (n=7), [ref 11]
	NJV 942	n=4	0.21±0.02	
	NJV 941	n=8	0.19±0.02	
	WQB-1	n=3	11±0.1	
	LKSD-3	n=4	12±0.04	
Neodynium (Nd, µg g^{-1})	SRM 1515	n=4	15.5±0.6	*17*
	SRM 1947	n=3	6.2±0.3	*7*
	NJV 942	n=4	0.72±0.08	
	NJV 941	n=8	0.69±0.06	
	WQB-1	n=3	40±0.3	
	LKSD-3	n=4	45±0.5	(44)
Samarium (Sm, µg g^{-1})	SRM 1515	n=4	2.8±0.1	*3*
	SRM 1947	n=3	0.99±0.06	*1*
	NJV 942	n=4	0.13±0.01	
	NJV 941	n=8	0.13±0.01	
	WQB-1	n=3	7.5±0.05	
	LKSD-3	n=4	7.9±0.1	(8)
Europium (Eu, µg g^{-1})	SRM 1515	n=4	0.25±0.01	*0.2*
	SRM 1947	n=3	0.19±0.01	*0.17*
	NJV 942	n=4	0.03±0.002	
	NJV 941	n=8	0.03±0.002	
	WQB-1	n=3	1.6±0.03	
	LKSD-3	n=4	1.5±0.01	(1.5)
Gadolinium (Gd, µg g^{-1})	SRM 1515	n=4	2.94±0.09	*3*
	SRM 1947	n=3	0.97±0.05	*1*
	NJV 942	n=4	0.12±0.01	
	NJV 941	n=8	0.13±0.01	
	WQB-1	n=3	7±0.2	
	LKSD-3	n=4	7±0.1	
Element/ Isotopes	**Materials**	**Numbers of analysis**	**measured values**	**Certified value**
Terbium (Tb, µg g^{-1})	SRM 1515	n=4	0.37±0.02	*0.4*
	SRM 1947	n=3	0.11±0.007	*0.1*

	NJV 942	n=4	0.02±0.002	
	NJV 941	n=8	0.02±0.002	
	WQB-1	n=3	0.95±0.02	
	LKSD-3	n=4	0.9±0.01	(1)
Dysprosium (Dy, µg g^{-1})	SRM 1515	n=4	1.78±0.08	1.80±0.2 (n=3), [ref 11]
	SRM 1947	n=3	0.52±0.03	0.51±0.02 (n=7), [ref 11]
	NJV 942	n=4	0.09±0.009	
	NJV 941	n=8	0.11±0.01	
	WQB-1	n=3	5.6±0.1	
	LKSD-3	n=4	5.1±0.04	(4.9)
Holium (Ho, µg g^{-1})	SRM 1515	n=4	0.27±0.01	0.28±0.03 (n=3), [ref 11]
	SRM 1947	n=3	0.08±0.004	0.08±0.01 (n=7), [ref 11]
	NJV 942	n=4	0.02±0.002	
	NJV 941	n=8	0.02±0.002	
	WQB-1	n=3	1.01±0	
	LKSD-3	n=4	0.93±0.008	
Erbium (Er, µg g^{-1})	SRM 1515	n=4	0.57±0.02	0.55±0.04 (n=3), [ref 11]
	SRM 1947	n=3	0.21±0.01	0.20±0.01 (n=7), [ref 11]
	NJV 942	n=4	0.05±0.006	
	NJV 941	n=8	0.07±0.006	
	WQB-1	n=3	3±0.2	
	LKSD-3	n=4	2.7±0.05	
Thulium (Tm, µg g^{-1})	SRM 1515	n=4	0.05±0.002	0.05±0.01 (n=3), [ref 11]
	SRM 1947	n=3	0.02±0.0004	0.02±0.0 (n=7), [ref 11]
	NJV 942	n=4	0.01±0.0005	
	NJV 941	n=8	0.01±0.001	
	WQB-1	n=3	0.42±0.02	
	LKSD-3	n=4	0.38±0.01	
Ytterbium (Yb, µg g^{-1})	SRM 1515	n=4	0.19±0.01	*0.3*
	SRM 1947	n=3	0.12±0.004	*0.2*
	NJV 942	n=4	0.05±0.005	
	NJV 941	n=8	0.06±0.006	
	WQB-1	n=3	2.8±0.1	
	LKSD-3	n=4	2.5±0.03	(2.7)
Lutetium (Lu, µg g^{-1})	SRM 1515	n=4	0.02±0.001	0.02±0.0 (n=3), [ref 11]
	SRM 1947	n=3	0.02±0.0001	0.02±0.0 (n=7), [ref 11]
	NJV 942	n=4	0.007±0.0006	
	NJV 941	n=8	0.01±0.001	
	WQB-1	n=3	0.41±0.02	
	LKSD-3	n=4	0.38±0.005	(0.4)
$^{143}Nd/^{144}Nd$	Rennes	n=22	0.511956± 0.000006	0.511973
	La Jolla	n=9	0.511844± 0.000012	0.511858
Hg concentration (ng g^{-1})	IPE 176 (Reed)	n=143	35.1±6.3	37.9±2.9
	NIST 1632d (Coal)	n=9	91.3±7.0	92.8±3.3
	BCR 482 (Lichen)	n=5	481.3±8.7	480±20
$\delta^{202}Hg$	ETH-Fluka	n=19	-1.43±0.15	-1.43±0.13 (2σ, n=80) [refs 12, 13, 14, 15, 16, 19]
	UM-Almaden	n=7	-0.52±0.13	-0.56±0.12 (2σ, n=133) [refs 12, 17, 18, 20]
Element/ Isotopes	**Materials**	**Numbers of analysis**	**measured values**	**Certified value**
$\delta^{202}Hg$	BCR-482	n=9	-1.53±0.09	-1.59±0.23 (2σ, n=10) [refs 19, 20]
	NIST 1632d	n=4	-1.86±0.15	-1.74±0.18 (2σ, n=46) [refs 12, 21, 22, 23, 24]
$\Delta^{199}Hg$	ETH-Fluka	n=19	0.05±0.13	0.08±0.05 (2σ, n=80) [refs 12, 13, 14, 15, 16, 19]

	UM-Almaden	n=7	-0.03±0.09	-0.03±0.06 (2σ, n=133) [refs 12, 17, 18, 20]
	BCR-482	n=9	-0.69±0.08	-0.62±0.06 (2σ, n=10) [refs 19, 20]
	NIST 1632d	n=4	-0.03±0.06	-0.04±0.18 (2σ, n=46) [refs 12, 21, 22, 23, 24]
Δ^{200}Hg	ETH-Fluka	n=19	-0.01±0.10	0.02±0.10(2σ, n=80) [refs 12, 13, 14, 15, 16, 19]
	UM-Almaden	n=7	0±0.09	0.01±0.06 (2σ, n=133) [refs 12, 17, 18, 20]
	BCR-482	n=9	0.08±0.10	-0.06±0.08 (2σ, n=10) [refs 19, 20]
	NIST 1632d	n=4	0.01±0.05	0.03±0.07 (2σ, n=46) [refs 12, 21, 22, 23, 24]
Δ^{201}Hg	ETH-Fluka	n=19	0.01±0.11	0.02±0.10(2σ, n=42) [refs 12, 13, 14, 15, 16, 19]
	UM-Almaden	n=7	-0.07±0.06	-0.04±0.06 (2σ, n=124) [refs 12, 17, 18, 20]
	BCR-482	n=9	-0.67±0.09	-0.64±0.08 (2σ, n=10) [refs 19, 20]
	NIST 1632d	n=4	-0.02±0.04	-0.03±0.08 (2σ, n=34) [refs 12, 21, 22, 23, 24]
Δ^{204}Hg	ETH-Fluka	n=21	0.01±0.25	-0.01±0.10(2σ, n=42) [refs 12, 13, 14, 15, 16, 19]
	UM-Almaden	n=7	-0.03±0.19	-0.01±0.09 (2σ, n=111) [refs 12, 17, 18, 20]
	BCR-482	n=9	-0.10±0.19	-0.07±0.18 (2σ, n=10) [refs 19, 20]
	NIST 1632d	n=4	0.08±0.08	-0.03±0.12 (2σ, n=26) [refs 12, 21, 22, 23, 24]

References:

[1] Wardenaar, E.C.P., 1987. A new hand tool for cutting peat profiles. *Canadian Journal of Botany*, *65*(8), pp.1772-1773.

[2] Belokopytov, I.E. and Beresnevich, V.V., 1955. Giktorf's peat borers. *Torfyanaya Promyshlennost*, *8*(9), p.10.

[3] De Vleeschouwer, F., Chambers, F.M. and Swindles, G.T. (2010) Coring and sub-sampling of peatlands for palaeoenvironmental research. Mires and Peat 7.

[4] Givelet, N., Le Roux, G., Cheburkin, A., Chen, B., Frank, J., Goodsite, M.E., Kempter, H., Krachler, M., Noernberg, T. and Rausch, N. (2004) Suggested protocol for collecting, handling and preparing peat cores and peat samples for physical, chemical, mineralogical and isotopic analyses. Journal of Environmental Monitoring 6(5), 481-492.

[5] Van Beek, P.; Souhaut, M.; Lansard, B.; Bourquin, M.; Reyss, J.-L.; Von Ballmoos, P.; Jean, P., LAFARA: a new underground laboratory in the French Pyrenees for ultra low-level gamma-ray spectrometry. *Journal of environmental radioactivity* 2013, *116*, 152-158.

[6] Piotrowska, N. (2013) Status report of AMS sample preparation laboratory at GADAM Centre, Gliwice, Poland. Nuclear Instruments and Methods in Physics Research Section B: Beam Interactions with Materials and Atoms 294, 176-181.

[7] Moreau, C., Caffy, I., Comby, C., Delqué-Količ, E., Dumoulin, J.P., Hain, S., Quiles, A., Setti, V., Souprayen, C., Thellier, B. and Vincent, J., 2013. Research and development of the Artemis 14 C AMS Facility: status report. *Radiocarbon*, *55*(2), pp.331-337.

[8] Delqué-Količ, E., Caffy, I., Comby-Zerbino, C., Dumoulin, J.P., Hain, S., Massault, M., Moreau, C., Quiles, A., Setti, V., Souprayen, C. and Tannau, J.F., 2013. Advances in handling small radiocarbon samples at the Laboratoire de Mesure du Carbone 14 in Saclay, France. *Radiocarbon*, *55*(2), pp.648-656.

[9] Sun, R., Enrico, M., Heimbürger, L.E., Scott, C. and Sonke, J.E., 2013. A double-stage tube furnace—acid-trapping protocol for the pre-concentration of mercury from solid samples for isotopic analysis. *Analytical and bioanalytical chemistry*, *405*(21), pp.6771-6781.

[10] Hansson, S.V., Claustres, A., Probst, A., De Vleeschouwer, F., Baron, S., Galop, D., Mazier, F. and Le Roux, G., 2017. Atmospheric and terrigenous metal accumulation over 3000 years in a French mountain catchment: Local vs distal influences. *Anthropocene*, *19*, pp.45-54.

[11] Vanneste, H., De Vleeschouwer, F., Martínez-Cortizas, A., Von Scheffer, C., Piotrowska, N., Coronato, A. and Le Roux, G. (2015) Late-glacial elevated dust deposition linked to westerly wind shifts in southern South America. Scientific reports 5, 11670.

[12] Enrico, M., 2015. Dépôts atmosphériques de mercure et compositions en isotopes stables du mercure dans les tourbières. Thesis.

[13] Jiskra, M., Wiederhold, J.G., Skyllberg, U., Kronberg, R.M., Hajdas, I. and Kretzschmar, R., 2015. Mercury deposition and re-emission pathways in boreal forest soils investigated with Hg isotope signatures. *Environmental science & technology*, *49*(12), pp.7188-7196.

[14] Smith, R.S., Wiederhold, J.G., Jew, A.D., Brown Jr, G.E., Bourdon, B. and Kretzschmar, R., 2014. Small-scale studies of roasted ore waste reveal extreme ranges of stable mercury isotope signatures. *Geochimica et Cosmochimica Acta*, *137*, pp.1-17.

[15] Xu, H.M., Sun, R.Y., Cao, J.J., Huang, R.J., Guinot, B., Shen, Z.X., Jiskra, M., Li, C.X., Du, B.Y., He, C. and Liu, S.X., 2019. Mercury stable isotope compositions of Chinese urban fine particulates in winter haze days: Implications for Hg sources and transformations. *Chemical Geology*, *504*, pp.267-275.

[16] Grigg, A.R., Kretzschmar, R., Gilli, R.S. and Wiederhold, J.G., 2018. Mercury isotope signatures of digests and sequential extracts from industrially contaminated soils and sediments. *Science of the Total Environment*, *636*, pp.1344-1354.

[17] Guédron, S., Amouroux, D., Sabatier, P., Desplanque, C., Develle, A.L., Barre, J., Feng, C., Guiter, F., Arnaud, F., Reyss, J.L. and Charlet, L., 2016. A hundred year record of industrial and urban development in French Alps combining Hg accumulation rates and isotope composition in sediment archives from Lake Luitel. *Chemical Geology*, *431*, pp.10-19.

[18] Kurz, A.Y., Blum, J.D., Washburn, S.J. and Baskaran, M., 2019. Changes in the mercury isotopic composition of sediments from a remote alpine lake in Wyoming, USA. *Science of The Total Environment*, *669*, pp.973-982.

[19] Obrist, D., Agnan, Y., Jiskra, M., Olson, C.L., Colegrove, D.P., Hueber, J., Moore, C.W., Sonke, J.E. and Helmig, D., 2017. Tundra uptake of atmospheric elemental mercury drives Arctic mercury pollution. *Nature*, *547*(7662), p.201.

[20] Fu, X., Zhang, H., Feng, X., Tan, Q., Ming, L., Liu, C. and Zhang, L., 2019. Domestic and transboundary sources of atmospheric particulate bound mercury in remote areas of China: evidence from mercury isotopes. *Environmental science & technology*.

[21] Sun, R., Enrico, M., Heimbürger, L.E., Scott, C. and Sonke, J.E., 2013. A double-stage tube furnace—acid-trapping protocol for the pre-concentration of mercury from solid samples for isotopic analysis. *Analytical and bioanalytical chemistry*, *405*(21), pp.6771-6781.

[22] Sun, R., Heimbürger, L.E., Sonke, J.E., Liu, G., Amouroux, D. and Berail, S., 2013. Mercury stable isotope fractionation in six utility boilers of two large coal-fired power plants. *Chemical Geology*, *336*, pp.103-111.

[23] Sun, R., Sonke, J.E., Heimbürger, L.E., Belkin, H.E., Liu, G., Shome, D., Cukrowska, E., Liousse, C., Pokrovsky, O.S. and Streets, D.G., 2014. Mercury stable isotope signatures of world coal deposits and historical coal combustion emissions. *Environmental science & technology*, *48*(13), pp.7660-7668.

[24] Sun, R., Sonke, J.E., Liu, G., Zheng, L. and Wu, D., 2014. Variations in the stable isotope composition of mercury in coal-bearing sequences: Indications for its provenance and geochemical processes. *International Journal of Coal Geology*, *133*, pp.13-23.

Chapter 1.

Recent ^{210}Pb, ^{137}Cs and ^{241}Am accumulation in an ombrotrophic peatland from Amsterdam Island (Southern Indian Ocean)

Objectifs et résumé

Le plomb 210 (^{210}Pb, $T_{1/2}$ = 22.3 ans) est un radionucléide naturel provenant de la désintégration du ^{222}Rn sous forme gazeuse ($T_{1/2}$ = 3.8 jours). Le ^{222}Rn s'échappe des surfaces continentales terrestres, pénètre dans l'atmosphère et se désintègre en ^{210}Pb, qui se fixe à son tour rapidement sur les aérosols submicroniques. Le ^{210}Pb se diffuse sur toute la surface de la Terre et peut se déposer par dépôt sec ou humide. En raison de leurs demi-vies relativement courte, le ^{222}Rn et le ^{210}Pb ont été utilisés comme traceurs pour déterminer l'origine des masses d'air, comprendre le temps de résidence des aérosols et générer des modèles climat-aérosol globaux. Le ^{210}Pb peut être utilisé pour construire des chronologies d'accumulation sédimentaires au cours des 150 dernières années. Les inventaires de ^{210}Pb sont également utilisés dans les études sur l'érosion des sols lorsque ces inventaires calculés pour les sédiments lacustres sont utilisés pour estimer les facteurs de focalisation du dépôt de polluants dans les lacs. Pour accéder à ces fonctions, l'étape préliminaire consiste à fournir une base de données globale des inventaires de ^{210}Pb. Cependant, il existe peu de données dans l'hémisphère sud, en particulier dans le sud de l'océan Indien.

Dans ce chapitre, nous présentons des données sur les radionucléides (^{210}Pb, ^{137}Cs et ^{241}Am) et reconstruisons la chronologie d'une tourbière de l'île d'Amsterdam (AMS) située dans le sud de l'océan Indien. AMS est située à mi-chemin de l'Afrique australe et de l'Australie, exempte de perturbations anthropiques. La tourbière est exclusivement alimentée par les apports atmosphériques et constitue donc un bon enregistreur des dépôts atmosphériques.

Les radionucléides de la tourbe ont été mesurés à l'aide d'un spectromètre gamma souterrain, à bruit de fond ultra-bas. Nous avons comparé les données avec une base de données de dépôt ^{210}Pb mise à jour. Nous avons trouvé un ^{210}Pb flux de 98 ± 6 Bq m^{-2} an^{-1} à AMS, en accord avec les données de Madagascar et de l'Afrique du Sud. Un flux élevé de ^{210}Pb observé à un endroit aussi éloigné peut résulter de l'activité accrue du ^{222}Rn et des précipitations fréquentes sur AMS. L'activité ^{222}Rn accrue peut elle-même être expliquée par les masses d'air continental traversant des zones continentales (par exemple l'Afrique australe et / ou Madagascar). Le flux de ^{210}Pb à AMS est supérieur aux valeurs provenant de latitudes similaires dans les régions côtières argentines et chiliennes, qui sont dominées par les vents marins d'ouest à faible activité ^{222}Rn. Nos données contribuent à la couverture de données ^{210}Pb sous-représentées dans les latitudes moyennes de l'hémisphère sud.

Nous appliquons le modèle taux d'apport constant (« *Constant Rate of Supply* – CRS ») à l'inventaire ^{210}Pb pour générer l'âge de tourbe récent. Étant donné que le ^{210}Pb peut être mobile dans la colonne de tourbe, la chronologie construite par ^{210}Pb seul peut se révéler imprécise. Le ^{137}Cs et l'^{241}Am sont des radionucléides artificiels principalement dérivés de retombées des essais de bombes nucléaires aériennes dans les années 60. Nous avons constaté que les pics de ^{137}Cs et de ^{241}Am dans la colonne de tourbe correspondent à la période 1960-1981 dérivée du modèle CRS. Nous concluons donc que le modèle d'accumulation de tourbe de ^{210}Pb CRS est validé par des chronomarqueurs indépendants, ^{137}Cs et ^{241}Am. Les radionucléides artificiels trouvés dans une île éloignée constituent également un signal anthropocène. Le sondage de tourbe présenté ici couvre une période d'environ 157 ans, ce qui indique un taux d'accumulation de la tourbe d'environ 0.75 mm an^{-1}.

Research article

Recent ^{210}Pb, ^{137}Cs and ^{241}Am accumulation in an ombrotrophic peatland from Amsterdam Island (Southern Indian Ocean)

*(*Published in *Journal of environmental radioactivity, 175, 164-169)*

Recent ^{210}Pb, ^{137}Cs and ^{241}Am accumulation in an ombrotrophic peatland from Amsterdam Island (Southern Indian Ocean)

Chuxian Li[1*], Gaël Le Roux[1], Jeroen Sonke[2], Pieter van Beek[3], Marc Souhaut[3], Nathalie Van der Putten[4], François De Vleeschouwer[1]

1 *EcoLab CNRS, Université de Toulouse, Castanet Tolosan, France.*

2 *Geoscience, Environment, Toulouse, Midi- Pyrénées Observatory, Toulouse, France.*

3 *LEGOS (CNRS/CNES/IRD/UPS), Midi- Pyrénées Observatory, Toulouse, France.*

4 *Department of Geology, Quaternary Sciences, Lund University, Lund, Sweden.*

*Corresponding author at: EcoLab (Laboratoire Ecologie Fonctionnelle et Environnement), ENSAT, Avenue de l'Agrobiopole, 31326 Castanet Tolosan, France

E-mail address: chuxian.li@ensat.fr

Abstract

Over the past 50 years, ^{210}Pb, ^{137}Cs and ^{241}Am have been abundantly used in reconstructing recent sediment and peat chronologies. The study of global aerosol-climate interaction is also partially depending on our understanding of ^{222}Rn-^{210}Pb cycling, as radionuclides are useful aerosol tracers. However, in comparison with the Northern Hemisphere, few data are available for these radionuclides in the Southern Hemisphere, especially in the South Indian Ocean. A peat core was collected in an ombrotrophic peatland from the remote Amsterdam Island (AMS) and was analyzed for ^{210}Pb, ^{137}Cs and ^{241}Am radionuclides using an underground ultra-low background gamma spectrometer. The ^{210}Pb Constant Rate of Supply (CRS) model of peat accumulations is validated by peaks of artificial radionuclides (^{137}Cs and ^{241}Am) that are related to nuclear weapon tests. We compared the AMS ^{210}Pb data with an updated ^{210}Pb deposition database. The ^{210}Pb flux of 98 ± 6 $Bq \cdot m^{-2} \cdot y^{-1}$ derived from the AMS core agrees with data from Madagascar and South Africa. The elevated flux observed at such a remote location may result from the enhanced ^{222}Rn activity and frequent rainfall in AMS. This enhanced ^{222}Rn activity itself may be explained by continental air masses passing over southern Africa and/or Madagascar. The ^{210}Pb flux at AMS is higher than those derived from cores collected in coastal areas in Argentina and Chile, which are areas dominated by marine westerly winds with low ^{222}Rn activities. We report a ^{137}Cs inventory at AMS of 144 ± 13 $Bq \cdot m^{-2}$ (corrected to 1969). Our data thus contribute to the under-represented data coverage in the mid-latitudes of the Southern Hemisphere.

Keywords: radionuclides, ^{210}Pb, ^{137}Cs, ^{241}Am, peat, Southern Indian Ocean

Highlights:

- First peat record of artificial radionuclides (^{137}Cs and ^{241}Am) in the Southern Indian Ocean.
- Updated world ^{210}Pb database with 47 new entries from the recent literature.
- ^{210}Pb inventory found in the peat core from Amsterdam Island is similar to those from South Africa and Madagascar.

One abstract + main text (3087 words) + 4 figures + supplementary information

1. Introduction

Lead-210 (^{210}Pb, $T_{½}$=22.3 years) dating is the most common method employed to estimate short-term (from years to decades) chronologies in peat, estuarine, fluvial, and lacustrine environments (Le Roux and Marshall, 2011; Robbins and Edgington, 1975; Benoit and Rozan, 2001; Humphires et al., 2010). ^{210}Pb originates from the decay of gaseous ^{222}Rn, which escapes from the Earth's continental crust to the atmosphere (Graustein and Turekian, 1990). ^{210}Pb adsorbs strongly to the surface of aerosols in the 0.1 ~ 0.5 μm diameter size range as soon as it is produced in the air (Knuth et al., 1983). ^{210}Pb-bearing aerosols are distributed globally by general atmospheric circulation and can be deposited on the Earth's surface mainly by precipitation, but also by dry fallout as well as convective updrafts (Knuth et al., 1983; Baskaran, 2011). The ^{210}Pb deposited from the atmosphere is called "unsupported ^{210}Pb" or "excess ^{210}Pb" (denoted $^{210}Pb_{ex}$), which should be distinguished from the ^{210}Pb produced inside the matrix (e.g. lake sediment) and which is, named "supported ^{210}Pb" (Guevara et al., 2003).

The Constant Rate of Supply (CRS) model based on $^{210}Pb_{ex}$ flux, which could be validated by nuclear fallout studies (e.g. ^{137}Cs, ^{241}Am), is by now widely used (e.g. Appleby et al., 2001; 2008). Another radionuclide that is widely used to derive ages is ^{137}Cs. With a half-life of 30.2 years, ^{137}Cs is considered as one of the important radionuclides among those from nuclear emissions (e.g. atmospheric nuclear weapon tests in the 1950s-1970s with the peak in 1963 in the Northern Hemisphere and the fallout from the Chernobyl accident in 1986), with respect to being a persistent tracer and an indicator of single-event chronology (Aoyama et al., 2006; Rodway-Dyer and Walling, 2010). In contrast, ^{241}Am - another artificial radionuclide - is strictly related to nuclear bomb testing in remote areas.

Up to now, most studies about the inventory of sediment radionuclides and radiochronology have been conducted in the Northern Hemisphere. Limited work has been carried out in the Southern Hemisphere, especially in the Indian Ocean. The scarcity of studies conducted in the Southern Hemisphere is partly due to the lower fallout of ^{210}Pb and ^{137}Cs, fewer continental surfaces and fewer man-made radionuclide emissions and fallout, which generally result in lower activities bordering on analytical detection limits (Owens and Walling, 1996; Bonotto and de Lima, 2006). In the Southern Hemisphere nuclear weapons fallout is about three times lower than that in the Northern Hemisphere. Consequently, the ^{137}Cs fallout peak is usually more difficult to identify in cores due to the relatively high measurement uncertainties associated with the low ^{137}Cs concentrations (Hancock et al., 2011). Southern Hemisphere investigations on ^{210}Pb and ^{137}Cs have been confined primarily to large land

masses, such as South America (Sanders et al., 2006; Guevara et al., 2003; Cisternas et al., 2001), Australia and New Zealand (Pfitzner et al., 2004; Hancock et al., 2011), South Africa and Madagascar (Humphries et al., 2010; Kading et al., 2009; Iva-novitch and Harmon, 1992; Rabesiranana et al., 2016) .

No studies on terrestrial sediment radionuclides and radiochronology exist for the Southern Indian Ocean, although the area is an important part of the global atmospheric and oceanic circulation patterns. Amsterdam Island (AMS, 37°S) is located just north of the Subtropical Front (at approximately 40°S, Orsi et al., 1995), where cool, low-salinity subpolar water submerges beneath warm, saline subtropical water (Prell et al., 1979). The island is located at the northern edge of both the Southern Westerly wind belt and the Antarctic Circumpolar Current.

The main objectives of this study were to investigate (1) to what extent observations in the Southern Indian Ocean could define Southern Hemisphere mid-latitude ^{210}Pb, ^{137}Cs and ^{241}Am background conditions for the last 100 years and (2) how ^{210}Pb levels are comparable between different matrices (e.g. wetland, sediment, glacier and atmospheric deposition) at different latitudes of the world, which could allow us to draw a new global sketch of ^{210}Pb flux.

In this paper, for the very first time the inventories and fluxes of ^{210}Pb and ^{137}Cs together with a ^{210}Pb-based peat accumulation rate for AMS are reported. This island is located in Southern Indian Ocean at 37°S and at 3400 km from the nearest land mass. The atmospheric conditions at this location offer the possibility to potentially define ^{210}Pb background concentrations, in a place with minimal perturbation from anthropogenic influences (Gaudichet et al., 1989; Angot et al., 2014). AMS is therefore an ideal site to investigate the background levels of ^{210}Pb, ^{137}Cs and ^{241}Am in the Southern Hemisphere, as well as to detect long-range transport of anthropogenic radionuclides.

2. Materials and methods

2.1. Study area

AMS (37°50'S, 77°32'E) is a small volcanic island with a surface of 55 km^2 and a maximum elevation of 881 m above sea level (a.s.l.). The center of the island is formed by a volcanic caldera in which an ombrotrophic peatland develops. The island is located at the northern edge of the westerly wind belt in the South Indian Ocean at a minimum distance of 3400 km and 5000 km upwind from the nearest land masses, respectively, Madagascar and South Africa. The climate in AMS is mild oceanic, with frequent clouds (Angot et al., 2014). The annual

precipitation is 1124 mm·y^{-1} based on 40-year annual average data from 1951 to 1990 (Meteo France data reported in Miller et al., 1992). The weather station is located at 29 m above sea level. However, although no record exists, the cloud accumulation at the top of the island makes the precipitation level much higher in the caldera than that recorded at the weather station. The orographic effect (Roe, 2005; Le Roux et al., 2008) would enhance precipitation and therefore, ^{210}Pb-bearing aerosols scavenging. Relatively higher volume of rainfall above 600 m a.s.l. also favors moss growth and peat accumulation in the caldera of AMS. The annual temperature is 13.8 °C at the weather station, while the average annual humidity is 80% with little seasonal variations. Located in the middle of the Indian Ocean, AMS is also at the crossroads of African, Australian and Southern American dust trajectories (Li et al., 2008; Lamy et al., 2014).

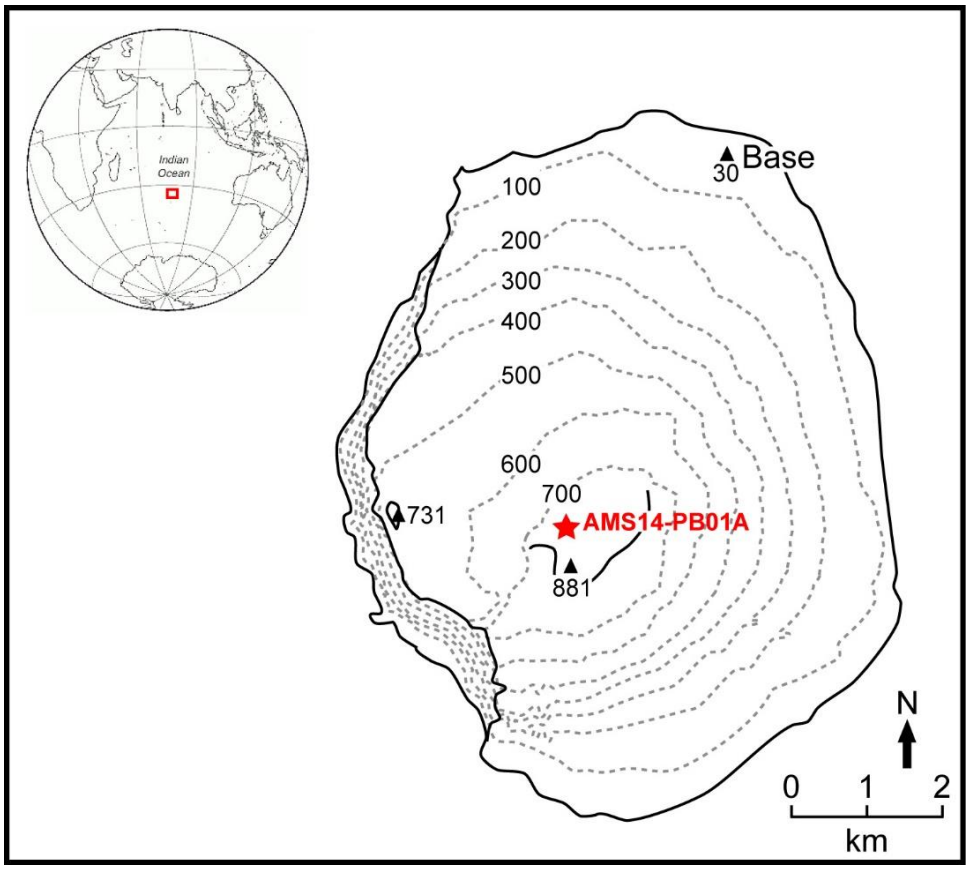

Figure 1. Sampling site in Amsterdam Island.

2.2. Core sampling and subsampling

One 5m-long peat sequence (AMS14-PB01A, 37°50.742´S, 77°32.898´E) was collected from the center of a raised bog at 738 m a.s.l. in December 2014 using a stainless steel Russian D-corer of 10 cm internal diameter and 50 cm length (Belokopytov and Beresnevich, 1955; De Vleeschouwer et al., 2014; Vanneste et al., 2016) (Fig. 1). A second (AMS14-PB01B, 4.15 m length) and a third core (AMS14-PB01C, top 1 m length) at the same site were collected and

stored as archives. All cores were photographed, described and wrapped in plastic film and PVC tubes before being shipped by boat to France in +4°C fridges. Cores were frozen and subsequently sliced at roughly 1-cm resolution using a clean sub-sampling procedure described in De Vleeschouwer et al., (2010). After being cleaned with MilliQ water and the edges removed (Givelet et al., 2004), the subsamples were dried using an ALPHA 1-4 LD plus freeze-dryer. Prior to freeze-drying, the dimensions of each subsample were measured using a vernier caliper in order to i) obtain the volume for calculating the dry bulk density and ii) to estimate the cut loss between each slice by comparing the cumulative slices thickness and the total length of the core. In this paper, we focus on last 100-150 years of peat accumulation representing the top 12 cm of the master core.

2.3. Radiometric measurements

Fifteen freeze-dried sample aliquots (approximately 0.3 g) were analyzed at the LAFARA underground laboratory located in Ferrières in the French Pyrénées (Van Beek et al., 2013). Prior to analysis, samples were sealed to prevent any ^{222}Rn loss and stored for a period of 3 weeks to ensure radioactive equilibrium between ^{226}Ra, ^{214}Pb and ^{214}Bi. The ^{210}Pb, ^{226}Ra, ^{137}Cs and ^{241}Am activities were determined using a well-type germanium detector that was protected from cosmic rays by 85 m of rock, thus yielding a very low background (Van Beek et al., 2013). The ^{210}Pb, ^{137}Cs and ^{241}Am were measured using the gamma lines at 46.5 keV, 661.7 keV and 59.5 keV, respectively. The ^{226}Ra was determined using the 295 keV, 351.9 keV and 609.3 keV gamma emissions of its decay chain descendants (^{214}Pb and ^{214}Bi). Because of the very low activities present in the peat samples and because the volume of material to be analyzed was small, each sample was analyzed for at least four days. We used RGU1, RGTH1 and IAEA-375 standards provided by IAEA to calibrate the detector.

Excess ^{210}Pb activities are calculated by correcting the total ^{210}Pb for the ^{210}Pb supported by ^{226}Ra. Since the ^{226}Ra activities were below the detection limit in the core, the $^{210}Pb_{ex}$ activities are equivalent to the total ^{210}Pb activities (supplementary Table S1). In the following, we report $^{210}Pb_{ex}$ activities. The detection limits achieved in this study (considering the low amount of material that was analyzed) were 20 $Bq.kg^{-1}$ for ^{210}Pb, 0.4 $Bq.kg^{-1}$ for ^{137}Cs and 0.6 $Bq.kg^{-1}$ for ^{241}Am.

2.4. Calculating decays, fluxes and inventories

Atmospheric ^{210}Pb fluxes $\mathbf{\Phi}$ ($Bq \cdot m^{-2} \cdot yr^{-1}$) were calculated using:

$$\Phi = \lambda \cdot I_{210Pb} \quad (1)$$

where λ is the ^{210}Pb decay constant (0.03114 yr^{-1}, $\lambda = \ln 2/T_{1/2}$) and I is the $^{210}Pb_{ex}$ inventory ($Bq \cdot m^{-2}$) in peat calculated from (Appleby, 1997):

$$I = \sum_{i=0}^{i=\infty} \rho(x) \cdot C(x) \cdot dx \quad (2)$$

where $\rho(x)$ ($g \cdot cm^{-3}$) is the dry bulk density, dx is the soil thickness (cm) and $C(x)$ is the excess ^{210}Pb activity ($Bq \cdot kg^{-1}$). (Sanchez-Cabeza et al., 2007) The ^{137}Cs inventory was also calculated using equation (2).

The formula for calculating ^{137}Cs cumulative decay corrected fallout at year 1969 (maximum fallout, according to Aoyama et al., 2006) is shown below,

$$CD_{1969} = \sum_{\tau}^{1969} D_{\tau} e^{-\lambda(1969-\tau)} \quad (3)$$

CD_{1969}: cumulative decay corrected fallout at year 1969 ($Bq \cdot m^{-2}$); λ: radioactive decay constant of ^{137}Cs (0.023 yr^{-1}, $\lambda = \ln 2/T_{1/2}$); D_{τ}: annual deposition of ^{137}Cs at year τ ($Bq \cdot m^{-2}$).

3. Results and discussion

3.1. Downcore distribution of ^{210}Pb, ^{137}Cs and ^{241}Am activities

Given that ombrotrophic peatlands are only depending on precipitation for their water balance, ^{210}Pb flux is assumed to be exclusively of atmospheric origin at AMS. This is confirmed by the absence of supported ^{210}Pb because no ^{226}Ra was detected. Except for the first sample that contained living Sphagnum moss, the $^{210}Pb_{ex}$ activities decrease with increasing depth down to approximately 12 cm. (Fig. 2 and supplementary Table S1). As shown in Fig. 2, the activities of ^{137}Cs and ^{241}Am displayed peaks at the same depth (4.4- 5.8 cm), with values of 22 ± 2 $Bq \cdot kg^{-1}$ and 7 ± 1 $Bq \cdot kg^{-1}$, respectively, indicating that these peaks can be related to nuclear bomb testing (Spalding et al., 2005).

The total $^{210}Pb_{ex}$ inventory was 3160 ± 200 $Bq \cdot m^{-2}$ with a corresponding $^{210}Pb_{ex}$ flux of 98 ± 6 $Bq \cdot m^{-2} \cdot y^{-1}$. According to equation (3), the corrected value for ^{137}Cs inventory on AMS in 1969 was 144 ± 13 $Bq \cdot m^{-2}$, which is two times lower than the modeled average inventory of 580 $Bq \cdot m^{-2}$ (range from 150 to 1430 $Bq \cdot m^{-2}$) at 35°S (Aoyama et al., 2006), but higher than the activity reported at 45°S in the same paper. Our observed ^{137}Cs inventory for AMS is thus close to the lower limit of these estimates at 35°S. ^{241}Am activity is relatively high showing potentially the immobility of this radioelement in the peat column compared to cesium. Despite this, the activity inventory ratio $^{137}Cs/^{241}Pu_{1969}$ = 1.2, derived from ^{137}Cs and ^{241}Am activities

respectively, is on the same order of magnitude that what can be found in Antarctica and sub-Antarctica islands. (Pourchet et al., 2003; Roos et al., 1994)

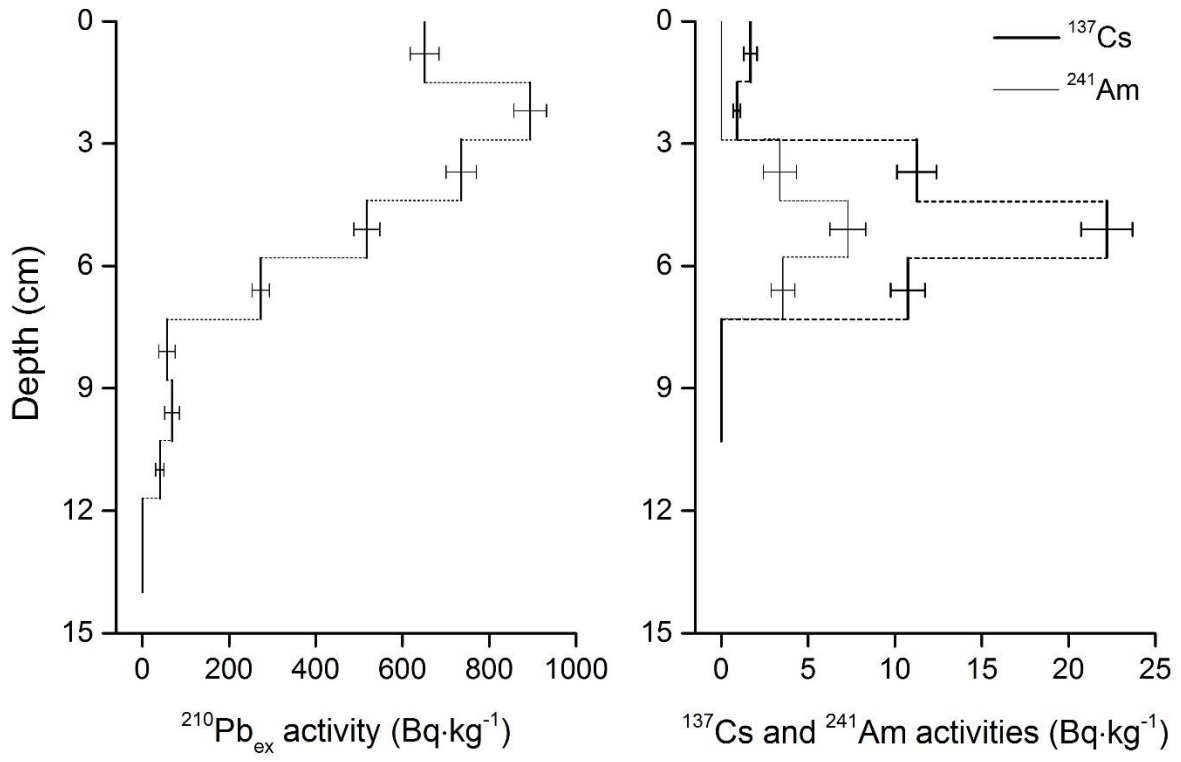

Figure 2. Vertical profiles of $^{210}Pb_{ex}$, ^{137}Cs and ^{241}Am activities in the peat core collected in Amsterdam Island.

3.2. ^{210}Pb chronology

Well-dated peat profiles are valuable archives of past environmental changes. The Constant Rate of Supply (CRS) model (Appleby et al., 1997; Binford, 1990) was applied to ^{210}Pb inventories calculated from the $^{210}Pb_{ex}$ data to generate ages. The peat core presented here spans a period of about 157 years, indicating a peat accumulation rate of about 0.75 mm·yr^{-1}.

Oldfield (1995) suggested that ^{210}Pb measurements alone cannot result in an accurate chronology of peat accumulation. However, when constrained by ^{241}Am and ^{137}Cs activity profiles in the upper part of a sequence, ^{210}Pb can provide good chronologies of peat accumulation. The $^{210}Pb_{ex}$ dates from the peat profile in AMS calculated using the CRS model were independently validated by ^{137}Cs and ^{241}Am that displayed highest activities between 1960 and 1981 (Fig. 3), corresponding to the period of nuclear weapon tests (i.e. in the 1960s). Moreover the detection of ^{241}Am excludes the possibility that ^{137}Cs post-depositional mobility processes would have shifted the ^{137}Cs activity maximum (Schettler et al., 2006-Part B).

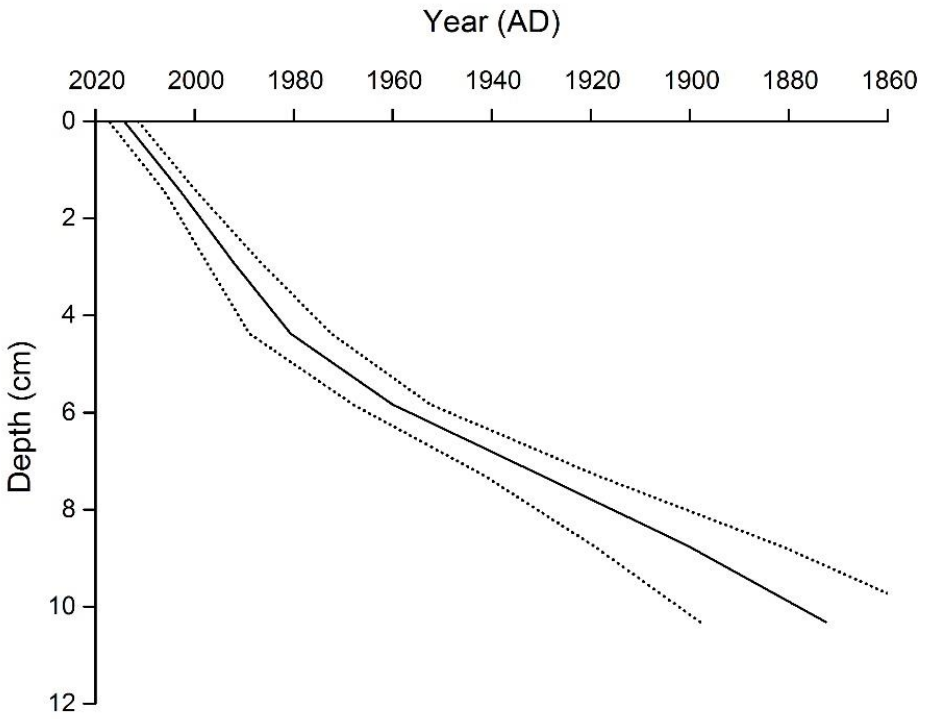

Figure 3. $^{210}Pb_{ex}$ inferred chronology based on CRS model.

3.3. ^{210}Pb flux in AMS compared with global ^{210}Pb depositional flux

We updated the database from Turekian et al., (1977) and Preiss, (1997) by compiling 47 new entries from the last 20 years. Global estimates of ^{210}Pb flux from the literature, integrated over 30°-latitudinal belts within different matrices, are shown in Fig. 4 and supplementary Table S2. Only terrestrial data, i.e. from wetlands (peatlands, salt marshes and swamps), sediments (lakes, estuarine and soil profiles), glaciers (ice core and firn) as well as atmospheric deposition (snow, precipitation plus dry fallout) are included.

Globally, the ^{210}Pb flux measured in wetland sequences show smaller uncertainties compared to fluxes measured from atmospheric deposition and sediment sequences (Fig. 4). The dominant ^{210}Pb input to wetlands is through the atmosphere in contrast to lake basins and the data are integrated over several years (1-cm layer represents a period of more than 10 years). The relatively larger uncertainty observed in atmospheric deposition could be explained by short-term measurements (i.e. annual) that can enhance different tropospheric contributions. Many factors (e.g., adjoining drainage areas) could alter the ^{210}Pb flux in sediment sequences.

In general, the ^{210}Pb flux is lower at high latitudes (>60° latitude) (Fig. 4), especially when measured in glaciers and atmospheric deposition, where the low density of land masses results in lower ^{222}Rn emissions. According to the existing data, the ^{210}Pb fluxes measured in

sediments are higher than those measured in the other three categories in the Northern Hemisphere, while in the Southern Hemisphere the values detected in wetlands are the highest (except between 60 ~ 90°S where no measurement exists). The ^{210}Pb fluxes from atmospheric deposition are similar to those from wetlands in the Northern Hemisphere (Fig. 4). Wetlands are found to be the appropriate archives for a good estimation of atmospheric flux, due to the absence of in-wash of sediments, and the low energy budget (absence of streams)(Preiss et al., 1996). However in the Southern Hemisphere, ^{210}Pb flux from wetlands and atmospheric deposition are not similar, which might be partially due to the scarcity of data (only 7 for wetlands) resulting in a non-representative dataset. Compared to the Northern Hemisphere, fewer data are available for the Southern Hemisphere, and thus more effort should be made in the future to fill this gap.

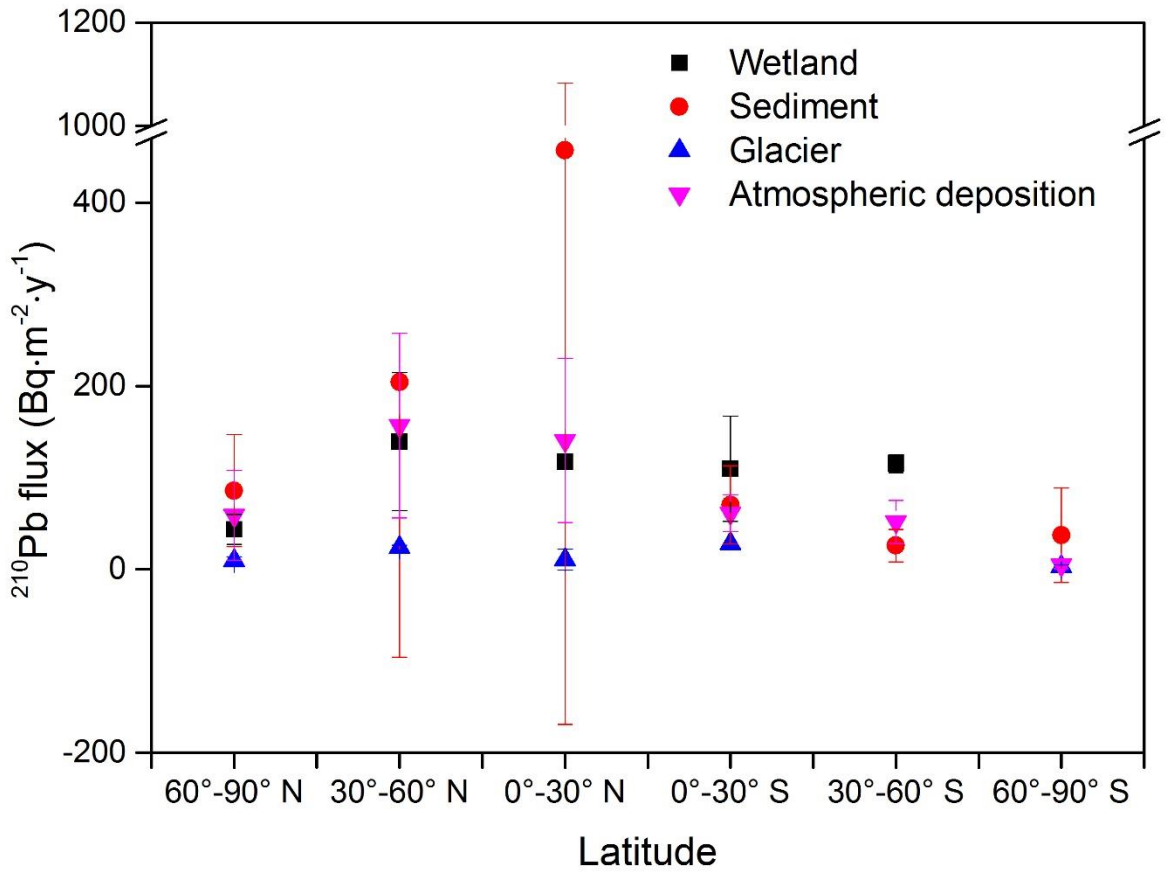

Figure 4. Global atmospheric depositional fluxes of ^{210}Pb among different matrices at different latitude. (Data assembled from supplementary Table S2)

In the peat core from AMS, the ^{210}Pb flux was 98 ± 6 Bq·m^{-2}·y^{-1}, which is higher than most values reported at around 40°S. For example, Baskaran (2011) found an average ^{210}Pb flux of 61 ± 2 Bq·m^{-2}·y^{-1} between 30 ~ 40°S and 42 Bq·m^{-2}·y^{-1} between 40 ~ 50°S based on

terrestrial or marine settings. Guelle et al. (1998) used three kinds of wet-scavenging schemes to simulate the ^{210}Pb distribution and found a flux of 28 ~ 34 $Bq \cdot m^{-2} \cdot y^{-1}$ between 30 and 60°S. The ^{210}Pb atmospheric deposition in Tasmania is 41.5 $Bq \cdot m^{-2} \cdot y^{-1}$ (42.5°S, 147.5°E) (Preiss, 1997). Rosen et al. (1957) found a much lower value (1.24 $Bq \cdot m^{-2} \cdot y^{-1}$) in Wellington (41°17'S), New Zealand based on the calculation of the ^{222}Rn flux. The estimated unsupported ^{210}Pb fluxes values from the global model made by Turekian et al. (1977) and El-Daoushy (1988) were ≤ 74 (in terrestrial settings) and 58.4 $Bq \cdot m^{-2} \cdot y^{-1}$, respectively. Unsupported ^{210}Pb flux from lake sediments in Northern Patagonia (from 40°30'S to 41°10'S) showed very low values, ranging between 4 and 48 $Bq \cdot m^{-2} \cdot y^{-1}$ (Guevara et al., 2003). The average ^{210}Pb flux from lake sediment in central Chile (36°51' S, 73°05' W) was 23.6 $Bq \cdot m^{-2} \cdot y^{-1}$ (Cisternas et al., 2001). However, when compared with a soil profile from Madagascar, we find almost the same value (95.8 $Bq \cdot m^{-2} \cdot y^{-1}$, Rabesiranana et al., 2016) as in AMS. Our value is also quite similar to other values obtained from swamps or salt marshes found in South Africa (139 ± 37 $Bq \cdot m^{-2} \cdot y^{-1}$, n=4, Humphires et al., 2010 ; Kading et al., 2009 ; Ivanovitch and Harmon, 1992). The ^{210}Pb flux in AMS is lower than some measurements conducted in wetlands between 30 and 60°N, e.g., Romania (between 133 ~ 277 $Bq \cdot m^{-2} \cdot y^{-1}$, Begy et al., 2016), China (254 and 421 $Bq \cdot m^{-2} \cdot y^{-1}$, Bao et al., 2010).

Depositional flux of ^{210}Pb at any given site depends on the local ^{222}Rn emanation rates and the relative proportion of maritime and continental air masses along with the differences in the amount and frequency of precipitation (Baskaran, 2011). The highly variable ^{210}Pb depositional fluxes give insight to the sources and sinks of aerosols. The study sites in Argentina and Chile (Cisternas et al., 2001; Guevara et al., 2003), showing much lower ^{210}Pb fluxes, are located at the coast near the Pacific Ocean, and are influenced by westerly winds bringing oceanic air masses. The contribution of sea salt for ^{210}Pb from oceanic ^{222}Rn is negligible. Global ^{222}Rn flux from continents is estimated to be around 1300-1800 $Bq \cdot m^{-2} \cdot d^{-1}$, which is around 2 orders of magnitude higher than that from the oceans (Samuelsson et al., 1986; Nazaroff, 1992). The ^{210}Pb flux at AMS is relatively high (discussed above). Despite the remoteness of the island, Angot et al. (2014) found that air masses passing over the southern African continent and/or Madagascar could enhance ^{222}Rn activity in AMS based on the study of back trajectory. Continental air masses originating from South Africa and/or Madagascar are enriched in ^{210}Pb that is then scavenged to clouds over the Indian Ocean. The regular orographic heavy rainfalls in the caldera at the top of AMS promote the deposition of ^{210}Pb from the South Africa and/or Madagascar air masses into the peatland, resulting in a ^{210}Pb flux on the island similar to those in South Africa and Madagascar.

4. Conclusion

For the very first time, radionuclide (^{210}Pb, ^{137}Cs, ^{241}Am) measurements conducted in a peat core taken from an ombrotrophic peatland on AMS are presented. The chronology based on ^{210}Pb using a CRS model is consistent with other chronomarkers (^{137}Cs and ^{241}Am), which allows the reconstruction of a peat mass accumulation rate of 0.75 $mm \cdot yr^{-1}$ for a period of 157 years. The ^{210}Pb flux of 98 ± 6 $Bq \cdot m^{-2} \cdot y^{-1}$ measured in the peat core is relatively high compared to many observations at around 40°S. This pattern might be explained by the fact that, most studies conducted in the mid-latitudes in Southern Hemisphere are located on the west side of the continents, close to the coast, and are highly influenced by westerly winds bringing air-masses with low ^{222}Rn activities. However, the ^{210}Pb flux at AMS is comparable to the ones in South Africa and Madagascar. This may be explained by the continental air mass enriched in ^{222}Rn originating from South Africa and/or Madagascar influencing AMS together with the frequent and heavy rainfalls at the top of the island which would enhance deposition. The ^{137}Cs inventory was 144 ± 13 $Bq \cdot m^{-2}$ (corrected to 1969). Since no terrestrial studies were conducted in the south Indian Ocean, the data reported here from AMS (^{210}Pb, ^{137}Cs and ^{241}Am) are of value for the global database.

Acknowledgements

We are grateful to Svante Björck, Bart Klink and Elisabeth Michel for their help during fieldwork. These results would never have been obtained if we had not had the incredible support of the Mission 66 of Amsterdam Island. Very special thanks to Alain Quivoron and Hubert Launay. The field expedition of this project was supported by IPEV project 1066 PARAD to FDV. We are very grateful to Nina Marchand (IPEV) for the incredible logistical support and Cédric Marteau for making the sampling possible in the protected areas of the TAAF Nature Reserve. Chuxian Li's PhD is supported by a scholarship from the Chinese Scholarship Council. We are grateful to EDF (Electricité De France) for allowing us to run our germanium detectors in the tunnel of Ferrières. We thank the European Union and Région Occitanie Pyrénées-Méditerranée for supporting the LAFARA underground laboratory through a FEDER funding (SELECT project). We finally thank the 4 anonymous reviewers for their useful comments that greatly improved the quality of this manuscript.

References:

Alvarez-Iglesias, P.; Quintana, B.; Rubio, B.; Pérez-Arlucea, M., Sedimentation rates and trace metal input history in intertidal sediments from San Simón Bay (Ría de Vigo, NW Spain) derived from 210 Pb and 137 Cs chronology. *Journal of Environmental Radioactivity* 2007, *98* (3), 229-250.

Angot, H.; Barret, M.; Magand, O.; Ramonet, M.; Dommergue, A., A 2-year record of atmospheric mercury species at a background Southern Hemisphere station on Amsterdam Island. *Atmospheric Chemistry and Physics* 2014, *14* (20), 11461-11473.

Aoyama, M.; Hirose, K.; Igarashi, Y., Re-construction and updating our understanding on the global weapons tests 137 Cs fallout. *Journal of Environmental Monitoring* 2006, *8* (4), 431-438.

Appleby, P. In *Dating recent sediments by 210Pb: Problems and solutions*, Proc. 2nd NKS/EKO-1 Seminar, Helsinki, 1997.

Appleby, P.; Birks, H. H.; Flower, R. J.; Rose, N.; Peglar, S. M.; Ramdani, M.; Kraïem, M. M.; Fathi, A. A., Radiometrically determined dates and sedimentation rates for recent sediments in nine North African wetland lakes (the CASSARINA Project). *Aquatic Ecology* 2001, *35* (3-4), 347-367; (a)

Appleby, P., Three decades of dating recent sediments by fallout radionuclides: a review. *The Holocene* 2008, *18* (1), 83-93. (b)

Baeza, A.; Del Rio, L.; Jimenez, A.; Miro, C.; Navarro, E.; Paniagua, J., Recent evolution of the overall radioactive levels in the ice of Livingston Island (Antarctica). *Applied radiation and isotopes* 1996, *47* (8), 811-819.

Bao, K.; Xia, W.; Lu, X.; Wang, G., Recent atmospheric lead deposition recorded in an ombrotrophic peat bog of Great Hinggan Mountains, Northeast China, from 210 Pb and 137 Cs dating. *Journal of Environmental Radioactivity* 2010, *101* (9), 773-779.

Baskaran, M., Po-210 and Pb-210 as atmospheric tracers and global atmospheric Pb-210 fallout: a review. *Journal of Environmental Radioactivity* 2011, *102* (5), 500-513.

Baskaran, M.; Naidu, A., 210 Pb-derived chronology and the fluxes of 210 Pb and 137 Cs isotopes into continental shelf sediments, East Chukchi Sea, Alaskan Arctic. *Geochimica et Cosmochimica Acta* 1995, *59* (21), 4435-4448.

Begy, R. C.; Kovacs, T.; Veres, D.; Simon, H., Atmospheric flux, transport and mass balance of 210 Pb and 137 Cs radiotracers in different regions of Romania. *Applied Radiation and Isotopes* 2016, *111*, 31-39.

Beks, J.; Eisma, D.; Van Der Plicht, J., A record of atmospheric 210 Pb deposition in The Netherlands. *Science of the total environment* 1998, *222* (1), 35-44.

Belokopytov, I.; Beresnevich, V., Giktorf's peat borers. *Torfyanaya Promyshlennost* 1955, *8*, 9-10.

Benmansour, M.; Mabit, L.; Nouira, A.; Moussadek, R.; Bouksirate, H.; Duchemin, M.; Benkdad, A., Assessment of soil erosion and deposition rates in a Moroccan agricultural field using fallout 137 Cs and 210 Pb ex. *Journal of environmental radioactivity* 2013, *115*, 97-106.

Benoit, G.; Rozan, T. F., 210Pb and 137Cs dating methods in lakes: a retrospective study. *Journal of Paleolimnology* 2001, *25* (4), 455-465.

Bindler, R.; Renberg, I.; Anderson, N. J.; Appleby, P. G.; Emteryd, O.; Boyle, J., Pb isotope ratios of lake sediments in West Greenland: inferences on pollution sources. *Atmospheric Environment* 2001, *35* (27), 4675-4685.

Binford, M. W., Calculation and uncertainty analysis of 210Pb dates for PIRLA project lake sediment cores. *Journal of Paleolimnology* 1990, *3* (3), 253-267.

Blake, W.; Wallbrink, P.; Wilkinson, S.; Humphreys, G.; Doerr, S.; Shakesby, R.; Tomkins, K., Deriving hillslope sediment budgets in wildfire-affected forests using fallout radionuclide tracers. *Geomorphology* 2009, *104* (3), 105-116.

Bonotto, D. M.; De Lima, J., 210Pb-derived chronology in sediment cores evidencing the anthropogenic occupation history at Corumbataí River basin, Brazil. *Environmental Geology* 2006, *50* (4), 595-611.

BRENNER M., Personal communication, 1999. Inform "Patrones de sedimentación temporal en la zona litoral del Huiñaimarca", M. W. BINFORD, M. BRENNER and D. R. ENGSTROM.

Cisternas, M.; Araneda, A.; Martinez, P.; Perez, S., Effects of historical land use on sediment yield from a lacustrine watershed in central Chile. *Earth Surface Processes and Landforms* 2001, *26* (1), 63-76.

De Vleeschouwer, F.; Chambers, F. M.; Swindles, G. T., Coring and sub-sampling of peatlands for palaeoenvironmental research. *Mires and Peat* 2010, *7*.

De Vleeschouwer, F.; Vanneste, H.; Mauquoy, D.; Piotrowska, N.; Torrejón, F.; Roland, T.; Stein, A.; Le Roux, G., Emissions from pre-Hispanic metallurgy in the South American atmosphere. *PloS one* 2014, *9* (10), e111315.

Deacon, G. E. R., 1966. The Subtropical Convergence. In: R. Fairbridge (Editor). The Encyclopedia of Oceanography, 1. Reinhold, New York, N.Y. pp. 884--885.

El-Daoushy, F., A summary on the lead-210 cycle in nature and related applications in Scandinavia. *Environment International* 1988, *14* (4), 305-319.

Farmer, J. G.; MacKenzie, A. B.; Graham, M. C.; Macgregor, K.; Kirika, A., Development of recent chronologies and evaluation of temporal variations in Pb fluxes and sources in lake sediment and peat cores in a remote, highly radiogenic environment, Cairngorm Mountains, Scottish Highlands. *Geochimica et Cosmochimica Acta* 2015, *156*, 25-49.

Fitzgerald, W. F.; Engstrom, D. R.; Lamborg, C. H.; Tseng, C.-M.; Balcom, P. H.; Hammerschmidt, C. R., Modern and historic atmospheric mercury fluxes in northern Alaska: Global sources and Arctic depletion. *Environmental science & technology* 2005, *39* (2), 557-568.

Foster, I. D.; Boardman, J.; Keay-Bright, J., Sediment tracing and environmental history for two small catchments, Karoo Uplands, South Africa. *Geomorphology* 2007, *90* (1), 126-143.

Fukuyama, T.; Onda, Y.; Takenaka, C.; Walling, D. E., Investigating erosion rates within a Japanese cypress plantation using Cs-137 and Pb-210ex measurements. *Journal of Geophysical Research: Earth Surface* 2008, *113* (F2).

Gallagher, D.; McGee, E.; Mitchell, P., A recent history of 14C, 137Cs, 210Pb, and 241Am accumulation at two Irish peat bog sites: an east versus west coast comparison. *Radiocarbon* 2001, *43*, 517-525.

García-Orellana, J.; Sánchez-Cabeza, J.; Masqué, P.; Avila, A.; Costa, E.; Loÿe-Pilot, M.; Bruach-Menchén, J., Atmospheric fluxes of 210Pb to the western Mediterranean Sea and the Saharan dust influence. *Journal of Geophysical Research: Atmospheres* 2006, *111* (D15).

Gaspar, L.; Navas, A.; Walling, D.; Machín, J.; Arozamena, J. G., Using 137 Cs and 210 Pb ex to assess soil redistribution on slopes at different temporal scales. Catena 2013, 102, 46-54.

Gaudichet, A.; Lefevre, R.; Gaudry, A.; Ardouin, B.; Lambert, G.; Miller, J., Mineralogical composition of aerosols at Amsterdam Island. Tellus B 1989, 41 (3), 344-352.

Givelet, N.; Le Roux, G.; Cheburkin, A.; Chen, B.; Frank, J.; Goodsite, M. E.; Kempter, H.; Krachler, M.; Noernberg, T.; Rausch, N., Suggested protocol for collecting, handling and preparing peat cores and peat samples for physical, chemical, mineralogical and isotopic analyses. Journal of Environmental Monitoring 2004, 6 (5), 481-492.

Graustein, W. C.; Turekian, K. K., Radon fluxes from soils to the atmosphere measured by 210Pb–226Ra disequilibrium in soils. Geophysical Research Letters 1990, 17 (6), 841-844.

Guelle, W.; Balkanski, Y.; Dibb, J. E.; Schulz, M.; Dulac, F., Wet deposition in a global size-dependent aerosol transport model: 2. Influence of the scavenging scheme on 210Pb vertical profiles, surface concentrations, and deposition. *Journal of Geophysical Research: Atmospheres* 1998.

Guevara, S. R.; Rizzo, A.; Sánchez, R.; Arribére, M., 210Pb fluxes in sediment layers sampled from Northern Patagonia lakes. *Journal of Radioanalytical and Nuclear Chemistry* 2003, *258* (3), 583-595.

Hancock, G.; Leslie, C.; Everett, S.; Tims, S.; Brunskill, G.; Haese, R., Plutonium as a chronomarker in Australian and New Zealand sediments: a comparison with 137 Cs. *Journal of Environmental Radioactivity* 2011, *102* (10), 919-929.

Holynska, B.; Ostachowicz, B.; Ostachowicz, J.; Samek, L.; Wachniew, P.; Obidowicz, A.; Wobrauschek, P.; Streli, C.; Halmetschlager, G., Characterisation of 210 Pb dated peat core by various X-ray fluorescence techniques. *Science of the total Environment* 1998, *218* (2), 239-248.

Humphries, M. S.; Benitez-Nelson, C. R., Recent trends in sediment and nutrient accumulation rates in coastal, freshwater Lake Sibaya, South Africa. *Marine and Freshwater Research* 2013, *64* (11), 1087-1099.

Humphries, M. S.; Kindness, A.; Ellery, W. N.; Hughes, J. C.; Benitez-Nelson, C. R., 137 Cs and 210 Pb derived sediment accumulation rates and their role in the long-term development of the Mkuze River floodplain, South Africa. *Geomorphology* 2010, *119* (1), 88-96.

Ivanovich, M.; Harmon, R. S., Uranium-series disequilibrium: applications to earth, marine, and environmental sciences. 2. 1992.

Kading, T.; Mason, R.; Leaner, J., Mercury contamination history of an estuarine floodplain reconstructed from a 210 Pb-dated sediment core (Berg River, South Africa). *Marine pollution bulletin* 2009, *59* (4), 116-122.

Kato, H.; Onda, Y.; Tanaka, Y., Using 137 Cs and 210 Pb ex measurements to estimate soil redistribution rates on semi-arid grassland in Mongolia. *Geomorphology* 2010, *114* (4), 508-519.

Klaminder, J.; Bindler, R.; Emteryd, O.; Appleby, P.; Grip, H., Estimating the mean residence time of lead in the organic horizon of boreal forest soils using 210-lead, stable lead and a soil chronosequence. *Biogeochemistry* 2006, *78* (1), 31-49.

Knuth, R. H., et al. "Size distribution of atmospheric Pb and 210 Pb in rural New Jersey: implications for wet and dry deposition." *Precipitation scavenging, dry deposition, and resuspension. Volume 2. Proceedings*. 1983.

Lamy, F.; Gersonde, R.; Winckler, G.; Esper, O.; Jaeschke, A.; Kuhn, G.; Ullermann, J.; Martínez-Garcia, A.; Lambert, F.; Kilian, R., Increased dust deposition in the Pacific Southern Ocean during glacial periods. Science 2014, 343 (6169), 403-407.

Le Roux, Gaël, et al. "Aerosol deposition and origin in French mountains estimated with soil inventories of 210 Pb and artificial radionuclides." *Atmospheric environment* 42.7 (2008): 1517-1524.

Le Roux, G., and W. A. Marshall. "Constructing recent peat accumulation chronologies using atmospheric fall-out radionuclides." Mires and Peat 7.1 (2011): e14.

Li, F., Ginoux, P., & Ramaswamy, V. (2008). Distribution, transport, and deposition of mineral dust in the Southern Ocean and Antarctica: Contribution of major sources. *Journal of Geophysical Research: Atmospheres*, *113*(D10).

Mabit, L.; Benmansour, M.; Abril, J.; Walling, D.; Meusburger, K.; Iurian, A.; Bernard, C.; Tarján, S.; Owens, P.; Blake, W., Fallout 210 Pb as a soil and sediment tracer in catchment sediment budget investigations: a review. *Earth-Science Reviews* 2014, *138*, 335-351.

MacKenzie, A.; Farmer, J.; Sugden, C., Isotopic evidence of the relative retention and mobility of lead and radiocaesium in Scottish ombrotrophic peats. *Science of the Total Environment* 1997, *203* (2), 115-127.

MacKenzie, A.; Logan, E.; Cook, G.; Pulford, I., Distributions, inventories and isotopic composition of lead in 210 Pb-dated peat cores from contrasting biogeochemical environments: implications for lead mobility. *Science of the Total Environment* 1998, *223* (1), 25-35.

McCaffrey, R.; Thomson, J. *Record of trace metal fluxes to a Connecticut salt marsh as determined by 210 Pb dating*; 1974.

Miller, J. M., et al. "A 10-year trajectory flow climatology for Amsterdam Island, 1980–1989." *Atmospheric Environment. Part A. General Topics* 27.12 (1993): 1909-1916.Nazaroff, W. W., Radon transport from soil to air. *Reviews of Geophysics* 1992, *30* (2), 137-160.

Nijampurkar, V.; Rao, D.; Clausen, H. B.; Kaul, M.; Chaturvedi, A., Records of climatic changes and volcanic events in an ice core from Central Dronning Maud Land (East Antarctica) during the past century. *Journal of Earth System Science* 2002, *111* (1), 39-49.

O'Farrell, C. R.; Heimsath, A. M.; Kaste, J. M., Quantifying hillslope erosion rates and processes for a coastal California landscape over varying timescales. *Earth Surface Processes and Landforms* 2007, *32* (4), 544-560.

Oldfield, F.; Richardson, N.; Appleby, P., Radiometric dating (210Pb, 137Cs, 241Am) of recent ombrotrophic peat accumulation and evidence for changes in mass balance. *The Holocene* 1995, *5* (2), 141-148.

Olid, C.; Garcia-Orellana, J.; Martínez-Cortizas, A.; Masqué, P.; Peiteado-Varela, E.; Sanchez-Cabeza, J.-A., Multiple site study of recent atmospheric metal (Pb, Zn and Cu) deposition in the NW Iberian Peninsula using peat cores. *Science of the total environment* 2010, *408* (22), 5540-5549.

Olid, C.; Garcia-Orellana, J.; Masqué, P.; Cortizas, A. M.; Sanchez-Cabeza, J. A.; Bindler, R., Improving the 210 Pb-chronology of Pb deposition in peat cores from Chao de Lamoso (NW Spain). *Science of the Total Environment* 2013, *443*, 597-607.

Olid, C.; Nilsson, M. B.; Eriksson, T.; Klaminder, J., The effects of temperature and nitrogen and sulfur additions on carbon accumulation in a nutrient-poor boreal mire: Decadal effects assessed using 210Pb peat chronologies. *Journal of Geophysical Research: Biogeosciences* 2014, *119* (3), 392-403.

Orsi, Alejandro H., Thomas Whitworth, and Worth D. Nowlin. "On the meridional extent and fronts of the Antarctic Circumpolar Current." *Deep Sea Research Part I: Oceanographic Research Papers* 42.5 (1995): 641-673.

Owens, P. N.; Walling, D. E., Spatial variability of caesium-137 inventories at reference sites: an example from two contrasting sites in England and Zimbabwe. *Applied Radiation and isotopes* 1996, *47* (7), 699-707.

Peters, A.; Gregor, D.; Wilkinson, P.; Spencer, C., Deposition of 210Pb to the Agassiz ice cap, Canada. *Journal of Geophysical Research: Atmospheres* 1997, *102* (D5), 5971-5978.

Pfitzner, J.; Brunskill, G.; Zagorskis, I., 137 Cs and excess 210 Pb deposition patterns in estuarine and marine sediment in the central region of the Great Barrier Reef Lagoon, north-eastern Australia. *Journal of Environmental Radioactivity* 2004, *76* (1), 81-102.

Porto, P.; Walling, D. E., Validating the use of 137 Cs and 210 Pb ex measurements to estimate rates of soil loss from cultivated land in southern Italy. *Journal of environmental radioactivity* 2012, *106*, 47-57.

Porto, P.; Walling, D. E.; Callegari, G., Using 137Cs and 210Pbex measurements to investigate the sediment budget of a small forested catchment in southern Italy. *Hydrological Processes* 2013, *27* (6), 795-806.

Porto, P.; Walling, D. E.; Callegari, G.; Catona, F., Using fallout lead-210 measurements to estimate soil erosion in three small catchments in Southern Italy. *Water, Air, & Soil Pollution: Focus* 2006, *6* (5-6), 657-667.

Porto, P.; Walling, D. E.; Capra, A., Using 137 Cs and 210 Pb ex measurements and conventional surveys to investigate the relative contributions of interrill/rill and gully erosion to soil loss from a small cultivated catchment in Sicily. *Soil and Tillage Research* 2014, *135*, 18-27.

Pourchet, M., et al. "Radionuclides deposition over Antarctica." *Journal of environmental radioactivity* 68.2 (2003): 137-158.

Preiss, N. Etude du 210 Pb d'origine atmosphérique dans l'air, la neige, les sols et les sédiments: Mesures, inventaires et interprétation à l'échelle globale. 1997.

Preiss, N.; Mélières, M. A.; Pourchet, M., A compilation of data on lead 210 concentration in surface air and fluxes at the air-surface and water-sediment interfaces. *Journal of Geophysical Research: Atmospheres* 1996, *101* (D22), 28847-28862.

Prell, Warren L., William H. Hutson, and Douglas F. Williams. "The subtropical convergence and late Quaternary circulation in the southern Indian Ocean." *Marine Micropaleontology* 4 (1979): 225-234.

Rabesiranana, N.; Rasolonirina, M.; Solonjara, A.; Ravoson, H.; Andriambololona, R.; Mabit, L., Assessment of soil redistribution rates by 137 Cs and 210 Pb ex in a typical Malagasy agricultural field. *Journal of environmental radioactivity* 2016, *152*, 112-118.

Robbins, J. A.; Edgington, D., Determination of recent sedimentation rates in Lake Michigan using Pb-210 and Cs-137. *Geochimica et Cosmochimica Acta* 1975, *39* (3), 285-304.

Rodway-Dyer, S.; Walling, D., The use of 137 Cs to establish longer-term soil erosion rates on footpaths in the UK. *Journal of environmental management* 2010, *91* (10), 1952-1962.

Roe, Gerard H. "Orographic precipitation." *Annu. Rev. Earth Planet. Sci.* 33 (2005): 645-671.

Roos, P., et al. "Deposition of 210Pb, 137Cs, 239+ 240Pu, 238Pu, and 241Am in the Antarctic Peninsula Area." *Journal of environmental radioactivity* 24.3 (1994): 235-251.

Rosen, R., Note on some observations of radon and thoron exhalation from the ground. *NZJ Sci. Technol* 1957, *38*, 644-654.

Samuelsson, C.; Hallstadius, L.; Persson, B.; Hedvall, R.; Holm, E.; Forkman, B., 222Rn and 210Pb in the Arctic summer air. *Journal of Environmental Radioactivity* 1986, *3* (1), 35-54.

Sanchez-Cabeza, J.-A.; Garcia-Talavera, M.; Costa, E.; Peña, V.; Garcia-Orellana, J.; Masqué, P.; Nalda, C., Regional calibration of erosion radiotracers (210Pb and 137Cs): atmospheric fluxes to soils (northern Spain). *Environmental science & technology* 2007, *41* (4), 1324-1330.

Sanders, C. J.; Santos, I. R.; Silva-Filho, E. V.; Patchineelam, S. R., Mercury flux to estuarine sediments, derived from Pb-210 and Cs-137 geochronologies (Guaratuba Bay, Brazil). *Marine Pollution Bulletin* 2006, *52* (9), 1085-1089.

Schettler, G.; Mingram, J.; Negendank, J. F.; Jiaqi, L., Palaeovariations in the East-Asian monsoon regime geochemically recorded in varved sediments of Lake Sihailongwan (Northeast China, Jilin Province). Part 2: a 200-year record of atmospheric lead-210 flux variations and its palaeoclimatic implications. *Journal of Paleolimnology* 2006, *35* (2), 271-288.

Spalding, Kirsty L., et al. "Forensics: age written in teeth by nuclear tests." Nature 437.7057 (2005): 333-334.

Suzuki, T.; Kamiyama, K.; Furukawa, T.; Fujii, Y., Lead-210 profile in firn layer over Antarctic ice sheet and its relation to the snow accumulation environment. *Tellus B* 2004, *56* (1), 85-92.Szczuciński, W.; Zajączkowski, M.; Scholten, J., Sediment accumulation rates in subpolar fjords–Impact of post-Little Ice Age glaciers retreat, Billefjorden, Svalbard. *Estuarine, Coastal and Shelf Science* 2009, *85* (3), 345-356.

Turekian, K. Y.; Nozaki, Y.; Benninger, L. K., Geochemistry of atmospheric radon and radon products. *Annual Review of Earth and Planetary Sciences* 1977, *5*, 227.

Tylmann, W.; Bonk, A.; Goslar, T.; Wulf, S.; Grosjean, M., Calibrating 210 Pb dating results with varve chronology and independent chronostratigraphic markers: problems and implications. *Quaternary Geochronology* 2016, *32*, 1-10.

Van Beek, P.; Souhaut, M.; Lansard, B.; Bourquin, M.; Reyss, J.-L.; Von Ballmoos, P.; Jean, P., LAFARA: a new underground laboratory in the French Pyrenees for ultra low-level gamma-ray spectrometry. *Journal of environmental radioactivity* 2013, *116*, 152-158.

Vanneste, H.; De Vleeschouwer, F.; Bertrand, S.; Martínez-Cortizas, A.; Vanderstraeten, A.; Mattielli, N.; Coronato, A.; Piotrowska, N.; Jeandel, C.; Roux, G. L., Elevated dust deposition in Tierra del Fuego (Chile) resulting from Neoglacial Darwin Cordillera glacier fluctuations. *Journal of Quaternary Science* 2016, *31* (7), 713-722.

Wakiyama, Y.; Onda, Y.; Mizugaki, S.; Asai, H.; Hiramatsu, S., Soil erosion rates on forested mountain hillslopes estimated using 137 Cs and 210 Pb ex. *Geoderma* 2010, *159* (1), 39-52.

Walling, D.; Collins, A.; Sichingabula, H., Using unsupported lead-210 measurements to investigate soil erosion and sediment delivery in a small Zambian catchment. *Geomorphology* 2003, *52* (3), 193-213.

Yu-Hong, Y.; Bai-Xing, Y.; Hui, Z., Estimating soil erosion in Northeast China using 137 Cs and 210 Pb ex. *Pedosphere* 2011, *21* (6), 706-711.

Zheng, J.-J.; Xiu-Bin, H.; Walling, D.; Zhang, X.-B.; Flanagan, D.; Yong-Qing, Q., Assessing soil erosion rates on manually-tilled hillslopes in the Sichuan Hilly Basin using 137 Cs and 210 Pb ex measurements. *Pedosphere* 2007, *17* (3), 273-283.

Supporting information

Table S1. $^{210}Pb_{ex}$, ^{137}Cs and ^{241}Am distribution in the peat core collected in Amsterdam Island.

Top Depth / *cm*	Bottom Depth / *cm*	Density / *g·cm^{-3}*	Mass of sample *g*	$^{210}Pb_{ex} \pm \sigma$ / *Bq·kg^{-1}*	$^{137}Cs \pm \sigma$ / *Bq·kg^{-1}*	$^{241}Am \pm \sigma$ / *Bq·kg^{-1}*	Year Interval
0	1.5	0.117	0.285	651 ± 34	1.7 ± 0.4	0	2014-2003
1.5	2.9	0.054	0.291	894 ± 37	0.9 ± 0.2	0	2003-1992
2.9	4.4	0.077	0.275	735 ± 35	11 ± 1	3 ± 1	1992-1981
4.4	5.8	0.107	0.286	517 ± 30	22 ± 2	7 ± 1	1981-1960
5.8	7.3	0.107	0.341	273 ± 20	11 ± 1	4 ± 1	1960-1930
7.3	8.8	0.128	0.267	57 ± 19	<LD	<LD	1930-1900
8.8	10.3	0.115	0.292	68 ± 17	<LD	<LD	1900-1873
10.3	11.7	0.160	0.271	40 ± 9	<LD	<LD	1873-1857
11.7	12.7	0.138	-	<LDn.m.i	<LDn.m.i	<LDn.m.i	1857-1848
12.7	14	0.127	0.300	<LD	<LD	<LD	1848-1836

< LD: below the Detection Limit; n.m.i: non-mesurement but with interpolation; The activities of $^{210}Pb_{ex} \pm \sigma$, $^{137}Cs \pm \sigma$ and $^{241}Am \pm \sigma$ are shown in *Bq·kg^{-1}* of dry material.

Table S2. Global depositional ^{210}Pb flux (Bq m^{-2} yr^{-1}) within different matrices at different latitudes.

	Wetland					Sediment					Glacier					Atmospheric deposition				
	Nr	mean	± σ	max	min	Nr	mean	± σ	max	min	Nr	mean	± σ	max	min	Nr	mean	± σ	max	min
60°-90° N	*8*	44	16	64	15	*58*	86	61	280	21	*19*	9	4.5	19.5	4.1	*9*	59	49	150	5.7
30°-60° N	*42*	140	75	421	23	*331*	205	301	3350	3.7	*4*	24	2.6	26.7	21	*66*	157	100	465	25
0°-30° N	*1*	117	*	117	117	*58*	457	626	3725	12	*4*	11	11	27	1.5	*20*	141	90	316.7	24
0°-30° S	*5*	110	58	192	40	*16*	70	43	162	9	*1*	28	*	*	*	*9*	61	20	95	32
30°-60° S	*2*	115	9.7	122.1	108.3	*11*	26	18	60	4	*0*	*	*	*	*	*21*	52	24	125	23
60°-90° S	*0*	*	*	*	*	*6*	37	51.4	137	1.2	*30*	2.9	2.1	8.2	0.7	*2*	5	4.3	8.0	1.9

(*: without data. Details please see the data compilation in the supplementary information)

Data updated from Preiss(thesis), 1997; Turekian et al., 1977; Guevara et al., 2003; Brenner et al., 1999; Cisternas et al., 2001; Bao et al., 2010; Rabesiranana et al., 2016; Begy et al., 2016; Farmer et al., 2015; MacKenzie et al., 1998; MacKenzie et al., 1997; Humphires et al., 2010; Kading et al., 2009; Alvarez-Iglesias et al., 2007; Appleby, 1997; Humphries and Benitez-Nelson, 2013; Foster et al., 2007; Baskaran and Naidu, 1995; Schettler et al., 2006; Holynska et al., 1998; Olid et al., 2010; Olid et al., 2013; Olid et al., 2014; Klaminder et al., 2006; Gallagher et al., 2001; Tylmann et al., 2016; Mabit et al., 2014; Benmansour et al., 2013; Blake et al., 2009; O'Farrell et al., 2007; Fukuyama et al., 2008; Gaspar et al., 2013; Kato et al., 2010; Porto et al., 2006; Porto and Walling, 2012; Porto et al., 2013; Porto et al., 2014; Wakiyama et al., 2010; Walling et al., 2003; Yang et al., 2011; Zheng et al., 2007; Fitzgerald et al., 2005; Suzuki et al., 2004; Bindler et al., 2001; Szczuciński et al., 2009; Peters et al., 1997; Baeza et al., 1996; Nijampurkar et al., 2002; Beks et al., 1998; García-Orellana et al., 2006)

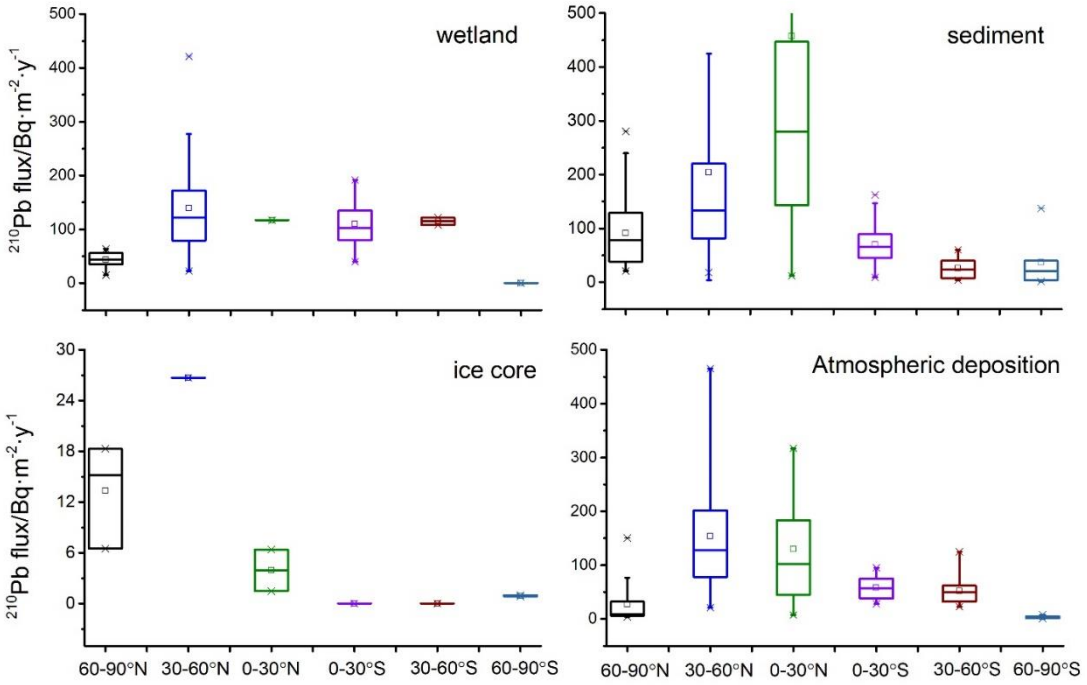

Figure S1. Global atmospheric depositional fluxes of ^{210}Pb among different matrices at different latitude belts (10° belt).

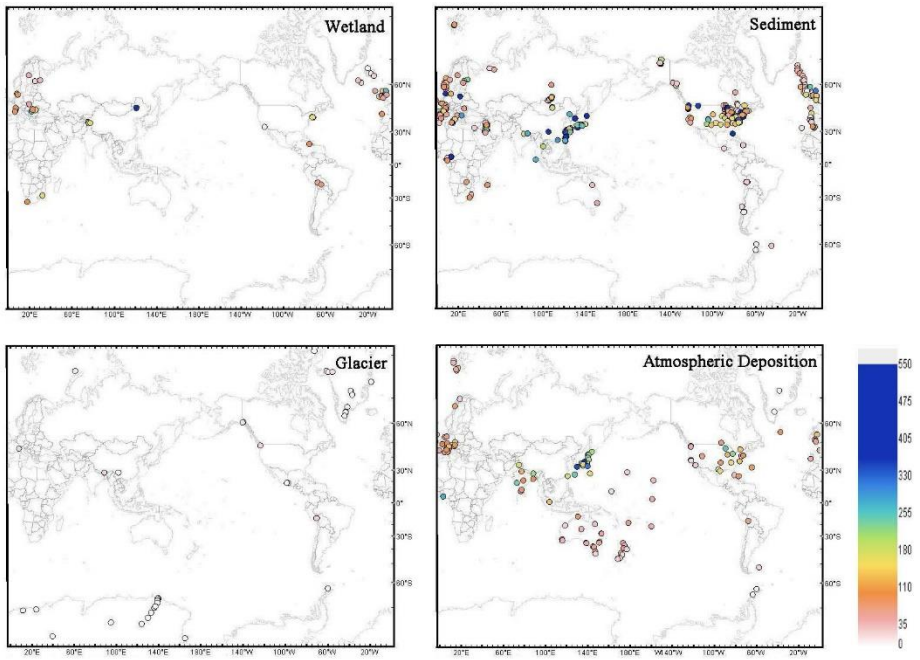

Figure S2. Location of the discrete data compiled in supplementary Table S3 (Shown in Appendix A) and used to make the extrapolated map

Chapter 2.

Holocene dynamics of the Southern Hemisphere westerly winds over the Indian Ocean inferred from a peat dust deposition record

Objectifs et résumé

Le réchauffement climatique a poussé de nombreux chercheurs à étudier les sources et les puits de CO_2. L'océan Austral au sud de 30°S représente plus de 40% de l'absorption anthropique de CO_2. Le rôle de l'océan Austral sur l'absorption, le transport et le stockage du CO_2 est contrôlé par le vent du sud-ouest (VSO). Des changements dans l'intensité / le déplacement des VSO peuvent réguler la remontée / la descente océanique du carbone inorganique dissous entre les profondeurs océaniques et la surface de la mer, entraînant un puits de carbone ou un effet supplémentaire sur le réchauffement climatique. Les VSO affectent également les trajectoires de précipitations et de poussières des latitudes moyennes de l'hémisphère sud. Malgré l'importance des VSO, on en sait très peu sur leurs variations à l'échelle millénaire, sur la manière dont ils ont influencé le système climatique passé et sur leur interaction avec les composants de surface terrestre (e.g., le CO_2 et les poussières). Peu d'études ont été menées sur la dynamique des VSO holocènes à cette limite nord (30-45°S), position latitudinale de de l'Amérique du Sud, de l'Afrique australe et de l'Australie.

Dans ce chapitre, nous présentons un enregistrement VSO à base des poussières atmosphériques dérivées d'un sondage de tourbe située sur l'île d'Amsterdam (AMS), au sud de l'océan Indien, à la limite nord des VSO. Le flux de poussières minérales a été utilisé pour suivre l'origine des poussières atmosphériques, leur transport sur de longues distances et leur dépôt ultérieurs. Le profil des poussières atmosphériques de AMS enregistre la dynamique des VSO grâce à un effet orographique continental minimal et à des perturbations anthropiques sur les dépôts atmosphériques à prédominance des VSO. Les résultats de datation au radiocarbone et les données de radionucléides de courte demi-vie (^{210}Pb, ^{137}Cs, ^{241}Am) garantissent une chronologie fiable pour ce profil de tourbe de 5 m de long et remontant à 6600 ans. La provenance des poussières a été déterminée à partir des signatures d'isotopiques du Nd (dénotées εNd) et des terres rares (TR) dans le sondage par rapport à un ensemble de données de référence des sources de poussières de l'hémisphère sud (HS).

Nous trouvons un mélange de poussières locales et distales déposées à AMS. Notre modèle de mélange combinant εNd et TR, montre un mélange relativement uniforme d'environ 40% de poussière locales, 15% d'Afrique australe et 45% du sud de l'Amérique du Sud tout au long du sondage. Cela indique un rôle prédominant de la poussière du sud de l'Amérique du Sud dans AMS, ce qui va à l'encontre de l'anticipation selon laquelle l'Afrique australe jouerait le

rôle principal dans la contribution de la poussière au sud de l'océan Indien vu sa proximité géographique. Les dépôts de poussière en Afrique australe ont toutefois doublé (32%) à partir de 1910AD.

Deux périodes de flux minimum de poussières minérales se produisent entre 6.2-4.9 cal. kyr BP et 3.9-2.7 cal. kyr BP, interprété comme une période avec VSO décalée et / ou renforcée vers l'équateur à sa limite nord. Inversement, périodes de flux de poussière plus élevés entre 6.6-6.2; 4.9-3.9; et 1.4 cal. kyr BP et au-delà sont interprétés comme VSO décalé et / ou affaibli poleward. Ces interprétations sont basées sur des vitesses de vent plus élevées conduisant à l'élimination de la poussière distale en chemin vers AMS, par turbulence et augmentation du dépôt humide. Les enregistrements VSO de l'Holocène publiés à son extrémité nord (33-41°S), de l'Amérique du Sud à l'Afrique du Sud jusqu'à l'Australie, montrent une grande variabilité au cours des 6.6 derniers mois. Nous pensons que cela reflète la variabilité climatique complexe du VSO dans les différents secteurs longitudinaux du HS.

Le récent changement de provenance de la poussière ne s'accompagne pas d'un dépôt accru de poussière à AMS. Nous suggérons donc que la dégradation des sols, l'agriculture et les conditions climatiques plus sèches en Afrique australe ont conduit à une mobilisation accrue de poussière provenant de cette zone.

Research article

Holocene dynamics of the Southern Hemisphere westerly winds over the Indian Ocean inferred from a peat dust deposition record

*(*Accepted by *Quaternary Science Reviews)*

Holocene dynamics of the southern westerly winds over the Indian Ocean inferred from a peat dust deposition record

Chuxian Li[1,2*], Jeroen E. Sonke[2], Gaël Le Roux[1], Nathalie Van der Putten[3], Natalia Piotrowska[4], Catherine Jeandel[5], Nadine Mattielli[6], Mathieu Benoit[2], Giles F.S. Wiggs[7], François De Vleeschouwer[1**]

1. EcoLab, Université de Toulouse, CNRS, INPT, UPS, Toulouse, France.

2. Laboratoire Géosciences Environnement Toulouse, Université de Toulouse, CNRS, IRD, UPS, Toulouse, France.

3. Faculty of Science, Earth Sciences, Cluster Earth and Climate, Vrije Universiteit Amsterdam, the Netherlands.

4. Institute of Physics-CSE, Silesian University of Technology, Gliwice, Poland.

5. LEGOS Université de Toulouse, CNRS, CNES, IRD, UPS, Toulouse, France.

6. Laboratoire G-Time, DGES, Université Libre de Bruxelles (ULB), Belgium.

7. School of Geography and the Environment, Oxford University Centre for the Environment, University of Oxford, South Parks Road, Oxford,OX1 3QY, United Kingdom.

* Corresponding author, chuxian.li@ensat.fr

At: EcoLab / Campus Ensat, Avenue de l'Agrobiopole, BP 32607 Auzeville Tolosane, 31326 Castanet-Tolosan, France

** Present address: Instituto Franco-Argentino para el Estudio del Clima y sus Impactos (UMI 3351 IFAECI/CNRS-CONICET-UBA), Universidad de Buenos Aires, Argentina

Abstract: The southern westerly winds (SWW) play a major role in climate variability in Southern Hemisphere mid- and high- latitudes, regulating rainfall, ocean circulation, and the Southern Ocean carbon sink. Despite their importance, little is known about millennial scale changes in the SWW and how they have influenced the climate system in the past and interacted with the Earth's surface elements, such as dust, nutrients and carbon. Here we present a dust record from a 6.6 kyr old peat core in Amsterdam Island (AMS) situated at the northern edge of the SWW (37°S) in the Southern Indian Ocean. Mineral dust flux was used to track atmospheric dust production, long-distance transport and subsequent deposition. Dust provenance was determined from rare earth element (REE) and Nd isotopic signatures (εNd) in the core, compared with a reference dataset of Southern Hemisphere dust sources. Using a multi-proxy mixing model, the εNd and REE ratios show a relatively uniform mixture of ca. 40% local, 15% Southern African and 45% Southern South American dust sources since 6.6 cal. kyr BP. However, from 1910 AD onwards, there is a doubling in the contribution from Southern Africa (32%). Two mineral dust flux minima occur at 6.2 - 4.9 cal. kyr BP and 3.9 - 2.7 cal. kyr BP, interpreted as periods with equatorward-shifted and/or strengthened SWW at the northern edge of the wind belts. Conversely, periods of higher dust flux at 6.6 - 6.2 cal. kyr BP, 4.9 - 3.9 cal. kyr BP, and 1.4 cal. kyr BP onwards are interpreted as poleward-shifted and/or weakened SWW. These interpretations are based on the findings that higher (lower) wind speeds lead to enhanced (less) removal of distal dust on the way to AMS, by wet deposition and turbulence. Published Holocene SWW records at the northern edge of the wind belt (33 - 41°S) covering South-America, Southern-Africa and Australia, show much variability over the last 6.6 kyr. We suggest this reflects complex regional climate variability of the SWW in the different SH longitudinal sectors, indicating that SWW are not zonally homogeneous at the northern edge of the wind belts. The recent shift in dust provenance is not accompanied by enhanced total dust deposition at AMS. We therefore suggest that human impact (e.g., land use changes) and drier climate conditions in Southern Africa have led to enhanced dust mobilization.

Keywords: Southern Westerlies; dust sources; peat; Amsterdam Island; anthropogenic activities.

1. Introduction

The strength and position of the southern westerly winds (SWW) vary seasonally due to changes in the sea surface temperature (Lamy et al., 2010). SWW shift equatorward and expand during the austral winter, while they move poleward and contract during the austral summer. Latitudinal displacement in annual-mean SWW position can be affected by both external factors (e.g., long-term orbital forced insolation changes, Varma et al., 2012, 2011), and internal factors (e.g., Southern Annual Mode changes, Gillett and Thompson, 2003). Changes in the annual-mean strength and position of SWW play a major role in climate variability of SH mid- and high latitudes (e.g., affecting precipitation pattern, Jenny et al., 2003). The SWW are also an important driver of ocean circulation, nutrient transport and the global carbon cycle (Kohfeld et al., 2013). Around 40% of anthropogenic CO_2 emissions are currently taken up by the Southern Ocean south of 35°S (Frölicher et al., 2015; Landschützer et al., 2015; Sabine et al, 2004). It has been suggested that poleward-shifts and intensification of the SWW can enhance upwelling of deep water with high concentrations of dissolved inorganic carbon, limiting the capacity of the ocean to absorb carbon at the surface, resulting in additional global warming (Denton et al., 2010; Hodgson and Sime, 2010; Lovenduski et al., 2008) .

An increase in SWW strength has been observed in recent decades (e.g., Hande et al., 2012; Marshall et al., 2006; Thompson and Solomon, 2002). Swart and Fyfe (2012) suggest that under high CO_2 emission scenarios, the SWW could shift up to 1.5° southwards and strengthen by up to 10% by the end of the 21st century (relative to the current annual-mean SWW position and strength). These changes will have significant environmental and climatic implications (Zickfeld et al., 2007). To understand the influence of SWW on Earth's climate requires a better knowledge of the interactions between SWW dynamics and climate in the past, especially in the Holocene (Fletcher and Moreno, 2012).

Up to now, a range of direct and indirect proxies in different stratigraphic archives (e.g., peat and sediment cores) have been used to reconstruct Holocene SWW fluctuations (e.g., Lamy et al., 2010; Moreno et al., 2010; Saunders et al., 2018, 2012; Van der Putten et al., 2008). However, no consensus has been reached on past intensity and/or latitudinal changes of the SWW at the whole wind belts. Some studies argue for a strengthening/equatorward shift of the SWW during the mid-Holocene (ca. 7 - 4 cal. kyr BP) relative to the early Holocene (ca. 11 - 7 cal. kyr BP) based on studies from Southern Africa (Fitchett et al., 2017; Humphries et al., 2017) , Southern South America (Jenny et al., 2003; Moreno et al., 2010) , Australia and New Zealand (Shulmeister, 1999). Other studies suggest a poleward displacement of the SWW

during the same period resulting in a decreased westerly influence in Southern Africa (Chase et al., 2013), Southern South America (Frugone-Álvarez et al., 2017; Lamy et al., 2010, 2001), Australia and New Zealand (Marx et al., 2011). These studies are mainly conducted on the continents, which are under the combined influence of SWW and other regional climate and orographic factors (e.g., the monsoon system in Australia and the presence of the Andes in South America).

Relatively few paleoclimatic studies (Lindvall et al., 2011; Ljung and Björck, 2007; Saunders et al., 2018, 2012; Van der Putten et al., 2012, 2008), have attempted to reconstruct Holocene SWW variability from oceanic islands where these factors are largely absent. Currently there are no SWW reconstructions at the northern edge of the SWW belt in the southern Indian Ocean. We address this by studying the Holocene mineral dust flux and its composition in peat profiles in Amsterdam Island (37°S). Mineral dust flux is a function of both changes in dust provenance, wind transport and deposition (Vanneste et al., 2015). Specifically, dust flux is a function of environmental factors, including aridity and air mass circulation over source areas (Marx et al., 2009; Thompson et al., 2002), dust atmospheric residence time (Betzer et al., 1988), as well as the strength and trajectories of transporting winds (Kohfeld et al., 2013). Changes in dust flux can be seen in the variabilities of geochemical and isotopic compositions (e.g., rare earth elements (REE) and Neodymium (Nd) isotopes, Vanneste et al., 2016, 2015). Amsterdam Island is remote and nearly free from human disturbance, which makes it an ideal location to measure dust flux and provenance, and determine past changes in wind dynamics (Gaudichet et al., 1989).

The specific objectives of this study were to: (1) investigate the dust flux in peat core from Amsterdam Island; (2) identify the provenance of the dust by comparing core samples with a reference dataset of dust geochemistry and isotopic signatures from the Southern Hemisphere; (3) interpret these measurements in terms of past changes in the dynamics of the SWW at their northern limit in the Indian ocean, through comparison with other Southern Hemisphere (SH) records; and (4) probe the anthropogenic impact on the Southern Hemisphere based on the dust variability in Amsterdam Island peat core. This study can also provide an observational dataset for climate model parameterizations, especially in terms of the future impact of changes in the SWW on continental rainfall and the global carbon cycle.

2. Material and Methods

2.1. Site description

Amsterdam Island (AMS, 37°50´S, 77°32´E) is a small (55 km^2) isolated volcanic island located 4200 km to the east of South Africa and 3200 km to the west of Australia (Fig. 1a, b). The island has steep cliffs along its western coast rising to a central caldera at 720 m above sea level (a.s.l., Flatberg et al., 2011; Doucet et al., 2003) (Fig. 1c). The highest point is Mont de La Dives at 881 m a.s.l.. AMS is currently at the northern edge of the SWW belt, and just north of the oceanic subtropical front (Orsi et al., 1995). It has a mild oceanic climate with frequent cloud formation at the caldera. Mean annual temperature at the meteorological station (27 m a.s.l.) is 14°C and annual precipitation is about 1100 mm (De Vleeschouwer et al., 2014; Lebouvier and Frenot, 2007). The wind strength is 7.4 m s^{-1} on average (Météo France data reported in Frenot and Valleix, 1990). However, climate conditions on the central plateau are harsher with a mean annual temperature of 7°C and twice as much rainfall (Frenot and Valleix, 1990). The soil around the central plateau is poorly developed and consists of water-saturated sandy loams developed to a maximum depth of 60 cm (Frenot and Valleix, 1990). The wetter conditions at higher altitudes of the island (above 500 m a.s.l.) favor moss growth (e.g., *Sphagnum* mosses) and peat accumulation, in particular on the central plateau (Flatberg et al., 2011).

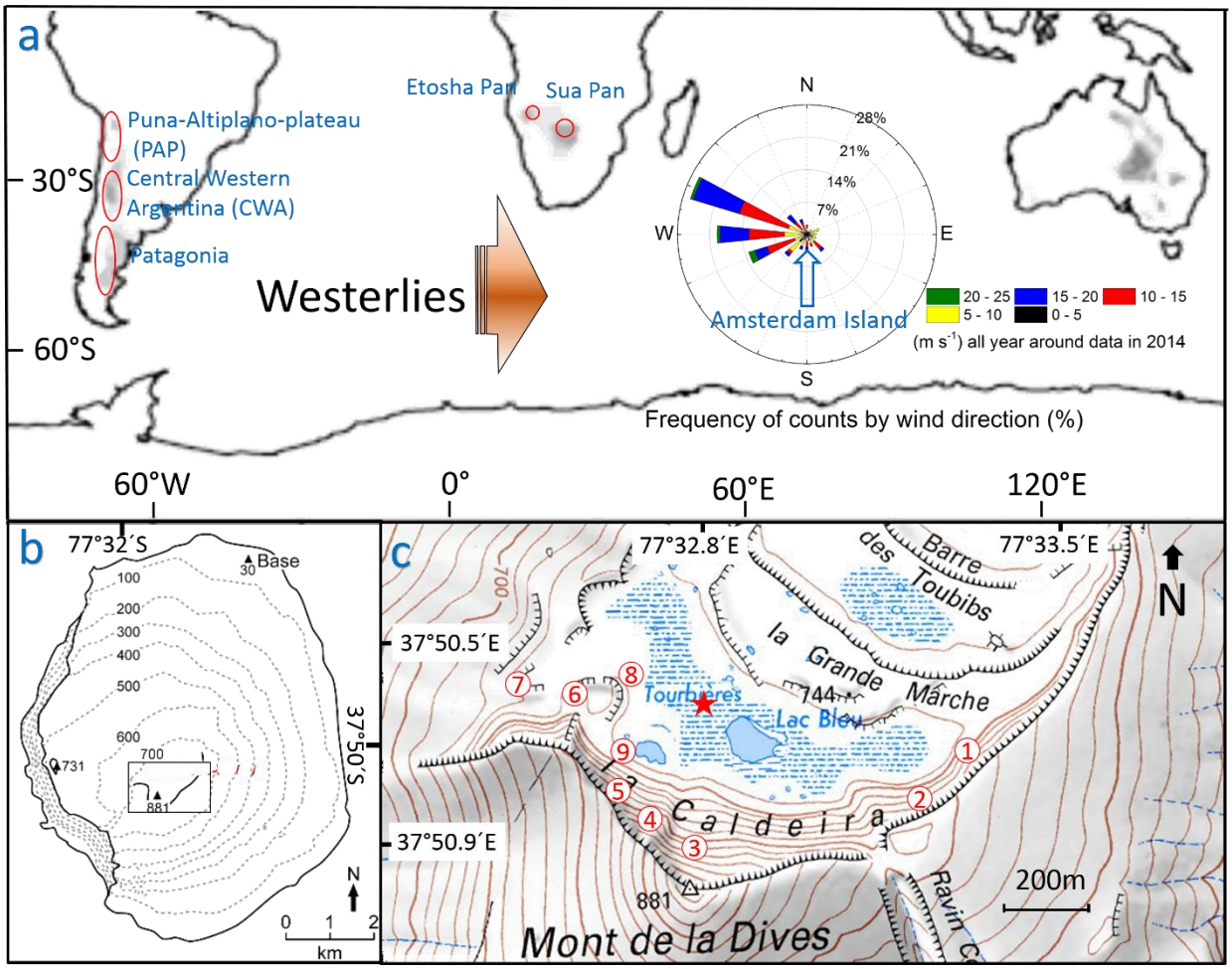

Fig. 1. Sampling sites on Amsterdam Island (AMS) and in the potential dust source areas in the Southern Hemisphere. (a) The core of the wind rose represents the location of Amsterdam Island. Wind rose data are courtesy of the Institut de Géosciences et de l'Environnement in Grenoble, France. The orange arrow represents Southern Westerly winds (SWW), whose core currently centers at 50-55°S (Saunder et al., 2018). The grey areas shown in Southern South America and Southern Africa, represents days per months (darker = more days) with dust activity (modified after Prospero et al., 2002). Red ellipses are soil sampling areas at Puna-Altiplano-Plateau, Central Western Argentina and Patagonia in Southern America (data from Gili et al., 2017); and dust/soil sampling sites at Sua Pan and Etosha Pan in Southern Africa. (b) Map of AMS. The black rectangle has been enlarged in Fig. c. (c) Locations of the peat coring site AMS14-PB01A (red star) and soil sampling sites (numbers shown in red) at AMS.

2.2. Sample collection and preparation

A 5 m-long peat sequence (AMS14-PB01A, 37°50.742´S, 77°32.898´E, Fig.1c) was collected from the center of the caldera peatland at 738 m a.s.l. (Fig. 1; Fig. S1) in December 2014 using

a 50 cm long Russian corer with an internal diameter of 10 cm (Belokopytov and Beresnevich 1955; De Vleeschouwer et al., 2014). Two further cores (AMS14-PB01B, 4.15 m length; AMS14-PB01C, top 1 m length) were collected and archived. Cores were photographed, described, wrapped in plastic film and PVC tubes, and shipped to France refrigerated at +4 °C. Cores were frozen and subsequently sliced at roughly 1-cm resolution using the sub-sampling procedure described in De Vleeschouwer et al., (2010) and Givelet et al., (2004).

To study the chemical and isotopic provenance of dust in the core, we assembled a reference dataset consisting of nine top soil samples from this island, representative of local dust sources (Fig. 1c), together with samples from the two major SH dust sources (Fig. 1a). These were identified from observational and modelling data (Bryant et al., 2007; Engelstaedter and Washington, 2007; Prospero et al., 2002; Vickery et al., 2013) and include: (1) Botswana and Namibia in Southern Africa; and (2) the Altiplano, Western Argentina and Patagonia in Southern South America. Australia is not considered as an important distal dust source for AMS because limited air masses originate from Australia according to the 14-day Hysplit back trajectory ensembles at AMS (Fig. S2, Text S1) and most Australian dust is transported eastward to the Pacific Ocean (Li et al., 2008). Chemical analysis on AMS also supports minimal present Australian dust contribution to AMS (Gaudichet et al., 1989). Specific reference dust/soil samples in this study were collected from (1) local; (2) Sua Pan (Botswana) and (3) Etosha Pan (Namibia) in Southern Africa (Fig. 1a, c). More information on Southern African dust/soil and local AMS soil are given in the supplementary information Text S2, Table S1 and Table S2, respectively. Dataset of Southern American surface sediments (including Puna-Altiplano-Plateau, Central Western Argentina and Patagonia) are from Gili et al., (2017).

2.3. Analyses and methods

2.3.1. Radiocarbon dating and age model reconstruction

Twenty peat samples were submitted for radiocarbon dating. Where possible monospecific terrestrial plant remains (brown mosses or *Sphagnum* mosses) were dated, and where there was insufficient material, both taxa were combined. Eleven of the radiocarbon samples were pre-treated and graphitized at the GADAM center (Gliwice, Poland, GdA code) (Piotrowska, 2013) and their ^{14}C concentration in graphite measured at the DirectAMS Laboratory (Bothell, WA, USA). The NIST Oxalic Acid II standard was used for normalization, and black coal was used as a blank. The other nine radiocarbon samples were pre-treated, graphitized and dated at

Plateforme Nationale LMC14 (CNRS-CEA Saclay, France, SacA code). Normalization of the measurements at LMC14 Laboratory was done with Oxalic Acid 1 standard. Blanks were carbonate and charcoal (for details see Delqué-Količ et al., 2013; Moreau et al., 2013).

The surface of the core was dated with ^{210}Pb using the Constant Rate Supply model (Appleby, 2001), together with four post-bomb radiocarbon dates (Goodsite et al., 2001; Hua, 2009). The ^{210}Pb Constant Rate Supply model has been validated by ^{137}Cs and ^{241}Am measurements (See Li et al., 2017 for details). An age-depth model was generated from a combination of radiocarbon dating, post-bomb and ^{210}Pb dating with the Bacon package version 2.2 updated in 2018 (Blaauw and Christen, 2011) within R software version 3.5 (R development Core Team, 2013) using the SHCal13 calibration curve (Hogg et al., 2013). For modelling, the core was divided into 101 sections. The prior settings were default 10 year/cm for accumulation rate (gamma distribution with shape 1.5), and memory was described by beta distribution with mem.strength = 4 and mem.mean = 0.7. The median modelled age was used for plotting the data against time.

2.3.2. Bulk density and ash content

The density (g m^{-3}) of 377 samples was obtained by measuring the volume of each sample, using a Vernier caliper, and weighing it after freeze-drying using an ALPHA 1e4 LD plus freeze-dryer. The ash content was determined as the weight difference before and after ashing the bulk peat samples in a furnace at 550°C for 5h.

2.3.3. Major and trace element analyses

We selected 101 freeze-dried AMS peat samples for elemental analysis based on the bulk density results. 100 mg of each selected peat samples was used and 50 mg of each reference soil/dust samples was used. These samples were digested in Teflon vials on a hot plate using an HNO_3-HF mixture (method modified from Vanneste et al., 2015, see supplementary information Table S3 for more details). Subsequently, concentrations of Al, Ti, K and Sr were determined by ICP-OES (IRIS Intrepid II) at Ecolab (Toulouse, France). Concentrations of trace elements (REE, Ga, Hf, Zr, Th, U, Cs, Rb, Pb), Mg and Ca were measured by quadrupole ICP-MS (Agilent Technologies 7500ce) at the *Observatoire Midi-Pyrénées* (Toulouse, France).

Synthetic multi-element calibration solutions were used to calibrate the ICP-OES and ICP-MS instruments. In addition, In-Re was added to both the ICP-MS calibration solutions and samples as an internal standard. Several certified reference materials (CRMs) were used for quality control: (1) NJV942 (*Sphagnum* peat, Swedish University of Agricultural Sciences,

Sweden); (2)NJV941 (*Carex* peat, Swedish University of Agricultural Sciences, Sweden); (3) SRM1515 (Apple leaves, NIST, US); (4) SRM1547 (Peach leaves, NIST, US); (5) LKSD-3 (lake sediment, CANMET Mining and Mineral Sciences Laboratories, Canada); and (6) WQB-1 (lake sediment, National Water Research Institute, USA). For further details on the quality control and quality assurance see supplementary information Text S3, Table S4 and Table S4bis.

2.3.4. Neodymium isotope analyses

43 freeze-dried samples from the AMS peat core, and reference soil samples from AMS (nine samples), Sua Pan (three soil and three dust samples), and Etosha Pan (three soil and three dust samples), were selected for Nd isotope analysis. The weight of the peat samples (160 mg - 950 mg) and soil/dust samples (68 mg - 275 mg) required for the analyses was based on their Nd concentrations and the sensitivity of the mass spectrometer. Before being digested in a mixture of concentrated HNO_3 and HF, samples were ashed in a furnace at 550°C for 5h (Vanneste et al., 2015). Subsequently, Nd was separated from the matrix within the sample solution using a two-column ion exchange technique. The Nd isotope composition of all the samples was determined by Thermal Ionization Mass Spectrometry (TRITON^{TM} Plus) at the *Observatoire Midi-Pyrénées* (Toulouse, France). Chemical blanks for Nd isotopic measurements were below the detection limit. The Nd standards Rennes ($^{143}Nd/^{144}Nd$ = 0.511973) and La Jolla ($^{143}Nd/^{144}Nd$ = 0.511858) were analyzed at every session to monitor instrumental drift. Measured values of La Jolla were 0.511844 ± 0.000012 (n=9) and of Rennes were 0.511956 ± 0.000006 (n=22). The three replicated samples gave consistent $^{143}Nd/^{144}Nd$ values within the error bars.

The Nd isotopic signatures, expressed in εNd notation are calculated by the equation (1).

$$\varepsilon Nd = \left(\frac{\left(\frac{^{143}Nd}{^{144}Nd}\right)_{Sample}}{\left(\frac{^{143}Nd}{^{144}Nd}\right)_{CHUR}} - 1 \right) \times 10^4 \qquad \text{(Eq.1)}$$

where CHUR is Chondritic Uniform Reservoir, representing a present day average earth value $(^{143}Nd/^{144}Nd)_{CHUR}$ = 0.512638 (Jacobsen and Wasserburg, 1980). εNd represents the deviation of $^{143}Nd/^{144}Nd$ in a sample from the value in CHUR.

2.4. Statistical methods

A principal component analysis (PCA) was performed on all the elemental data (REE, Mg, Ca, Ga, Rb, Zr, Cs, Hf, Th, U, Al, Pb, Ti, K, Sr) using the 'psych' package (Revelle, 2019) within

R software (R Decelopment Core Team, 2013). Each principal component groups a set of elements with similar variations along the peat profile. A varimax rotation is also performed for maximizing the variances of the squared loadings in the components in order to facilitate the interpretation (Abdi and Williams, 2010; Vanneste et al., 2016).

Change point analysis was performed with the Change-Point Analyzer 2.0 software (Taylor Enterprises Inc., IL, http://www.variation.com) to identify significant shifts in the key proxies through the Holocene (e.g., Castino et al., 2016; Killick et al., 2010; Reid et al., 2016) . The method (Taylor, 2000a) is based on the mean-shift model under the procedure of a combination of time-series cumulative sum charts and bootstrapping to detect change. The cumulative sums are the cumulative sums of differences between the values and the average (for details on the method see Taylor, 2000a; 2000b). The cumulative sum chart is optimal at detecting shifts in the mean (Taylor, 2000a). 10,000 bootstraps were performed and only changes with probabilities of >99% were considered.

2.5 Source end-members mixing calculation

The potential distal dust sources are discussed at a continental scale (e.g., Southern South America and Southern Africa) because our initial mixing model attempts have shown that the sources cannot be resolved on a sub-continental scale. Puna-Altiplano-Plateau, Central Western Argentina and Patagonia were grouped together as the Southern South American dust source end-member. Sua Pan and Etosha Pan were grouped as the Southern African end-member. The contributions of different source end-members were calculated based on the method of ratio-to-ratio relationships in the mixing balance described in Albarède, (1996) as equation 2:

$$\left(\frac{C^{i2}}{C^{i1}}\right)_{mix} = \frac{\sum_{j=1}^{n} C_j^{i2} f_j}{C_{mix}^{i1}} \qquad \text{(Eq. 2)}$$

Where C^{i1} and C^{i2} are the REE concentrations or Nd isotopes in a mixture of n components j and represents each component (end-member). f is the fraction of component j in the mixed dust depositing at AMS. Details on the calculation are reported in Table S5.

3. Results

3.1. Core description

The total length of the core is 500 cm. Between 500 cm and 340 cm depth, a compacted, in general relatively well-preserved peat deposit was formed. The peat is laminated, showing a

cm-scale alternation between fibrous well preserved *Sphagnum*-dominated layers and more amorphous less well preserved layers. From 340 cm to 20 cm the peat becomes less compacted showing different units of more or less well preserved peat, with visible plant macrofossils in some parts. The top 20 cm of the core reflects the modern vegetation which consists mainly of brown mosses together with some *Sphagnum* spp. (Fig. S3).

3.2. Bulk density and ash content

The density profile of the AMS peat core shows a general decreasing trend with an abrupt drop at ~315 cm (Fig. 2a). From 500 cm to 315 cm, the median density is 0.17 g cm^{-3} (0.08 - 0.26 g cm^{-3}) with relatively higher values between 340 cm and 315 cm. From 315 cm upwards, the density is lower with a median value of 0.12 g cm^{-3} (0.05 - 0.16 g cm^{-3}). The ash content in the AMS peat core mirrors partly the density profile and shows a general decreasing trend from bottom to top (Fig. 2b), varying between 2.63% and 0.34%. The abrupt decrease between 340 cm and 315 cm present in the density profile is not as prominent in the ash content.

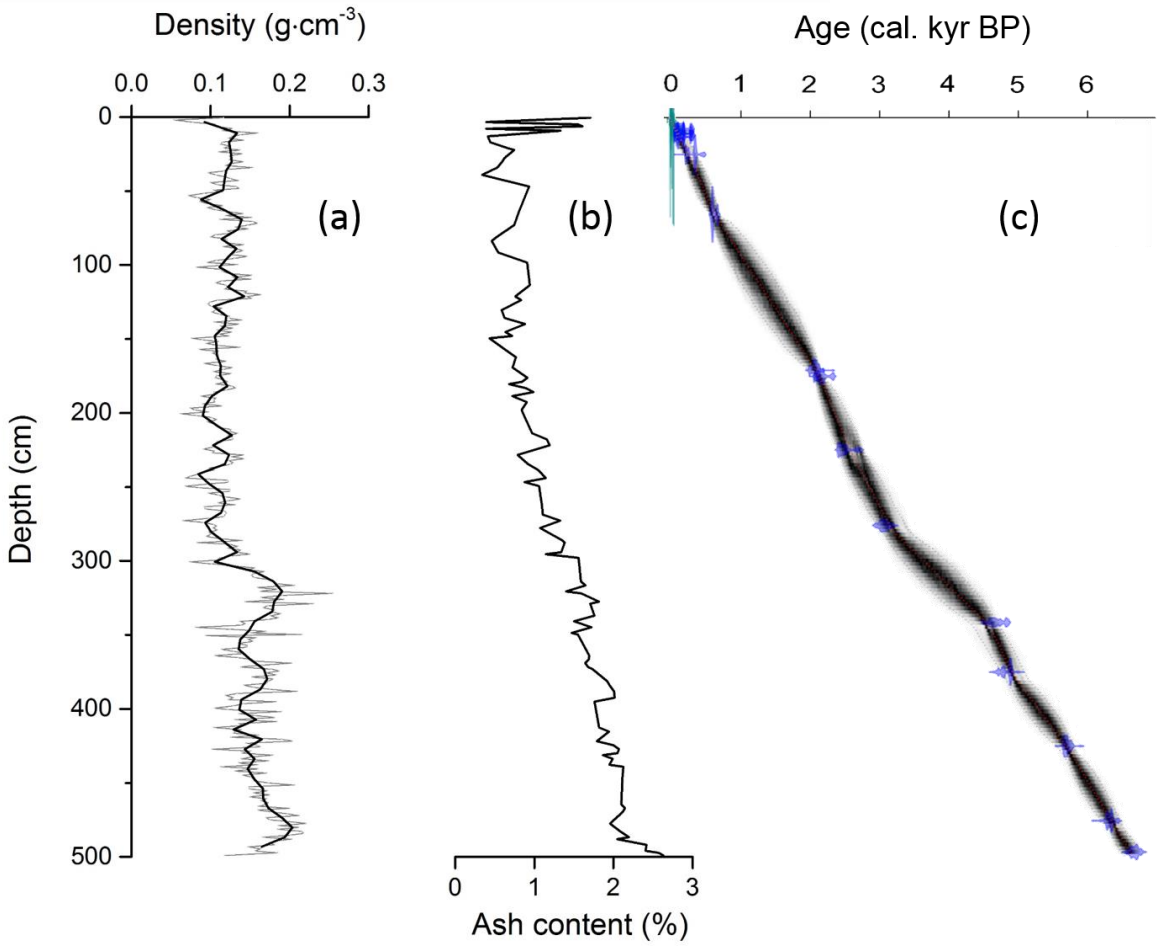

Fig. 2. (a) Density (black line = for 5-point smoothing), (b) ash content and (c) age depth model (^{14}C in blue, ^{210}Pb Constant-Rate-Supply model in green) of the AMS peat core. For details on the top 50 cm chronology, we refer to Fig. S4 in supplementary information.

3.3. Geochronology

Radiocarbon and calibrated ages are shown in Table 1. The ^{210}Pb, ^{137}Cs and ^{241}Am results are published in Li et al., (2017). The ^{210}Pb Constant Rate Supply model is in good agreement with post-bomb ^{14}C ages. The age-depth model of the core was based on a combination of radiocarbon dating, post-bomb and ^{210}Pb dating (Fig. 2c; Fig. S4). The model shows that the peat sequence spans the last 6.6 kyr (Table S6), with a mean accumulation rate of 0.76 mm yr^{-1}.

Table 1. Radiocarbon dating results from Amsterdam Island peat sequence. Four samples were dated to a post-bomb period (Goodsite et al., 2001; Hua, 2009; Spalding et al., 2005) and the results calibrated using SH zone 1-2 calibration curve (Hua et al., 2013) by Calibomb software (Stuiver and Reimer, 2003). Other results were calibrated using the SHCal13 calibration curve (Hogg et al., 2013). Age-depth modelling was performed with Bacon, R routine (Blaauw and Christen, 2011).

Lab ID	**Mid-Point Depth (cm)**	**Material dated**	**pMC***	**Calibrated age (median)**	**Selected calibrated intervals (years BP)**
SacA50049	2.0	*Chorisondontium*/*Dicranoloma* stems + leaves	107.18 ± 0.28		[-58 ; -53]
SacA50050	3.5	Brown moss stems	120.36 ± 0.30		[-37 ; -35]
SacA50051	4.9	Brown moss + liverworts stems	146.21 ± 0.32		[-24 ; -22]
SacA50052	6.4	Brown moss + liverworts stems	116.81 ± 0.28		[-10 ; -10]
Lab ID	**Mid-Point Depth (cm)**	**Material dated**	**14C age (yr BP)**	**Calibrated age (median)**	**Calibrated age range with 95.4% probability (BP)**
SacA50053	7.8	Brown moss stems	135 ± 30	8	1 - 16
SacA50054	9.4	Brown moss stems	115 ± 30	26	14 - 39
SacA50055	10.8	Brown moss stems + leaves	80 ± 30	44	27 - 62

SacA50056	12.0	Brown moss stems + *Chorisondontium*/*Dicranoloma* leaves	160 ± 30	57	33 - 96
SacA50057	13.2	Brown moss stems	70 ± 30	65	35 - 127
GdA-4136	24.9	brown moss stems	275 ± 25	198	150 - 310
GdA-4558	65.4	Residue (*Sphagnum* dominated)	595 ± 25	561	510 - 640
GdA-4560	170.7	Brown moss stems	2100 ± 25	2028	1920 - 2105
GdA-4137	174.8	Brown moss stems	2170 ± 30	2076	2005 - 2145
GdA-4138	224.4	Brown moss stems	2430 ± 30	2530	2365 - 2700
GdA-4139	275.4	Brown moss stems	2925 ± 30	3092	2930 - 3330
GdA-4561	340.9	Brown moss stems	4145 ± 35	4485	4225 - 4645
GdA-4140	374.4	*Sphagnum*	4285 ± 30	4850	4700 - 5025
GdA-4141	424.4	*Sphagnum*+ brown moss	4960 ± 30	5630	5500 - 5745
GdA-4142	474.8	*Sphagnum* stems	5515 ± 35	6280	6140 - 6410
GdA-4143	495.9	*Sphagnum* stems	5860 ± 35	6565	6420 - 6700

*pMC: percent modern carbon

3.4. Peat REE and Nd isotopic signatures

The concentration of the entire REE suite varies between 0.18 and 1.26 µg g^{-1} (Table S7). The variations in the down core concentrations of fourteen REE elements (La, Ce, Pr, Nd, Sm, Eu, Gd, Tb, Dy, Ho, Er, Tm, Yb and Lu) are similar to each other. The Nd concentration profile is plotted as an example (Fig. 3a). The εNd signature at the bottom of the peat core is -0.8 ± 0.2 (2σ, n=1). There is a general decreasing trend in εNd values between 6.6 - 5.4 cal. ky BP, followed by an approximately three-fold increase at 4.4 - 3.9 cal. kyr BP. The lowest εNd

values occur at 3.3 - 2.7 cal. kyr BP, after which the εNd fluctuates with an overall increasing trend since 2.7 cal. kyr BP. The Holocene peat εNd profile is relatively constant centering at -2 ± 1.2 (1σ, n=34, Fig. 3b,Table S7), except for the last 100 years showing more distinct negative signatures with an average value of -7 ± 1.5 (1σ, n=7).

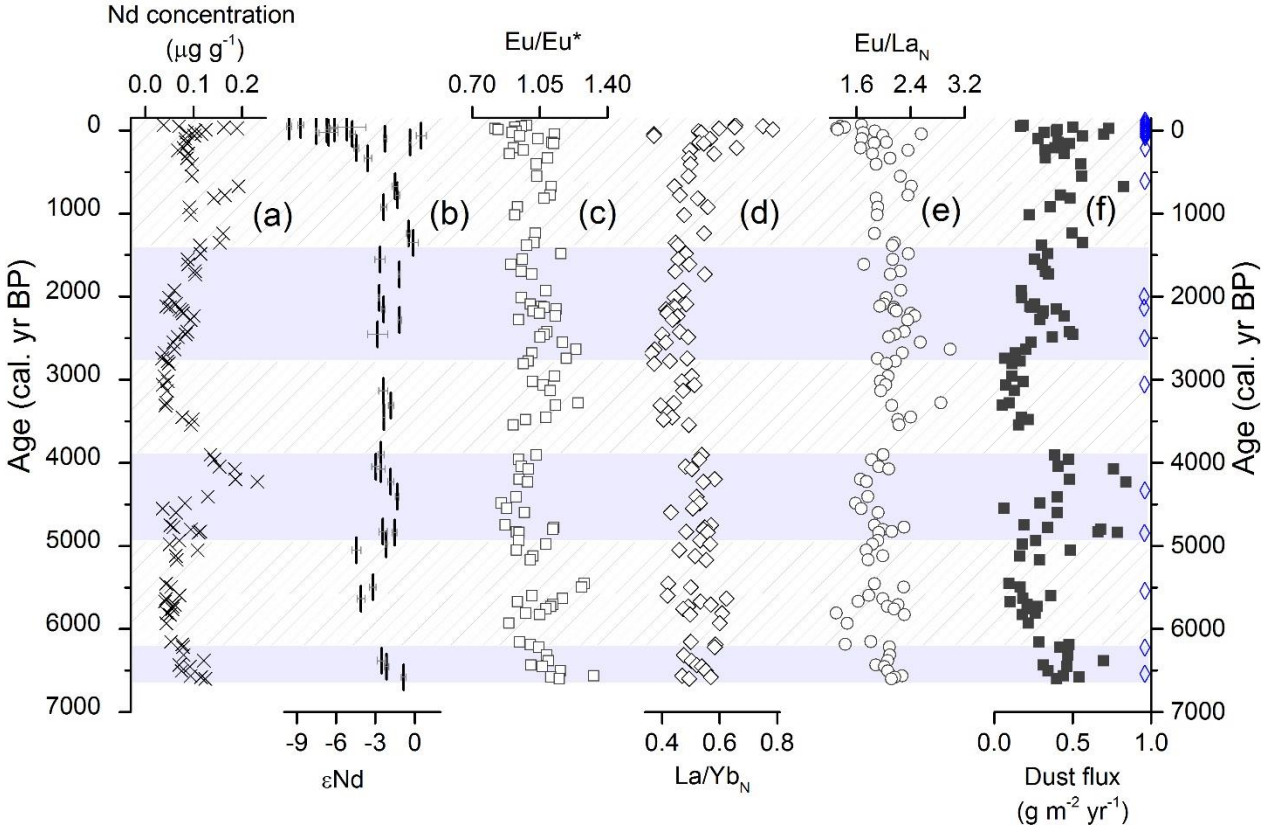

Fig. 3. Profiles of (a) Nd concentration (μg g^{-1}); (b) Epsilon Neodymium (εNd); (c) Eu/Eu*; (d) La/Yb_N; (e) Eu/La_N; and (f) REE–based dust flux (g m^{-2} yr^{-1}) in AMS peat core. Diamonds represent the ^{14}C dated peat layers (20 in total). The blue and white shading are the zones determined by change point analysis for AMS dust flux.

REE ratios can be used for dust provenance-tracing. The Eu anomaly (Eu/Eu*) was calculated with the equation Eu/Eu* = [Eu]/(([Sm]+[Gd])/2). The ratios of La/Yb and Eu/La have been normalized to Upper Continental Crust (Wedepohl, 1995). Peat average Eu/Eu*, La/Yb_N and Eu/La_N values since the last 6.6 kyr are 1.03 ± 0.10, 0.50 ± 0.07 and 2.01 ± 0.30 (1σ, n=101), respectively. The signatures of peat Eu/Eu*, La/Yb_N and Eu/La_N remain relatively constant during the last 6.6 kyr (Fig. 3c, d, e), except for the last 100 years, which are characterized by an overall decreasing trend in Eu/Eu* and Eu/La_N ratios, and an increasing trend in La/Yb_N ratio.

4. Discussion

4.1. Elemental proxy interpretation

The results of the PCA are reported in Fig. 4a and Fig. S5. The first component (PC1), explains 70% of the total variance and consists of the entire REE suite and Ga, U, Th, Hf, Zr, Ti, Al (Fig. 4b, c), which are known to be immobile and conservative elements. The second component (PC2), accounts for 14% of the total variance and consists of K, Rb, Pb, and Cs (Fig. 4d, e). The variability of this component is mainly driven by changes in the top part of the core, caused by biological uptake and recycling by the surface moss vegetation (principally K, Rb and, to a lesser extent Cs based on Fig. 4a) as well as anthropogenic Pb deposition (Damman, 1978; Shotyk, 1997). The third component (PC3), explains 12% of the total variance, and includes Sr, Ca and Mg (Fig. 4f, g), which show higher values towards the bottom of the core (Shotyk, 1997).

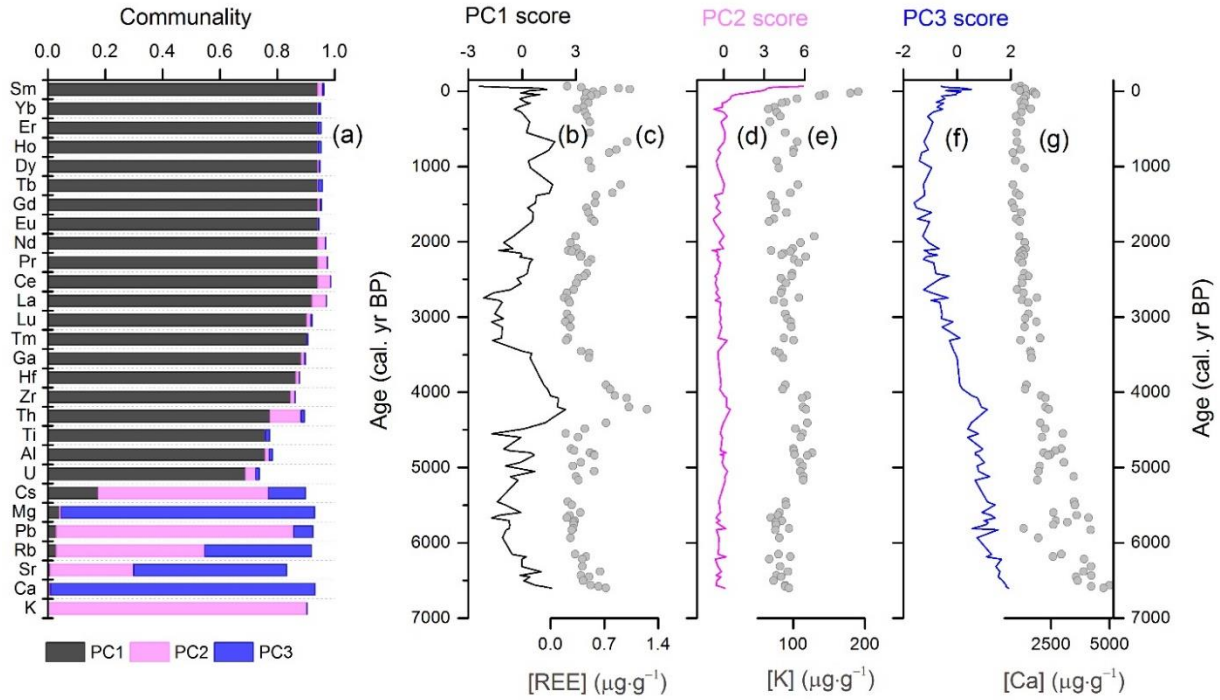

Fig. 4. (a) Relative importance of each principal component (PC) for each chemical element; (b-g) PC scores (i.e. transformed variable values for each sample) and their respective representative elements. All the representative elements are shown as concentration (µg g^{-1}).

4.2. Dust deposition

The REE, also reflected by PC1, represent immobile and conservative elements. Therefore, the mineral deposition rate (dust flux, g m^2 yr^{-1}) was calculated as equation 3:

$$\text{Dust flux}_i = \frac{\sum[REE]_i \times peat\ vertical\ AR_i \times density_i}{\sum[REE]_{UCC}} \times 10000 \quad \text{(Eq. 3)}$$

Where $\sum[REE]_i$ is the sum of all REE concentrations (µg g^{-1}) in sample i, $peat\ vertical\ AR_i$ is the peat accumulation rate (cm yr^{-1}), obtained by $depth\ length_i/age\ interval_i$), $density_i$ is the density of the sample (g cm^{-3}), $\sum[REE]_{UCC}$ is the sum of the REE concentrations in the upper continental crust (Wedepohl, 1995).

The dust flux profile shown in Fig.3, varies from 0.05 - 0.84 g m^2 yr^{-1} with a median value of 0.32 g m^2 yr^{-1} (Fig. 3f). The REE-based AMS dust flux is comparable to the late Holocene ^{232}Th reconstructed dust flux of 0.5 - 1.0 g m^{-2} yr^{-1} over the Western Indian Ocean (Kienast et al., 2016). Individual dust flux values are sensitive to spikes in REE concentration, to the ^{14}C age model, and to the peat density. The highest dust fluxes are recorded between 4.2 cal. kyr BP and 4.8 cal. kyr BP, and are related to maxima in REE concentration and peat accumulation rate. We applied a change-point analysis to identify changes in the probability distribution of the dust flux. Four change-points with >99% confidence level, were identified: 6.2 cal. kyr BP; 4.9 cal. kyr BP; 3.9 cal. kyr BP; 2.7 cal. kyr BP and 1.4 cal. kyr BP. We therefore separate the dust flux profile into six zones for discussion (see blue and white shading on Fig. 3, and section 4.4): (1) 6.6 - 6.2 cal. kyr BP; (2) 6.2 - 4.9 cal.kyr BP; (3) 4.9 - 3.9 cal. kyr BP; (4) 3.9 - 2.7 cal. kyr BP; (5) 2.7 - 1.4 cal. kyr BP; (6) 1.4 cal. kyr BP to the present (2014 AD).

The median ash content of 1.3% (n=101) in AMS peat core is low compared to the 2.9% recorded in a peat core from Tierra del Fuego in Southern South America (Vanneste et al., 2016) and 12.9% from a core in the Mfabeni peatland in Southern Africa (Humphries et al., 2017). The low ash content suggests limited groundwater inputs, even in the deeper minerotrophic part of the bog (detailed explanations for trophic status see Supplementary Information Text S4 and Fig. S6).

4.3. Dust provenance

Studies on atmospheric deposition at AMS, using ^{222}Rn, ^{210}Pb and air mass back trajectories suggested some continental inputs to AMS, in particular from Southern Africa (Angot et al., 2014; Gaudichet et al., 1989; Polian et al., 1986), and Southern South America (Fig. S2). Comparison of εNd values in the AMS peat sequence with the reference datasets of the potential dust source end-members (local, Southern Africa, and Southern South America) show that εNd values of the peat samples lie between the local and continental dust sources (Fig. 5,

Fig. S7). This also suggests that AMS can potentially receive dust from local, Southern African, and Southern South American sources.

The AMS soil samples display slightly higher Eu/Eu* (median 1.24, Fig. 5) and lower La/Yb_N ratios (median 0.27, Fig. 5) compared to the peat samples. The Southern African end-member (including both Sua Pan and Etosha Pan) has Eu/Eu* ratios that are close to those for the AMS peat samples, but show higher La/Yb_N ratios (median 1.04). In comparison with the peat samples, Eu/Eu* ratios are relatively lower and La/Yb_N ratios are analogous in the Southern American end-member (including Puna-Altiplano-Plateau, Central Western Argentina and Patagonia, Gili et al., 2017). The average εNd value of the AMS soil samples is 3.9 ± 0.2 (2σ, n = 7, Fig. 5b), much higher than those in the peat samples (εNd -9.6 - 0.5). The Southern African end-member has a more negative signature of -24 ± 1.7 (1σ, n=11, Fig. 5b). Both εNd (median 3.84) and Eu/La_N (median 3.52) are higher in the local soils than in the Southern African end-member (median εNd = -24.72, median Eu/La_N = 1.44). The εNd signatures in the Southern South American end-member overlap with those in the peat samples, while the Eu/La_N ratios are relatively lower in the Southern South American end-member.

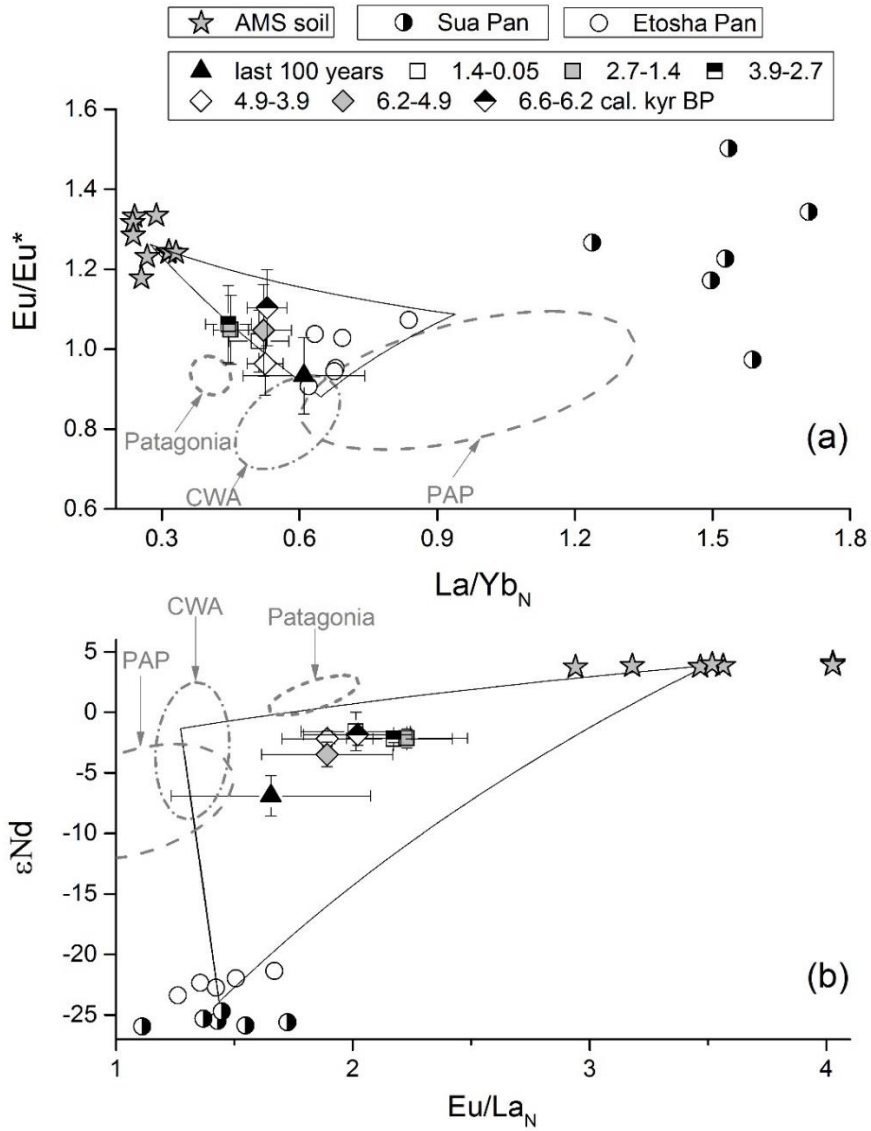

Fig. 5. Relationships of La/Yb$_N$ vs Eu/Eu* (a), and Eu/La$_N$ vs εNd (b) in AMS peat together with its Potential Source Areas (normalized to UCC, Wedepohl, 1995). Peat samples are shown as triangles/squares/diamonds, with different shapes representing different periods of the last 100 years (number of samples based on Fig. 5a, n = 8), 1.4 - 0.05 cal. kyr BP (n = 17), 2.7 - 1.4 cal. kyr BP (n = 21), 3.9 - 2.7 cal. kyr BP (n = 13), 4.9 - 3.9 cal. kyr BP (n = 15), 6.2 - 4.9 cal. kyr BP (n = 17), and 6.6 - 6.2 cal. kyr BP (n = 10), respectively. Black-edge stars: AMS soils; Half-open circles: dust/soil in Sua Pan; Open circles: dust/soil in Etosha Pan. Puna-Altiplano-Plateau (PAP, nine data points), Central Western Argentina (CWA, five data points) and Patagonia (11 data points) are shown in Elipses (mean data with 95% confidence level, Gili et al., 2017); The black lines in (a) and (b) represent the End-member mixing lines among AMS soil, Southern Africa (Sua Pan + Etosha Pan) and Southern South America (PAP + CWA + Patagonia) (see supplementary information Table S5 for detailed calculations, after Albarède, 1996).

Using the multi-proxy mixing model (Fig. 5), εNd and REE ratios indicate that the peat received approximately 40% of dust from local sources, 15% from Southern Africa and 45% from Southern South America. Dust source proportions were relatively constant over the last 6.6 kyr, except during the last 100 years (Table 2). Since 1910 AD, the model estimates a relative decrease in the local dust input (15%), while the relative contribution of Southern South Africa doubled (32%), with the Southern South American dust component (53%) showing little significant change.

Table 2. The mean dust contributions of local, Southern African and Southern American dust to the AMS peat sampling site during the Holocene (kyr) and last 100 years. Estimates are based on a REE proxy mass balance model. Potential African and South American dust sources are lumped (see text). Uncertainty range corresponds to 1σ.

Time interval (kyr)	local	Southern Africa	Southern America
the last 100 years	15% (5%-25%)	32% (25%-40%)	53% (40%-65%)
1.4 -0.05	41% (35%-50%)	15% (10%-20%)	44% (30%-55%)
2.7-1.4	44% (35%-55%)	12% (5%-20%)	44% (30%-55%)
3.9-2.7	46% (40%-55%)	15% (10%-20%)	39% (25%-50%)
4.9-3.9	36% (30%-40%)	9% (5%-15%)	55% (40%-70%)
6.2-4.9	35% (25%-40%)	15% (5%-25%)	50% (35%-70%)
6.6-6.2	41% (35%-45%)	9% (5%-15%)	50% (45%-60%)

In addition to an important local dust contribution (40%), likely from weathered basalt cliffs adjacent to the AMS peat bog, the mixing model indicates that from 6.6 kyr BP to 1910 AD, Southern South America is an important contributor of dust (45%; Table 2). The 14-day back trajectories show the air masses passing AMS that partially originate from Southern South America, covering the Puna-Altiplano-Plateau, Central Western Argentina and Patagonia (Fig. S2). This is also supported by modern dust observations. For example, combining ground/satellite observations and atmospheric modelling, Gaiero et al., (2013) found that large dust storms at the Puna-Altiplano-Plateau (15° and 26°S) can be developed and injected into the high-altitude subtropical jet stream of the SWW, which hence can be transported over long distances (Gaiero, 2007). Dust from the Central Western Argentinean lowlands (between ~27° and ~39°S), can also be uplifted by strong vertical air motion and be entrained into the SWW (Gili et al., 2017). Once lifted into the troposphere, dust can be transported over thousands of kilometers from its source area (Mahowald et al., 2005). Johnson et al., (2011) have shown that Patagonian dust travels along the SWW pathways to the Southern Indian Ocean during dust

outbreak events in the austral summer, potentially reaching the Southern Indian Ocean in a short period of time (days).

The mixing model also confirms a small (9 - 15%) but significant proportion of Southern African dust through most of the Holocene (Table 2; Fig. 6). The Makgadikgadi Basin in Botswana represented by our Sua Pan samples is the principal persistent dust source in Southern Africa, with a general maximum dust emission activity in August-October (Prospero et al., 2002). The prevailing winds in the area of Sua Pan (Fig. 1a) are tropical Easterlies that bring moisture from the Indian Ocean (Bryant et al., 2007). Etosha Pan situated in the semi-north of Namibia is a second principal Southern African dust source with prevailing northeasterly winds (Vickery et al., 2013; Von Holdt et al., 2017). Both Sua Pan and Etosha Pan are characterized by a proportion of northwesterly winds (Piketh, 2002; Von Holdt et al., 2017), confirming that dust from Sua Pan and Etosha pan can be transported eastward into the Indian Ocean (Fig. S2).

4.2 Lower dust input under equatorward-shifted/strengthened SWW

The dust provenance mixing model showed that the relative proportion of dust contributions from local, Southern African and Southern South American sources remained more or less constant over the mid- to late Holocene at AMS. The estimated dust deposition flux (g m^{-2} yr^{-1}), however, varied substantially on millennial timescales (Fig. 3a), likely resulting from changes in the position and/or intensity of SWW. It is important to realize that a northward shift in SWW may result in multiple antagonistic effects on dust: in dust source areas, an increase in SWW strength may mobilize more dust. However, stronger SWW are characterized by more humid conditions and more rainfall at least at the western to central sectors of the regions, leading to denser vegetation and soil dust immobilization. Additionally, in the case of the high altitude Puna-Altiplano-Plateau and Sua Pan/Etosha Pan, the dust source areas do not directly lie within the SWW belts, but their dust mobilizations can be influenced by SWW (see section 4.2). The net effect of stronger SWW on dust emission therefore depends on local geography, meteorology and vegetation (Marx et al., 2018). Studies on climate variability in AMS dust source areas indicate enhanced dryness (e.g., relative higher dust availability) during 6.2 - 4.9 cal. kyr BP and 3.9 - 2.7 cal. kyr BP in both Puna-Altiplano-Plateau (Pueyo et al., 2011) and Southern Africa (Chase et al., 2017; Chevalier and Chase, 2015; Cohen and Tyson, 1995; Cordova et al., 2017; Nash et al., 2006). Dust mobilization in these source areas should therefore have been constant or possibly enhanced during these two periods.

During periods of equatorward shifted and/or strengthened SWW potentially enhanced dust mobilization will be subjected to more intense removal by rainfall and by turbulence via dry deposition during transport (Miller et al., 1993; Moody et al., 1991). Evidence for this is based on the relationship between rainfall chemistry and seasonal and inter-annual large-scale atmospheric circulation patterns at AMS. Moody et al., (1991) observed minima in rainfall anion concentrations (non-sea salt Cl and SO_4, from continental origin) during austral winters, characterized by stronger winds and enhanced precipitation. Distal dust records such as AMS, thousands of kilometers away from dust sources, will overall tend to register decreased distal dust deposition during stronger and/or equatorward shifted SWW due to the dominant effect of dust removal during transport (Li et al., 2008). Stronger SWW with higher precipitation can decrease local dust mobility by increasing local vegetation cover and humidity. We therefore suggest that the AMS mineral dust flux minima from 6.2 - 4.9 cal. kyr BP and 3.9 - 2.7 cal. kyr BP represent periods of equatorward shifted and/or strengthened SWW at this northern edge with higher wind speed and enhanced precipitation over the dust transport trajectories, regardless of the potential enhanced dust mobility at the source areas during these two periods. Conversely, the three episodes of higher dust inputs (6.6 - 6.2 cal. kyr BP; 4.9- 3.9 cal. kyr BP; 1.4 cal. kyr BP to present) represent periods of poleward-shifted and/or weakened SWW accompanied by overall lower wind speeds and lower precipitation along the air mass trajectories from the Southern Africa and Southern South America continents to AMS, together with relatively higher local dust availability. The intermediate period from 2.7 - 1.4 cal. kyr BP (Fig. 3f), identified by the change-point analysis, is a dust flux transition period characterized by gradual poleward displacement of the SWW.

The timing and strength of the reconstructed environmental changes at AMS from 4.9 to 3.9 cal. kyr BP suggest these were part of a larger regional drought event, widely observed around the Indian Ocean. For example, enhanced dry conditions have been found based on the abrupt increased dust deposition in both Kilimanjaro ice cores (~4.0 cal. kyr BP, Thompson et al., 2002) and in the Gulf of Oman marine sediment record (4.0 ± 0.1 cal. kyr BP, Cullen et al., 2000), based on the positive sea surface salinity in a Northern Red Sea sediment core (~4.2 cal. kyr BP, Arz et al., 2006), and based on the reduced annual rainfall evident in the Arabian sea sediment core (~4.2 cal. kyr BP, Staubwasser et al., 2003). This mega-drought has potentially led to some of the greatest societal upheavals in historical times (e.g., Egyptian Old Kingdom in the Nile Valley and Akkadian Empire in Mesopotamia, Weiss, 2016). The severe dry conditions are explained by changes in the monsoon system and extra–tropical airflow during winter (e.g., Cullen et al., 2000; Staubwasser et al., 2003), which was suggested to follow

variability in solar activity (Cullen et al., 2000; Neff et al., 2001). Weaker SWW at AMS associated with the mega-drought event, suggests a close teleconnection between SWW and other climate features (e.g., monsoon system) in Indian Ocean sector around 4 cal. kyr BP.

We compare the AMS dust deposition record to other SH paleoclimate records from different longitudes at the northern edge of SWW (33 - 41°S, Fig. 6). We find that the AMS dust flux (Fig. 6d) broadly anti-correlates with magnetic susceptibility in an oceanic minerotrophic peat core from Nightingale Island (37°S, Fig. 6e, Lindvall et al., 2011). Magnetic susceptibility is a proxy for surface runoff to this peat mire and therefore tracks rainfall in a very different manner to our dust deposition proxy in the ombrotrophic AMS peat core (for explanations on trophic status see supplementary Text S4). Both AMS and Nightingale cores suggest that the SWW moved poleward at 4.9 - 3.9 cal. kyr BP, and equatorward at 6.2 - 4.9 cal. kyr BP and 3.9 - 2.7 cal. kyr BP. Other published proxy records do not show coherent trends with these two SWW proxy records over the past 6.6 kyr. For example, AMS dust flux, Nightingale Island magnetic susceptibility and Southern Chile pollen composition (Moreno et al., 2010), indicate a poleward shift in SWW from 4.9 to 3.9 cal. kyr BP (Fig. 6a, d, e), where other records show no trend (Fig. 6c, g, h), or an equatorward shift in SWW (Fig. 6b, f). Subsequently, during 3.9 - 2.7 cal. kyr BP period, the AMS dust flux, Nightingale Island magnetic susceptibility (Lindvall et al., 2011), Southern Chilean marine iron (Lamy et al., 2001), Central Chilean precipitation (Jenny et al., 2003), and South African nitrogen isotope records (Chase et al., 2013) (Fig. 6d, e, b, g, h, respectively), suggest an equatorward shift in SWW. Conversely the Chilean pollen (Moreno et al., 2010), Western South Atlantic Oxygen isotope (Voigt et al., 2015) and Southeast Australian westerly positon records (Marx et al., 2011) (Fig 6a, c, f), show no change in SWW from 3.9 - 2.7 cal. kyr BP. We speculate that the reasons for the observed variability in SWW proxy records are, 1/ the dependence of SWW proxies on complex regional climate factors, and 2/ uncertainty in interpreting these paleo-records due to dating uncertainties, and resolution and inherent complexity of proxies used. A limitation of the AMS peat record is that it does not extend to the late glacial period, where stronger trends in climate proxies have been previously detected (e.g., Kuhnt et al., 2015; Lamy et al., 2010, see Fig. S8). The variations in SWW in the last 6.6 kyr that we infer from the AMS dust record should therefore be regarded as moderate changes, compared to the oscillations in SWW that have been associated with glacial/inter-glacial periods (e.g., De Deckker et al., 2012; Van der Putten et al., 2015). Essentially, the ensemble of paleo-climate records shown in Fig. 6, suggests that SWW are not homogeneous across at its northern zone (33 - 41°S) over the last

6.6 kyr. More well-dated Holocene records using multiple proxies, and advanced Earth system climate models are needed to understand the geographical variability in SWW dynamics.

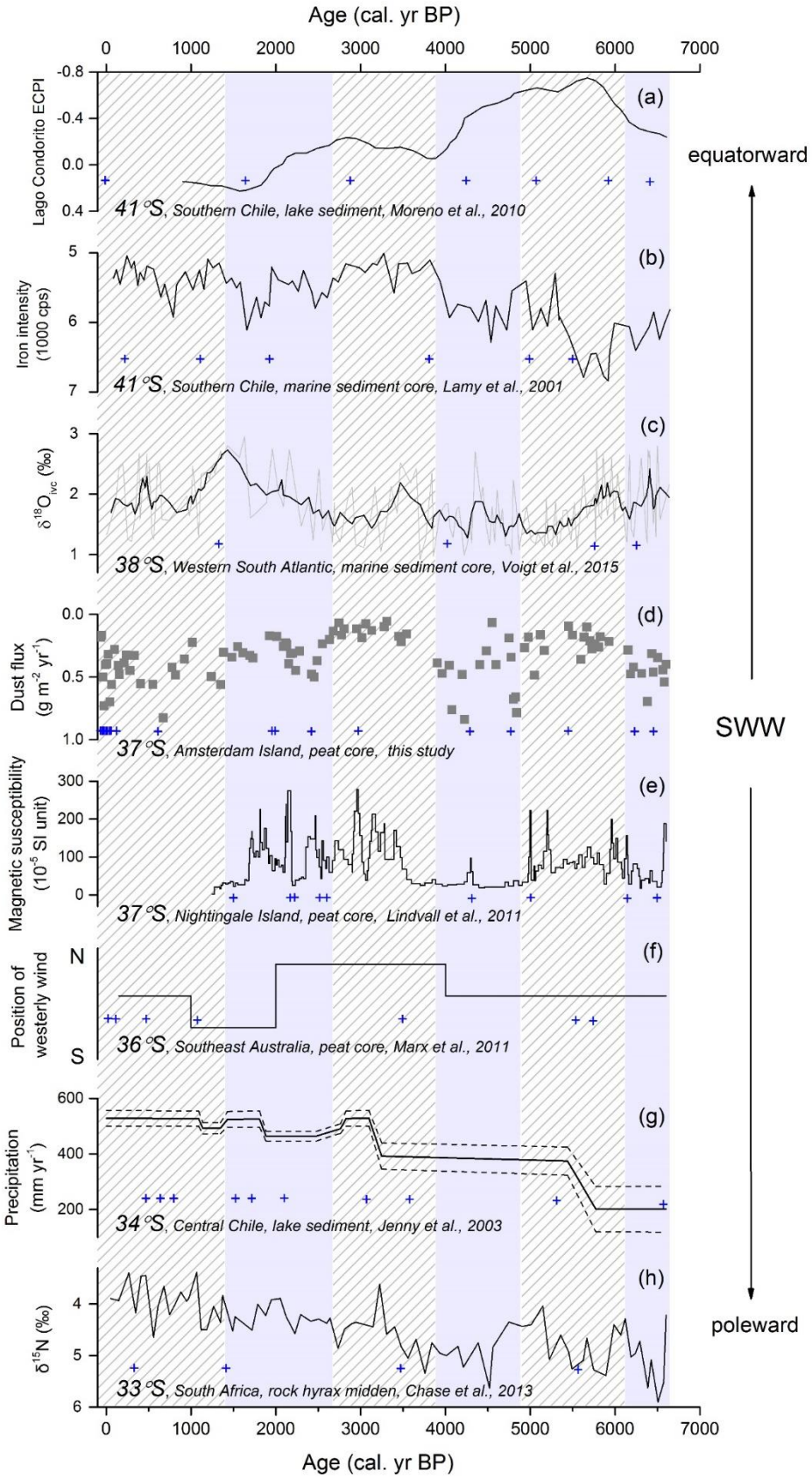

Fig. 6. Proxy records for wind position/strength at the northern SWW margin. (a) Pollen index *Eucryphia* + *Caldcluvia/podocarps* (ECPI) from lake sediment core at Lago Condorito from Southern Chile (Moreno et al., 2010); (b) Iron intensity from marine core GeoB 3313-1 in Southern Chile (Lamy et al., 2001); (c) Ice volume corrected *Globorotalia inflata* $\delta^{18}O$ ($\delta^{18}O_{ivc}$) from marine sediment GeoB13862-1 in Western South Atlantic (Voigt et al., 2015). Black line represents for the 5-point smoothing; (d) AMS mineral dust deposition from this study; (e) Magnetic susceptibility from a peat core in Nightingale Island, Southern Atlantic (Lindvall et al., 2011); (f) Shift in the position of SWW described in Marx et al., (2011); (g) Precipitation reconstruction from Lake Aculeo in Central Chile (Jenny et al., 2003); (h) $\delta^{15}N$-derived humidity from the hyrax middens Seweweekspoort-1-5 in South Africa (Chase et al., 2013). The blue and white shading are the zones determined by change point analysis for AMS dust flux. Crosses indicate ^{14}C dates.

4.3 Climatic and anthropogenic influences in the last 100 years

The last 100 years (1910 - 2014 AD) display distinct REE and εNd signatures compared to the rest of the core (Fig. 5; Fig. S9). This is accompanied by a quantitative increase in dust deposition from Southern Africa (Fig. 7). The overall dust flux, however, is not significantly different during the last 100 years compared to the 1.4 cal. kyr BP to present and 4.9 - 3.9 cal. kyr BP periods, both characterized by relatively high dust flux and poleward position of the SWW. We therefore suggest that other factors than the position of the SWW play a role in the recent shift in dust provenance from Southern Africa. There is evidence of recent anthropogenic disturbances in the Southern part of the African continent. For example, there is a major shift from grass-dominated to sedge-dominated vegetation in the Okavango Delta (Northern Botswana) due to grazing and fires (Nash et al., 2006). Remote sensing also clearly shows the effects of land clearing, agriculture, and land degradation around Etosha Pan in Namibia (Strain and Engle, 1996). Land degradation in recent years is also found in South Africa (Hoffman and Todd, 2000). These changes to the local landscape enhance soil availability and erosion, thereby promoting a relative increase of distal dust availability and subsequent inputs aligned along the prevailing winds to AMS. Enhanced South African dust input to AMS during the past 100 years may alternatively be caused by an overall drying trend over the South African continent as a response to human-climate interaction IPCC, 2007). A general trend towards greater aridity and widespread drought in Southern Africa has indeed been recorded since the 19th century (e.g., Kelso and Vogel, 2007; Nicholson, 2001; Nicholson et al., 2012; Riedel et al., 2012), supporting our findings.

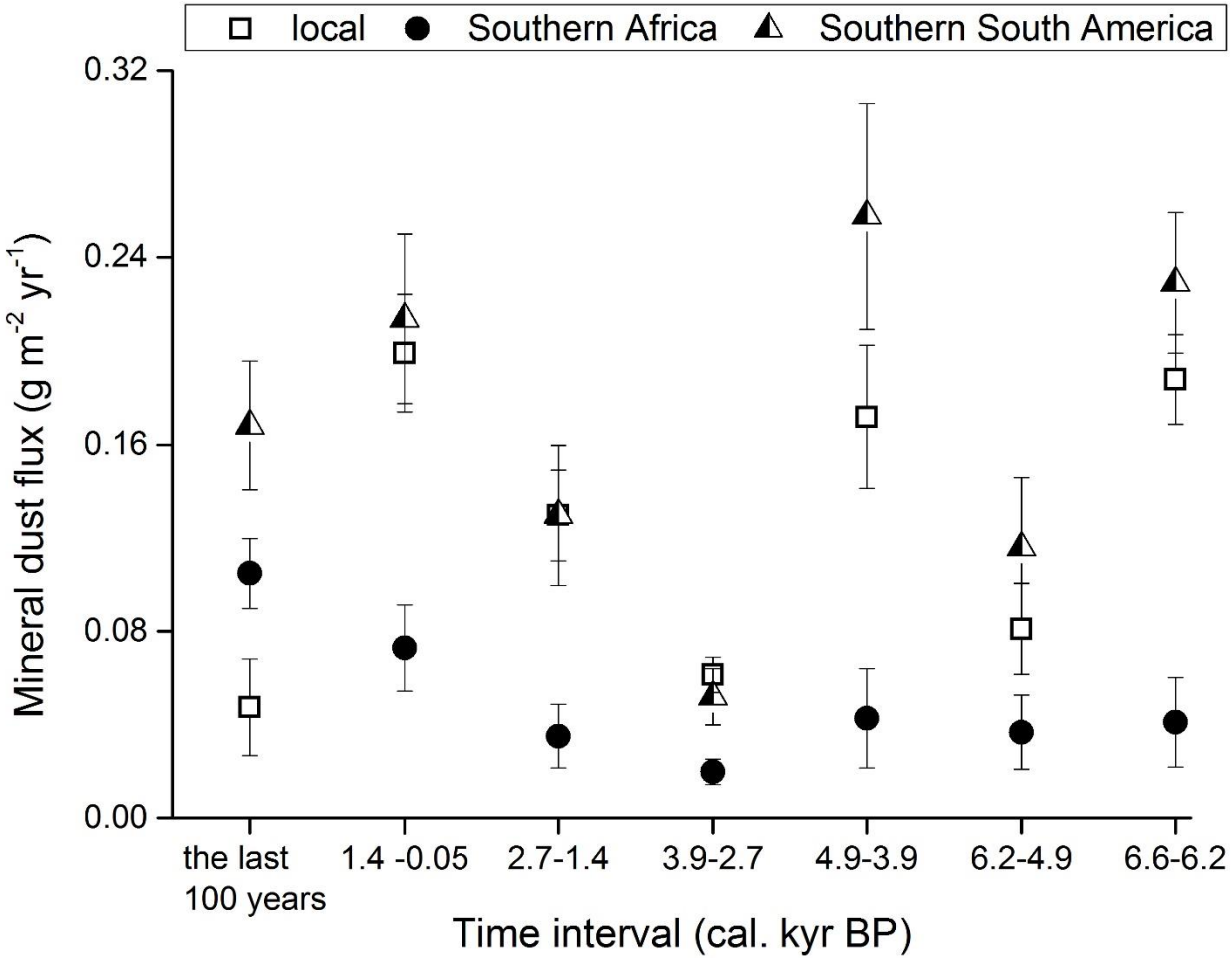

Fig. 7. The mineral dust contributions of local, Southern Africa and Southern South America (g m^{-2} yr^{-1}, 1σ) during different time intervals.

5. Conclusions

Understanding Holocene dust cycling and climate change in the Southern Hemisphere is hampered by a paucity of high-resolution records in some sectors. We provide the first Holocene mineral dust record from an Amsterdam Island peat core in the Southern Indian Ocean. Southern South America and Southern Africa have been found to be the main distal dust sources to AMS. Since 6.6 cal. kyr BP ago, except for the last 100 years, the dust inputs from local, Southern South America and Southern Africa remained relatively constant, with the former two as the main dust contributors. We interpret millennial scale shifts in dust deposition rates to be caused by shifts in the SWW at AMS. A comparison of inferred SWW dynamics at AMS to other Southern Hemisphere SWW proxy records at the northern edge of the wind belts shows both similarities and differences, which suggests SWW were not zonally homogeneous from mid to late Holocene (Lamy et al., 2019). In the last 100 years, the dust

contribution from Southern Africa doubles, possibly as a result of higher dust availability due to a drier climate, and over-grazing, agriculture and land degradation by human influences. We suggest that anthropogenic activities play an important role in the SH dust cycle during last 100 years.

Acknowledgements:

Many thanks for the support of the Mission 66 of Amsterdam Island, without which the field trip could not be possible. We are grateful to Svante Björck, Bart Klink and Elisabeth Michel for the peat sample coring. A very special thanks to Alain Quivoron and Hubert Launay for their continuous directive and logistical support during and after fieldwork on Amsterdam Island. Combined fieldwork was funded by the French Polar Institute (IPEV, Brest, France) through the IPEV Programmes 1066 "PARAD" (to F. De Vleeschouwer) and 1065 PALATIO (to N. Van der Putten and E. Michel). We are grateful to Nina Marchand (IPEV) for the logistical support, Cédric Marteau for making the sampling possible in the protected areas of the TAAF Nature Reserve, and Olivier Magand and Isabelle Jouvie for collecting the local soil samples. We thank the members of the Dust Observations for Models (DO4) team for access to field samples from southern Africa. We are grateful to Dominic Hodgson for his very helpful discussions and comments on the draft. We thanks to Jan-Berend Stuut for the Australian samples (shown in supplementary information) and his comments on the draft. We are grateful to Marie-José Tavella, David Baqué, Camille Duquenoy, Aurélie Marquet, and Stéphanie Mounic for their help with sample analysis. The additional radiocarbon ages were obtained as part of the Idex Peat3 project of the University of Toulouse and through the national service support: Artemis-INSU-CNRS (to G. Le Roux). Chuxian Li's PhD is supported by a scholarship from the Chinese Scholarship Council.

References:

Abdi, H. and Williams, L.J. (2010) Principal component analysis. Wiley interdisciplinary reviews: computational statistics 2(4), 433-459.Albarède, F., 1996. Introduction to geochemical modeling, 1. paperback ed. (with corr.). ed. Cambridge Univ. Press, Cambridge, pp1-34.

Angot, H., Barret, M., Magand, O., Ramonet, M., Dommergue, A., 2014. A 2-year record of atmospheric mercury species at a background Southern Hemisphere station on Amsterdam Island. Atmos. Chem. Phys. 14, 11461–11473. https://doi.org/10.5194/acp-14-11461-2014

Appleby, P. G. "Chronostratigraphic techniques in recent sediments. In 'Tracking environmental change using lake sediments. Volume 1: basin analysis, coring, and chronological techniques'.(Eds WM Last, JP Smol) pp. 171–203." (2001).

Arz, H.W., Lamy, F., Pätzold, J., 2006. A Pronounced Dry Event Recorded Around 4.2 ka in Brine Sediments from the Northern Red Sea. Quat. res. 66, 432–441. https://doi.org/10.1016/j.yqres.2006.05.006

Belokopytov, I. and Beresnevich, V. (1955) Giktorf's peat borers. Torfyanaya Promyshlennost 8, 9-10.

Betzer, P.R., Carder, K.L., Duce, R.A., Merrill, J.T., Tindale, N.W., Uematsu, M., Costello, D.K., Young, R.W., Feely, R.A., Breland, J.A., Bernstein, R.E., Greco, A.M., 1988. Long–range transport of giant mineral aerosol particles. Nature 336, 568–571. https://doi.org/10.1038/336568a0

Blaauw, M., Christen, J.A., 2011. Flexible paleoclimate age-depth models using an autoregressive gamma process. Bayesian Anal. 6, 457–474. https://doi.org/10.1214/11-BA618

Bryant, R.G., Bigg, G.R., Mahowald, N.M., Eckardt, F.D., Ross, S.G., 2007. Dust emission response to climate in southern Africa. J. Geophys. Res. 112, D09207. https://doi.org/10.1029/2005JD007025

Castino, F., Bookhagen, B., Strecker, M.R., 2016. River-discharge dynamics in the Southern Central Andes and the 1976-77 global climate shift: Discharge Dynamics in the Central Andes. Geophys. Res. Lett. 43, 11,679-11,687. https://doi.org/10.1002/2016GL070868

Chase, B.M., Boom, A., Carr, A.S., Meadows, M.E., Reimer, P.J., 2013. Holocene climate change in southernmost South Africa: rock hyrax middens record shifts in the southern westerlies. Quaternary Science Reviews 82, 199–205. https://doi.org/10.1016/j.quascirev.2013.10.018

Chase, B.M., Chevalier, M., Boom, A., Carr, A.S., 2017. The dynamic relationship between temperate and tropical circulation systems across South Africa since the last glacial maximum. Quaternary Science Reviews 174, 54–62. https://doi.org/10.1016/j.quascirev.2017.08.011

Chevalier, M., Chase, B.M., 2015. Southeast African records reveal a coherent shift from high- to low-latitude forcing mechanisms along the east African margin across last glacial–interglacial transition. Quaternary Science Reviews 125, 117–130. https://doi.org/10.1016/j.quascirev.2015.07.009

Cohen, A.L., Tyson, P.D., 1995. Sea-surface temperature fluctuations during the Holocene off the south coast of Africa: implications for terrestrial climate and rainfall. The Holocene 5, 304–312. https://doi.org/10.1177/095968369500500305

Cordova, C.E., Scott, L., Chase, B.M., Chevalier, M., 2017. Late Pleistocene-Holocene vegetation and climate change in the Middle Kalahari, Lake Ngami, Botswana. Quaternary Science Reviews 171, 199–215. https://doi.org/10.1016/j.quascirev.2017.06.036

Cullen, H. M., deMenocal, P. B., Hemming, S., Hemming, G., Brown, F. H., Guilderson, T., & Sirocko, F. (2000). Climate change and the collapse of the Akkadian empire: Evidence from the deep sea. Geology, 28(4), 379-382.

Damman, A.W.H., 1978. Distribution and Movement of Elements in Ombrotrophic Peat Bogs. Oikos 30, 480. https://doi.org/10.2307/3543344

De Deckker, P., Moros, M., Perner, K., Jansen, E., 2012. Influence of the tropics and southern westerlies on glacial interhemispheric asymmetry. Nature Geosci 5, 266–269. https://doi.org/10.1038/ngeo1431

De Vleeschouwer, F., Chambers, F.M. and Swindles, G.T. (2010) Coring and sub-sampling of peatlands for palaeoenvironmental research. Mires and Peat 7.

De Vleeschouwer, F., Vanneste, H., Mauquoy, D., Piotrowska, N., Torrejón, F., Roland, T., Stein, A., Le Roux, G., 2014. Emissions from Pre-Hispanic Metallurgy in the South American Atmosphere. PLoS ONE 9, e111315. https://doi.org/10.1371/journal.pone.0111315

Delqué-Količ, E., Caffy, I., Comby-Zerbino, C., Dumoulin, J.P., Hain, S., Massault, M., Moreau, C., Quiles, A., Setti, V., Souprayen, C., Tannau, J.F., Thellier, B., Vincent, J., 2013. Advances in Handling Small Radiocarbon Samples at the Laboratoire de Mesure du Carbone 14 in Saclay, France. Radiocarbon 55, 648–656. https://doi.org/10.1017/S0033822200057805

Denton, G.H., Anderson, R.F., Toggweiler, J.R., Edwards, R.L., Schaefer, J.M., Putnam, A.E., 2010. The Last Glacial Termination. Science 328, 1652–1656. https://doi.org/10.1126/science.1184119

Doucet, S., Giret, A., Weis, D. and Scoates, J., 2003. Géologie des îles Amsterdam et Saint Paul. GEOLOGUES-PARIS-, pp.10-14.

Engelstaedter, S., Washington, R., 2007. Temporal controls on global dust emissions: The role of surface gustiness: TEMPORAL CONTROLS. Geophys. Res. Lett. 34. https://doi.org/10.1029/2007GL029971

Fitchett, J.M., Mackay, A.W., Grab, S.W., Bamford, M.K., 2017. Holocene climatic variability indicated by a multi-proxy record from southern Africa's highest wetland. The Holocene 27, 638–650. https://doi.org/10.1177/0959683616670467

Flatberg, I., Whinam, J., Lebouvier, M., 2011. Three species of Sphagnum endemic to Île Amsterdam, Terres Australes et Antarctiques Françaises: S. cavernulosum sp. nov ., S. complanatum sp. nov . and S. islei. Journal of Bryology 33, 105–121. https://doi.org/10.1179/1743282010Y.0000000019

Fletcher, M.-S., Moreno, P.I., 2012. Have the Southern Westerlies changed in a zonally symmetric manner over the last 14,000 years? A hemisphere-wide take on a controversial problem. Quaternary International 253, 32–46. https://doi.org/10.1016/j.quaint.2011.04.042

Frenot, Y. and Valleix, T. (1990) Carte des sols de l'Ile Amsterdam (Terres Australes et Antarctiques Françaises), Université, Station Biologique de Paimpont.

Frölicher, T.L., Sarmiento, J.L., Paynter, D.J., Dunne, J.P., Krasting, J.P., Winton, M., 2015. Dominance of the Southern Ocean in Anthropogenic Carbon and Heat Uptake in CMIP5 Models. J. Climate 28, 862–886. https://doi.org/10.1175/JCLI-D-14-00117.1

Frugone-Álvarez, M., Latorre, C., Giralt, S., Polanco-Martínez, J., Bernárdez, P., Oliva-Urcia, B., Maldonado, A., Carrevedo, M.L., Moreno, A., Delgado Huertas, A., Prego, R., Barreiro-Lostres, F., Valero-Garcés, B., 2017. A 7000-year high-resolution lake sediment record from coastal central Chile (Lago Vichuquén, 34°S): implications for past sea level and environmental variability: HIGH-RESOLUTION LAKE SEDIMENT RECORD FROM CENTRAL CHILE. J. Quaternary Sci. 32, 830–844. https://doi.org/10.1002/jqs.2936

Gaiero, D.M., 2007. Dust provenance in Antarctic ice during glacial periods: From where in southern South America? Geophys. Res. Lett. 34, L17707. https://doi.org/10.1029/2007GL030520

Gaiero, D.M., Simonella, L., Gassó, S., Gili, S., Stein, A.F., Sosa, P., Becchio, R., Arce, J., Marelli, H., 2013. Ground/satellite observations and atmospheric modeling of dust storms originating in the high Puna-Altiplano deserts (South America): Implications for the interpretation of paleo-climatic archives: DUST STORMS FROM PUNA-ALTIPLANO DESERTS. J. Geophys. Res. Atmos. 118, 3817–3831. https://doi.org/10.1002/jgrd.50036

Gaudichet, A., Lefèvre, R., Gaudry, A., Ardouin, B., Lambert, G., Miller, J.M., 1989. Mineralogical composition of aerosols at Amsterdam Island. Tellus B 41B, 344–352. https://doi.org/10.1111/j.1600-0889.1989.tb00313.x

Gili, S., Gaiero, D.M., Goldstein, S.L., Chemale, F., Jweda, J., Kaplan, M.R., Becchio, R.A., Koester, E., 2017. Glacial/interglacial changes of Southern Hemisphere wind circulation from the geochemistry of South American dust. Earth and Planetary Science Letters 469, 98–109. https://doi.org/10.1016/j.epsl.2017.04.007

Gillett, N.P., Thompson, D.W., 2003. Simulation of recent Southern Hemisphere climate change. Science 302 (5643), 273e275. https://doi.org/10.1126/science.1087440.

Givelet, N., Le Roux, G., Cheburkin, A., Chen, B., Frank, J., Goodsite, M.E., Kempter, H., Krachler, M., Noernberg, T., Rausch, N., Rheinberger, S., Roos-Barraclough, F., Sapkota, A., Scholz, C., Shotyk, W., 2004. Suggested protocol for collecting, handling and preparing peat cores and peat samples for physical, chemical, mineralogical and isotopic analyses. J. Environ. Monit. 6, 481–492. https://doi.org/10.1039/B401601G

Goodsite, M.E., Rom, W., Heinemeier, J., Lange, T., Ooi, S., Appleby, P.G., Shotyk, W., van der Knaap, W.O., Lohse, C., Hansen, T.S., 2001. High-Resolution AMS 14 C Dating of Post-Bomb Peat Archives of Atmospheric Pollutants. Radiocarbon 43, 495–515. https://doi.org/10.1017/S0033822200041163

Hande, L.B., Siems, S.T., Manton, M.J., 2012. Observed Trends in Wind Speed over the Southern Ocean: SOUTHERN OCEAN WIND TRENDS. Geophys. Res. Lett. 39, n/a-n/a. https://doi.org/10.1029/2012GL051734

Hodgson, D.A., Sime, L.C., 2010. Southern westerlies and CO2. Nature Geosci 3, 666–667. https://doi.org/10.1038/ngeo970

Hoffman, M.T., Todd, T., 2000. A national review of land degradation in South Africa: the influence of biophysical and socio-economic factors. J. South. Afr. Stud. 26 (4), 743e758.

Hogg, A.G., Hua, Q., Blackwell, P.G., Niu, M., Buck, C.E., Guilderson, T.P., Heaton, T.J., Palmer, J.G., Reimer, P.J., Reimer, R.W., Turney, C.S.M., Zimmerman, S.R.H., 2013. SHCal13 Southern Hemisphere Calibration, 0–50,000 Years cal BP. Radiocarbon 55, 1889–1903. https://doi.org/10.2458/azu_js_rc.55.16783

Hua, Q., 2009. Radiocarbon: A chronological tool for the recent past. Quaternary Geochronology 4, 378–390. https://doi.org/10.1016/j.quageo.2009.03.006

Hua, Q., Barbetti, M., Rakowski, A.Z., 2013. Atmospheric radiocarbon for the period 1950e2010. Radiocarbon 55 (4), 2059e2072. https://doi.org/10.2458/azu_js_rc.v55i2.16177.

Humphries, M.S., Benitez-Nelson, C.R., Bizimis, M., Finch, J.M., 2017. An aeolian sediment reconstruction of regional wind intensity and links to larger scale climate variability since the last deglaciation from the east coast of southern Africa. Global and Planetary Change 156, 59–67. https://doi.org/10.1016/j.gloplacha.2017.08.002

Jacobsen, S.B., Wasserburg, G.J., 1980. Sm-Nd isotopic evolution of chondrites. Earth and Planetary Science Letters 50, 139–155. https://doi.org/10.1016/0012-821X(80)90125-9

Jenny, B., Wilhelm, D., Valero-Garcés, B., 2003. The Southern Westerlies in Central Chile: Holocene precipitation estimates based on a water balance model for Laguna Aculeo (33°50′S). Climate Dynamics 20, 269–280. https://doi.org/10.1007/s00382-002-0267-3

Johnson, M.S., Meskhidze, N., Kiliyanpilakkil, V.P., Gassó, S., 2011. Understanding the transport of Patagonian dust and its influence on marine biological activity in the South Atlantic Ocean. Atmos. Chem. Phys. 11, 2487–2502. https://doi.org/10.5194/acp-11-2487-2011

Kelso, C., Vogel, C., 2007. The climate of Namaqualand in the nineteenth century. Climatic Change 83, 357–380. https://doi.org/10.1007/s10584-007-9264-1

Kienast, S.S., Winckler, G., Lippold, J., Albani, S., Mahowald, N.M., 2016. Tracing dust input to the global ocean using thorium isotopes in marine sediments: ThoroMap: ThoroMap. Global Biogeochem. Cycles 30, 1526–1541. https://doi.org/10.1002/2016GB005408

Killick, R., Eckley, I.A., Ewans, K., Jonathan, P., 2010. Detection of changes in variance of oceanographic time-series using changepoint analysis. Ocean Engineering 37, 1120–1126. https://doi.org/10.1016/j.oceaneng.2010.04.009

Kohfeld, K.E., Graham, R.M., de Boer, A.M., Sime, L.C., Wolff, E.W., Le Quéré, C., Bopp, L., 2013. Southern Hemisphere westerly wind changes during the Last Glacial Maximum: paleo-data synthesis. Quaternary Science Reviews 68, 76–95. https://doi.org/10.1016/j.quascirev.2013.01.017

Kuhnt, W., Holbourn, A., Xu, J., Opdyke, B., De Deckker, P., Röhl, U., Mudelsee, M., 2015. Southern Hemisphere control on Australian monsoon variability during the late deglaciation and Holocene. Nat Commun 6, 5916. https://doi.org/10.1038/ncomms6916

Lamy, F., Chiang, J.C.H., Martínez-Méndez, G., Thierens, M., Arz, H.W., Bosmans, J., Hebbeln, D., Lambert, F., Lembke-Jene, L., Stuut, J.-B., 2019. Precession modulation of the South Pacific westerly wind belt over the past million years. Proc Natl Acad Sci USA 116, 23455–23460. https://doi.org/10.1073/pnas.1905847116

Lamy, F., Hebbeln, D., Röhl, U., Wefer, G., 2001. Holocene rainfall variability in southern Chile: a marine record of latitudinal shifts of the Southern Westerlies. Earth and Planetary Science Letters 185, 369–382. https://doi.org/10.1016/S0012-821X(00)00381-2

Lamy, F., Kilian, R., Arz, H.W., Francois, J.-P., Kaiser, J., Prange, M., Steinke, T., 2010. Holocene changes in the position and intensity of the southern westerly wind belt. Nature Geosci 3, 695–699. https://doi.org/10.1038/ngeo959

Lamy, F., Chiang, J.C.H., Martínez-M_endez, G., Thierens, M., Arz, H.W., Bosmans, J., Hebbeln, D., Lambert, F., Lembke-Jene, L., Stuut, J.-B., 2019. Precession modulation of the South Pacific westerly wind belt over the past million years. Proc. Natl. Acad. Sci. U.S.A. 116, 23455e23460. https://doi.org/10.1073/pnas.1905847116.

Landschützer, P., Gruber, N., Haumann, F.A., Rödenbeck, C., Bakker, D.C.E., van Heuven, S., Hoppema, M., Metzl, N., Sweeney, C., Takahashi, T., Tilbrook, B., Wanninkhof, R., 2015. The reinvigoration of the Southern Ocean carbon sink. Science 349, 1221–1224. https://doi.org/10.1126/science.aab2620

Lebouvier, M. and Frenot, Y., 2007. and Île Saint-Paul temperate. All have endemic species amongst their biota. The Terres Australes et Antarctiques Françaises (TAAF) is. In Papers and Proceedings of the Royal Society of Tasmania (Vol. 141, No. 1, p. 23). Royal Society of Tasmania.

Li, C., Le Roux, G., Sonke, J., van Beek, P., Souhaut, M., Van der Putten, N., De Vleeschouwer, F., 2017. Recent 210 Pb, 137 Cs and 241 Am accumulation in an ombrotrophic peatland from Amsterdam Island (Southern Indian Ocean). Journal of Environmental Radioactivity 175–176, 164–169. https://doi.org/10.1016/j.jenvrad.2017.05.004

Li, F., Ginoux, P., Ramaswamy, V., 2008. Distribution, transport, and deposition of mineral dust in the Southern Ocean and Antarctica: Contribution of major sources. J. Geophys. Res. 113, D10207. https://doi.org/10.1029/2007JD009190

Lindvall, H., Björck, S., Holmgren, S., Ljung, K., Van der Putten, N., Porter, C., 2011. A Holocene peat record in the central South Atlantic: an archive of precipitation changes. GFF 133, 195–206. https://doi.org/10.1080/11035897.2011.633708

Ljung, K., Björck, S., 2007. Holocene climate and vegetation dynamics on Nightingale Island, South Atlantic—an apparent interglacial bipolar seesaw in action? Quaternary Science Reviews 26, 3150–3166. https://doi.org/10.1016/j.quascirev.2007.08.003

Lovenduski, N.S., Gruber, N., Doney, S.C., 2008. Toward a mechanistic understanding of the decadal trends in the Southern Ocean carbon sink: SOUTHERN OCEAN CO 2 FLUX TRENDS. Global Biogeochem. Cycles 22, n/a-n/a. https://doi.org/10.1029/2007GB003139

Mahowald, N.M., Baker, A.R., Bergametti, G., Brooks, N., Duce, R.A., Jickells, T.D., Kubilay, N., Prospero, J.M., Tegen, I., 2005. Atmospheric global dust cycle and iron inputs to the ocean: ATMOSPHERIC IRON DEPOSITION. Global Biogeochem. Cycles 19, n/a-n/a. https://doi.org/10.1029/2004GB002402

Marshall, G.J., Orr, A., van Lipzig, N.P.M., King, J.C., 2006. The Impact of a Changing Southern Hemisphere Annular Mode on Antarctic Peninsula Summer Temperatures. J. Climate 19, 5388–5404. https://doi.org/10.1175/JCLI3844.1

Marx, S.K., Kamber, B.S., McGowan, H.A., Denholm, J., 2011. Holocene dust deposition rates in Australia's Murray-Darling Basin record the interplay between aridity and the position of the mid-latitude westerlies. Quaternary Science Reviews 30, 3290–3305. https://doi.org/10.1016/j.quascirev.2011.07.015

Marx, S.K., Kamber, B.S., McGowan, H.A., Petherick, L.M., McTainsh, G.H., Stromsoe, N., Hooper, J.N., May, J.-H., 2018. Palaeo-dust records: A window to understanding past environments. Global and Planetary Change 165, 13–43. https://doi.org/10.1016/j.gloplacha.2018.03.001

Marx, S.K., McGowan, H.A., Kamber, B.S., 2009. Long-range dust transport from eastern Australia: A proxy for Holocene aridity and ENSO-type climate variability. Earth and Planetary Science Letters 282, 167–177. https://doi.org/10.1016/j.epsl.2009.03.013

Miller, J.M., Moody, J.L., Harris, J.M., Gaudry, A., 1993. A 10-year trajectory flow climatology for Amsterdam Island, 1980–1989. Atmospheric Environment. Part A. General Topics 27, 1909–1916. https://doi.org/10.1016/0960-1686(93)90296-B

Moody, J.L., Pszenny, A.A.P., Gaudry, A., Keene, W.C., Galloway, J.N., Polian, G., 1991. Precipitation composition and its variability in the southern Indian Ocean: Amsterdam Island, 1980–1987. J. Geophys. Res. 96, 20769. https://doi.org/10.1029/91JD01921

Moreau, C., Caffy, I., Comby, C., Delqué-Količ, E., Dumoulin, J.-P., Hain, S., Quiles, A., Setti, V., Souprayen, C., Thellier, B., Vincent, J., 2013. Research and Development of the

Artemis 14 C AMS Facility: Status Report. Radiocarbon 55, 331–337. https://doi.org/10.1017/S0033822200057441

Moreno, P.I., Francois, J.P., Moy, C.M., Villa-Martínez, R., 2010. Covariability of the Southern Westerlies and atmospheric CO2 during the Holocene. Geology 38, 727–730. https://doi.org/10.1130/G30962.1

Nash, D.J., Meadows, M.E., Gulliver, V.L., 2006. Holocene environmental change in the Okavango Panhandle, northwest Botswana. Quaternary Science Reviews 25, 1302–1322. https://doi.org/10.1016/j.quascirev.2005.11.004

Nicholson, S., 2001. Climatic and environmental change in Africa during the last two centuries. Clim. Res. 17, 123–144. https://doi.org/10.3354/cr017123

Nicholson, S.E., Dezfuli, A.K., Klotter, D., 2012. A Two-Century Precipitation Dataset for the Continent of Africa. Bull. Amer. Meteor. Soc. 93, 1219–1231. https://doi.org/10.1175/BAMS-D-11-00212.1

Orsi, A.H., Whitworth, T., Nowlin, W.D., 1995. On the meridional extent and fronts of the Antarctic Circumpolar Current. Deep Sea Research Part I: Oceanographic Research Papers 42, 641–673. https://doi.org/10.1016/0967-0637(95)00021-W

IPCC, 2007, in Parry, M.L. (Eds.). Climate change 2007 - impacts, adaptation and vulnerability: contribution of Working Group II to the Fourth Assessment Report of the Intergovernmental Panel on Climate Change, 1. publ. ed. Cambridge Univ. Press, Cambridge.

Piketh, S.J., 2002. Chemical evidence of long-range atmospheric transport over southern Africa. J. Geophys. Res. 107, 4817. https://doi.org/10.1029/2002JD002056

Piotrowska, N., 2013. Status report of AMS sample preparation laboratory at GADAM Centre, Gliwice, Poland. Nuclear Instruments and Methods in Physics Research Section B: Beam Interactions with Materials and Atoms 294, 176–181. https://doi.org/10.1016/j.nimb.2012.05.017

Polian, G., Lambert, G., Ardouin, B., Jegou, A., 1986. Long-range transport of continental radon in subantarctic and antarctic areas. Tellus B: Chemical and Physical Meteorology 38, 178–189. https://doi.org/10.3402/tellusb.v38i3-4.15126

Prospero, J.M., Ginoux, P., Torres, O., Nicholson, S.E., Gill, T.E., 2002. Environmental characterization of global sources of atmospheric soil dust identified with the NIMBUS 7 Total Ozone Mapping Spectrometer (TOMS) absorbing aerosol product. Rev. Geophys. 40, 1002. https://doi.org/10.1029/2000RG000095

Pueyo, J.J., Sáez, A., Giralt, S., Valero-Garcés, B.L., Moreno, A., Bao, R., Schwalb, A., Herrera, C., Klosowska, B., Taberner, C., 2011. Carbonate and organic matter sedimentation and isotopic signatures in Lake Chungará, Chilean Altiplano, during the last 12.3kyr. Palaeogeography, Palaeoclimatology, Palaeoecology 307, 339–355. https://doi.org/10.1016/j.palaeo.2011.05.036

R Development Core Team, 2013. R: A Language and Environment for Statistical Computing. R version 3.0.0. R Foundation for Statistical Computing, Vienna, Austria.

Reid, P.C., Hari, R.E., Beaugrand, G., Livingstone, D.M., Marty, C., Straile, D., Barichivich, J., Goberville, E., Adrian, R., Aono, Y., Brown, R., Foster, J., Groisman, P., Hélaouët, P., Hsu, H.-H., Kirby, R., Knight, J., Kraberg, A., Li, J., Lo, T.-T., Myneni, R.B., North, R.P., Pounds, J.A., Sparks, T., Stübi, R., Tian, Y., Wiltshire, K.H., Xiao, D., Zhu, Z., 2016. Global impacts of the 1980s regime shift. Glob Change Biol 22, 682–703. https://doi.org/10.1111/gcb.13106

Revelle, 2019. Procedures for Psychological, Psychometric, and Personality Research. https://personality-project.org/r/psych/

Riedel, F., Erhardt, S., Chauke, C., Kossler, A., Shemang, E., Tarasov, P., 2012. Evidence for a permanent lake in Sua Pan (Kalahari, Botswana) during the early centuries of the last millennium indicated by distribution of Baobab trees (Adansonia digitata) on "Kubu Island." Quaternary International 253, 67–73. https://doi.org/10.1016/j.quaint.2011.02.040

Sabine, C.L. et al., 2004. The Oceanic Sink for Anthropogenic CO2. Science 305, 367–371. https://doi.org/10.1126/science.1097403

Saunders, K.M., Kamenik, C., Hodgson, D.A., Hunziker, S., Siffert, L., Fischer, D., Fujak, M., Gibson, J.A.E., Grosjean, M., 2012. Late Holocene changes in precipitation in northwest Tasmania and their potential links to shifts in the Southern Hemisphere westerly winds. Global and Planetary Change 92–93, 82–91. https://doi.org/10.1016/j.gloplacha.2012.04.005

Saunders, K.M., Roberts, S.J., Perren, B., Butz, C., Sime, L., Davies, S., Van Nieuwenhuyze, W., Grosjean, M., Hodgson, D.A., 2018. Holocene dynamics of the Southern Hemisphere westerly winds and possible links to CO2 outgassing. Nature Geosci 11, 650–655. https://doi.org/10.1038/s41561-018-0186-5

Shotyk, W., 1997. Atmospheric deposition and mass balance of major and trace elements in two oceanic peat bog profiles, northern Scotland and the Shetland Islands. Chemical Geology 138, 55–72. https://doi.org/10.1016/S0009-2541(96)00172-6

Shulmeister, J., 1999. Australasian evidence for mid-holocene climate change implies precessional control of Walker Circulation in the Pacific. Quaternary International 57–58, 81–91. https://doi.org/10.1016/S1040-6182(98)00052-4

Spalding, K.L., Buchholz, B.A., Bergman, L.E., Druid, H., Fris_en, J., 2005. Forensics: age written in teeth by nuclear tests. Nature 437 (7057), 333. https://doi.org/10.1038/437333a.

Staubwasser, M., Sirocko, F., Grootes, P.M., Segl, M., 2003. Climate change at the 4.2 ka BP termination of the Indus valley civilization and Holocene south Asian monsoon variability: SOUTH ASIAN HOLOCENE CLIMATE CHANGE. Geophys. Res. Lett. 30. https://doi.org/10.1029/2002GL016822

Strain, P., and Engle, F. 1996. Looking at Earth. Turner, Atlanta, Ga, pp304.

Swart, N.C., Fyfe, J.C., 2012. Observed and simulated changes in the Southern Hemisphere surface westerly wind-stress. Geophys. Res. Lett. 39 (16) https://doi.org/10.1029/2012GL052810.

Taylor, W. (2000a). Change-Point Analyzer 2.3 shareware program, Taylor Enterprises, Libertyville, Illinois. Retrieved from http://www.variation.com/cpa/

Taylor, W. (2000b). Change-Point Analysis: A Powerful New Tool for Detecting Changes. Retrieved from http://www.variation.com/cpa/tech/changepoint.html

Thompson, D.W.J., Solomon, S., 2002. Interpretation of Recent Southern Hemisphere Climate Change. Science 296, 895–899. https://doi.org/10.1126/science.1069270

Thompson, L.G., Mosley-Thompson, E., Davis, M.E., Henderson, K.A., Brecher, H.H., Zagorodnov, V.S., Mashiotta, T.A., Lin, P.-N., Mikhalenko, V.N., Hardy, D.R., 2002. Kilimanjaro Ice Core Records: Evidence of Holocene Climate Change in Tropical Africa. Science 298, 589–593. https://doi.org/10.1126/science.1073198

Van der Putten, N., Hébrard, J.-P., Verbruggen, C., Van de Vijver, B., Disnar, J.-R., Spassov, S., de Beaulieu, J.-L., De Dapper, M., Keravis, D., Hus, J., Thouveny, N., Frenot, Y., 2008. An integrated palaeoenvironmental investigation of a 6200 year old peat sequence from Ile de la Possession, Iles Crozet, sub-Antarctica. Palaeogeography, Palaeoclimatology, Palaeoecology 270, 179–195. https://doi.org/10.1016/j.palaeo.2008.09.014

Van der Putten, N., Mauquoy, D., Verbruggen, C., Björck, S., 2012. Subantarctic peatlands and their potential as palaeoenvironmental and palaeoclimatic archives. Quaternary International 268, 65–76. https://doi.org/10.1016/j.quaint.2011.07.032

Van der Putten, N., Verbruggen, C., Björck, S., Michel, E., Disnar, J.-R., Chapron, E., Moine, B.N., de Beaulieu, J.-L., 2015. The Last Termination in the South Indian Ocean: A unique terrestrial record from Kerguelen Islands (49°S) situated within the Southern Hemisphere

westerly belt. Quaternary Science Reviews 122, 142–157. https://doi.org/10.1016/j.quascirev.2015.05.010

Vanneste, H., De Vleeschouwer, F., Bertrand, S., Martínez-Cortizas, A., Vanderstraeten, A., Mattielli, N., Coronato, A., Piotrowska, N., Jeandel, C., Roux, G.L., 2016. Elevated dust deposition in Tierra del Fuego (Chile) resulting from Neoglacial Darwin Cordillera glacier fluctuations: NEOGLACIAL ELEVATED DUST DEPOSITION IN TIERRA DEL FUEGO. J. Quaternary Sci. 31, 713–722. https://doi.org/10.1002/jqs.2896

Vanneste, H., De Vleeschouwer, F., Martínez-Cortizas, A., von Scheffer, C., Piotrowska, N., Coronato, A., Le Roux, G., 2015. Late-glacial elevated dust deposition linked to westerly wind shifts in southern South America. Sci Rep 5, 11670. https://doi.org/10.1038/srep11670

Varma, V., Prange, M., Lamy, F., Merkel, U., Schulz, M., 2011. Solar-forced shifts of the Southern Hemisphere Westerlies during the Holocene. Clim. Past 7, 339–347. https://doi.org/10.5194/cp-7-339-2011

Varma, V., Prange, M., Merkel, U., Kleinen, T., Lohmann, G., Pfeiffer, M., Renssen, H., Wagner, A., Wagner, S., Schulz, M., 2012. Holocene evolution of the Southern Hemisphere westerly winds in transient simulations with global climate models. Clim. Past 8, 391–402. https://doi.org/10.5194/cp-8-391-2012

Vickery, K.J., Eckardt, F.D., Bryant, R.G., 2013. A sub-basin scale dust plume source frequency inventory for southern Africa, 2005–2008. Geophys. Res. Lett. 40, 5274–5279. https://doi.org/10.1002/grl.50968

Voigt, I., Chiessi, C.M., Prange, M., Mulitza, S., Groeneveld, J., Varma, V., Henrich, R., 2015. Holocene shifts of the southern westerlies across the South Atlantic: Holocene shifts of Southern Westerlies. Paleoceanography 30, 39–51. https://doi.org/10.1002/2014PA002677

Von Holdt, J.R., Eckardt, F.D., Wiggs, G.F.S., 2017. Landsat identifies aeolian dust emission dynamics at the landform scale. Remote Sensing of Environment 198, 229–243. https://doi.org/10.1016/j.rse.2017.06.010

Wedepohl, K.H. (1995) The composition of the continental crust. Geochimica et Cosmochimica Acta 59(7), 1217-1232.

Weiss, H., 2016. Global megadrought, societal collapse and resilience at 4.2-3.9 ka BP across the Mediterranean and west Asia. PAGES Mag 24, 62–63. https://doi.org/10.22498/pages.24.2.62

Zickfeld, K., Fyfe, J.C., Saenko, O.A., Eby, M., Weaver, A.J., 2007. Response of the global carbon cycle to human-induced changes in Southern Hemisphere winds. Geophys. Res. Lett. 34, L12712. https://doi.org/10.1029/2006GL028797

Supporting information

Fig. S1. Peat coring site at the center of the caldera peatland at Amsterdam Island. Yellow cross represents for the peat coring site.

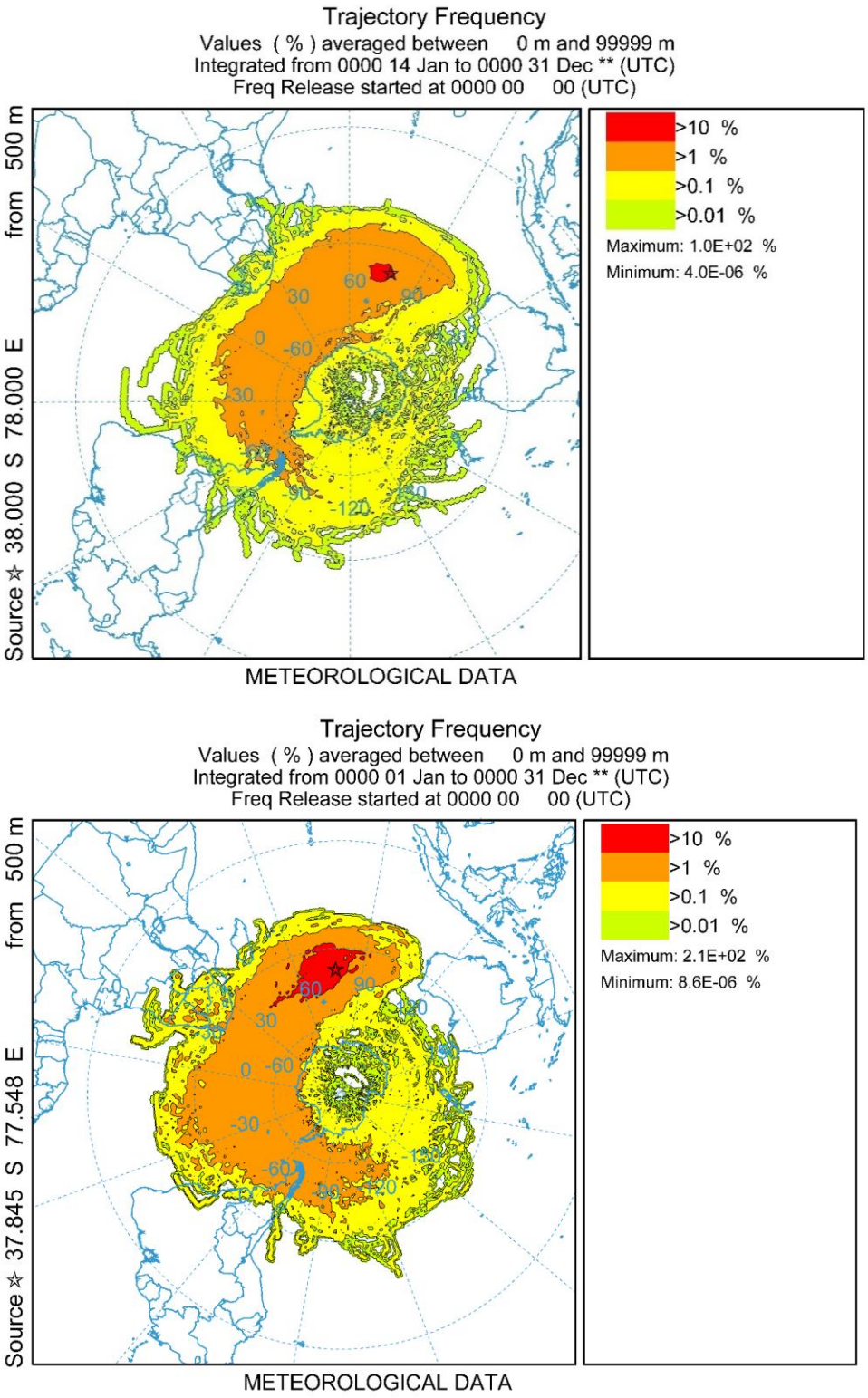

Fig. S2. 14-day back trajectories ensemble for the whole year of 1968 (a) and 1982 (b) illustrate that a significant number of air masses travelled from Southern South America and Southern Africa to Amsterdam Island (black open star).

Text S1. Back trajectory calculation

Fourteen-day back trajectories in one-whole year (e.g., 1968 and 1982, Fig. S5), were run by the Hybrid Single Particle Lagrangian Integrated Trajectory (HYSPLIT) model (Stein et al., 2015). The meteorological data are accessed via NOAA Air Resource Laboratory (ftp://arlftp.arlhq.noaa.gov/archives/reanalysis/). The back trajectories ended at the sampling site at a height of 500 m above ground level to represent the air masses within the planetary boundary layer reaching the sampling site (De Vleeschouwer et al., 2014). The calculation for the duration of each trajectory is set to 14 days with a temporal resolution of 6h (analyses at 00:00, 06:00, 12:00, 18:00 UTC). It leads to over 1400 trajectories being computed for one year. The model then counts the number of trajectories that fall within each grid cell (set 1.0 degree) covering the Southern Hemisphere. Finally, trajectory frequency (F) is calculated for the sum of the number of trajectories (T) that passed through each grid cell (i, j):

$$F_{i,j} = 100 \sum \frac{T_{i,j,k}}{k}$$

k: the total number of trajectories. All the trajectories are counted if they occur in the source location grid cell.

Text S2. Continental sample collection and preparation

Three Etosha Pan atmospheric dust samples were collected downwind of the Pan at a height of 1.6 m by a BSNE horizontal flux sampler for 14-30 days. Similar dust sampling methods were applied to the dust sample collection at Sua Pan, except for one, which was collected at a height of 0.25 m. Three soil samples from Sua Pan and three from Etosha Pan were collected from loose sediments. Geochemical and isotopic results from Southern South American samples are taken from Gili et al., (2017).

Text S3. Analytical performance of the major and trace elements

The measured blanks were negligible (<0.2%) for all the elements investigated in the different matrices. Recoveries of Al and K by ICP-OES for all the Certified Reference Materials (CRMs) were within 80-120% of certified/information values, except Ti which was 78% for NJV942 and NJV941. The median recoveries of Ga, Hf, Zr, Th, Cs, Rb, Pb, Mg and Ca measured in all the CRMs by ICP-MS were all within 85% of the certified/information/provisional values with the exception of Th (68%) and U (123%) in SRM 1515, and Pb (79%) in NJV941. Good recoveries are reported for REE (> 80%) in all the CRMs, except Eu (123%) in SRM 1515, and Yb (62% and 58% for SRM 1515 and SRM 1547, respectively). The REE value provided for SRM 1515 and SRM 1547 are however only informative (see Table S4 and Table S4bis).

In order to verify the influence of Ba and Gd oxide interferences on Eu and Yb during ICP-MS measurements (i.e., interference of $^{135}Ba^{16}O$ on ^{151}Eu and $^{158}Gd^{16}O$ on ^{174}Yb), Ba and Gd oxides were measured. We found that BaO and GdO represent less than 0.1% and 0.5% of Eu and Yb concentrations in samples respectively, which are negligible. We also compared our Eu and Yb results of SRM1515 and SRM1547 with results from Vanneste et al. (2016), who performed the measurements under similar conditions. The two sets of Eu results are comparable (0.25 ± 0.01 vs 0.26 ± 0.01 µg g^{-1} for SRM1515, 0.19 ± 0.01 vs 0.17 ± 0.01 µg g^{-1} for SRM1947). The Yb results between this study and Vanneste et al. (2016) are also similar (0.19 ± 0.01 vs 0.19 ± 0.02 µg g^{-1} for SRM1515, 0.12 ± 0.004 vs 0.12 ± 0.01 µg g^{-1} for SRM1547).

Fig. S3. Photo of the top 50 cm peat section.

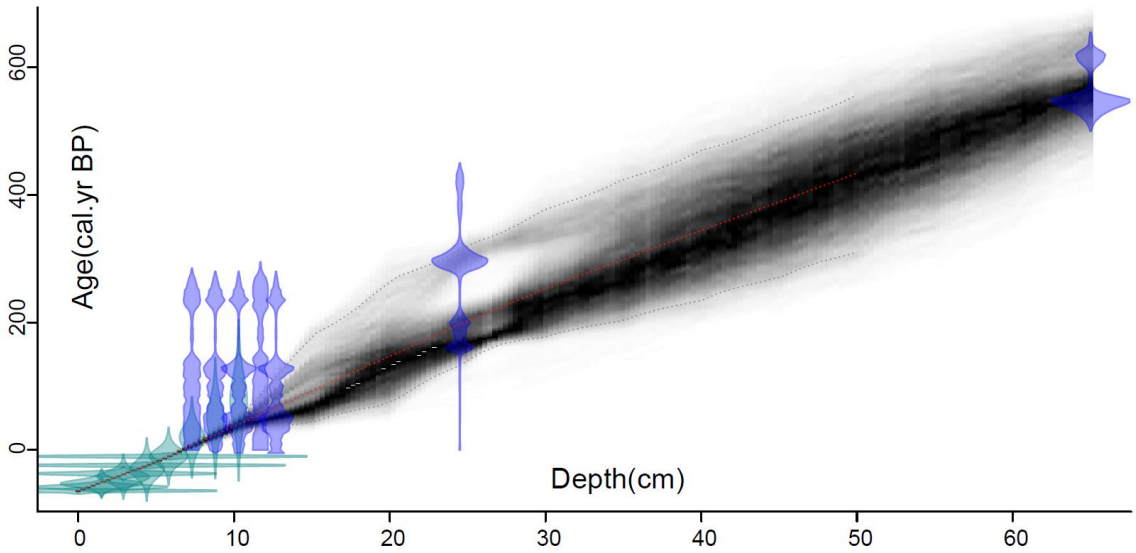

Fig. S4. Age model of top 50 cm depth (^{14}C in blue, ^{210}Pb Constant-Rate-Supply model in green) in the AMS peat core.

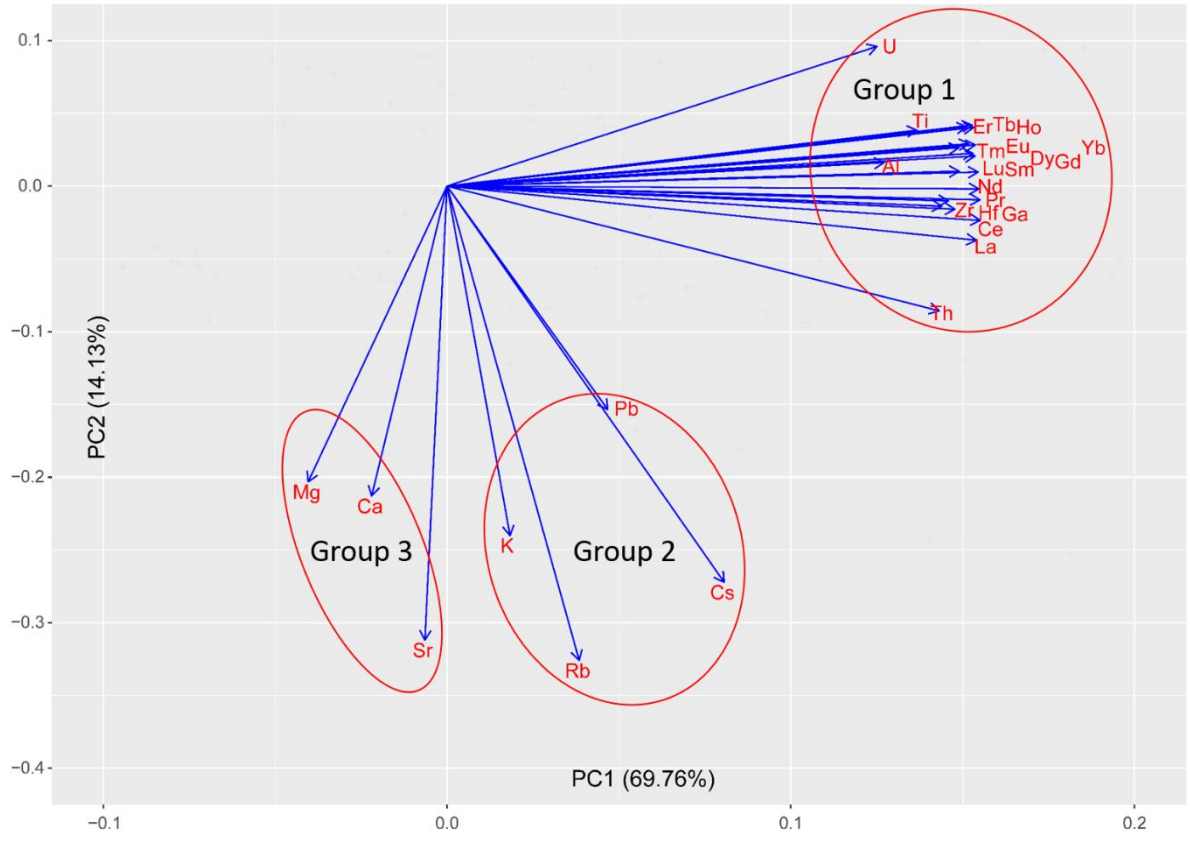

Fig. S5. Biplot of the principal component analysis of the major and trace elements. Percentage of variance of component 1 and 2 are shown on the axis.

Text S4. Trophic status defined in the AMS peat core

The profile of PC3 scores (Fig. 4f) roughly follows the ash profile (R^2=0.82, P<0.001, two-sided *t*-test), with a general decreasing upward trend. The Ca profile (Fig. 4g, Fig. S6), a PC3 representative element, probably illustrates a mobility from upper section and accumulation at the lower part of the core (Shotyk, 1997), and/or a basalt weathering and subsequent Ca diffusion upwards to ~4.2 cal. kyr BP (340 cm depth) (Le Roux and shotyk, 2006), and/or a lateral input from adjacent areas before ~4.2 cal. kyr BP during its minertrophic stage. Minerotrophic conditions are characterized by atmospheric input, surface runoff and underground diffusion. Minerotrophic conditions at the AMS peat coring site possibly prevailed at depths of 500 cm - 340 cm based on its relatively higher signatures in density (Fig. 2a), ash content (Fig. 2b) and PC3 signature (before ~4.2 cal. kyr BP, Fig. 4f, g), compared to the 315 cm - 0 cm section. Only fed by atmospheric inputs, ombrotrophic conditions are distinguished based on its low signatures in density, ash content and PC3 score from 315 - 0 cm (since ~3.7 cal. kyr BP). The 340 cm - 315 cm section corresponds to a transitional stage (from minerotrophic to ombrotrophic).

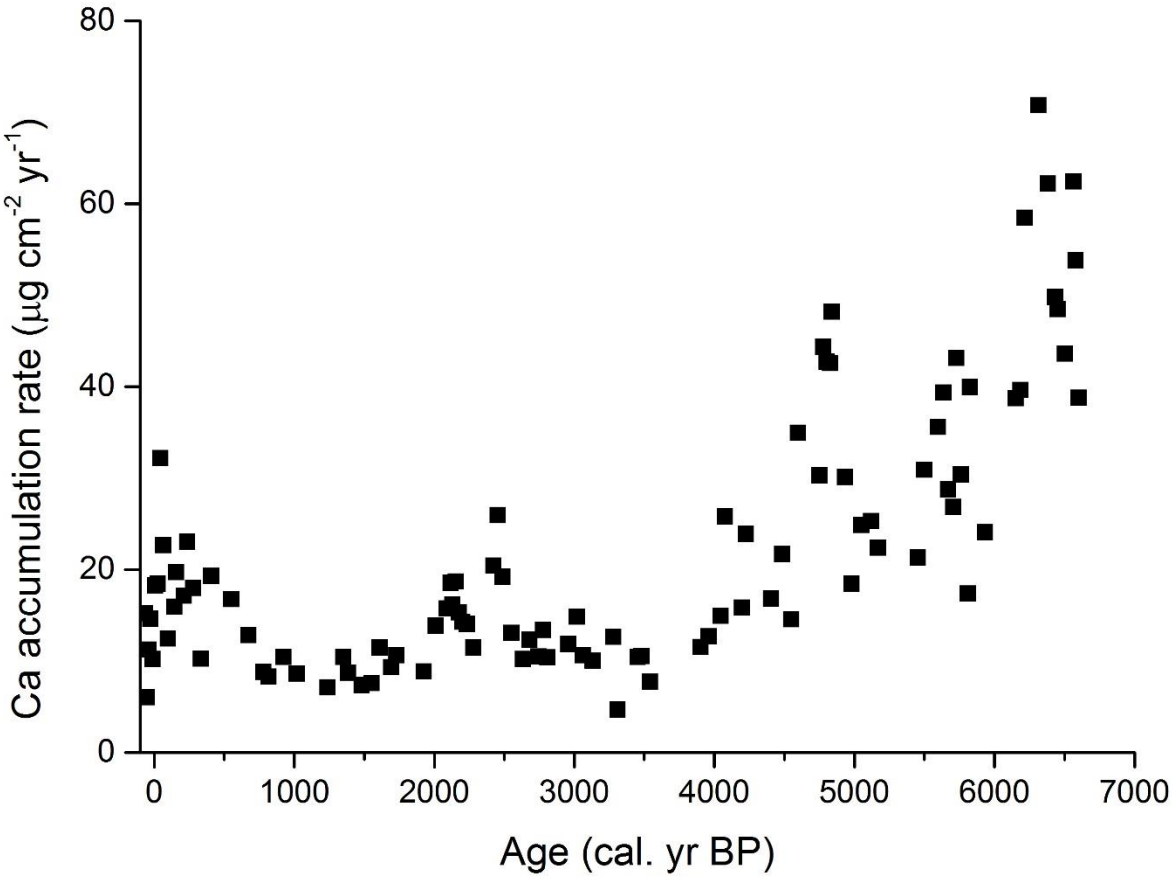

Fig. S6. Profile of Ca accumulation rate (µg cm^{-2} yr^{-1}).

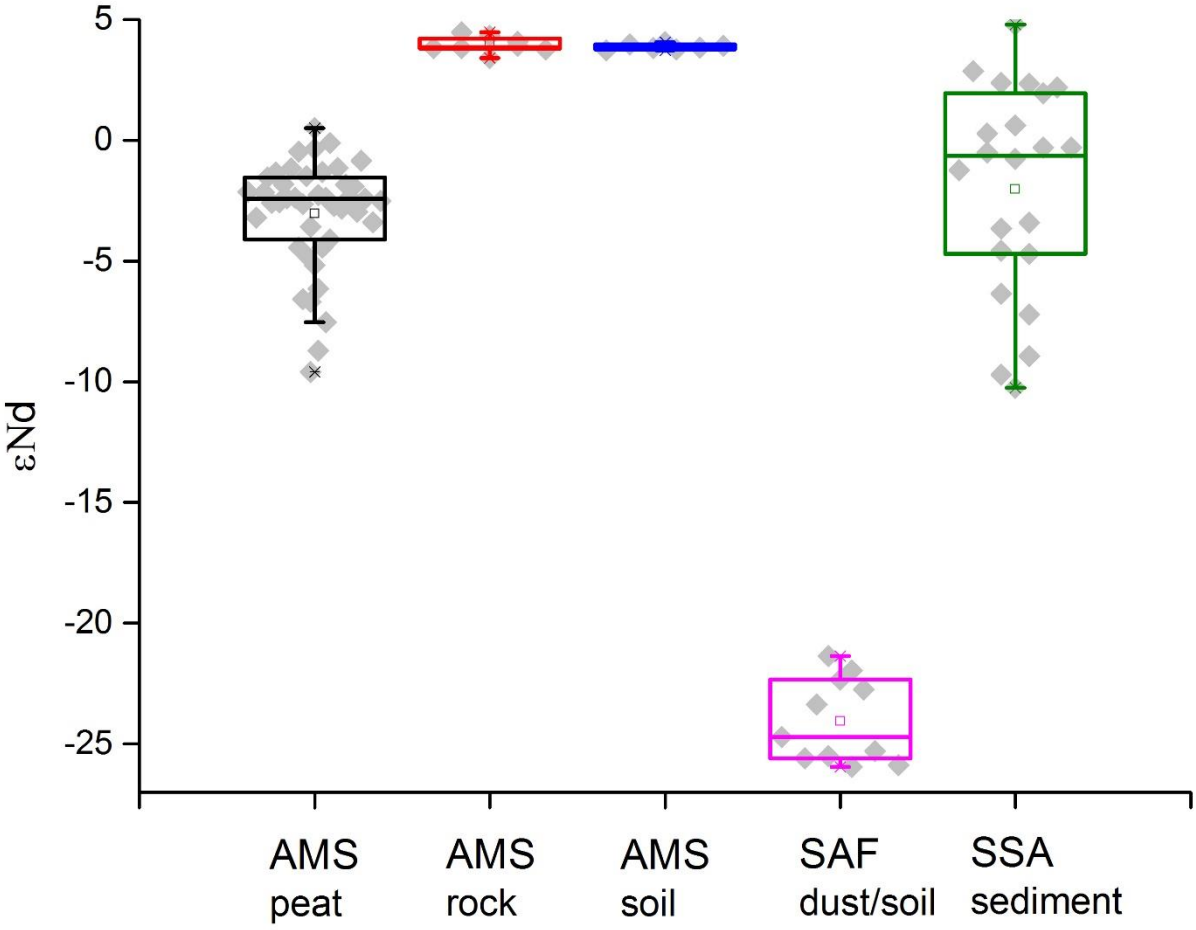

Fig. S7. Nd isotopic signatures between AMS peat and its representing PSAs. AMS soil this study: data from top soil bulk samples; AMS rock Doucet et al., 2004: data from bulk rock; Southern Africa (SAF) this study: data in Sua Pan and Etosha Pan from dust and top soil bulk samples; Southern South America (SSA) Gili et al., 2017: data in Puna-Altiplano-Plateau, Central Western Argentina and Patagonia from sediment samples.

Please note that there is no difference in AMS rock and AMS soil in terms of the Nd isotopic composition (εNd).

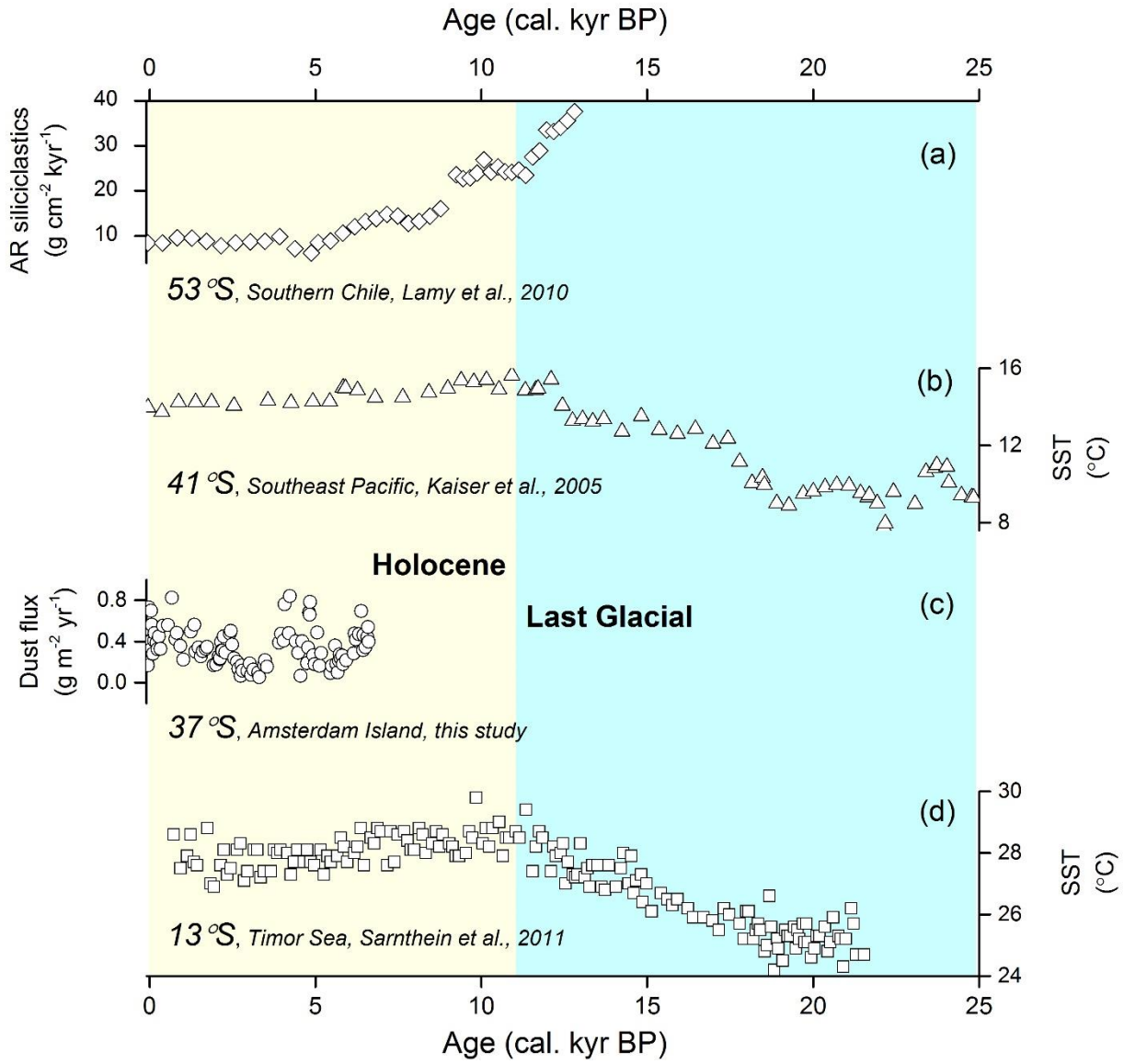

Fig. S8. Proxy records for climate variations since last Glacial period. (a) Accumulation Rate of siliciclastic material (g cm^{-2} kyr^{-1}) at Lake Site TM1 (Lamy et al., 2010); (b) Alkenone-based Sea surface temperature (SST, °C) reconstruction at Marine Site 1233 over the last 25 kyr (Kaiser et al., 2005); (c) Mineral dust deposition (g m^{-2} yr^{-1}) from Amsterdam Island peatland (this study); (d) Sea surface temperature (SST, °C) record at Marine Site MD01-2378 (Sarnthein et al., 2011).

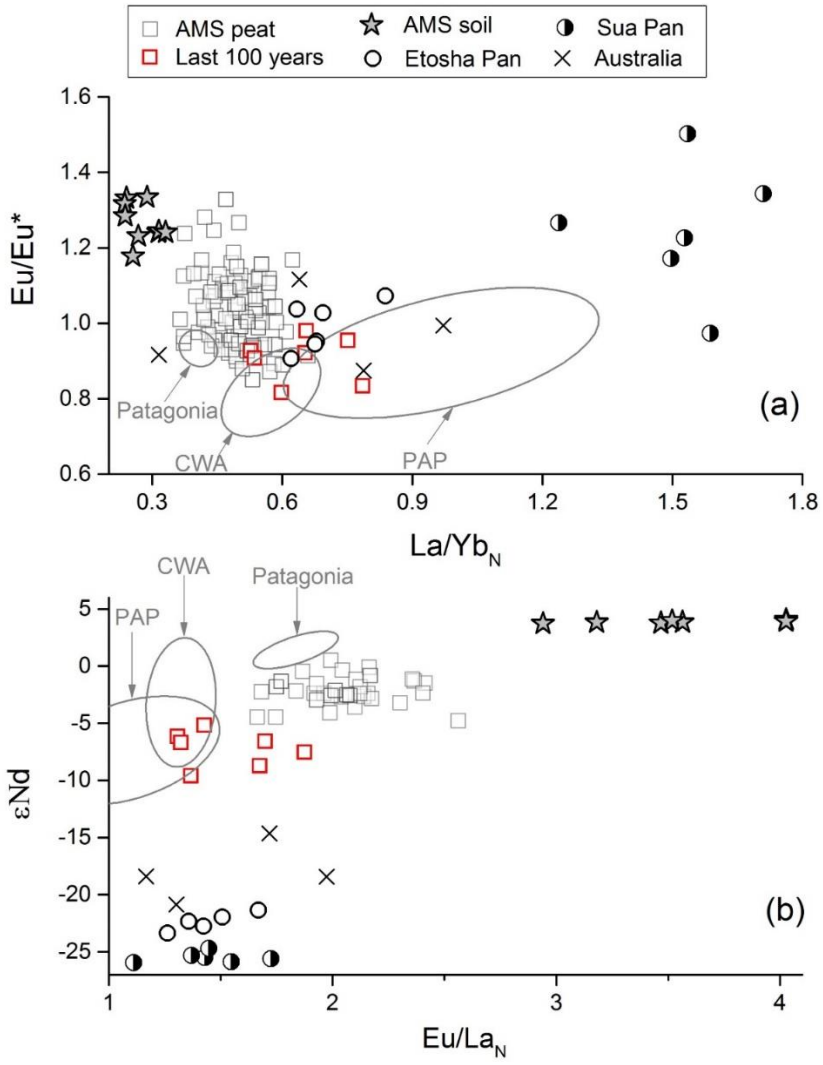

Fig. S9. Relationships of La/Yb$_N$ vs Eu/Eu* (a), and Eu/La$_N$ vs εNd (b) in AMS peat and its representing Potential Source Areas (normalized to UCC, Wedepohl, 1995). Peat samples are shown in grey squares. Black stars: AMS soils; Half-open circles: dust/soil in Sua Pan; and Open circle: dust/soil in Etosha Pan; Crosses: Deserts of Northwest Australia (sample courtesy of Jan Berend Stuut, NIOZ, Netherlands. Australian samples have been processed the same way as Southern African soil/dust. Australian data shown here is only for a comparison with other sources). Puna-Altiplano-Plateau (PAP, 9 data points), Central Western Argentina (CWA, 5 data points) and Patagonia (11 data points) are shown in Elipses (mean data with 95% confidence level, Gili et al., 2017); The black lines in (a) and (b) represent the End-member mixing lines among AMS soil, Southern Africa (SP+EP) and Southern South America (PAP+CWA+Patagonia) (see Table S6 for detailed calculations, after Albarede, 2002). Red squares represent the peat samples in the last 120 years.

References :

De Vleeschouwer, F., et al. (2014): "Emissions from pre-Hispanic metallurgy in the South American atmosphere." PloS one 9.10: e111315.

Doucet, Sonia, et al. (2004): "Geochemical and Hf–Pb–Sr–Nd isotopic constraints on the origin of the Amsterdam–St. Paul (Indian Ocean) hotspot basalts." *Earth and Planetary Science Letters* 218.1-2: 179-195.

Gili, S., et al. (2017):"Glacial/interglacial changes of Southern Hemisphere wind circulation from the geochemistry of South American dust." Earth and Planetary Science Letters 469: 98-109.

Kaiser, J. et al. (2005): A 70-kyr sea surface temperature record off southern Chile (Ocean Drilling Programm Site 1233). Paleoceanography, 20(4), PA4009.

Lamy, F et al. (2010): Holocene changes in the position and intensity of the southern westerly wind belt. Nature Geoscience, 3(10), 695-699.

Le Roux, G. and Shotyk, W. (2006): Weathering of inorganic matter in bogs. Developments in Earth Surface Processes 9, 197-215.

Sarnthein, M et al. (2011): Tropical warming in the Timor Sea led deglacial Antarctic warming and atmospheric CO2 rise by more than 500 yr. Earth and Planetary Science Letters, 302, 337-348.

Shotyk, W. (1997): Atmospheric deposition and mass balance of major and trace elements in two oceanic peat bog profiles, northern Scotland and the Shetland Islands. *Chemical Geology*, *138*(1-2), pp.55-72.

Stein, A. F., et al. (2015): "NOAA's HYSPLIT atmospheric transport and dispersion modeling system." Bulletin of the American Meteorological Society 96.12: 2059-2077.

Chapter 3.

Holocene Hg isotope variability in a peat core from the northern edge of Southern Hemisphere westerly winds

Objectifs et résumé

Le mercure (Hg) a attiré l'attention de la société humaine en raison de sa haute toxicité et de ses rejets anthropiques substantiels dans l'environnement. Diverses approches ont été utilisées pour étudier son cycle biogéochimique, telles que la surveillance à long terme et à grande échelle, les mesures de spéciation du mercure et les modèles de récepteurs statistiques multivariés. Les développements des indicateurs de substitution des isotopes stables du Hg au cours des deux dernières décennies ont ouvert une voie prometteuse pour étudier les sources, la transformation et le dépôt du Hg atmosphérique provenant d'émissions tant naturelles qu'anthropiques.

Le mercure contient sept isotopes stables (196, 198-202, 204 amu), qui peuvent subir un fractionnement dépendant de la masse (MDF) et un fractionnement indépendant de la masse (MIF) dans l'environnement lors du mélange à la source et de la transformation du mercure. Le MDF (rapporté comme δ^{202}Hg) est un phénomène environnemental courant, impliqué dans les réactions physiques, chimiques et biotiques. Les MDF peuvent aider à mieux discerner les processus de transformation du mercure et ses dépôts préférentiels sur différentes matrices. Le MIF des isotopes impairs du Hg (indiqué sous les noms Δ^{199}Hg et Δ^{201}Hg) se produit principalement lors de réactions photochimiques en milieu naturel en raison de l'effet isotopique magnétique. Le mécanisme de MIF des isotopes du Hg (même Δ^{200}Hg et Δ^{204}Hg) n'est toujours pas complètement compris, même si une anomalie positive des précipitations a conduit à une spéculation sur l'oxydation du mercure dans la haute atmosphère. Le Δ^{200}Hg est insensible à la modification photochimique dans la zone critique de la Terre.

Une tourbière reçoit du Hg principalement par l'absorption de Hg^0 par la végétation et par les précipitations. Le Δ^{200}Hg présente des signatures distinctes en Hg^0 et dans les précipitations, ce qui permet de distinguer les dépôts secs (absorption de Hg^0) et les dépôts humides (précipitations). Les vents du sud-ouest (VSO) sont l'une des principales caractéristiques du l'hémisphère Sud (HS), qui contrôle la pluviosité dans les zones situées à l'intérieur de sa ceinture. À son tour, les précipitations reconstituées et les dépôts secs dans la ceinture des VSO peuvent refléter la dynamique de ceux-ci. Cependant, depuis la moitié de l'Holocène, la communauté scientifique n'a pas de consensus quant à la position et / ou la force des VSO reconstitués à partir d'archives de sédiments, de tourbe et de glace via divers paramètres (e.g., macrofossiles et apport minérotrophe). Ce manque de consensus est probablement dû à l'influence accrue du climat régional ou local dans le contexte d'une variabilité climatique

holocène moindre par rapport à l'intervalle glaciaire et interglaciaire, ou à l'absence de variables de substitution quantifiées efficaces. Les signatures même uniformes MIF dans Hg^0 et les précipitations peuvent donner une idée de la quantification des dépôts secs et humides sur les tourbières et donc de la dynamique des VSO.

Dans ce chapitre, nous présentons les signatures isotopiques du mercure dans un sondage de tourbe de 6.6 kyr de l'île d'Amsterdam, situé à la limite nord des VSO. Les résultats montrent que les signatures $\delta^{202}Hg$ négatives sont présentes dans tout le profil de la tourbe (-0.66 ± 0.24, n = 58), ce qui indique une absorption préférentielle de l'isotope léger du Hg par la végétation. Les variations des profils $\Delta^{199}Hg$ et $\Delta^{200}Hg$ présentent des tendances similaires (avant le 19ème siècle, corrélations de Pearson, r = 0.79, p <0.001). Le sondage de tourbe de AMS montre un décalage $\Delta^{199}Hg$ de -1.3 entre le 19ème et le 20ème siècle, ce qui pourrait refléter des changements dans la composition isotopique du stock de mercure atmosphérique dans les latitudes moyennes de l'HS, en réponse à une augmentation des émissions industrielles et à une photo-réduction accrue.

En comparaison avec les signatures conservatrices de $\Delta^{200}Hg$ dans Hg^0 et dans les précipitations, nous trouvons que les dépôts secs de Hg^0 dominent dans l'ensemble du profil de tourbe de AMS (> 60%). Les dépôts humides de mercure augmentent au cours des années 3000BC-4200BC et 700BC-2000BC. Ces deux périodes humides proposées pour le mercure s'accordent globalement avec le déplacement de VSO reconstruit par la poussière et orienté vers l'équateur à sa limite nord. Il indique que les isotopes stables du mercure peuvent quantifier différents processus de dépôt et, par conséquent, la dynamique du VSO.

Cette étude est la première à rapporter les signatures historiques des isotopes du Hg dans une tourbière de l'HS et à confirmer que les isotopes du Hg peuvent être utilisés en tant que nouveaux substituts paléo-climatiques quantitatifs. Nos résultats aident à mieux comprendre la réaction de l'atmosphère actuelle face à l'évolution des émissions de mercure et à améliorer la modélisation du cycle biogéochimique mondial du mercure.

Research article

Holocene Hg isotope variability in a peat core from the northern edge of Southern Hemisphere westerly winds

(*Li et al., in preparation*)

Holocene Hg isotope variability in a peat core from the northern edge of Southern Hemisphere westerly winds

Chuxian Li[1, 2], Jeroen E. Sonke[2], Maxime Enrico[1, 2], Gaël Le Roux[1], François De Vleeschouwer[1,3]

1. EcoLab, Université de Toulouse, CNRS, INPT, UPS, Toulouse, France.

2. Laboratoire Géosciences Environnement Toulouse, Université de Toulouse, CNRS, IRD, UPS, Toulouse, France.

3. Instituto Franco-Argentino para el Estudio delClima y sus Impactos (UMI 3351 IFAECI/CNRS-CONICET-UBA), Universidad de Buenos Aires, Argentina

Abstract: The development of mercury (Hg) stable isotope proxies has provided a powerful tool to investigate the sources, transformation and deposition of atmospheric Hg from both natural and anthropogenic origin. Limited knowledge is about the impact of past climate on the Hg isotope deposition on the terrestrial environment and whether Hg isotopes can be used as climatic proxies. Here, we present Hg isotope signatures in a 6.6 kyr old peat core from Amsterdam Island, which is located at the Indian Ocean within the northern edge of the Southern Hemisphere Westerly Winds (SWW) belt. Results show negative δ^{202}Hg in the whole peat profile (-0.66 ± 0.24‰, n=58), indicating a preferential light Hg isotope uptake by vegetation. Δ^{199}Hg and Δ^{200}Hg correlate during pre-anthropogenic Hg pollution period (4600BC-1171AD, r=0.82, P<0.001), oscillating between Hg^0 and rainfall Hg^{II} end-members, and co-vary with dust deposition. We find that vegetation uptake of Hg^0 dominates Hg sequestration in the whole AMS peat profile (>60%). Hg^{II} wet deposition is enhanced during 3000BC-4200BC and 700BC-2000BC. These two periods broadly coincide with the equatorward-displacement of the SWW belt at its northern edge, inferred from dust proxies. Our findings illustrate the potential of Hg stable isotopes to understand paleo-precipitation trends and corresponding SWW dynamics. Recent peat layers show larger, 1.0‰, Δ^{199}Hg variability from mid-19th to mid-20th centuries that could reflect changes in the isotopic composition of the SH atmospheric Hg pool in response to growing industrial emissions and/or changes in Hg photochemistry.

Keywords: Hg stable isotopes; paleoclimate; peat; Southern westerly winds; precipitation proxy

Introduction

Mercury is an element that emitted to atmosphere mainly in the gaseous elemental form (Hg^0, > 95%, Lindberg and Stratton, 1998). Hg^0 can source from natural processes (e.g., volcanic eruptions, degassing of the Earth's crust) and anthropogenic activities (e.g., mining, waste incineration). Hg deposition over Earth's surface occurs by vegetation Hg^0 uptake (dry deposition, Jiskra et al., 2018), Hg^{II} wet and dry deposition (Sprovieri et al., 2017), and Hg^0 gas exchange with aqueous water bodies including the Oceans.

Recent developments in determination of Hg stable isotopes have opened new and promising avenues to investigate global Hg biogeochemical cycling (Sonke and Blum et al., 2013). Hg has seven stable isotopes (196, 198-202, 204 amu), which can undergo mass dependent fractionation (MDF) and mass independent fractionation (MIF) in the environment (Bergquist and Blum, 2007; Blum et al., 2014). MDF (reported as $\delta^{202}Hg$) is a common environmental phenomenon, which is involved in physical, chemical and biotic reactions (Estrade et al., 2009; Zheng et al., 2018). MDF can help quantify Hg transformations and identify atmospheric Hg deposition pathways (e.g., Demers et al., 2013; Enrico et al., 2016). MIF of odd Hg isotopes (reported as $\Delta^{199}Hg$ and $\Delta^{201}Hg$) occurs primarily during aqueous photochemical reactions in the natural environment due to the magnetic isotope effect, while both geogenic and anthropogenic Hg exhibit near 0‰ $\Delta^{199}Hg$ and $\Delta^{201}Hg$ (Zambardi et al., 2009; Sun et al., 2016; Xu et al., 2017).

In the past decade, dozens of studies have applied Hg isotopic tracers to investigate sources and processes of Hg from natural background and anthropogenic emission. Present-day background Hg^0 in air far from anthropogenic emission sources displays moderate positive $\delta^{202}Hg$ (0.49 ± 0.38‰, 1σ, n=71) and slightly negative $\Delta^{199}Hg$ values (-0.18 ± 0.06‰, 1σ, n=71) (Enrico et al., 2016; Gratz et al., 2010; Chen et al., 2012; Demers et al., 2013; Obrist et al., 2017; Sherman et al., 2010; Fu et al., 2016a; 2016b). Moderate positive $\delta^{202}Hg$ can be explained by preferential light isotope uptake by foliage (Demers et al., 2013; Enrico et al., 2016; Jiskra et al., 2018), and/or atmospheric oxidation of Hg^0 (Fu et al., 2016b). Anthropogenic emissions drive urban air isotopic composition to lower $\delta^{202}Hg$ (-0.40 ± 0.54‰, 1σ, n=184) and near-zero $\Delta^{199}Hg$ values (-0.09 ± 0.11‰, 1σ, n=184) (Gratz et al., 2010; Wang et al., 2015; Yuan et al., 2018; Rolison et al., 2012; Demers et al., 2015; Yu et al., 2016; Xu et al., 2017; Fu et al., 2018; Yamakawa et al., 2017; 2019). Anthropogenic Hg sources are mainly from coal combustion (Muntean et al., 2014; Sun et al., 2016), metallurgy and cement production (Zhang et al., 2015).

Even though environmental processes driving MDF and odd MIF still need further investigations, Hg isotope signatures can be used to trace sources, transformation and deposition of atmospheric Hg (Sonke, 2011; Blum et al., 2014), on both spatial and temporal scales.

MDF and odd MIF in ^{210}Pb-dated Northern Hemisphere sediments was used to understand the history of Hg contamination by local point sources since the 19th century in Lake Michigan, US (Yin et al., 2016a), South River, US (Washburn et al., 2018) and in the French Alpine lake Luitel (Guedron et al., 2016). Studies in Tibetan lakes have indicated different Hg deposition pathways, Hg photo-reduction and the influence of ice cover fluctuation (Yin et al., 2016b). In Lost Lake, US, Hg isotopes highlight the influence of photochemical reduction on Hg either in rainfall droplets prior to deposition, and/or in lake water column since industrialization (Kurz et al., 2019). Historical arctic ice cores show changes in atmospheric Hg isotopic composition over 19th to 20th centuries and potential influence by anthropogenic emissions (Zdanowicz et al., 2016).

Only a few studies so far have used Hg isotopes to investigate long historical natural Hg dynamics (pre- 1450AD). By MDF and MIF proxies, Gleason et al., (2017) has found that terrestrial, organic carbon-rich Hg dominated Hg input in the Arctic Ocean sediments since the Eocene. Sial et al. (2016) has shown a volcanic origin for the Hg in the Cretaceous-Paleogene boundary. Enrico et al. (2017) has reconstructed Holocene Hg^0 concentrations based on peat Hg variability. Cooke et al. (2013) has illustrated the cinnabar (HgS)-dominated pollution in the Andes during Inca (pre-1400AD) and Colonial periods (1532-1821AD). Relatively little attention has been given to the potential of Hg deposition to reconstruct climate variability.

Seasonality affects Hg deposition to terrestrial archives by changes in primary productivity, snow cover and subsequent Hg sequestration (Obrist et al., 2017; Jiskra et al., 2018). Marine dust fertilization can also alter Hg deposition to land ice by changes in oceanic Hg biological reduction (Vandal et al., 1993), and halogen-induced Hg^0 oxidation (Jitaru et al., 2009). One of the main SH climate features is the Southern Hemisphere westerly winds (SWW), which play important roles in regulating rainfall, dust trajectories and the southern ocean carbon sink (Hodgson and Sime, 2010). The variability of SWW has been studied using various wind proxies in sediment and peat archives across the SH (e.g., Moreno et al., 2010; Lamy et al., 2001; Saunders et al., 2018). Paleoclimate proxies show important variability of the SWW at different geographical locations in the SH (Li et al., submitted; Chapter 2). This variability is probably due to regional/ local climate trends, or due to the lack of effective quantitative proxies.

MIF of even Hg isotopes (reported as Δ^{200}Hg and Δ^{204}Hg) has the potential to quantify Hg wet deposition via rainfall and snowfall (Enrico et al., 2016). Even MIF isn't observed in anthropogenic Hg sources, but it is present in precipitation (Gratz et al., 2010; Chen et al., 2012; Demers et al., 2013; Enrico et al., 2016; Obrist et al., 2017) and in ambient atmospheric Hg^0 (Enrico et al., 2016). Currently, the mechanisms leading to even MIF still remain unclear, even though some studies speculate it as a result of Hg^0 photo-oxidation above the tropopause (Chen et al., 2012) or due to nuclear volume effects (Gratz et al., 2010). In general, Hg^0 is characterized by negative Δ^{200}Hg (-0.06 ± 0.02‰, 1σ, n=71) and positive Δ^{204}Hg (0.07 ± 0.05‰, 1σ, n=32) (Enrico et al., 2016; Gratz et al., 2010; Demers et al., 2013; Obrist et al., 2017; Sherman et al., 2010; Fu et al., 2016a; 2016b). Different from Hg^0, rainfall Hg^{II} is characterized by positive Δ^{200}Hg (0.19 ± 0.13‰, 1σ, n=77) and negative Δ^{204}Hg (-0.16 ± 0.17‰, 1σ, n=17) (Enrico et al., 2016; Gratz et al., 2010; Chen et al., 2012; Demers et al., 2013; Obrist et al., 2017). The distinct even MIF signatures in Hg^0 and rainfall have been used to quantify Hg dry and wet deposition to peat bogs (Enrico et al., 2016).

Peat bogs are formed by decomposed vegetation, which exclusively registers atmospheric inputs and can therefore register past climate signals (e.g., Saunders et al., 2018). Peat bogs sequester Hg mainly by vegetation Hg^0 uptake and to a lesser extent by Hg^{II} dry deposition and by rainfall wet deposition (Enrico et al., 2016). High natural organic matter contents lead to anoxic conditions in peat and inhibit Hg reduction to Hg^0 (Gu et al., 2011), and can therefore well retain the deposited Hg after peat decay and submerged under the water table.

Amsterdam Island is a remote island, located at the northern edge of SWW, sensitive to the displacement of SWW and free from human disturbance. It is an ideal location to study the relationship between climate variability and the historical natural Hg deposition. The objectives of this study are to: 1) investigate for the first time the SH mid-latitude historical Hg stable isotope signatures; 2) estimate the dry and wet deposition based on the Hg isotope composition, and then compare the Hg-based environmental change to dust-flux based climate dynamics.

Methods and materials

Study site and peat sampling

Amsterdam Island is an isolated island located at the Southern Indian Ocean with halfway between South Africa and Australia. It rose up from the Ocean before 700 kyr BP. This island is ca. 9.2 km long and 7.4 km wide, which has an elliptic surface area of 55 km^2 (Frenot and Valleix, 1990) (Figure 1A). Almost all the coast is characterized by vertical cliffs (Doucet et al.,

2004). It has a mild oceanic weather with annual temperature of 14°C and annual precipitation of 1120 mm. AMS is at the northern margin of SWW, characterized by winds dominantly from west and northwest with an average speed of 7.4 m s^{-1} (Frenot and Valleix, 1990). Air flow from continental regions is favored in austral late winter and early spring (Moody et al., 1991). More rainfall occurs in austral winter with average 22.6 days per month when SWW shift equatorward, while in austral summer rainfall frequency drops to 17.5 days per month when SWW move poleward (Moody et al., 1991). Since early works in the 1960s (Berthios et al., 1969), many scientific researches have been carried out in this island, investigating from volcano origin (Gunn et al., 1975), to CO_2 variations (Gaudry et al., 1983), to seasonal variation in precipitation composition (Moody et al., 1991), and to radionuclide fallouts (Li et al., 2017). AMS has peat deposits, with a large portion located at the Caldeira with a height of 771m. The peat sequences are sampled at the Caldeira peatland (Figure 1B), which is dominated by brown moss species and *Sphagnum*. Peat collection and sub-sampling details see methods in Chapter 1 and 2.

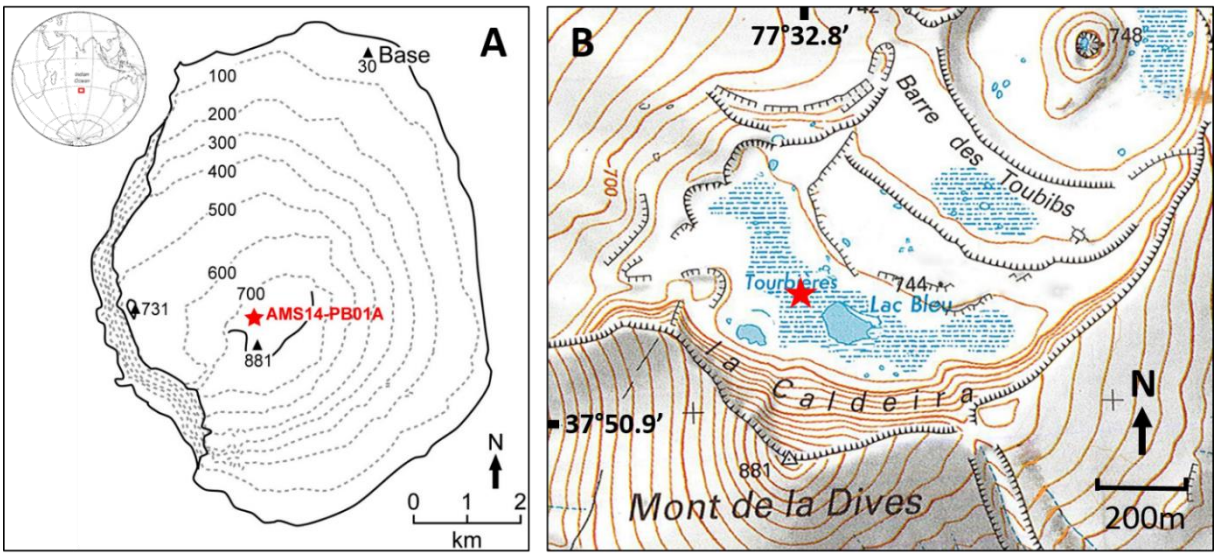

Figure 1. (A) Location of Amsterdam Island and peat sampling site (red star); (B) Enlarged version of peat sampling site (red star) at the central part (caldeira) of this island.

Hg extraction and purification

Freeze-dried peat was analyzed for total Hg concentration (THg) by Milestone Direct Mercury Analyzer (DMA80). For details of analytical performance on THg see "Methods" section. Variable amounts of peat samples were used for extracting Hg for isotope analysis based on peat Hg concentration and optimum quantity of Hg required (1ppb, MC-ICP-MS). Peat Hg was

extracted using combustion and acid trapping methods (Sun et al., 2013). Briefly, we burnt peat samples in a double tube furnace at 1000°C and trapped the released gaseous Hg with a 40 vol.% inverse *aqua regia* solution (2:1 HNO_3: HCl). The solution was then determined for Hg concentration by cold vapor atomic fluorescence spectroscopy (CV-AFS). The extraction yields were in the range 83%-116%.

Due to the matrix effect on the some of the peat samples on MC-ICP-MS measurements, we further purified the Hg in inverse *aqua regia* solution after oven combustion. The purification system consisted of a 250ml glass vessel where we adding 10 ml sample solution, 40 ml 10% $SnCl_2$ and 150 ml Milli-Q water, and a 15ml falcon tube with again 40 vol.% inverse *aqua regia*. The sample solution was purged by bubbling Hg free argon (300 mL min^{-1}) for 1h. The purification yields were in the range 97%-106% (n=4).

Hg stable isotope measurements

Peat Hg stable isotopes were measured in 20% (v/v) inverse *aqua regia* using cold-vapor multi-collector inductively coupled mass spectrometry (CV-MC-ICP-MS, Thermo-Finnigan Neptune, Midi-Pyrenees Observatory, Toulouse, France). Sample isotopic ratios were corrected for mass bias by bracketing using the international standard NIST SRM 3133. Results are reported as δ-values in per mil (‰) by referencing to NIST SRM 3133, representing to Hg mass dependent fractionation (see Eq.1).

$$\delta^{XXX}\text{Hg} = \{[(^{XXX}\text{Hg}/^{198}\text{Hg})_{sample}/(^{XXX}\text{Hg}/^{198}\text{Hg})_{SRM3133}]-1\} \text{ X } 1000 \quad \text{(Eq.1)}$$

MIF is calculated based on the deviations of δ-values from the theoretical MDF (see Eq.2):

$$\Delta^{XXX}\text{Hg} = \delta^{XXX}\text{Hg} - \beta\text{X } \delta^{202}\text{Hg} \quad \text{(Eq.2)}$$

Where XXX represents for 199, 200, 201 and 204. Symbol β is 0.252, 0.502, 0.752 and 1.493 for ^{199}Hg, ^{200}Hg, ^{201}Hg and ^{204}Hg, respectively (Bergquist and Blum, 2007).

Analytical control of Hg isotope measurements are assessed by analyzing ETH-Fluka, UM-Almaden and procedural standards (Coal, NIST 1632d, n= 5; Lichen, BCR482, n=5). ETH-Fluka displayed δ^{202} and Δ^{199}Hg of -1.43 ± 0.15 (2σ, n=19) and 0.05± 0.13 (2σ, n=19), respectively. UM-Almaden showed δ^{202} and Δ^{199}Hg of -0.52 ± 0.13 (2σ, n=7) and -0.03 ± 0.09 (2σ, n=7), respectively. Hg isotopic signatures in procedural standards are reported in the "***Methods***" section (for ^{199}Hg, ^{200}Hg, ^{201}Hg and ^{204}Hg).

Hg enrichment in dust

We compare the relationship between Hg and dust to those in the continental crust for the estimation of peat Hg concentration enrichment on peat REE-based dust concentration (EF_{Hg}-

$_{dust}$, Eq. 3. method similar to Jitaru et al., 2009). $Crust_{Hg}$ is 56 ng g^{-1}, and $Crust_{dust}$ is the sum of the REE concentrations in the upper continental crust wth 148 µg g^{-1} (Rudnick and Gao, 2003).

$$EF_{Hg\text{-}dust} = (Peat_{Hg}/Peat_{dust})/(Crust_{Hg}/Crust_{dust}) \quad \text{(Eq.3)}$$

Hg isotopes mass balance

Even Hg MIF is suggested to be conservative over the Earth surface. The distinct difference of $\Delta^{200}Hg$ between Hg^0 and rainfall Hg^{II} can be used to quantify the source of historical peat Hg. $\Delta^{200}Hg$ values in both Hg^0 and rainfall Hg^{II} used in this study are from remote NH mid-latitude sites (Enrico et al., 2016; Gratz et al., 2010; Demers et al., 2013; Fu et al., 2016a; 2016b; Chen et al., 2012) due to lack of data in the SH.

$$\Delta^{XXX}Hg_{peat} = \alpha * \Delta^{XXX}Hg_{GEM} + \beta * \Delta^{XXX}Hg_{rainfall} \quad \text{(Eq. 4)}$$

$$\alpha + \beta = 1 \quad \text{(Eq. 5)}$$

Results and discussion

Relationships between HgAR and dust flux in the peat core

Hg accumulation rates (HgAR) are relatively constant between 4650BC and 1170AD (2.6 ± 1.7 µg m^{-2} yr^{-1}, 1σ, n= 82), except two periods with elevated HgAR (2500BC-2000BC and 500BC-0AD) (Figure 2A). Since 1170AD, HgAR have increased gradually and peaked during 20th century (Figure 2A). HgAR are significantly correlated with REE-based dust flux during the pre-industrial period (pre-1880AD, Pearson correlation, $P < 0.001$, r=0.6). Both HgAR and dust flux increase significantly during the periods of 3000BC-2000BC (Figure 2A; 2B). The $EF_{Hg\text{-}dust}$ ranges from 61 to 721 in the whole core with 136 ± 60 (n=16) for 3000BC-2000BC high-dust interval. It suggests an insignificant contribution from atmospheric mineral dust to peat Hg. The co-variation between HgAR and dust flux may be explained by the influence of ecological change and/or climate variability. A recent study has indicated that Hg dry deposition by vegetation Hg^0uptake dominates peat Hg sequestration (Enrico et al., 2016). Enhanced peat growth can accumulate more Hg by Hg^0 uptake, similar to CO_2. Elevated HgAR can therefore result from enhanced peat primary productivity, or from elevated atmospheric Hg^0 levels. The net peat accumulation rate during 3000BC-2000BC is not significantly different from the previous periods (Krustal-Wallis test, P =0.48), which can be explained by a combination of synchronous changes in the primary productivity and decomposition rate. While higher primary productivity can be achieved by increased dust-transported nutrient input at 3000BC-2000BC,

higher decomposition rate may also occur under enhanced peat oxidation at the acrotelm (top sequence above the water table, Ingram, 1978; Clymo, 1984) during relatively drier climate when SWW shifts polewards (SWW information see Chapter 2). But the changes in primary productivity and decomposition alone might not be enough to explain the correlation between dust flux and Hg deposition.

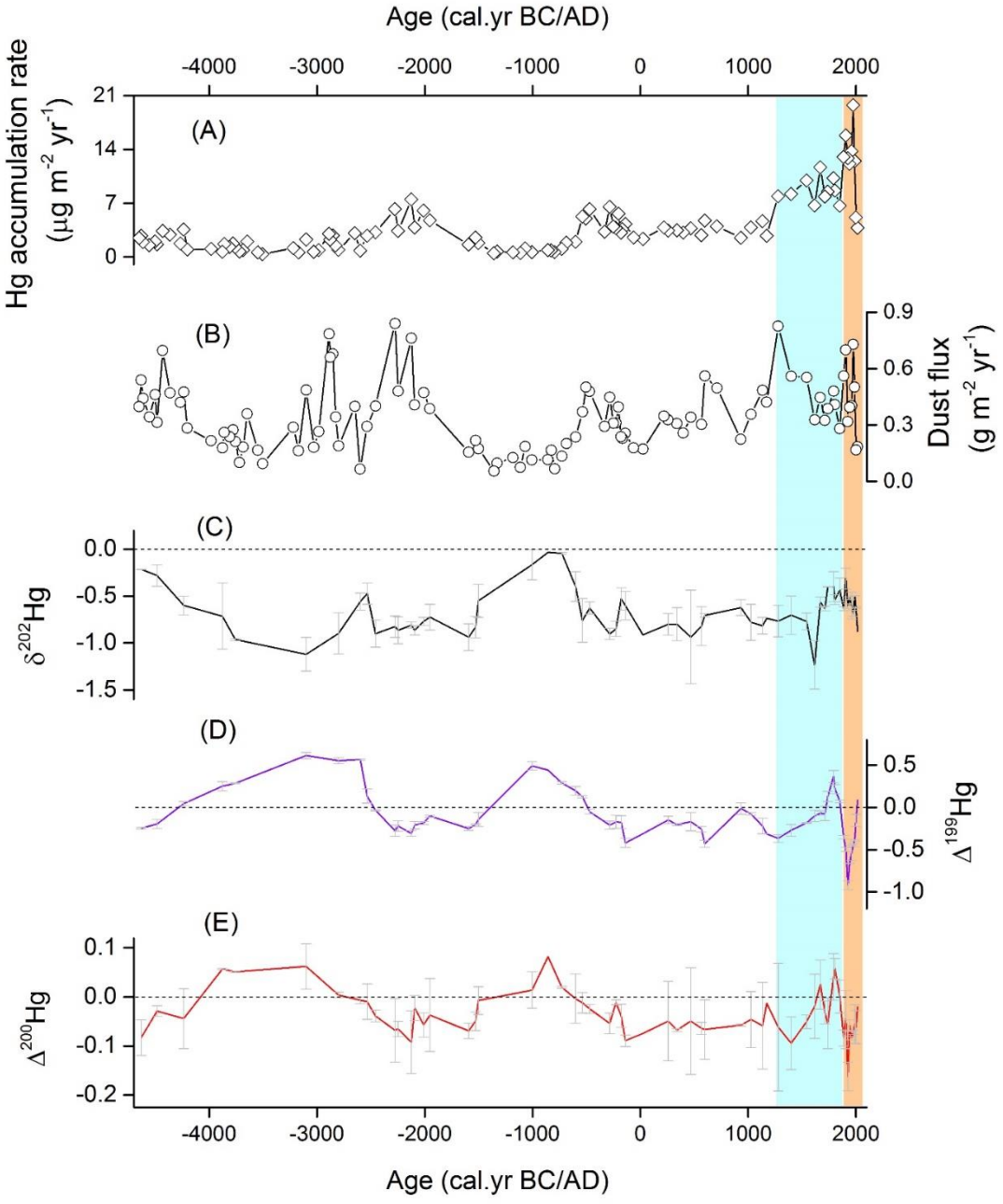

Figure 2. Profiles of Hg accumulation rate (μg m^{-2} yr^{-1}), dust flux (g m^{-2} yr^{-1}), δ^{202}Hg (‰), Δ^{199}Hg (‰) and Δ^{200}Hg (‰) in the AMS peat core. Light green shading spans the interval of pre-industrial Hg pollution (1280-1850AD), while orange shading covers the industrial period (post-1850AD).

Another possible explanation for the dust *vs.* HgAR correlation may be elevated Hg^0 concentration and/or enhanced deposition of gaseous oxidized Hg (GOM) during 3000BC-2000BC. Poleward-shifted SWW during this period can enhance upwelling of deep water with high concentrations of dissolved CO_2 and Hg^0 resulting in Hg^0 evasion and therefore higher atmospheric Hg^0 (Denton et al., 2010; Hodgson and Sime, 2010). Poleward-shifted SWW shows an "austral summer-like" climate pattern in the SH. In austral summer, the oceanic region located southwest of AMS is highly productive and potentially produces halogen species (Angot et al., 2014), which can effectively oxidize Hg^0 to GOM. Subsequently, GOM can be scavenged by particles and deposit to the peatland. A previous study on historical atmospheric Hg depletion over Antarctica, has shown that GOM can be efficiently scavenged by mineral dust and subsequently deposit as particulate Hg during glacial periods (Jitaru et al., 2009). A strikingly high Hg concentration was also found in an Antarctic ice core during the last glacial maximum (Vandal et al., 1993), which corresponds to the high dust flux over the East Antarctic Ice sheet during the same period (Baccolo et al., 2018). Note that a proportion of deposited Hg to terrestrial environment can be photo-chemically reduced and emitted as Hg^0 (Fitzgerald and Lamborg, 2003). Briefly, the coherence between HgAR and dust flux may result from a mix of factors controlled by SWW dynamics (e.g., halogen, upwelling and dust availability), rather than peat bog ecological change only.

Natural background Hg stable isotope distributions (pre-14th century AD)

Peat δ^{202}Hg before 1280AD is characterized by negative values (Figure 2C), ranging from -1.12‰ to -0.04‰ (average δ^{202}Hg =-0.68 ± 0.26‰, 1σ, n=39). The negative δ^{202}Hg agrees with vegetation Hg studies in the NH (negative δ^{202}Hg, e.g., Demers et al., 2013; Jiskra et al., 2015; Zheng et al., 2016; Enrico et al., 2016; Yu et al., 2016). It confirms the preferential uptake of light Hg isotopes by vegetation, possibly related to diffusion and/or intra-cellular oxidation by enzymatic processes (Rutter et al., 2011), regardless of the vegetation species and geological substrate (Zheng et al., 2016). Peat δ^{202}Hg shows a general decreasing trend from 4650BC to 1590BC in a range of -0.21‰ to -1.12‰. Afterwards, δ^{202}Hg increases up to -0.04 ± 0.01‰ (2σ) at 730BC. Peat δ^{202}Hg remains relatively constant between 600BC and 1171AD (-0.74 ± 0.15‰, 1σ, n=17, Figure 2C).

Profiles of peat Δ^{199}Hg and Δ^{200}Hg show coherent trends from 4600BC to 1171AD (Figure 2D; 2E), fluctuating at centennial scales (Pearson correlations, r=0.82, P<0.001). Δ^{199}Hg and Δ^{200}Hg increase from 4600BC to 3000BC in a range of -0.25‰ to 0.61‰ and -0.08‰ to 0.06‰,

respectively. Subsequently, Δ^{199}Hg decreases down to -0.31 ± 0.03‰ and Δ^{200}Hg down to -0.09 ± 0.06‰ around 2125BC. From 1600BC to 150BC, both increase again and peak at 850BC (0.44‰ for Δ^{199}Hg, 0.08‰ for Δ^{200}Hg), followed by decreasing trends until 150BC. Between 24AD and 1170AD, both fluctuate minimally with values of -0.22 ± 0.12‰ (1σ, n=10) for Δ^{199}Hg and -0.05 ± 0.02‰ (1σ, n=10) for Δ^{200}Hg. Atmospheric odd-mass Hg isotopes show distinct signatures in Hg^0 and rainfall Hg^{II}, yet are not ideal source tracers due to potential post-depositional odd-MIF (Sonke, 2011; Demers et al., 2013; Enrico et al., 2016). Even-mass Hg isotopes are found to be conservative at the Earth's surface, free from post-depositional MIF (e.g. Jiskra et al., 2017). The positive correlation between peat Δ^{199}Hg and Δ^{200}Hg suggests their variations are caused by similar processes, or reflect similar Hg deposition sources, predominantly wet or dry deposition.

Hg isotope signatures during pre-industrial Hg pollution period (1280-1850AD)

Substantial debate exists on the historical Hg emission sources, such as, the amount of Hg emitted to the atmosphere from different sectors (e.g., Silver/gold mining, liquid Hg^0 productions, Sun et al., 2016; Horowitz et al., 2014; Streets 2011; 2017). There is also little knowledge about Hg pollution from the pre-industrial period, especially in a hemispheric scale. Hg flux during 1280-1850AD period increases 2.7 folds from the natural background period (Figure 2A), which can be explained either by enhanced peat primary productivity, or elevated atmospheric Hg level due to the Hg pollution.

No significant difference in δ^{202}Hg, Δ^{199}Hg and Δ^{200}Hg is observed during the pre-industrial Hg pollution period (1280-1850AD) relative to these three Hg isotopes from previous natural background period. Peat δ^{202}Hg, Δ^{199}Hg and Δ^{200}Hg values from 1280AD to 1850AD are -0.64 ± 0.25‰, -0.03 ± 0.23‰ and -0.02 ± 0.05‰ (1σ, n=10), respectively. Profiles of peat δ^{202}Hg, Δ^{199}Hg and Δ^{200}Hg, however, display general increasing trends, which are in agreement with Hg isotope signatures of liquid Hg^0. Liquid Hg^0 production dominates anthropogenic Hg emissions to the atmosphere during Spanish large-scale mining (14^{th}-19^{th} century AD, Cooke et al., 2013; Streets et al., 2011). Bulk Hg evaporated from Au/Ag amalgam is suggested to conserve the Hg isotope composition of liquid Hg^0 used for amalgamation (Sun et al., 2016). A global compilation of δ^{202}Hg in commercial liquid Hg^0 shows a value of -0.38 ± 0.34‰ (1σ, n=13, Sun et al., 2016). Anthropogenic Hg emission, including liquid Hg^0 production shows no odd and even MIF with signatures near-zero for Δ^{199}Hg and Δ^{200}Hg. Anthropogenic Hg deposition from the silver/gold mining sector with higher isotopic signatures can be responsible

for the increasing peat δ^{202}Hg, Δ^{199}Hg and Δ^{200}Hg values during the pre-industrial Hg pollution period. We therefore suggest that elevated HgAR between 1280-1850AD (Figure 2A) results from anthropogenic Hg deposition, predominately from silver/gold mining. Note that we cannot exclude the contribution of enhanced primary productivity on high peat Hg sequestration, and the influence of changes in Hg deposition pathways on the Hg isotope distribution.

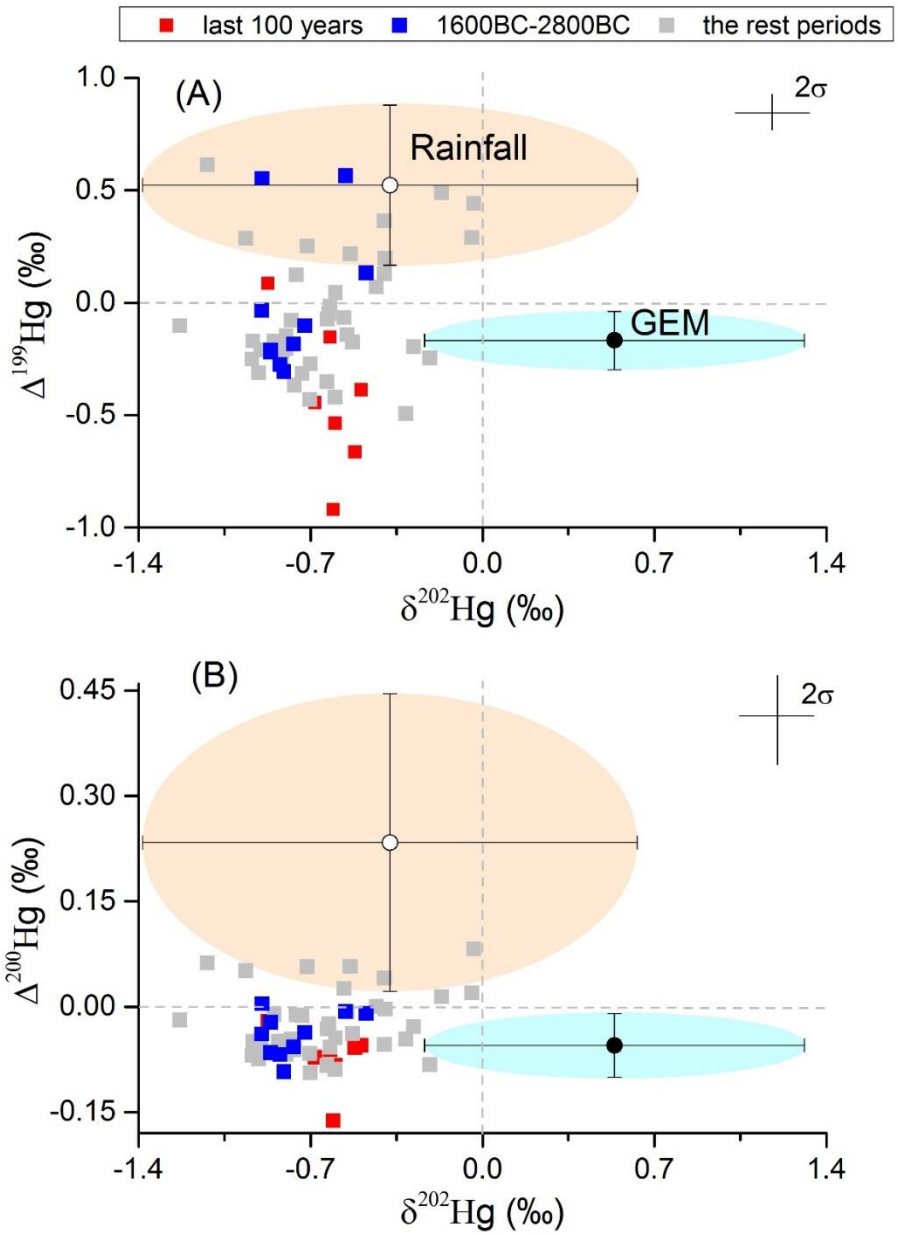

Figure 3. (A) Ratios of δ^{202}Hg vs Δ^{199}Hg and (B) δ^{202}Hg vs Δ^{200}Hg in AMS peat (squares) in comparison with isotopic signatures in Hg^0 (denoted as GEM, cyan shadow, mean ± 2σ) and rainfall (orange shadow, mean ± 2σ) from remote sites in mid latitudes of Northern hemisphere (NH). Red, blue and grey squares represent for periods of the last 100 years, 1600BC-2800BC and the rest, respectively. NH Hg^0 data (n=59) is from Enrico et al., (2016);

Gratz et al., (2010); Demers et al., (2013); Fu et al., (2016a); (2016b). NH rainfall data (n=74) is from Enrico et al., (2016); Gratz et al., (2010); Chen et al., (2012); Demers et al., (2013).

Changing Hg sources since the industrialization (post-1850AD)

Since the industrialization, AMS peat δ^{202}Hg has not shown much variation with an average value of -0.59 ± 0.15‰ (1σ, n=9). Peat δ^{202}Hg during industrial era is insignificantly different from the natural background period from 4600BC to 1280AD (-0.68‰ ± 0.26‰, 1σ, n=39, Kruskal-Wallis test, *P*=0.10). Peat Δ^{199}Hg profile shows variability from 1850AD onwards (Figure 2D). It falls gradually from 0.07± 0.01‰ (2σ) at 1850AD to the lowest values at 1924AD (-0.92 ± 0.05‰, 2σ). The decreasing trend of peat Δ^{199}Hg profile from 1850AD to 1924AD can be partially explained by global anthropogenic Hg emissions since industrialization, which is characterized by mean Δ^{199}Hg of -0.04‰ (probability of 10% (-0.07 ‰) to 90% (-0.01‰), Sun et al., 2016). Most of recent peat Δ^{199}Hg fall out of the range of the atmospheric Hg^0 mean ± 2σ (-0.17 ± 0.13‰), characterized by much more negative values (Figure 2D; Figure 3A), which is probably as a result of intra-cellular photoreduction at the bog surface. Photochemical reduction leading to negative Δ^{199}Hg signatures in residual peat Hg can occur when peat Hg is coordinated to dissolved organic matter thiol functional groups, DOM-S, Zheng and Hintelmann, 2009; Luo et al., 2017. Present-day SH anthropogenic Hg emissions are 4.3 ± 1.7 times higher than natural primary emissions (volcano source, see chapter 3). Since 1850s, the amount of atmospheric aqueous DOM has also been increased due to the increase in fossil fuel combustion (Baken et al., 2011; Stubbins et al., 2012). By analogy, recent study on particulate Hg isotopic signatures also found photo-reduced low Δ^{199}Hg value in Chinese PM2.5 (e.g., down to -1.1‰, Xu et al., 2019). AMS peat Δ^{199}Hg since 1850AD shows strong negative correlation with Hg flux (R^2 = 0.53), which in part can be explained by different relative Hg contribution from dry and wet deposition. Briefly, we interpret the recent shift in peat Δ^{199}Hg to be as results of both atmospheric photochemical process and different source contribution (dry/ wet deposition).

Peat Δ^{200}Hg shows a decreasing trend from 19th to 20th century (0‰ to -0.05‰) and subsequently remains relatively constant until 2001AD, except one lowest value occurring at 1924AD (-0.16‰ ± 0.03‰) for unclear reason. This Δ^{200}Hg profile suggests a stepwise increase in the relative contribution from peat vegetation Hg^0 uptake, which further indicates that AMS has gradually become drier probably as a result of poleward-shifted and/ or weakened SWW since the 19th century.

Climate implication based on Hg isotope mass balance calculation results

We adopt the period divisions for dust flux based on change point analysis to interpret the Hg isotope mass balance results, because the one of the main objectives of this study is to compare Hg-isotope-derived environmental change to dust-flux-based climate variability. Thus, the whole profile is divided into 7 sections for discussions: 4200BC-4650BC; 3000BC-4200BC; 2000BC-3000BC; 700BC-2000BC; 600AD-700BC; 1900AD-600AD and the last 100 years.

We use a binary mixing model based on Δ^{200}Hg signatures (Eq. 4; Eq. 5). We find that Hg^0 dry deposition dominates Hg sequestration in AMS peat since mid-Holocene (>60%, Figure 4, Table S1). Vegetation Hg^0 uptake as dominant Hg pathway to AMS peat is consistent with the findings in Pyrenean peat (Enrico et al., 2016) and supports the role of terrestrial vegetation as a Hg^0 pump (Jiskra et al., 2018). Precise calculation of the Hg contribution from dry/wet deposition cannot be accessed due to lack of local/regional Hg^0 and rainfall isotope data. We therefore only focus on the broad trend of dry/wet deposition variations. Binary mixing model results show that the proportion of Hg wet deposition increases significantly during 3000BC-4200BC and 700BC-2000BC. These two periods with enhanced Hg wet contribution correspond to the low dust flux periods, which are characterized with equatorward-displacement SWW. When SWW shifts equatorward, more rainfall occurs at AMS (Moody et al., 1991). Enhanced rainfall has the potential to scavenge more Hg and subsequently increase Hg wet deposition to AMS peat. Interestingly, total HgAR is lower during these two wet-deposition periods relative to dryer periods. Enrico et al. (2017) observed that the artificial draining of a peat bog resulted in a strong negative shift in Δ^{200}Hg and increase in HgAR, which they attributed to increased PP. By analogy, we suggest that during wet periods, the AMS peat bog becomes water-logged, with relatively lower vegetation growth and consequently lower HgAR. Sequences of 4200BC-4650BC, 2000BC-3000BC, and post-700BC, are characterized by low proportions of Hg wet deposition (0-8%, Figure 4). These low Hg wet deposition periods are coeval with the relatively high dust flux (Figure 5), and high HgAR which is explained by the poleward-located SWW with less rainfall at AMS. In summary, Hg deposition to AMS peat is able to reflect the SWW dynamics by using Hg isotopes.

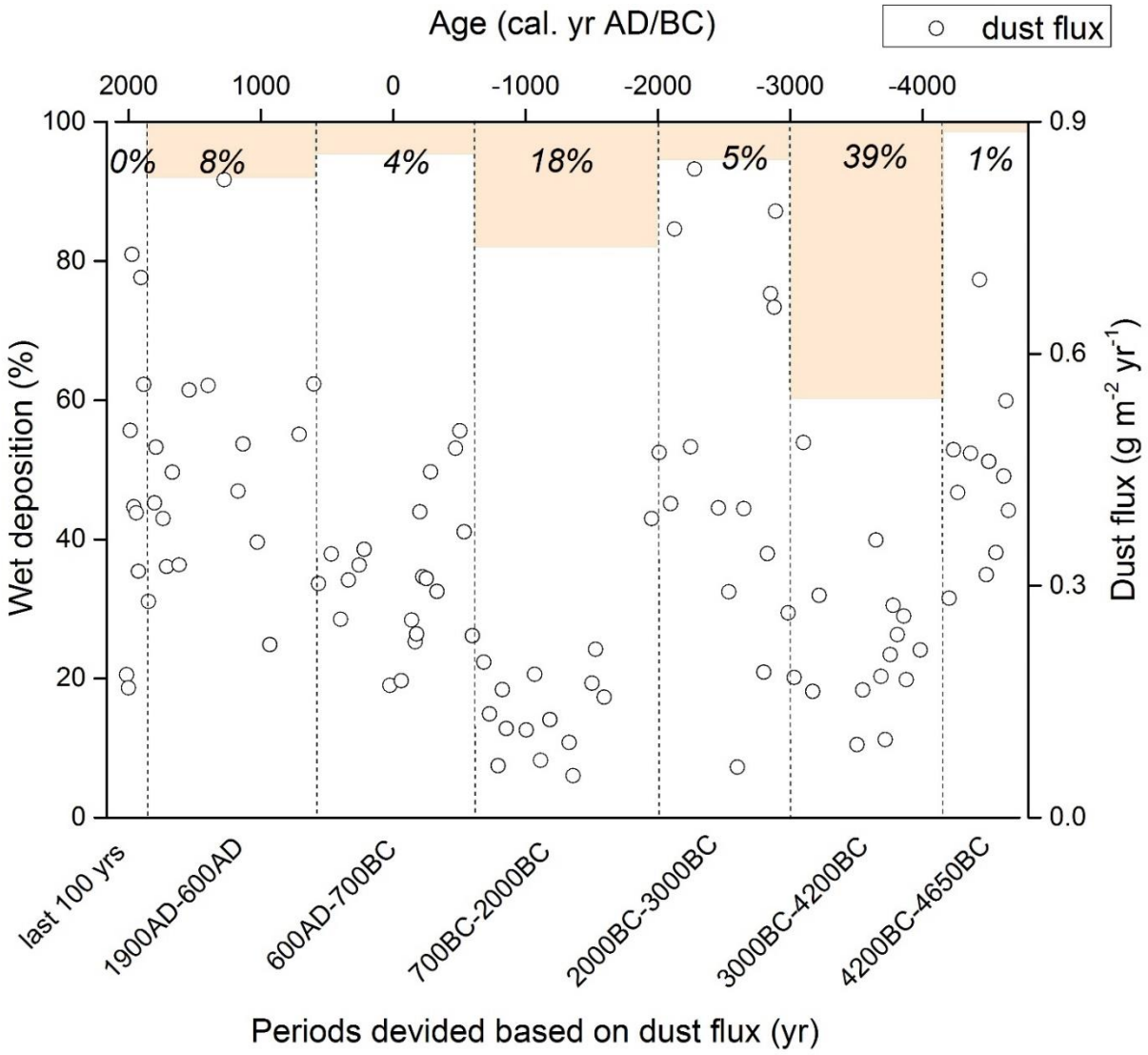

Figure 4. Relative contribution of Hg wet (orange bar, numbers) and dry (white bar) deposition to AMS peat based on the Hg isotopic composition during different periods. Dust flux variations are presented in comparison to Hg isotope-derived deposition. Dust periods were identified based on change point analysis (Chapter 2).

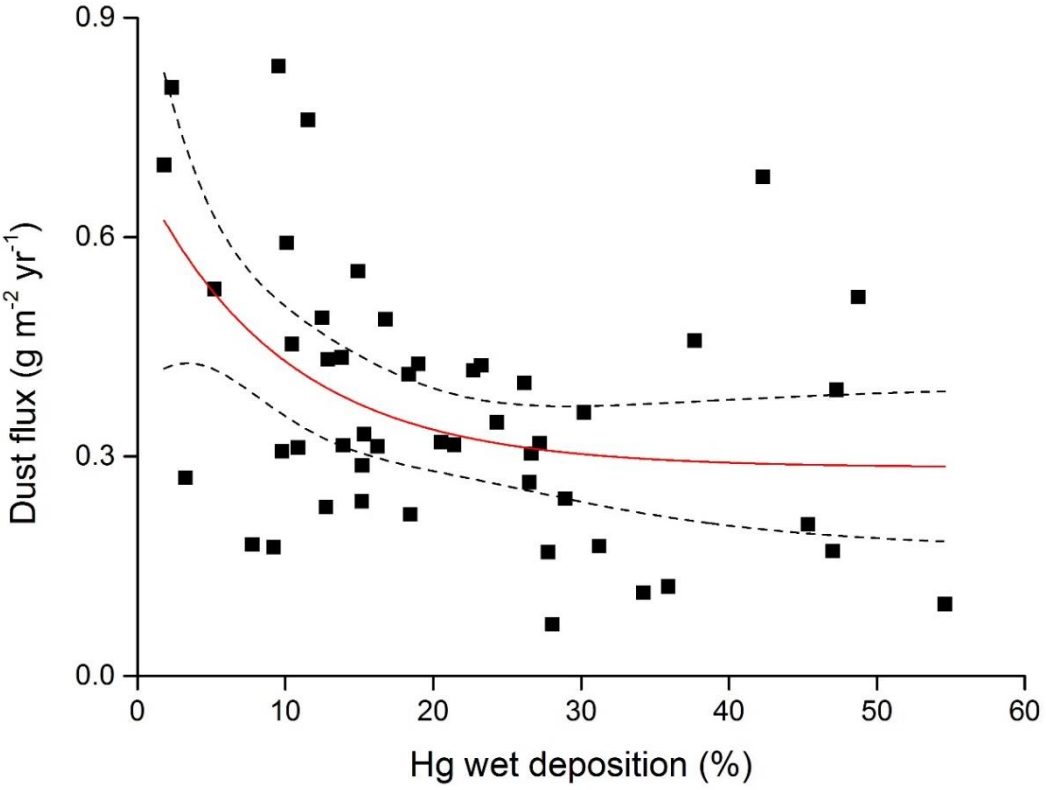

Figure 5. Correlation between Hg wet deposition (in %) and dust flux (g m-2 yr-1) in AMS peat record (*P* = 0.01). Exponential decay regression is used (red line), with 95% confidence level bands shown in black dash lines.

Conclusions

Hg deposition from the atmosphere to terrestrial environments is affected by atmospheric circulation (e.g., Chen et al., 2012). A change in the deposition pathways (dry/wet) under different climatic regimes can alter the Hg isotopic composition at the targeted receptors (e.g., Enrico et al., 2016). In this study we find that SWW variability signals can be seen in the Hg isotopic distribution in the AMS peat profiles. Deposition pathways based on Hg isotopic composition is comparable to the dust-flux-based SWW dynamics. This finding highlights the potential of peat Hg stable isotopes to be indicators for environmental change, which may be an important contribution to our knowledge on past climate variability. Changes in the peat Hg isotopic composition during the past 150 years reflect modifications in the SH atmospheric Hg pool in response to growing industrial emissions and/or changes in Hg photochemistry. This study is of particular interest due to the current global warming, the need to better understand the past and to better constrain future modelling on both Hg cycling and climate.

References:

Amos, H.M., Sonke, J.E., Obrist, D., Robins, N., Hagan, N., Horowitz, H.M., Mason, R.P., Witt, M., Hedgecock, I.M., Corbitt, E.S. and Sunderland, E.M., 2015. Observational and modeling constraints on global anthropogenic enrichment of mercury. *Environmental science & technology*, *49*(7), pp.4036-4047.

Angot, H., Barret, M., Magand, O., Ramonet, M. and Dommergue, A., 2014. A 2-year record of atmospheric mercury species at a background Southern Hemisphere station on Amsterdam Island. *Atmospheric Chemistry and Physics*, *14*(20), pp.11461-11473.

Baccolo, G., Delmonte, B., Albani, S., Baroni, C., Cibin, G., Frezzotti, M., Hampai, D., Marcelli, A., Revel, M., Salvatore, M.C. and Stenni, B., 2018. Regionalization of the atmospheric dust cycle on the periphery of the East Antarctic ice sheet since the last glacial maximum. *Geochemistry, Geophysics, Geosystems*, *19*(9), pp.3540-3554.

Bergquist, B.A. and Blum, J.D., 2007. Mass-dependent and-independent fractionation of Hg isotopes by photoreduction in aquatic systems. *Science*, *318*(5849), pp.417-420.

Berthios, J., Schlich, R. and Patriat, Ph., 1968. Carte Bathymetrique du Sud de l'Ocean Indien. 1st edition.

Bieser, J., Slemr, F., Ambrose, J., Brenninkmeijer, C., Brooks, S., Dastoor, A., DeSimone, F., Ebinghaus, R., Gencarelli, C., Geyer, B. and Gratz, L.E., 2017. Multi-model study of mercury dispersion in the atmosphere: Vertical distribution of mercury species.

Biester, H., Bindler, R., Martinez-Cortizas, A. and Engstrom, D.R., 2007. Modeling the past atmospheric deposition of mercury using natural archives. *Environmental science & technology*, *41*(14), pp.4851-4860.

Blum, J.D., Sherman, L.S. and Johnson, M.W., 2014. Mercury isotopes in earth and environmental sciences. *Annual Review of Earth and Planetary Sciences*, *42*, pp.249-269.

Chen, J., Hintelmann, H., Feng, X. and Dimock, B., 2012. Unusual fractionation of both odd and even mercury isotopes in precipitation from Peterborough, ON, Canada. *Geochimica et Cosmochimica Acta*, *90*, pp.33-46.

Cooke, C.A., Hintelmann, H., Ague, J.J., Burger, R., Biester, H., Sachs, J.P. and Engstrom, D.R., 2013. Use and legacy of mercury in the Andes. *Environmental science & technology*, *47*(9), pp.4181-4188.

Demers, J.D., Blum, J.D. and Zak, D.R., 2013. Mercury isotopes in a forested ecosystem: Implications for air-surface exchange dynamics and the global mercury cycle. *Global Biogeochemical Cycles*, *27*(1), pp.222-238.

Demers, J.D., Sherman, L.S., Blum, J.D., Marsik, F.J. and Dvonch, J.T., 2015. Coupling atmospheric mercury isotope ratios and meteorology to identify sources of mercury impacting a coastal urban-industrial region near Pensacola, Florida, USA. *Global Biogeochemical Cycles*, *29*(10), pp.1689-1705.

Doucet, S., Weis, D., Scoates, J.S., Debaille, V. and Giret, A., 2004. Geochemical and Hf–Pb–Sr–Nd isotopic constraints on the origin of the Amsterdam–St. Paul (Indian Ocean) hotspot basalts. *Earth and Planetary Science Letters*, *218*(1-2), pp.179-195.

Enrico, M., Le Roux, G., Heimbürger, L.E., Van Beek, P., Souhaut, M., Chmeleff, J. and Sonke, J.E., 2017. Holocene atmospheric mercury levels reconstructed from peat bog mercury stable isotopes. *Environmental science & technology*, *51*(11), pp.5899-5906.

Enrico, M., Roux, G.L., Marusczak, N., Heimbürger, L.E., Claustres, A., Fu, X., Sun, R. and Sonke, J.E., 2016. Atmospheric mercury transfer to peat bogs dominated by gaseous elemental mercury dry deposition. *Environmental science & technology*, *50*(5), pp.2405-2412.

Estrade, N., Carignan, J., Sonke, J.E. and Donard, O.F., 2009. Mercury isotope fractionation during liquid–vapor evaporation experiments. *Geochimica et Cosmochimica Acta*, *73*(10), pp.2693-2711.

Fitzgerald, W.F. and Lamborg, C.H., 2003. Geochemistry of mercury in the environment. *Treatise on geochemistry*, *9*, p.612.

Fitzgerald, W.F., Engstrom, D.R., Lamborg, C.H., Tseng, C.M., Balcom, P.H. and Hammerschmidt, C.R., 2005. Modern and historic atmospheric mercury fluxes in northern Alaska: Global sources and Arctic depletion. *Environmental science & technology*, *39*(2), pp.557-568.

Frenot, Y. and Valleix, T. (1990) Carte des sols de l'Ile Amsterdam (Terres Australes et Antarctiques Françaises), Université, Station Biologique de Paimpont.

Fu, X., Marusczak, N., Heimbürger, L.E., Sauvage, B., Gheusi, F., Prestbo, E.M. and Sonke, J.E., 2016a. Atmospheric mercury speciation dynamics at the high-altitude Pic du Midi Observatory, southern France. *Atmospheric Chemistry and Physics*, *16*(9), p.5623.

Fu, X., Zhu, W., Zhang, H., Sommar, J., Yu, B., Yang, X., Wang, X., Lin, C.J. and Feng, X., 2016b. Depletion of atmospheric gaseous elemental mercury by plant uptake at Mt. Changbai, Northeast China. *Atmospheric Chemistry and Physics*, *16*(20), pp.12861-12873.

Fu, X., Yang, X., Tan, Q., Ming, L., Lin, T., Lin, C.J., Li, X. and Feng, X., 2018. Isotopic Composition of Gaseous Elemental Mercury in the Marine Boundary Layer of East China Sea. *Journal of Geophysical Research: Atmospheres*, *123*(14), pp.7656-7669.

Gaudry, A., Ascencio, J.M. and Lambert, G., 1983. Preliminary study of CO2 variations at Amsterdam Island (Territoire des Terres Australes et Antarctiques Francaises). *Journal of Geophysical Research: Oceans*, *88*(C2), pp.1323-1329.

Gleason, J.D., Blum, J.D., Moore, T.C., Polyak, L., Jakobsson, M., Meyers, P.A. and Biswas, A., 2017. Sources and cycling of mercury in the paleo Arctic Ocean from Hg stable isotope variations in Eocene and Quaternary sediments. *Geochimica et Cosmochimica Acta*, *197*, pp.245-262.

Gratz, L.E., Keeler, G.J., Blum, J.D. and Sherman, L.S., 2010. Isotopic composition and fractionation of mercury in Great Lakes precipitation and ambient air. *Environmental Science & Technology*, *44*(20), pp.7764-7770.

Guédron, S., Amouroux, D., Sabatier, P., Desplanque, C., Develle, A.L., Barre, J., Feng, C., Guiter, F., Arnaud, F., Reyss, J.L. and Charlet, L., 2016. A hundred year record of industrial and urban development in French Alps combining Hg accumulation rates and isotope composition in sediment archives from Lake Luitel. *Chemical Geology*, *431*, pp.10-19.

Gunn, B.M., Watkins, N.D., Trzcienski Jr, W.E. and Nougier, J., 1975. The Amsterdam-St. Paul volcanic province, and the formation of low Al tholeiitic andesites. *Lithos*, *8*(2), pp.137-149.

Hodgson, D.A. and Sime, L.C., 2010. Palaeoclimate: Southern westerlies and CO 2. *Nature Geoscience*, *3*(10), p.666.

Horowitz, H.M., Jacob, D.J., Amos, H.M., Streets, D.G. and Sunderland, E.M., 2014. Historical mercury releases from commercial products: Global environmental implications. *Environmental science & technology*, *48*(17), pp.10242-10250.

Horowitz, H.M., Jacob, D.J., Zhang, Y., Dibble, T.S., Slemr, F., Amos, H.M., Schmidt, J.A., Corbitt, E.S., Marais, E.A. and Sunderland, E.M., 2017. A new mechanism for atmospheric mercury redox chemistry: implications for the global mercury budget. *Atmospheric Chemistry and Physics*, *17*(10), pp.6353-6371.

Jiskra, M., Sonke, J.E., Obrist, D., Bieser, J., Ebinghaus, R., Myhre, C.L., Pfaffhuber, K.A., Wängberg, I., Kyllönen, K., Worthy, D. and Martin, L.G., 2018. A vegetation control on seasonal variations in global atmospheric mercury concentrations. *Nature Geoscience*, *11*(4), p.244.

Jiskra, M., Wiederhold, J.G., Skyllberg, U., Kronberg, R.M., Hajdas, I. and Kretzschmar, R., 2015. Mercury deposition and re-emission pathways in boreal forest soils investigated with Hg isotope signatures. *Environmental science & technology*, *49*(12), pp.7188-7196.

Jitaru, P., Gabrielli, P., Marteel, A., Plane, J.M., Planchon, F.A., Gauchard, P.A., Ferrari, C.P., Boutron, C.F., Adams, F.C., Hong, S. and Cescon, P., 2009. Atmospheric depletion of mercury over Antarctica during glacial periods. *Nature Geoscience*, *2*(7), p.505.

Kurz, A.Y., Blum, J.D., Washburn, S.J. and Baskaran, M., 2019. Changes in the mercury isotopic composition of sediments from a remote alpine lake in Wyoming, USA. *Science of The Total Environment*, *669*, pp.973-982.

Lamy, F., Hebbeln, D., Röhl, U. and Wefer, G. (2001) Holocene rainfall variability in southern Chile: a marine record of latitudinal shifts of the Southern Westerlies. Earth and Planetary Science Letters 185(3), 369-382.

Lebouvier, M. and Frenot, Y., 2007. and Île Saint-Paul temperate. All have endemic species amongst their biota. The Terres Australes et Antarctiques Françaises (TAAF) is. In *Papers and Proceedings of the Royal Society of Tasmania* (Vol. 141, No. 1, p. 23). Royal Society of Tasmania.

Li, C., Le Roux, G., Sonke, J., van Beek, P., Souhaut, M., Van der Putten, N. and De Vleeschouwer, F., 2017. Recent 210Pb, 137Cs and 241Am accumulation in an ombrotrophic peatland from Amsterdam Island (Southern Indian Ocean). *Journal of environmental radioactivity*, *175*, pp.164-169.

Lindberg, S.A. and Stratton, W.J., 1998. Atmospheric mercury speciation: concentrations and behavior of reactive gaseous mercury in ambient air. *Environmental science & technology*, *32*(1), pp.49-57.

Luo, H.W., Yin, X., Jubb, A.M., Chen, H., Lu, X., Zhang, W., Lin, H., Yu, H.Q., Liang, L., Sheng, G.P. and Gu, B., 2017. Photochemical reactions between mercury (Hg) and dissolved organic matter decrease Hg bioavailability and methylation. *Environmental pollution*, *220*, pp.1359-1365.

Michael, R., Stuart, A.L., Trotz, M.A. and Akiwumi, F., 2016. Source apportionment of wet-deposited atmospheric mercury in Tampa, Florida. *Atmospheric research*, *170*, pp.168-175.

Moody, J.L., Pszenny, A.A.P., Gaudry, A., Keene, W.C., Galloway, J.N. and Polian, G., 1991. Precipitation composition and its variability in the southern Indian Ocean: Amsterdam Island, 1980–1987. *Journal of Geophysical Research: Atmospheres*, *96*(D11), pp.20769-20786.

Moreno, P.I., Francois, J.P., Moy, C.M. and Villa-Martínez, R., 2010. Covariability of the Southern Westerlies and atmospheric CO2 during the Holocene. *Geology*, *38*(8), pp.727-730.

Muntean, M., Janssens-Maenhout, G., Song, S., Selin, N.E., Olivier, J.G., Guizzardi, D., Maas, R. and Dentener, F., 2014. Trend analysis from 1970 to 2008 and model evaluation of EDGARv4 global gridded anthropogenic mercury emissions. *Science of the Total Environment*, *494*, pp.337-350.

Obrist, D., Agnan, Y., Jiskra, M., Olson, C.L., Colegrove, D.P., Hueber, J., Moore, C.W., Sonke, J.E. and Helmig, D., 2017. Tundra uptake of atmospheric elemental mercury drives Arctic mercury pollution. *Nature*, *547*(7662), p.201.

Rolison, J.M., Landing, W.M., Luke, W., Cohen, M. and Salters, V.J.M., 2013. Isotopic composition of species-specific atmospheric Hg in a coastal environment. *Chemical Geology*, *336*, pp.37-49.

Rutter, A.P., Schauer, J.J., Shafer, M.M., Creswell, J.E., Olson, M.R., Robinson, M., Collins, R.M., Parman, A.M., Katzman, T.L. and Mallek, J.L., 2011. Dry deposition of gaseous elemental mercury to plants and soils using mercury stable isotopes in a controlled environment. *Atmospheric environment*, *45*(4), pp.848-855.

Saunders, K.M., Roberts, S.J., Perren, B., Butz, C., Sime, L., Davies, S., Van Nieuwenhuyze, W., Grosjean, M. and Hodgson, D.A., 2018. Holocene dynamics of the Southern Hemisphere westerly winds and possible links to CO2 outgassing. *Nature geoscience*, *11*, pp.650-655.

Sherman, L.S., Blum, J.D., Johnson, K.P., Keeler, G.J., Barres, J.A. and Douglas, T.A., 2010. Mass-independent fractionation of mercury isotopes in Arctic snow driven by sunlight. *Nature Geoscience*, *3*(3), p.173.

Sial, A.N., Chen, J., Lacerda, L.D., Frei, R., Tewari, V.C., Pandit, M.K., Gaucher, C., Ferreira, V.P., Cirilli, S., Peralta, S. and Korte, C., 2016. Mercury enrichment and Hg isotopes in Cretaceous–Paleogene boundary successions: Links to volcanism and palaeoenvironmental impacts. *Cretaceous Research*, *66*, pp.60-81.

Sonke, J.E., 2011. A global model of mass independent mercury stable isotope fractionation. *Geochimica et Cosmochimica Acta*, *75*(16), pp.4577-4590.

Sprovieri, F., Pirrone, N., Bencardino, M., D'Amore, F., Angot, H., Barbante, C., Brunke, E.G., Arcega-Cabrera, F., Cairns, W., Comero, S. and Diéguez, M.D.C., 2017. Five-year records of mercury wet deposition flux at GMOS sites in the Northern and Southern hemispheres. *Atmospheric Chemistry and Physics*, *17*(4), pp.2689-2708.

Sprovieri, F., Pirrone, N., Bencardino, M., D'Amore, F., Carbone, F., Cinnirella, S., Mannarino, V., Landis, M., Ebinghaus, R., Weigelt, A. and Brunke, E.G., 2016. Atmospheric mercury concentrations observed at ground-based monitoring sites globally distributed in the

framework of the GMOS network. *Atmospheric chemistry and physics*, *16*(18), pp.11915-11935.

Streets, D.G., Devane, M.K., Lu, Z., Bond, T.C., Sunderland, E.M. and Jacob, D.J., 2011. All-time releases of mercury to the atmosphere from human activities. *Environmental science & technology*, *45*(24), pp.10485-10491.

Streets, D.G., Horowitz, H.M., Jacob, D.J., Lu, Z., Levin, L., Ter Schure, A.F. and Sunderland, E.M., 2017. Total mercury released to the environment by human activities. *Environmental science & technology*, *51*(11), pp.5969-5977.

Sun, R., Heimbürger, L.E., Sonke, J.E., Liu, G., Amouroux, D. and Berail, S., 2013. Mercury stable isotope fractionation in six utility boilers of two large coal-fired power plants. *Chemical Geology*, *336*, pp.103-111.

Sun, R., Streets, D.G., Horowitz, H.M., Amos, H.M., Liu, G., Perrot, V., Toutain, J.P., Hintelmann, H., Sunderland, E.M. and Sonke, J.E., 2016. Historical (1850–2010) mercury stable isotope inventory from anthropogenic sources to the atmosphere. *Elem Sci Anth*, *4*.

United Nations Environment Programme: Global mercury assessment, 2018, pp. 8.

Vandal, G.M., Fitzgerald, W.F., Boutron, C.F. and Candelone, J.P., 1993. Variations in mercury deposition to Antarctica over the past 34,000 years. *Nature*, *362*(6421), p.621.

Wang, Z., Chen, J., Feng, X., Hintelmann, H., Yuan, S., Cai, H., Huang, Q., Wang, S. and Wang, F., 2015. Mass-dependent and mass-independent fractionation of mercury isotopes in precipitation from Guiyang, SW China. *Comptes Rendus Geoscience*, *347*(7-8), pp.358-367.

Washburn, S.J., Blum, J.D., Kurz, A.Y. and Pizzuto, J.E., 2018. Spatial and temporal variation in the isotopic composition of mercury in the South River, VA. *Chemical Geology*, *494*, pp.96-108.

Xu, H., Sonke, J.E., Guinot, B., Fu, X., Sun, R., Lanzanova, A., Candaudap, F., Shen, Z. and Cao, J., 2017. Seasonal and annual variations in atmospheric Hg and Pb isotopes in Xi'an, China. *Environmental science & technology*, *51*(7), pp.3759-3766.

Xu, H.M., Sun, R.Y., Cao, J.J., Huang, R.J., Guinot, B., Shen, Z.X., Jiskra, M., Li, C.X., Du, B.Y., He, C. and Liu, S.X., 2019. Mercury stable isotope compositions of Chinese urban fine particulates in winter haze days: Implications for Hg sources and transformations. *Chemical Geology*, *504*, pp.267-275.

Yamakawa, A., Moriya, K. and Yoshinaga, J., 2017. Determination of isotopic composition of atmospheric mercury in urban-industrial and coastal regions of Chiba, Japan, using cold vapor multicollector inductively coupled plasma mass spectrometry. *Chemical Geology*, *448*, pp.84-92.

Yamakawa, A., Takami, A., Takeda, Y., Kato, S. and Kajii, Y., 2019. Emerging investigator series: investigation of mercury emission sources using Hg isotopic compositions of atmospheric mercury at the Cape Hedo Atmosphere and Aerosol Monitoring Station (CHAAMS), Japan. *Environmental Science: Processes & Impacts*.

Yin, R., Lepak, R.F., Krabbenhoft, D.P. and Hurley, J.P., 2016a. Sedimentary records of mercury stable isotopes in Lake Michigan. *Elem Sci Anth*, *4*.

Yin, R., Lepak, R.F., Krabbenhoft, D.P. and Hurley, J.P., 2016b. Sedimentary records of mercury stable isotopes in Lake Michigan. *Elem Sci Anth*, *4*.

Yu, B., Fu, X., Yin, R., Zhang, H., Wang, X., Lin, C.J., Wu, C., Zhang, Y., He, N., Fu, P. and Wang, Z., 2016. Isotopic composition of atmospheric mercury in China: new evidence for sources and transformation processes in air and in vegetation. *Environmental science & technology*, *50*(17), pp.9262-9269.

Yuan, S., Chen, J., Cai, H., Yuan, W., Wang, Z., Huang, Q., Liu, Y. and Wu, X., 2018. Sequential samples reveal significant variation of mercury isotope ratios during single rainfall events. *Science of the total environment*, *624*, pp.133-144.

Zambardi, T., Sonke, J.E., Toutain, J.P., Sortino, F. and Shinohara, H., 2009. Mercury emissions and stable isotopic compositions at Vulcano Island (Italy). *Earth and Planetary Science Letters*, *277*(1-2), pp.236-243.

Zdanowicz, C.M., Krümmel, E.M., Poulain, A.J., Yumvihoze, E., Chen, J., Štrok, M., Scheer, M. and Hintelmann, H., 2016. Historical variations of mercury stable isotope ratios in Arctic glacier firn and ice cores. *Global Biogeochemical Cycles*, *30*(9), pp.1324-1347.

Zhang, L., Wang, S., Wang, L., Wu, Y., Duan, L., Wu, Q., Wang, F., Yang, M., Yang, H., Hao, J. and Liu, X., 2015. Updated emission inventories for speciated atmospheric mercury from anthropogenic sources in China. *Environmental science & technology*, *49*(5), pp.3185-3194.

Zheng, W. and Hintelmann, H., 2009. Mercury isotope fractionation during photoreduction in natural water is controlled by its Hg/DOC ratio. *Geochimica et Cosmochimica Acta*, *73*(22), pp.6704-6715.

Zheng, W., Demers, J.D., Lu, X., Bergquist, B.A., Anbar, A.D., Blum, J.D. and Gu, B., 2018. Mercury Stable Isotope Fractionation during Abiotic Dark Oxidation in the Presence of Thiols and Natural Organic Matter. *Environmental science & technology*.

Zheng, W., Obrist, D., Weis, D. and Bergquist, B.A., 2016. Mercury isotope compositions across North American forests. *Global Biogeochemical Cycles*, *30*(10), pp.1475-1492.

Supporting formation

Table S1 Hg deposition to the AMS peat bog during each period (μg m^{-2} yr^{-1}, total, dry and wet), estimated from the relative contribution of Hg dry/ wet deposition and total HgAR.

Periods	Total Hg flux	Dry Hg flux (mean±2σ)	Wet Hg flux (mean±2σ)
last 100 yrs	12.0	12 ± 3.4	0
1900AD-600AD	7.4	6.8 ± 2.1	0.6 ± 0.18
600AD-700BC	3.9	3.8 ± 0.7	0.1 ± 0.03
700BC-1600BC	1.4	1.2 ± 0.4	0.3 ± 0.10
2000BC-3000BC	4.0	3.7 ± 0.8	0.2 ± 0.05
3000BC-4200BC	1.4	0.9 ± 0.03	0.5 ± 0.02
4200BC-4650BC	2.7	2.6 ± 0.5	0.03 ± 0.01

Chapter 4.

Unequal anthropogenic enrichment of mercury in Earth's northern and southern hemispheres

Objectifs et résumé

Le mercure (Hg) est un élément naturel et principalement issu du dégazage de la croûte terrestre (e.g., volcanisme). Il peut avoir de graves conséquences sur l'environnement lorsqu'il est rejeté en grande quantité et / ou transformé en une forme hautement toxique, le méthylmercure. Le méthylmercure est une toxine extrêmement préoccupante, qui peut facilement se bio-amplifier dans la chaîne alimentaire, entraînant des effets néfastes sur la santé des animaux sauvages (par exemple, oiseaux chanteurs) et des humains (neurotoxicité pour le fœtus et les enfants; problèmes cardiovasculaires chez l'adulte). Au cours des siècles passés, les activités humaines ont fortement modifié le transfert de mercure depuis la surface de la terre vers l'atmosphère moderne. Les estimations des émissions de Hg anthropiques depuis 1850 suggèrent qu'un total de 1540 Gg aurait été rejeté jusqu'en 2010, dont 470 Gg dans l'atmosphère. Les principaux rejets anthropiques de mercure proviennent de l'extraction artisanale et à petite échelle de l'or, de la combustion du charbon et de la production de mercure, de soude caustique et de ciment. Plus de 95% du mercure atmosphérique existe sous forme de mercure gazeux élémentaire (Hg^0), qui a un long temps de séjour dans l'atmosphère (plusieurs mois) permettant sa dispersion dans l'hémisphère avant son dépôt à la surface de la Terre, y compris dans des régions éloignées.

Les tendances historiques des variations naturelles et anthropiques du mercure peuvent être évaluée par les archives naturelles de séquestration du mercure (par exemple, les sédiments, la tourbe et la glace). Depuis les premiers travaux sur les carottes de sédiments lacustres dans les années 1970, des dizaines de carottes de sédiments éloignées datées au ^{210}Pb ont enregistré une augmentation du taux d'accumulation de mercure (HgAR) d'un facteur 3 depuis l'ère préindustrielle (1450-1880AD) jusqu'au 20ème siècle. La tourbe reçoit principalement du Hg absorbé par les plantes. Un nombre croissant d'études de carottes de tourbe ont été utilisées pour étudier les tendances historiques des dépôts de mercure. Il y a dix ans, Biester et al. avaient suggéré que la tourbe était un enregistreur historique du mercure moins fiable par rapport aux sédiments lacustres. Selon lui, l'enrichissement préindustriel enregistré dans les sédiments et la tourbe étaient en désaccord par un facteur de 10. Ces auteurs ont supposé que la mobilité du ^{210}Pb dans la colonne de tourbe a conduit à des reconstitutions de l'âge inexactes et à un taux d'accumulation de Hg peu fiable. Jusqu'en 2015, Amos et al. a examiné les études de tourbe publiées et a trouvé un enrichissement en Hg similaire (x3) depuis la période préindustrielle, en corrigeant une incohérence de temps de référence pour les archives de tourbe et de sédiment de

Biester et al. La tourbe a donc été suggérée comme une archive fiable pour les dépôts historiques de mercure.

Des sédiments et des carottes de tourbe datés au radiocarbone plus longs et plus anciens, qui enregistrent les changements dans l'accumulation naturelle du Hg à l'époque précoloniale, avant les pratiques minières à grande échelle, indiquent une différence plus importante des dépôts de Hg. Les enregistrements millénaires des sédiments et de la tourbe montrent que le taux de HgAR a déjà augmenté 5 fois au cours de la transition vers la période précoloniale aux environs de 1450AD (Amos et al., 2015). Les facteurs d'enrichissement anthropiques de tous les temps ($EF_{alltime}$, rapport entre le 20ème siècle et le HgAR antérieur à 1450AD), déterminés dans les enregistrements de sédiments et de tourbe, vont donc de 16 à 26. Les valeurs obtenues pour Hg $EF_{alltime}$ sont principalement basées sur les archives de l'hémisphère Nord (HN) où la majorité des émissions anthropiques historiques de mercure ont eu lieu. Seuls trois enregistrements de tourbe de l'hémisphère sud (HS) ont été étudiés pour HgAR, mais ils sont tous incomplets (absence de chronologie récente ou de profil continu d'HgAR daté au ^{14}C), empêchant donc une évaluation complète de l'enrichissement en Hg atmosphérique dans l'HS.

Dans ce chapitre, nous présentons les HgAR dans quatre enregistrements de tourbe bien datés : l'île d'Amsterdam, les îles Malouines, ainsi que les tourbières de *Andorra* et *Harberton* (Terre de Feu, Argentine). Nous passons ensuite en revue tous les HgAR disponibles dans les sédiments et les tourbières tourbe de l'HS, comparons les facteurs d'enrichissement en mercure dans l'HN et discutons des résultats dans le contexte des émissions volcaniques de mercure révisées, des émissions historiques publiées de mercure anthropique et du cycle de mercure dans les deux hémisphères.

Nous observons que, contrairement aux enregistrements de l'HN, il n'y a qu'une faible augmentation (x1.4) des dépôts de mercure depuis le la période pré-anthropique (<1450AD) jusqu'à la période préindustrielle (1450-1880AD) dans l'SH. Nous constatons une augmentation d'un facteur 2 ultérieure des dépôts de Hg dans l'HS, de la période préindustrielle à la période industrielle du 20ème siècle dans les enregistrements combinés de tourbe et de sédiments. L'enrichissement absolu (x4) de Hg dans l'HS est bien inférieur à l'enrichissement absolu (x16) de Hg dans l'HN. Nous attribuons cette différence à une combinaison d'émissions anthropiques de Hg plus faibles dans le SH, et d'émissions marines de Hg plus élevées dans le SH, soutenues par une accumulation de Hg de fond naturel x2 plus élevée dans la tourbe du SH.

Dans l'ensemble, nos résultats suggèrent que les niveaux de fond de mercure dans les deux hémisphères sont différents et doivent être pris en compte dans les rapports internationaux d'évaluation du mercure et les objectifs de la politique environnementale.

Research article

Unequal anthropogenic enrichment of mercury in Earth's northern and southern hemispheres

(Under review in *Environmental Science & Technology*)

Unequal anthropogenic enrichment of mercury in Earth's northern and southern hemispheres.

Chuxian Li[1,2], Jeroen E. Sonke[2$], Gaël Le Roux[1], Natalia Piotrowska[3], Nathalie Van der Putten[4], Stephen J. Roberts[5], Tim Daley[6], Emma Rice[6], Roland Gehrels[7], Maxime Enrico[1,2,8], Dmitri Mauquoy[9], Thomas P. Roland[10], François De Vleeschouwer[11]

1. EcoLab, Université de Toulouse, CNRS, INPT, UPS, Toulouse, France.

2. Laboratoire Géosciences Environnement Toulouse, Université de Toulouse, CNRS, IRD, UPS, Toulouse, France.

3. Silesian University of Technology, Institute of Physics-CSE, Gliwice, Poland.

4. Faculty of Science, Vrije Universiteit Amsterdam, the Netherlands.

5. British Antarctic Survey, Cambridge, UK

6. School of Geography, Earth and Environmental Sciences, Plymouth University, Plymouth PL4 8AA, UK

7. Department of Environment & Geography, University of York, Heslington, York YO10 5NG, UK

8. Harvard John A. Paulson School of Engineering & Applied Sciences, Harvard University, Cambridge, MA, USA

9. Geography and Environment, School of Geosciences, University of Aberdeen, St Mary's Building, Aberdeen, AB24 3UF, UK

10. Geography, College of Life and Environmental Sciences, University of Exeter, UK

11. Instituto Franco-Argentino para el Estudio delClima y sus Impactos (UMI 3351 IFAECI/CNRS-CONICET-UBA), Universidad de Buenos Aires, Argentina

[$] Corresponding author: *jeroen.sonke@get.omp.eu*

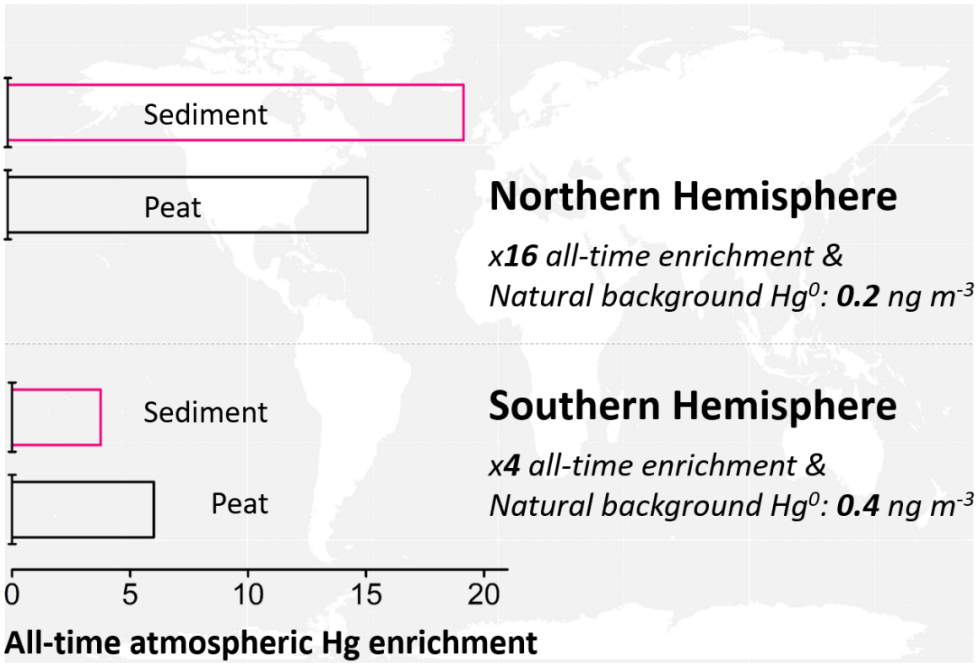

Abstract: Remote northern (NH) and southern hemisphere (SH) lake sediment and peat records of mercury (Hg) deposition show a ×3 to ×5 Hg enrichment since pre-industrial times (<1880AD), leading to the common perception that global atmospheric Hg enrichment is uniform. Longer radiocarbon-dated NH sediment and peat records document an earlier ×5 increase in Hg deposition from natural background (<1450AD) to pre-industrial (1450-1880AD) periods. Longer SH peat records are scarce however, which we address here by reconstructing atmospheric Hg deposition to 4 remote SH peatlands. We observe that contrary to NH records, there is only a small ×1.3 increase in SH Hg deposition across the natural background to pre-industrial periods. We find a subsequent ×2 increase in SH Hg deposition from the pre-industrial to the industrial 20th century period in combined peat and sediment records. The ×4 all-time SH Hg enrichment observed is far lower than the ×16 all-time enrichment in NH Hg deposition. We attribute this difference to a combination of lower anthropogenic Hg emissions in the SH, and higher natural atmospheric SH Hg levels, supported by ×2 higher natural background Hg accumulation in SH peat. We suggest that the higher SH natural Hg levels reflect the SH land-ocean distribution, with higher marine SH Hg emissions driven by transport of NH Hg to the SH by the Ocean conveyor belt. Our findings also suggest that atmospheric background Hg levels in the SH and NH (0.4 and 0.2 ng m^{-3}) are different and should be taken into account for environmental policy.

Main text:

Mercury (Hg) is a toxic trace metal that affects wildlife and human health [1–4]. Hg is discharged into the environment by natural processes, such as volcanism and weathering, and by human activities, including mining, coal burning and intentional use [5–7]. Elemental Hg^0, the dominant form of emissions, has a long atmospheric residence time of 6 to 12 months, which allows for its intra-hemispheric dispersion before being deposited to the Earth's surface, including remote environments [8]. Assessments of the extent of global Hg pollution have relied upon natural archives of Hg accumulation (e.g. sediment [9,10], peat [11], ice cores [12]), and on estimates of natural and anthropogenic Hg emissions [7]. Estimates of all-time anthropogenic Hg release suggest that a total of 1540 Gg has been released up to 2010, of which 470 Gg has been emitted to the atmosphere [7].

Since early work on lake sediment cores in the 1970s [13], hundreds of remote ^{210}Pb dated sediment cores have documented an approximate three- to five-fold increase in Hg accumulation rates (HgAR) from pre-industrial (1760-1880 AD) times to the late 20th century [1,9,10,14–16]. For some time, it was believed that sediment records were superior to peat records in recording atmospheric HgAR [14]. Inferred, higher Hg accumulation in peat records was thought to be related to ^{210}Pb mobility, and peat mass loss during remineralization. A recent review study [15] indicated that earlier peat vs sediment comparisons [14] used different reference periods to calculate Hg enrichment. Using coherent reference periods, dozens of peat archives and a small number glacier ice cores of atmospheric deposition also document 3 to 5-fold enrichment factors, similar to sediment records, since pre-industrial times (EF_{preind}) [1,15]. Both sediment and peat records have strengths and weaknesses, with ^{210}Pb and Hg mobility during sediment diagenesis and peat decomposition being potential factors of bias. Yet, both archives at remote locations record broadly similar Hg accumulation profiles across the past millennium, despite differences in archive functioning, and therefore warrant further comparison across Earth's two hemispheres. Regarding archive functioning, lake sediments integrate Hg deposition to a larger watershed, Hg storage in soils, followed by Hg run-off and in-lake cycling leading to a longer Hg residence-time before deposition to sediments. Peatlands integrate Hg deposition directly from the atmosphere [15,17,18], leading to a more direct response of peat archives to atmospheric Hg^0 levels. This can generally be recognized by the 2-fold drop in HgAR from the 1970s to the 1990s in peat [15], which is absent in sediment records, and which mirrors the well-documented decrease in Hg emissions and observed atmospheric Hg^0 levels [7,19,20]. A review of Hg stable

isotope composition of peat and lake sediments indicates that in both media, 75% of Hg derives from vegetation uptake of atmospheric Hg^0 [17], which further justifies comparing both archives.

Longer radiocarbon-dated NH sediment and peat cores probe changes in the natural background Hg accumulation during pre-colonial times, before large-scale mining practices, and indicate a more dramatic difference in Hg deposition. Millennial sediment and peat records show that HgAR already increased five-fold during the earlier transition from pre-large-scale mining to pre-colonial times around approximately 1450 AD [15]. All-time anthropogenic Hg enrichment factors ($EF_{alltime}$, the ratio of 20th century to pre-1450AD HgAR), determined in sediment and peat records therefore ranges from 16 to 26 [15]. The cause for the increase in NH Hg enrichment around 1450AD is debated. Hg inventory and modeling studies have argued for enhanced Hg emissions from Spanish colonial silver and gold mining [21–23]. Other studies argue that Hg associated with mining has been immobilized in mining waste, rather than volatilized [10,24]. A study on Hg stable isotopes in peat has recently shown evidence how enhanced deforestation during the Middle Ages may have impacted regional atmospheric Hg dynamics in Europe with lower vegetation uptake of Hg, and wood burning emissions leading to enhanced atmospheric Hg concentrations and deposition [19]. What nearly all the above cited studies have in common, is that they are situated in the northern hemisphere (NH) where the majority of historical anthropogenic Hg emissions have taken place. Lake sediment records of Hg accumulation have been studied in the SH and will be reviewed here. Three southern hemisphere (SH) peat records have been studied for HgAR [25,26], but are all incomplete (see Methods, and Extended Data 2) and preclude a rigorous assessment of SH atmospheric Hg enrichment based on both sediment and peat archives.

In this study we extend the limited number of peat archives studied in the SH, by investigating Hg accumulation rates in four radiocarbon and ^{210}Pb and ^{14}C bomb-pulse dated SH peat records. We then review all the existing SH sediment and peat HgAR (Extended Data 2), compare Hg enrichments factors to the NH, and discuss findings in the context of revised volcanic Hg emissions, published historical anthropogenic Hg emissions, and Hg cycling in both hemispheres. We do not include glacier ice cores in our review, due to the limited number of studies available, and we do not consider marine sediment records. Four reference time periods, operationally defined for NH natural archives elsewhere [15,16], will be used throughout: natural background (pre-1450AD), pre-industrial period (1450-1880 AD), 20th century extended HgAR maximum (20Cmax, approximately from 1940-1990; see also Methods), and the recent post-1990 modern period.

Methods

The study sites. We investigate 4 cores from remote ombrotrophic peat bogs in the SH mid-latitudes: Amsterdam Island (AMS, S-Indian Ocean), Falkland Islands (SCB, San Carlos bog, Islas Malvinas, S-Atlantic Ocean), Andorra and Harberton (AND, HAR, Tierra del Fuego, Argentina) (SI Appendix Table S1; Figure S1; Text S1; Extended Data 1). These four sites are situated in the Southern Westerly wind belt, far away from anthropogenic Hg sources, which makes them ideal recorders of SH remote atmospheric Hg deposition trends. Details about the field campaigns and sampling sites are given in SI Appendix Table S1 and Text S1. After collection, all the cores were photographed, described and packed in plastic film and PVC tubes and shipped to EcoLab, Toulouse, France. There, the cores were cut and processed following published trace metal clean protocols, freeze-dried and stored dry until analysis.

Chronology. Age model output of the AMS peat core is adopted from [28]. In brief, a total of 20 samples were picked for plant macrofossils and subsequently radiocarbon-dated at the LMC14 Artemis Laboratory (Saclay, France, SacA code) or GADAM center (Gliwice, Poland, GdA code). Recent age control in the AMS peat core is based upon 4 post-bomb radiocarbon dates [29] together with ^{210}Pb dating using the constant rate of supply model, and ^{137}Cs, ^{241}Am [30]. A total of 9 samples of plant macrofossils/charcoal from SCB 10 and 13 samples of *Sphagnum* macrofossils from AND and HAR respectively, were radiocarbon dated. These radiocarbon samples were pre-treated and graphitized at the GADAM center (Gliwice, Poland, GdA code) [31]. Subsequently, their ^{14}C concentration in graphite was measured at the DirectAMS Laboratory (Bothell, WA, USA; [32]). The NIST Oxalic Acid II standard was used for normalization, and black coal used as a blank. A total of 22 samples from the top 62 cm of the SCB peat core were selected for ^{210}Pb measurement by alpha counting to constrain the recent age (see Extended Data 1). The recent age control of the AND and HAR peat cores derive from 5 and 10 post-bomb radiocarbon dates, respectively [29,33].

Details of radiocarbon dates are summarized in SI Appendix Table S2. Age-depth models were generated from a combination of radiocarbon dating, post-bomb and ^{210}Pb dating with the Bacon package within R software [34], using the SHCal13 calibration curve for positive ^{14}C ages [35], while the post-bomb radiocarbon dates were calibrated with SH zone 1-2 curve [36]. The prior settings and model outputs are presented in SI Appendix Figure S2. The modelled median age was used for calculating and plotting HgAR against time (Figure 1). The average age uncertainties (1-sigma) derived from the age-depth models range from 1-5 years for the topmost part of the cores, up to ca. 100 years around 1000 AD. The investigated peat profiles of AMS,

SCB, AND, and HAR cover periods of 6600, 2000, 200 and 800 years, respectively. Corresponding mean peat accumulation rates are 0.76, 0.85, 3.6 and 0.91 mm yr^{-1} respectively.

Peat Hg accumulation rates (HgAR). HgAR is calculated as the product of Hg concentration (ng g^{-1}), peat density (g cm^{-3}) and peat mass accumulation rate (g m^{-2} yr^{-1}). Peat density was determined for each 1 cm slice by measuring its volume using a Vernier caliper and dry peat mass after freeze-drying. Peat samples were analyzed for total Hg (THg) concentration on a combustion cold vapor atomic absorption spectrometer (CV-AAS, Milestone DMA-80) at the University of Toulouse, France. The IPE 176 CRM (Reed / *Phragmites communis*), NIST 1632d (Coal), and BCR 482 (Lichen) were analyzed with mean recoveries ranging from 93-100% (SI Appendix Table S3). Replicate/triplicate analyses of THg in peat samples were found to vary by less than 6% (1σ). Profiles of peat Hg concentration in AMS, SCB, AND, and HAR are shown in SI Appendix Figure S5. Peat mass accumulation rate was determined from the age models and dry peat mass. All raw data is summarized in Extended Data 1.

Literature review, reference time periods and statistics. Based on a literature review we retained the remote HgAR records from SH lake sediments and peat records in Southern South America, lake sediments in New Zealand, lake sediments in East Africa, and lake sediments in Antarctica (see Extended data 2 for details). We did not retain: a lake sediment core 6 km downstream from the Potosi mine (Bolivia) with pronounced local mining influences on HgAR [38]; a lake sediment core in the Patagonian volcanic zone with multiple tephra layers associated with high HgAR [39]. Two remote Bolivian cores and one Peruvian core also showed evidence for the release of Hg due to regional Spanish colonial mining activities [26,40], but were retained in Extended Data 2. NH remote sediment and peat records were updated from [15]. Extended Data 2 indicates which records were only partially used, often due to lack of recent ^{210}Pb or ^{14}C bomb pulse dates. This applies in particular to three SH peat records, where one lacks a recent ^{210}Pb chronology and therefore 20Cmax and pre-industrial HgAR [26], one lacks pre-1988 layers [37], and one is nearly complete [25], except for the 1826-1935 period, which we extrapolate (see Extended Data 2).

We use four reference time periods, based on previous studies and which were originally operationally derived for NH natural archives [15]: natural background (pre-1450AD), pre-industrial period (1450-1880AD), 20th century extended HgAR maximum (20Cmax, approx. 1940-1990), and the recent, modern period (post-1990AD). The operational cut-off years, e.g. 1450, 1880, 1990, are mean values based on the remote NH sediment (n=49) and peat cores (n=19) reviewed here. In other words, each archive and each regional context shows variation

in the exact timing of gradual or abrupt increases (~1450, ~1880) or decreases (~1990) in HgAR (Extended Data 2). Several long SH sediment records probe the effect of climate change on variations in HgAR during the Holocene and since the last glacial maximum. Depending on watershed type and location these studies document substantial natural variability in HgAR that is beyond the scope of this study, but no less important. Therefore, in order to assess to the best of our ability the impact of humans on recent, millennial atmospheric Hg enrichment, we integrated natural background HgAR between on average -1700BC to 1450AD, but on occasion as far back as 10,000BC (Extended Data 2).

Statistical descriptions are parametric (mean, standard deviation (SD)) for normally distributed HgAR and enrichment factors (EF), and non-parametric (median, Q25% and Q75% quartiles, interquartile range (IQR)) for non-normally distributed HgAR and EF. Outlier tests were performed only on EFs, and observations were excluded (in *italics* in Extended Data 2) when they exceeded 2*SD around the mean, or 1.5*IQR around Q25% and Q75%. All data generated or analyzed during this study are included in the SI Appendix.

Results & Discussion

HgAR profiles in the four SH peat records show maximum levels during the 20th century (Figure 1). Natural background (pre-1450 AD) levels in the HAR, SCB and AMS cores show mean HgAR of 4.9 ± 3.5 μg m^{-2} yr^{-1} (mean, 1σ, n=3, Figure 1). Pre-industrial HgAR in the four cores averages 5.9 ± 2.5 μg m^{-2} yr^{-1}, 20Cmax HgAR is 20 ± 7.9 μg m^{-2} yr^{-1}, and modern HgAR is 9.7 ± 2.9 μg m^{-2} yr^{-1} (means, 1σ, n=4, Figure 1). Whereas absolute HgAR for the different time periods vary between cores, the relative HgAR changes within a core are similar and can be expressed by enrichment factors, EF. The four SH cores show evidence for 3.1-fold (mean, 1σ=1.6) enhanced net Hg deposition during the 20Cmax, compared to the pre-industrial period (EF_{preind}, Table 1), which at first sight appears similar to NH natural archives. SH historical HgARs have thus far been studied in 18 lake sediment and 3 peat cores (see Methods and Extended Data 2 for full list). Figure 2 summarizes HgAR and EF in all published SH sediment and peat records, as well as updated NH data for the reference periods of interest (Extended Data 2). The temporal evolution of HgAR in peat and sediment cores is similar between the NH and SH in a broad sense (Figure 2a, b). HgAR increases stepwise from natural background to pre-industrial and then to 20Cmax periods in both sediment and peat archives. Similar to NH peat records [15], modern-day (post-1990) HgAR in SH peat decreases by a factor of 2 from 20Cmax values (SI Appendix Figure S4), in line with declining global anthropogenic Hg emissions and deposition from the 1970s to 2000s (Figure S6 [19,20]). Sediment records in both

the NH and SH do not record this decrease (Figure S4), presumably due to the longer residence of Hg in lake catchment soils, leading to a slower recovery of Hg levels in soil run-off into lakes.

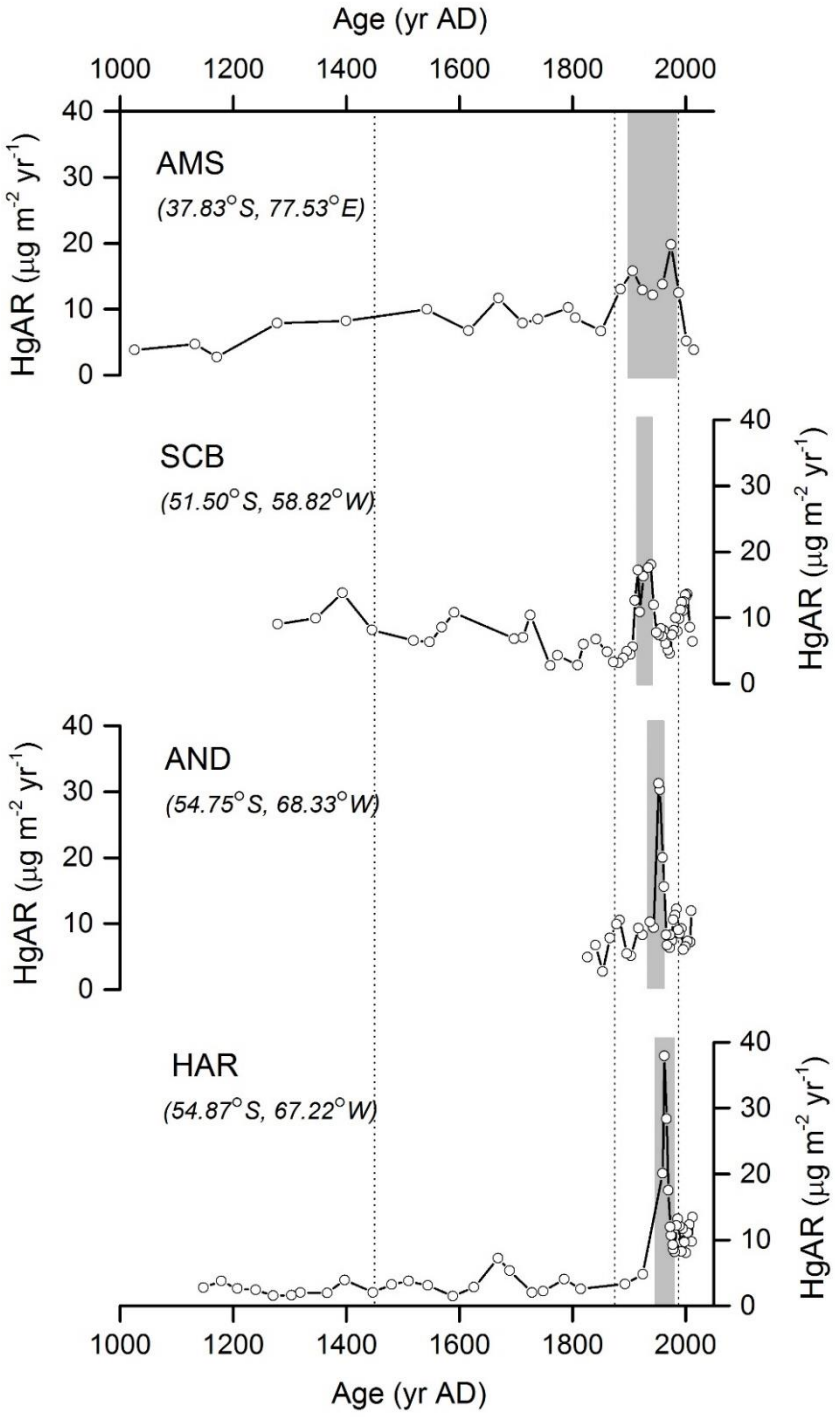

Figure 1. Profiles of Hg accumulation rates (HgAR) in the peat cores from Amsterdam Island (AMS), Falkland Islands (SCB, Islas Malvinas), Andorra and Harberton (AND, HAR, Tierra del Fuego). Vertical dashed lines operationally separate the natural background (pre-1450AD), pre-industrial (1450-1880AD), the extended 20th century maximum HgAR (20Cmax, grey bars) and modern (post-1990AD) reference periods, following reference [15]).

Table 1. Hg accumulation rate (HgAR) enrichment factor observed in the peat profiles from this study. AMS, Amsterdam Island; SCB, the Falkland Islands; AND, HAR, Andorra and Harberton, Argentina. 'Pre-ind', pre-industrial; '20Cmax', extended 20th century maximum HgAR (see Methods); 'p/b', pre-industrial/background.

	Pre-ind/ background ($EF_{p/b}$)	20Cmax/Pre-ind (EF_{Preind})	20Cmax/background ($EF_{Alltime}$)
AMS	1.6	1.7	2.7
SCB	0.6	2.5	1.5
AND		3.0	
HAR	1.4	5.3	7.3

The historical evolution of trends in hemispheric HgARs are shown in EF_{preind} and $EF_{alltime}$ diagrams (Figure 2c, 2d). Pre-industrial to 20Cmax enrichment in HgAR (EF_{preind}) is higher in peat compared to sediment in both NH and SH (Kruskal-Wallis test, NH, P=0.006; SH, P=0.09). EF_{preind} is higher in the NH than in the SH for sediment (3.2 vs 1.8), but not peat (4.6 vs 3.1; Kruskal-Wallis test, peat, P=0.15; sediment P=0.0004; Figure 2c, 2d; Figure 3a). We find in particular that in long, millennial NH records, HgAR increased 3.9-fold in peat and 4.2-fold in sediments across the natural background to pre-industrial periods ($EF_{p/b}$, Figure 2c, d, Table 2). On the contrary, $EF_{p/b}$ in SH millennial records show negligible, mean 1.2-fold enrichment in peat, to a small, median 1.4-fold enrichment in sediments across the natural background (<1450AD) to pre-industrial periods. Consequently, all-time NH enrichment factors, $EF_{alltime}$, reach 16 in peat and 19 in sediments and are larger than the 6.0-fold and 3.8-fold Hg all-time enrichment in SH peat and sediments (Table 2; Figure 3B; Kruskal-Wallis test, P = 0.02 for peat, P = 0.1 for sediment). Historical Hg emission inventory and associated box modeling studies have suggested that the 4-fold increase in NH HgAR across around 1450AD is related to Spanish colonial Hg and silver mining [7,21]. This interpretation has been refuted by studies arguing that the associated emissions are overestimated [10] and references therein). Estimating silver and gold mining Hg emissions hinges on ill-constrained emission factors. SH archives show little evidence of Spanish colonial mining impacts in South-America on large scale SH atmospheric Hg deposition (Figure 2). Similarly, neither NH peat, nor sediment records show evidence of a pronounced late 19th century peak in HgAR, in contrast to large estimated N-American gold-rush Hg emissions [7]. We therefore suggest the 4-fold NH increase in HgAR around 1450AD is more likely related to demography driven changes in land-use (e.g. deforestation, wood, peat combustion, urbanization etc.), than to direct Spanish colonial mining

emissions of Hg to the global pool. In summary, our findings based on combined sediment and peat archive HgAR observations, suggest that all-time atmospheric Hg enrichment during the 20Cmax period (1940-1990) reached 11-fold globally ($EF_{alltime}$ = 4-26, 25%-75% quartiles, n=38), 16-fold in the NH ($EF_{alltime}$ = 10-30, 25%-75% quartiles, n=27), and 4-fold in the SH ($EF_{alltime}$ = 2-6, 25%-75% quartiles, n=11). Atmospheric Hg levels decreased from the 1970's to the 2000's by a factor of about 2, a trend that is recorded in the peat archive HgAR (Figure S4, S6). Natural background to modern period (1990-2010) Hg enrichment, $EF_{mod/bck}$, based on peat archives, is currently 10-fold globally (±7.7, 1σ, n=18), 12 in the NH (±7.5, 1σ, n=14) and 3 in the SH (±2.5, 1σ, n=4).

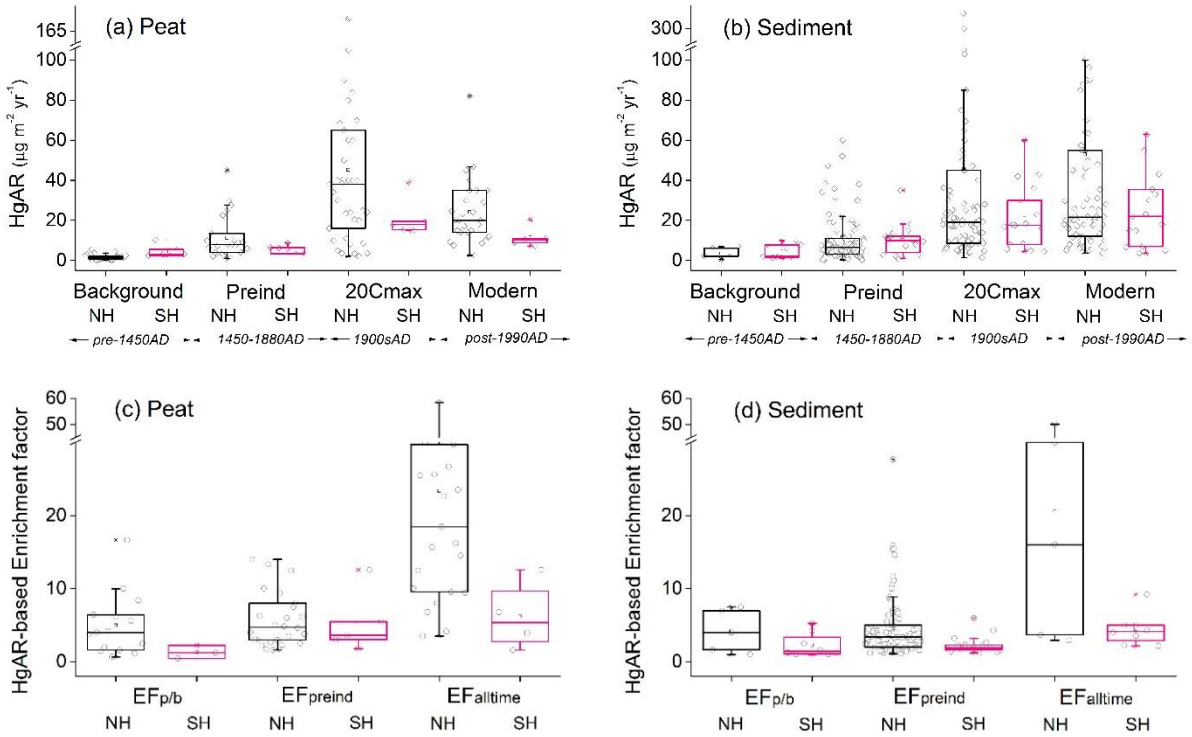

Figure 2. Review of published Hg accumulation rates (HgAR) and enrichment factors (EF) in NH and SH peat and sediment cores for different reference time periods. HgAR (µg m^{-2} yr^{-1}) and EF in peat (A), (C) and sediment (B), (D) profiles during different periods: Natural background (pre-1450AD), pre-industrial (1450-1880AD), extended 20th century maximum (20Cmax, defined as the broad 20th century HgAR peak, and modern period (post-1990AD). $EF_{p/b}$: EF from natural background to pre-industrial period. EF_{preind}: EF from pre-industrial to 20Cmax. $EF_{alltime}$: EF from natural background to 20Cmax.

Table 2. Summary of Hg accumulation rate (HgAR) enrichment factors (EF) in global peat and sediment records. 'Pre-ind', pre-industrial; '20Cmax', extended 20th century maximum HgAR (see Methods); 'p/b', pre-industrial/background; 'modern/back', 'modern/background'; NH, northern hemisphere; SH, southern hemisphere.

	Pre-ind /background ($EF_{p/b}$)		20Cmax/pre-ind (EF_{Preind})		20Cmax/background ($EF_{alltime}$)		Modern/ background ($EF_{modern/back}$)	
Global-sediment	1.6	n=13	2.9	n=101	4.3	n=11	5.0	n=11
Global-peat	2.5	n=17	4.3	n=30	14.5	n=25	10.3	n=18
NH-sediment+peat	4.0	n=20	3.3	n=111	16.2	n=27	12.2	n=20
SH-sediment+peat	1.3	n=10	1.9	n=19	4.3	n=11	3.5	n=9
NH-sediment	4.2	n=5	3.2	n=86	19.0	n=5	22.5	n=5
NH-peat	3.9	n=14	4.6	n=25	16.2	n=21	12.3	n=14
SH-sediment	1.4	n=8	1.8	n=15	3.8	n=7	5.0	n=6
SH-peat	1.2	n=3	3.1	n=4	6.0	n=4	3.1	n=4

[1]the number of records, n, do not always add up due to the 2σ outlier tests applied, for ex. SH sediment, n=8, SH peat, n=3, but SH sediment+peat, n=10. See Methods and Extended Data 2 for details on outlier tests.

In the following sections we will further discuss this sizeable difference in hemispheric $EF_{alltime}$ in terms of NH and SH Hg emissions, and in terms of natural background HgAR. The all-time NH and SH enrichment factors based on Hg deposition to natural archives can be directly compared to independent estimates of NH and SH emission factors, i.e. $EF_{emission}$, the ratio of primary, i.e. first time, total Hg emission flux to natural Hg emission flux ($EF_{emission} = F_{anthro}+F_{natural}/(F_{natural}$; Table 3). In doing so, we make the assumption that re-emission of previously deposited natural and anthropogenic Hg is proportional to primary emissions. By separating NH and SH emission factors we also assume limited hemispheric exchange of atmospheric Hg, supported by the short global lifetime of Hg of 5 months in state of the art atmospheric Hg models [8]. Global anthropogenic Hg emissions to the atmosphere have been estimated at 2.4 ± 0.5 Gg yr^{-1} during the 20Cmax period (1940-1990) [7]. Natural Hg emissions are the sum of volcanic degassing and crustal degassing from naturally enriched soils. Passive, non-eruptive, volcanic degassing is an important direct natural source of Hg to the atmosphere, with a previously estimated total flux of 76 ± 30 Mg yr^{-1} (1σ) based on observed Hg/SO_2 ratios of 7.8 ± 1.5 × 10^{-6} and a global passive degassing SO_2 flux of 9.7 Tg yr^{-1} [41,42]. Recent advances in remote sensing of SO_2 from 2005-2015 indicate a higher SO_2 flux of 23.0 ± 2.3 Tg yr^{-1} (1σ) [43], which we use here to revise the global passive volcanic degassing Hg flux to 179 ± 39 Mg yr^{-1} (1σ). Eruptive volcanic SO_2 emissions are indicated to be one order of magnitude smaller

than passive degassing at 2.6 ± 2.6 Tg yr^{-1} [43]. Assuming similar Hg/SO_2 ratios, we estimate eruptive volcanic Hg emissions at 20 ± 20 Mg yr^{-1}, and total volcanic Hg emissions as the sum of eruptive and passive emissions at 200 ± 60 Mg yr^{-1} (1σ). Global emissions from naturally enriched soils can be estimated from reviews of flux chamber and soil Hg studies [44,45] and equal 135 ± 40 Mg yr^{-1} (1σ, Table 3). These bottom-up estimates indicate that global anthropogenic 20Cmax Hg emissions of 2.4 Gg yr^{-1} have been 7.3 times larger than global natural Hg emissions of 0.34 Gg yr^{-1}, and result in a global $EF_{emission}$ of 8.2. Volcanic SO_2 emissions are similar for the NH and SH (11.8 vs. 11.2 Tg yr^{-1}) [43], leading to NH and SH Hg emission budgets of 0.1 Gg yr^{-1} each. We scale naturally enriched soil emissions with continental surface area, to estimate 91 and 44 Mg yr^{-1} in NH and SH. The 20Cmax 2.4 Gg yr^{-1} global anthropogenic Hg emissions to the atmosphere were released for 80% to the NH and 20% to the SH [7]. We therefore estimate hemispheric $EF_{emission}$, for the NH at 11.2 ± 4.6 and for the SH at 4.4 ± 1.5 (1σ). The SH $EF_{emission}$ of 4.4 is in good agreement with the natural archive-based SH $EF_{alltime}$ of 4. The NH $EF_{emission}$ of 11 however, underestimates the NH $EF_{alltime}$ of 16 by 43%, suggesting that either the 2.0 ± 0.5 Gg yr^{-1} NH anthropogenic Hg emissions to air [7] are underestimated, or that the NH natural primary emissions of 91 ± 27 Mg yr^{-1} are overestimated. There is a final caveat in this analysis that deserves a mention: We assume that the ill-constrained, but potentially important, submarine volcanic Hg flux [46] is locally or regionally deposited to marine sediments before any of it can be emitted to the atmosphere. This assumption is based on evidence for Hg scavenging in submarine hydrothermal plumes [47,48].

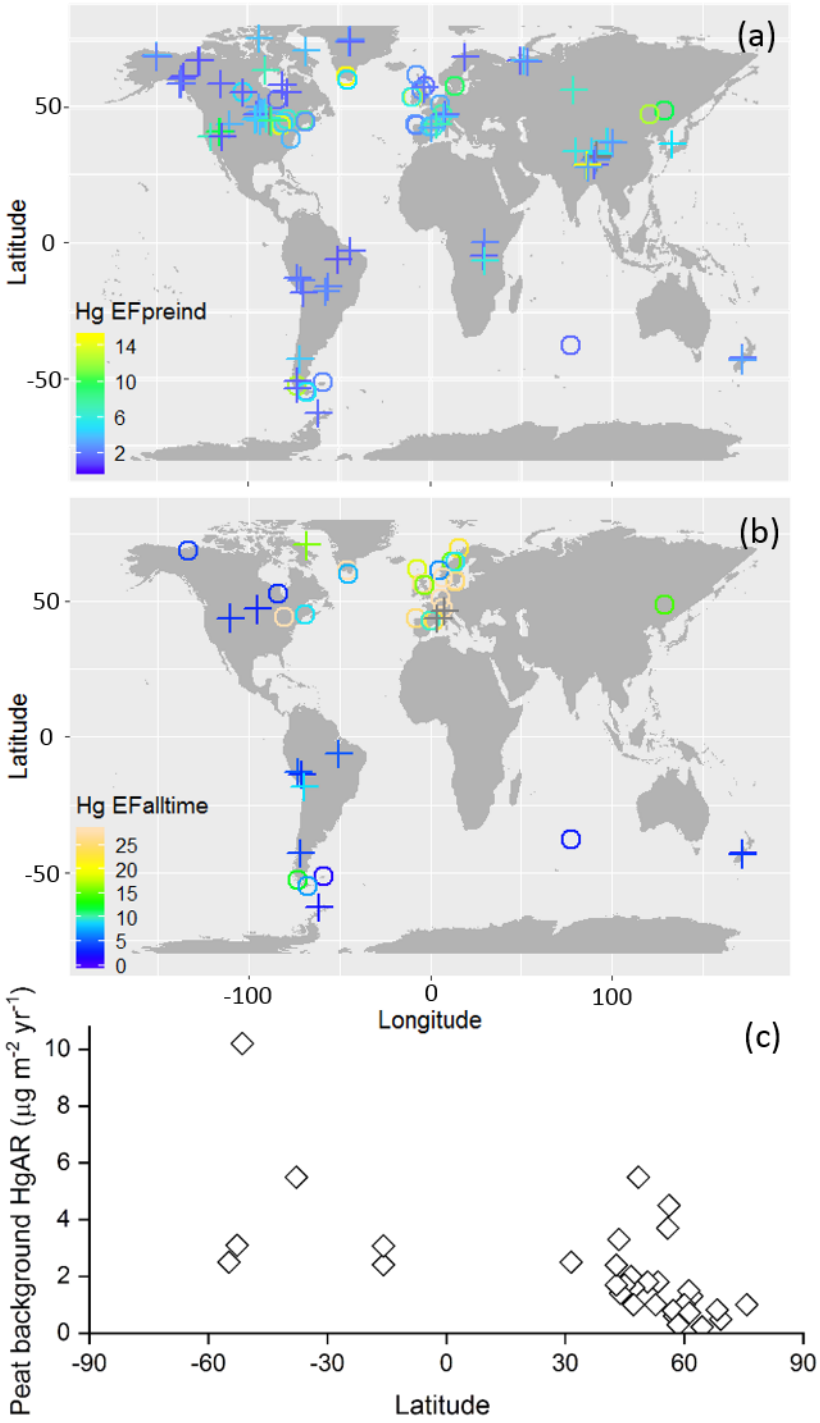

Figure 3. Hg enrichment factors between different reference time periods and peat background Hg accumulation rate. Enrichment factors (EF) in Hg accumulation rates for a) 20th century industrial relative to pre-industrial periods ($EF_{pre\text{-}ind}$, 1450-1880AD). b) 20th century industrial relative to natural background periods ($EF_{alltime}$, pre-1450AD century). Circles represent peat cores, and crosses sediment cores. c) Natural background Hg accumulation rate (pre-1450AD HgAR) in peat cores as a function of latitude. For details see Extended Data 2.

Table 3. Summary of natural and anthropogenic Hg emissions to the atmosphere (mean ± 1σ)

	NH	1σ	SH	1σ
passive volcanic degassing (this study) Mg y^{-1}	92	20	87	19
eruptive volcanic degassing (this study) Mg y^{-1}	10	10	10	10
crustal degassing (44, 45) Mg y^{-1}	91	27	44	13
anthropogenic 20Cmax emissions (7) Mg y^{-1}	2000	500	480	20
Mean $EF_{emission}$	11.2	4.6	4.4	1.5
Median $EF_{alltime}$	16.1	10-30 IQR	4.0	2-6 IQR

The important difference in NH and SH $EF_{alltime}$ is not only related to hemispheric differences in primary Hg emissions, but also to differences in natural background atmospheric Hg levels and HgAR. A notable outcome of the new SH peat records is that the natural SH background HgAR of 4.3 μg m^{-2} yr^{-1} in the SH mid-latitudes (30-60ºS) is x2 higher than the NH background HgAR of 1.7 μg m^{-2} yr^{-1} in the NH mid-latitudes (Kruskal-Wallis test, *P*=0.02, Figures 2a, 3c, S3). We therefore suggest that the marked NH/SH mid-latitude difference in HgAR is driven by ×2.5 higher natural atmospheric Hg levels in the SH, rather than climate factors. Climate factors, such as temperature and length of growth season only become visible in NH high latitude (>60ºN), where HgAR becomes limited by peat bog primary productivity, via the vegetation Hg^0 pump (18). The observation that the SH natural background HgAR is x2.5 higher than the NH background is likely an additional reason why the NH $EF_{alltime}$ of 16 is so much larger than the SH $EF_{alltime}$ of 4. Inter-hemispheric trends in atmospheric Hg have been previously investigated [49,50]. Observed mean atmospheric Hg^0 levels across monitoring networks for the modern, 1990-2010 period were 1.8 ng m^{-3} in the NH and 1.2 ng m^{-3} in the SH [51,52]. Modern-day SH Hg^0 levels are therefore higher than what would be expected based on estimates of modern NH and SH primary Hg emissions of 1.6 and 0.7 Gg yr^{-1} (Table 3). A key difference between the NH and SH is the land-ocean distribution, with the SH being only 19% land covered and the NH 39%. The land-ocean distribution plays an important role in atmospheric boundary layer Hg dynamics. A study on atmospheric Hg^0 seasonality, which is more pronounced in the NH and quasi-absent in the SH, suggested that the vegetation Hg pump, i.e. the foliar uptake of Hg^0 and sequestration in soils, is an important driver of NH atmospheric Hg^0 seasonality [18]. The SH has a smaller terrestrial vegetation and soil pool, and therefore likely has relatively higher atmospheric Hg^0 due to a weaker vegetation Hg pump. In addition coupled ocean-atmosphere Hg chemistry and transport models find stronger marine Hg^0 evasion in the SH than in the NH, mainly due to upwelling of Hg rich deep waters in the Southern Ocean [16,53].

The model studies suggest that SH atmospheric Hg^0 is largely controlled by these SH marine Hg^0 emissions [8,16]. These findings were recently confirmed by long-term observations on Hg^0 seasonality at the Cape Point, South-Africa monitoring station [54]. The 2-fold higher SH natural background HgAR in peat therefore echoes the higher than expected modern SH atmospheric Hg^0 levels, and both can potentially be explained by the hemispheric land-ocean distribution. We suggest here that the Ocean conveyor belt plays an important role in shuttling NH marine Hg to the SH in order to sustain the marine evasion driven, elevated natural atmospheric Hg levels in the SH. Such a mechanism is supported by the long estimated deep Ocean Hg lifetime, in excess of 1000 yr [16].

We use peat $EF_{modern/back}$ for both hemispheres (Table 2) to estimate what natural atmospheric Hg^0 levels may have been during pre-1450AD times. Dividing modern-day mean NH and SH atmospheric Hg^0 levels of 1.8 and 1.2 ng m^{-3} by $EF_{modern/back}$ yields natural background atmospheric Hg levels of 0.2 and 0.4 ng m^{-3} for the NH and SH. In summary, the lower SH enrichment in atmospheric Hg is due to a combination of lower SH anthropogenic Hg emissions, and higher SH background Hg levels driven by a lower SH land/ocean ratio which limits the terrestrial vegetation Hg pump and sustains higher natural marine Hg emissions. Observations and model simulations will need to assess if and when NH Ocean waters, charged with multiple centuries of anthropogenic Hg will resurface in the SH. Overall, our findings suggest that both background Hg levels and all-time Hg enrichment in the NH and SH are different and should be taken into account in environmental policy objectives.

Acknowledgements

Field work was funded by the French Polar Institute (IPEV, Brest, France) through the IPEV Programmes 1066 "PARAD" (to F.D.V.) and 1065 PALATIO (to N.V.P. and E. Michel). J.E.S. acknowledges funding from the H2020 ERA-PLANET (689443) iGOSP and iCUPE programmes. We thank the South Atlantic Environmental Research Institute (SAERI) for providing laboratory facilities in the Falkland Islands and E. Brook (Falkland Islands Government Training Centre) for logistical support. We are grateful to N. Marchand (IPEV) for the logistical support, C. Marteau for making the sampling possible in very restricted areas of the TAAF Nature Reserve, and N. Roberts for help processing the San Carlos core and scientific discussions. We thank A. Coronato, R. López and V. Pancotto from CADIC-CONICET (Ushuaia) for the field campaigns in Andorra and Harberton. Radiocarbon ages were obtained as part of the Idex Peat3 project of the University of Toulouse and through the national service

support: Artemis-INSU-CNRS (to G.L.R.). C.L.'s PhD is supported by a scholarship from the China Scholarship Council.

Author Contributions

J.E.S and F.D.V initiated and designed the project. All authors were involved in all field sampling and/or laboratory analyses. C.L. and J.E.S wrote the manuscript on which all authors commented.

Data availability statement

All data generated or analyzed during this study are included in this published article (and its SI Appendix). Extended Data 1 and 2, please see separated files.

References

(1) UNEP. *Global Mercury Assessment 2018*; 2018.

(2) Sunderland, E. M.; Li, M.; Bullard, K. Decadal Changes in the Edible Supply of Seafood and Methylmercury Exposure in the United States. *Environ. Health Perspect.* 2018, *126* (1), 017006. https://doi.org/10.1289/EHP2644.

(3) Mason, R. P.; Choi, A. L.; Fitzgerald, W. F.; Hammerschmidt, C. R.; Lamborg, C. H.; Soerensen, A. L.; Sunderland, E. M. Mercury Biogeochemical Cycling in the Ocean and Policy Implications. *Environ. Res.* 2012, *119*, 101–117. https://doi.org/10.1016/j.envres.2012.03.013.

(4) Chen, C. Y.; Driscoll, C. T.; Eagles-Smith, C. A.; Eckley, C. S.; Gay, D. A.; Hsu-Kim, H.; Keane, S. E.; Kirk, J. L.; Mason, R. P.; Obrist, D.; et al. A Critical Time for Mercury Science to Inform Global Policy. *Environ. Sci. Technol.* 2018, *52* (17), 9556–9561. https://doi.org/10.1021/acs.est.8b02286.

(5) Pirrone, N.; Cinnirella, S.; Feng, X.; Finkelman, R. B.; Friedli, H. R.; Leaner, J.; Mason, R.; Mukherjee, A. B.; Stracher, G. B.; Streets, D. G.; et al. Global Mercury Emissions to the Atmosphere from Anthropogenic and Natural Sources. *Atmospheric Chem. Phys.* 2010, *10* (13), 5951–5964. https://doi.org/10.5194/acp-10-5951-2010.

(6) Pacyna, E. G.; Pacyna, J. M.; Sundseth, K.; Munthe, J.; Kindbom, K.; Wilson, S.; Steenhuisen, F.; Maxson, P. Global Emission of Mercury to the Atmosphere from Anthropogenic Sources in 2005 and Projections to 2020. *Atmos. Environ.* 2010, *44* (20), 2487–2499. https://doi.org/10.1016/j.atmosenv.2009.06.009.

(7) Streets, D. G.; Horowitz, H. M.; Jacob, D. J.; Lu, Z.; Levin, L.; ter Schure, A. F. H.; Sunderland, E. M. Total Mercury Released to the Environment by Human Activities. *Environ. Sci. Technol.* 2017, *51* (11), 5969–5977. https://doi.org/10.1021/acs.est.7b00451.

(8) Horowitz, H. M.; Jacob, D. J.; Zhang, Y.; Dibble, T. S.; Slemr, F.; Amos, H. M.; Schmidt, J. A.; Corbitt, E. S.; Marais, E. A.; Sunderland, E. M. A New Mechanism for Atmospheric Mercury Redox Chemistry: Implications for the Global Mercury Budget. *Atmospheric Chem. Phys.* 2017, *17* (10), 6353–6371. https://doi.org/10.5194/acp-17-6353-2017.

(9) Fitzgerald, W. F.; Engstrom, D. R.; Mason, R. P.; Nater, E. A. The Case for Atmospheric Mercury Contamination in Remote Areas. *Environ. Sci. Technol.* 1998, *32* (1), 1–7. https://doi.org/10.1021/es970284w.

(10) Engstrom, D. R.; Fitzgerald, W. F.; Cooke, C. A.; Lamborg, C. H.; Drevnick, P. E.; Swain, E. B.; Balogh, S. J.; Balcom, P. H. Atmospheric Hg Emissions from Preindustrial Gold and Silver Extraction in the Americas: A Reevaluation from Lake-Sediment Archives. *Environ. Sci. Technol.* 2014, *48* (12), 6533–6543. https://doi.org/10.1021/es405558e.

(11) Martínez-Cortizas, A. Mercury in a Spanish Peat Bog: Archive of Climate Change and Atmospheric Metal Deposition. *Science* 1999, *284* (5416), 939–942. https://doi.org/10.1126/science.284.5416.939.

(12) Schuster, P. F.; Krabbenhoft, D. P.; Naftz, D. L.; Cecil, L. D.; Olson, M. L.; Dewild, J. F.; Susong, D. D.; Green, J. R.; Abbott, M. L. Atmospheric Mercury Deposition during the Last

270 Years: A Glacial Ice Core Record of Natural and Anthropogenic Sources. *Environ. Sci. Technol.* 2002, *36* (11), 2303–2310. https://doi.org/10.1021/es0157503.

(13) Thomas, R. L. The Distribution of Mercury in the Sediments of Lake Ontario. *Can. J. Earth Sci.* 1972, *9* (6), 636–651. https://doi.org/10.1139/e72-054.

(14) Biester, H.; Bindler, R.; Martinez-Cortizas, A.; Engstrom, D. R. Modeling the Past Atmospheric Deposition of Mercury Using Natural Archives. *Environ. Sci. Technol.* 2007, *41* (14), 4851–4860. https://doi.org/10.1021/es0704232.

(15) Amos, H. M.; Sonke, J. E.; Obrist, D.; Robins, N.; Hagan, N.; Horowitz, H. M.; Mason, R. P.; Witt, M.; Hedgecock, I. M.; Corbitt, E. S.; et al. Observational and Modeling Constraints on Global Anthropogenic Enrichment of Mercury. *Environ. Sci. Technol.* 2015, *49* (7), 4036–4047. https://doi.org/10.1021/es5058665.

(16) Zhang, Y.; Jaeglé, L.; Thompson, L.; Streets, D. G. Six Centuries of Changing Oceanic Mercury: Anthropogenic Mercury in Ocean. *Glob. Biogeochem. Cycles* 2014, *28* (11), 1251–1261. https://doi.org/10.1002/2014GB004939.

(17) Enrico, M.; Roux, G. L.; Marusczak, N.; Heimbürger, L.-E.; Claustres, A.; Fu, X.; Sun, R.; Sonke, J. E. Atmospheric Mercury Transfer to Peat Bogs Dominated by Gaseous Elemental Mercury Dry Deposition. *Environ. Sci. Technol.* 2016, *50* (5), 2405–2412. https://doi.org/10.1021/acs.est.5b06058.

(18) Jiskra, M.; Sonke, J. E.; Obrist, D.; Bieser, J.; Ebinghaus, R.; Myhre, C. L.; Pfaffhuber, K. A.; Wängberg, I.; Kyllönen, K.; Worthy, D.; et al. A Vegetation Control on Seasonal Variations in Global Atmospheric Mercury Concentrations. *Nat. Geosci.* 2018, *11* (4), 244–250. https://doi.org/10.1038/s41561-018-0078-8.

(19) Enrico, M.; Le Roux, G.; Heimbürger, L.-E.; Van Beek, P.; Souhaut, M.; Chmeleff, J.; Sonke, J. E. Holocene Atmospheric Mercury Levels Reconstructed from Peat Bog Mercury Stable Isotopes. *Environ. Sci. Technol.* 2017, *51* (11), 5899–5906. https://doi.org/10.1021/acs.est.6b05804.

(20) European Monitoring and Evaluation Programme. https://www.emep.int/ 2016.

(21) Streets, D. G.; Devane, M. K.; Lu, Z.; Bond, T. C.; Sunderland, E. M.; Jacob, D. J. All-Time Releases of Mercury to the Atmosphere from Human Activities. *Environ. Sci. Technol.* 2011, *45* (24), 10485–10491. https://doi.org/10.1021/es202765m.

(22) Streets, D. G.; Horowitz, H. M.; Lu, Z.; Levin, L.; Thackray, C. P.; Sunderland, E. M. Five Hundred Years of Anthropogenic Mercury: Spatial and Temporal Release Profiles. *Environ. Res. Lett.* 2019, *14* (8), 084004. https://doi.org/10.1088/1748-9326/ab281f.

(23) Amos, H. M.; Jacob, D. J.; Streets, D. G.; Sunderland, E. M. Legacy Impacts of All-Time Anthropogenic Emissions on the Global Mercury Cycle: GLOBAL IMPACTS OF LEGACY MERCURY. *Glob. Biogeochem. Cycles* 2013, *27* (2), 410–421. https://doi.org/10.1002/gbc.20040.

(24) Cooke, C. A.; Hintelmann, H.; Ague, J. J.; Burger, R.; Biester, H.; Sachs, J. P.; Engstrom, D. R. Use and Legacy of Mercury in the Andes. *Environ. Sci. Technol.* 2013, *47* (9), 4181–4188. https://doi.org/10.1021/es3048027.

(25) Biester, H.; Kilian, R.; Franzen, C.; Woda, C.; Mangini, A.; Schöler, H. F. Elevated Mercury Accumulation in a Peat Bog of the Magellanic Moorlands, Chile (53°S) – an Anthropogenic Signal from the Southern Hemisphere. *Earth Planet. Sci. Lett.* 2002, *201* (3–4), 609–620. https://doi.org/10.1016/S0012-821X(02)00734-3.

(26) Guédron, S.; Ledru, M.-P.; Escobar-Torrez, K.; Develle, A. L.; Brisset, E. Enhanced Mercury Deposition by Amazonian Orographic Precipitation: Evidence from High-Elevation Holocene Records of the Lake Titicaca Region (Bolivia). *Palaeogeogr. Palaeoclimatol. Palaeoecol.* 2018, *511*, 577–587. https://doi.org/10.1016/j.palaeo.2018.09.023.

(27) De Vleeschouwer, F., Chambers, F.M. and Swindles, G.T.,. Coring and Sub-Sampling of Peatlands for Palaeoenvironmental Research. *Mires and peat*. 2010, *7*.

(28) Li, C.; Sonke, J.E.; Le Roux, G.; Van der Putten, N.; Piotrowska, N.; Jeandel C.; Mattielli N.; Benoit M.; Wiggs G.F.S.; De Vleeschouwer F. Holocene Dynamics of the Southern Hemisphere Westerly Winds over the Indian Ocean Inferred from a Peat Dust Deposition Record. *Quaternary Science Reviews* 2020, 231, 106169.

(29) Goodsite, M. E.; Rom, W.; Heinemeier, J.; Lange, T.; Ooi, S.; Appleby, P. G.; Shotyk, W.; van der Knaap, W. O.; Lohse, C.; Hansen, T. S. High-Resolution AMS ^{14}C Dating of Post-Bomb Peat Archives of Atmospheric Pollutants. *Radiocarbon* 2001, *43* (2B), 495–515. https://doi.org/10.1017/S0033822200041163.

(30) Appleby, P. G. Chronostratigraphic Techniques in Recent Sediments. In *Tracking Environmental Change Using Lake Sediments*; Last, W. M., Smol, J. P., Eds.; Kluwer Academic Publishers: Dordrecht, 2002; Vol. 1, pp 171–203. https://doi.org/10.1007/0-306-47669-X_9.

(31) Piotrowska, N. Status Report of AMS Sample Preparation Laboratory at GADAM Centre, Gliwice, Poland. *Nucl. Instrum. Methods Phys. Res. Sect. B Beam Interact. Mater. At.* 2013, *294*, 176–181. https://doi.org/10.1016/j.nimb.2012.05.017.

(32) Zoppi, U.; Crye, J.; Song, Q.; Arjomand, A. Performance Evaluation of the New AMS System at Accium BioSciences. *Radiocarbon* 2007, *49* (1), 171–180. https://doi.org/10.1017/S0033822200041990.

(33) Davies, L. J.; Appleby, P.; Jensen, B. J. L.; Magnan, G.; Mullan-Boudreau, G.; Noernberg, T.; Shannon, B.; Shotyk, W.; van Bellen, S.; Zaccone, C.; et al. High-Resolution Age Modelling of Peat Bogs from Northern Alberta, Canada, Using Pre- and Post-Bomb 14C, 210Pb and Historical Cryptotephra. *Quat. Geochronol.* 2018, *47*, 138–162. https://doi.org/10.1016/j.quageo.2018.04.008.

(34) Blaauw, M.; Christen, J. A. Flexible Paleoclimate Age-Depth Models Using an Autoregressive Gamma Process. *Bayesian Anal.* 2011, *6* (3), 457–474. https://doi.org/10.1214/11-BA618.

(35) Hogg, A. G.; Hua, Q.; Blackwell, P. G.; Niu, M.; Buck, C. E.; Guilderson, T. P.; Heaton, T. J.; Palmer, J. G.; Reimer, P. J.; Reimer, R. W.; et al. SHCal13 Southern Hemisphere Calibration, 0–50,000 Years Cal BP. *Radiocarbon* 2013, *55* (4), 1889–1903. https://doi.org/10.2458/azu_js_rc.55.16783.

(36) Hua, Q.; Barbetti, M.; Rakowski, A. Z. Atmospheric Radiocarbon for the Period 1950–2010. *Radiocarbon* 2013, *55* (4), 2059–2072. https://doi.org/10.2458/azu_js_rc.v55i2.16177.

(37) Lamborg, C. H.; Fitzgerald, W. F.; Damman, A. W. H.; Benoit, J. M.; Balcom, P. H.; Engstrom, D. R. Modern and Historic Atmospheric Mercury Fluxes in Both Hemispheres: Global and Regional Mercury Cycling Implications: MODERN AND HISTORIC FLUXES OF ATMOSPHERIC MERCURY. *Glob. Biogeochem. Cycles* 2002, *16* (4), 51-1-51–11. https://doi.org/10.1029/2001GB001847.

(38) Cooke, C. A.; Balcom, P. H.; Kerfoot, C.; Abbott, M. B.; Wolfe, A. P. Pre-Colombian Mercury Pollution Associated with the Smelting of Argentiferous Ores in the Bolivian Andes. *AMBIO* 2011, *40* (1), 18–25. https://doi.org/10.1007/s13280-010-0086-4.

(39) Ribeiro Guevara, S.; Meili, M.; Rizzo, A.; Daga, R.; Arribére, M. Sediment Records of Highly Variable Mercury Inputs to Mountain Lakes in Patagonia during the Past Millennium. *Atmospheric Chem. Phys.* 2010, *10* (7), 3443–3453. https://doi.org/10.5194/acp-10-3443-2010.

(40) Cooke, C. A.; Balcom, P. H.; Biester, H.; Wolfe, A. P. Over Three Millennia of Mercury Pollution in the Peruvian Andes. *Proc. Natl. Acad. Sci.* 2009, *106* (22), 8830–8834. https://doi.org/10.1073/pnas.0900517106.

(41) Bagnato, E.; Tamburello, G.; Avard, G.; Martinez-Cruz, M.; Enrico, M.; Fu, X.; Sprovieri, M.; Sonke, J. E. Mercury Fluxes from Volcanic and Geothermal Sources: An Update. *Geol. Soc. Lond. Spec. Publ.* 2015, *410* (1), 263–285. https://doi.org/10.1144/SP410.2.

(42) Andres, R. J.; Kasgnoc, A. D. A Time-Averaged Inventory of Subaerial Volcanic Sulfur Emissions. *J. Geophys. Res. Atmospheres* 1998, *103* (D19), 25251–25261. https://doi.org/10.1029/98JD02091.

(43) Carn, S. A.; Fioletov, V. E.; McLinden, C. A.; Li, C.; Krotkov, N. A. A Decade of Global Volcanic SO2 Emissions Measured from Space. *Sci. Rep.* 2017, *7* (1), 44095. https://doi.org/10.1038/srep44095.

(44) Kocman, D.; Horvat, M.; Pirrone, N.; Cinnirella, S. Contribution of Contaminated Sites to the Global Mercury Budget. *Environ. Res.* 2013, *125*, 160–170. https://doi.org/10.1016/j.envres.2012.12.011.

(45) Agnan, Y.; Le Dantec, T.; Moore, C. W.; Edwards, G. C.; Obrist, D. New Constraints on Terrestrial Surface–Atmosphere Fluxes of Gaseous Elemental Mercury Using a Global Database. *Environ. Sci. Technol.* 2016, *50* (2), 507–524. https://doi.org/10.1021/acs.est.5b04013.

(46) Fitzgerald, W.F. and Lamborg, C.H.,. Geochemistry of Mercury. Treatise on Geochemistry: Volume 9: Environmental Geochemistry; 2004.

(47) Lamborg, C. H.; Von Damm, K. L.; Fitzgerald, W. F.; Hammerschmidt, C. R.; Zierenberg, R. Mercury and Monomethylmercury in Fluids from Sea Cliff Submarine Hydrothermal Field, Gorda Ridge. *Geophys. Res. Lett.* 2006, *33* (17), L17606. https://doi.org/10.1029/2006GL026321.

(48) Bowman, K. L.; Hammerschmidt, C. R.; Lamborg, C. H.; Swarr, G. J.; Agather, A. M. Distribution of Mercury Species across a Zonal Section of the Eastern Tropical South Pacific Ocean (U.S. GEOTRACES GP16). *Mar. Chem.* 2016, *186*, 156–166. https://doi.org/10.1016/j.marchem.2016.09.005.

(49) Slemr, F.; Seiler, W.; Schuster, G. Latitudinal Distribution of Mercury over the Atlantic Ocean. *J. Geophys. Res.* 1981, *86* (C2), 1159. https://doi.org/10.1029/JC086iC02p01159.

(50) Bieser, J.; Slemr, F.; Ambrose, J.; Brenninkmeijer, C.; Brooks, S.; Dastoor, A.; DeSimone, F.; Ebinghaus, R.; Gencarelli, C. N.; Geyer, B.; et al. Multi-Model Study of Mercury Dispersion in the Atmosphere: Vertical and Interhemispheric Distribution of Mercury Species. *Atmospheric Chem. Phys.* 2017, *17* (11), 6925–6955. https://doi.org/10.5194/acp-17-6925-2017.

(51) Sprovieri, F.; Pirrone, N.; Bencardino, M.; D' Amore, F.; Carbone, F.; Cinnirella, S.; Mannarino, V.; Landis, M.; Ebinghaus, R.; Weigelt, A.; et al. Atmospheric Mercury Concentrations Observed at Ground-Based Monitoring Sites Globally Distributed in the Framework of the GMOS Network. *Atmospheric Chem. Phys.* 2016, *16* (18), 11915–11935. https://doi.org/10.5194/acp-16-11915-2016.

(52) Zhang, Y.; Jacob, D. J.; Horowitz, H. M.; Chen, L.; Amos, H. M.; Krabbenhoft, D. P.; Slemr, F.; St. Louis, V. L.; Sunderland, E. M. Observed Decrease in Atmospheric Mercury Explained by Global Decline in Anthropogenic Emissions. *Proc. Natl. Acad. Sci.* 2016, *113* (3), 526–531. https://doi.org/10.1073/pnas.1516312113.

(53) Strode, S. A.; Jaeglé, L.; Selin, N. E.; Jacob, D. J.; Park, R. J.; Yantosca, R. M.; Mason, R. P.; Slemr, F. Air-Sea Exchange in the Global Mercury Cycle: MERCURY AIR-SEA EXCHANGE. *Glob. Biogeochem. Cycles* 2007, *21* (1). https://doi.org/10.1029/2006GB002766.

(54) Bieser, J.; Angot, H.; Slemr, F.; Martin, L. *Atmospheric Mercury in the Southern Hemisphere; Part 2: Source Apportionment Analysis at Cape Point Station, South Africa*; preprint; Gases/Field Measurements/Troposphere/Chemistry (chemical composition and reactions), 2020. https://doi.org/10.5194/acp-2020-63.

Supporting information

Table S1. Details of the coring sites in this investigation

Location	Site name	coordinates	Elevation (m a.s.l)	Precipitation (mm yr^{-1})	Coring date	Label core	core length (m)
Amsterdam Island	Central plateau	37.83°S, 77.53°E	738	1124	11/2014	AMS14-PB01	5
Falkland Islands (Islas Malvinas)	San Carlos bog	51.50°S, 58.82°W	8	575	2013	SCB13-PB01C	1.7
Valle de Andorra	Andorra	54.75°S, 68.22°W	198	450-600	02/2012	AND12-PB01W1	0.77
Estancia Harberton	Harberton	54.87°S, 67.22°W	26	600	02/2012	HAR12-PB01W1	0.92

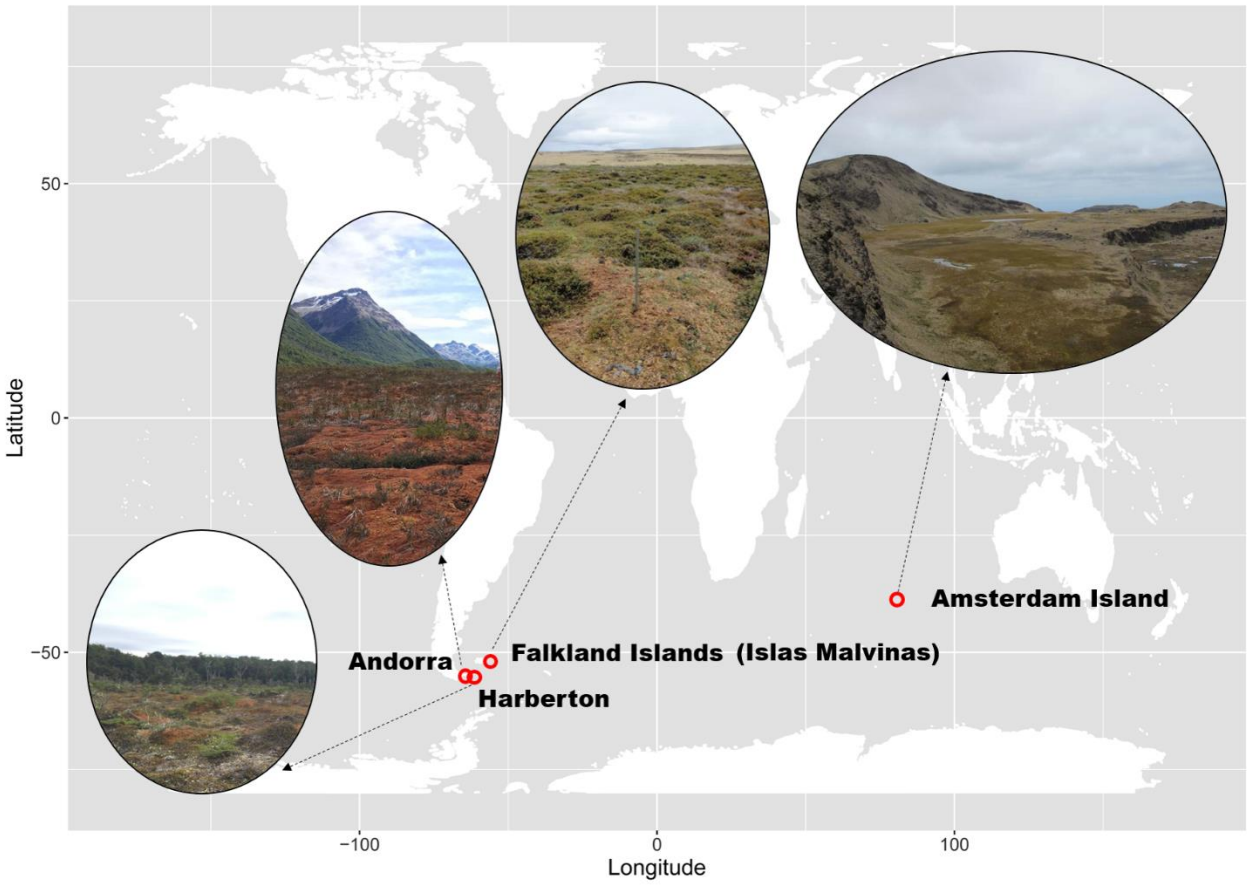

Figure S1. Location of Amsterdam Island (AMS), Falkland Islands (SCB, Islas Malvinas), Andorra (AND) and Harberton (HAR).

Text S1 Core sites:

Amsterdam Island (AMS): A 5 m-long peat sequence (AMS14-PB01A) was collected from the most elevated area of the peatland at 738 m a.s.l. in December 2014 using a stainless steel Russian D-corer of 10 cm internal diameter and 50 cm length. The mean annual temperature at the meteorological station (27 m a.s.l.) is 14°C and annual precipitation is about 1100 mm yr^{-1}

(1). For details about AMS coring site see (2). The vegetation at the coring site is characterized by bryophytes (brown mosses together with liverworts and some *Sphagnum* species), *Blechnum penna-marina*, *Scirpus aucklandicus*, *Trisetum insularis* and scattered stands of *Agrostis delislei*. Based on low resolution plant macrofossil data for the last 1000 years of a peat core taken close to the AMS14-PB01A core, with an independent age-depth model, the macrofossil record is dominated by higher plant epidermis (c. 70%) until about 400 cal yr BP. For the last 400 years, bryophytes are dominant (70-80%), mainly composed of brown mosses and liverworts, with little occurrence of *Sphagnum* spp. Ash content is <2wt% throughout the core and, together with major element profiles, suggests the site to be ombrotrophic to at least 3.5m depth.

The Falkland Islands (SCB, Islas Malvinas): 'San Carlos bog' is located on the western side of East Falkland Islands (SCB13-PB01C). The native vegetation is treeless and dominated by mosses, grasses and dwarf shrubs (3-4). A 1.7 m-long peat sequence was collected from a hummock with an upper monolith section (0 - 50 cm) and lower Russian core section (5). The surface vegetation of the bog is dominated by *Sphagnum magellanicum, Hymenophyllum caespitosum*, *Gaultheria pumila*, *Oreobulis obtusangulus*, *Gunnera magellanica* and *Myrteola nummularia*. *Sphagnum* is found to be more than 80% to a depth of 65 cm and followed by herbaceous compacted peat to the bottom. The annual precipitation and temperature are 575 mm yr^{-1} and 7°C, respectively (data sources from the Falkland Islands Government reported in (4).

Andorra (AND): An ombrotrophic peat monolith (0.72 m length, AND12-PB01W1) was collected at Andorra bog using a stainless steel Wardenaar corer (6). The AND peat profile is dominated >96% by *Sphagnum magellanicum*. The annual precipitation and temperature are 450-600 mm yr^{-1} and 6°C, respectively (7).

Harberton (HAR): An ombrotrophic peat monolith (0.73 m length, HAR12-PB01W1) was sampled at Harberton Bog by a stainless steel Wardenaar corer (6). The bog surface is dominated >80% by *Sphagnum magellanicum* with a sparse cover of *Marsippospermum grandiflorum* and *Empetrum rubrum* (8). The annual precipitation and temperature are around 600 mm yr^{-1} and 6°C, respectively (8).

Table S2 Accelerator Mass Spectrometry ^{14}C dating of plant macrofossils from all the four peat cores.

Core name	Lab ID	Mid-Point Depth (cm)	material	Conventional ^{14}C Age (yr BP, ± 1σ)	Calibrated age (median, AD/BC)	Modelled age AD/BC (95.4% probability range)
AMS*	SacA50049	2.0	*Chorisondontium*/*Dicranolo ma* stems + leaves	-557 ± 21	2008 AD	1997-2001 AD
AMS*	SacA50050	3.5	Brown moss stems	-1489 ± 20	1987 AD	1985-1987 AD
AMS*	SacA50051	4.9	Brown moss + liverworts stems	-3052 ± 18	1974 AD	1973-1979 AD
AMS*	SacA50052	6.4	Brown moss + liverworts stems	-1248 ± 20	1960 AD	1956-1962 AD
AMS*	SacA50053	7.8	Brown moss stems	135 ± 30	1942 AD	1938-1950 AD
AMS*	SacA50054	9.4	Brown moss stems	115 ± 30	1928 AD	1917-1937 AD
AMS*	SacA50055	10.8	Brown moss stems + leaves	80 ± 30	1912 AD	1895-1923 AD
AMS*	SacA50056	12.0	Brown moss stems + *Chorisondontium*/*Dicranolo ma* leaves	160 ± 30	1893 AD	1854-1917 AD
AMS*	SacA50057	13.2	brown moss stems	70 ± 30	1885 AD	1823-1915 AD
AMS*	GdA-4136	24.9	brown moss stems	275 ± 25	1752 AD	1640-1800 AD
AMS*	GdA-4558	65.4	Residue (Sphagnum dominated)	595 ± 25	1389 AD	1310-1440 AD
AMS*	GdA-4560	170.7	Brown moss stems	2100 ± 25	78 BC	155 BC-30 AD
AMS*	GdA-4137	174.8	brown moss stems	2170 ± 30	126 BC	195-55 BC
AMS*	GdA-4138	224.4	brown moss stems	2430 ± 30	580 BC	750-415 BC
AMS*	GdA-4139	275.4	brown moss stems	2925 ± 30	1142 BC	1380-980 BC
AMS*	GdA-4561	340.9	brown moss stems	4145 ± 35	2535 BC	2965-2275 BC
AMS*	GdA-4140	374.4	*Sphagnum*	4285 ± 30	2900 BC	3075-2750 BC
AMS*	GdA-4141	424.4	*Sphagnum*+ brown moss	4960 ± 30	3680 BC	3795-3550 BC
AMS*	GdA-4142	474.8	*Sphagnum* stems	5515 ± 35	4330 BC	4460-4190 BC
AMS*	GdA-4143	495.9	*Sphagnum* stems	5860 ± 35	4615 BC	4750-4470 BC
SCB	SUERC-51676	76.5	*Sphagnum*	153 ± 37	1694 AD	1597-1737 AD
SCB	GdA-3755	99.9	Undefined peat macrofossils	814 ± 41	1256 AD	1147-1345 AD
SCB	GdA-4744	109.8	Charcoal + Monoctyledons undifferentiated (leaf bases)	1553 ± 25	1009 AD	876-1152 AD
SCB	GdA-4745	123.7	Monoctyledons undifferentiated (leaf bases)	1261 ± 21	804 AD	688-896 AD
SCB	GdA-4746	146.3	Monoctyledons undifferentiated (leaf bases)	1661 ± 25	428 AD	277-532 AD
SCB	GdA-4742	154.3	Charcoal + Monoctyledons undifferentiated (leaf bases)	2882 ± 22	252 AD	19 BC-396 AD
SCB	GdA-3756	164.3	Undefined peat macrofossils	11582 ± 50	36 AD	376 BC-254 AD
AND	SacA50058	0.6	*Sphagnum*	-594 ± 19	2004 AD	2007-2014 AD
AND	SacA50059	13.1	*Sphagnum*	-1749 ± 19	1983 AD	1985-2000 AD
AND	SacA50060	34.3	*Sphagnum*	-2839 ± 17	1974 AD	1969-1976 AD
AND	SacA50061	41.0	*Sphagnum*	-2695 ± 18	1964 AD	1961-1967 AD
AND	SacA50062	47.6	*Sphagnum*	-67 ± 21	1954 AD	1947-1958 AD
AND	SacA50063	54.6	*Sphagnum*	120 ± 30	1926 AD	1902-1942 AD
AND	SacA50064	61.9	*Sphagnum*	140 ± 30	1893 AD	1856-1919 AD
AND	SacA50065	68.8	*Sphagnum*	160 ± 30	1863 AD	1814-1893 AD
AND	GdA-3032	73.2	*Sphagnum*	193 ± 23	1843 AD	1787-1876 AD
AND	SacA50066	76.1	*Sphagnum*	150 ± 30	1831 AD	1769-1865 AD
HAR	SacA42507	0.3	*Sphagnum*	-424 ± 21	2010 AD	2010-2019 AD
HAR	SacA42508	4.7	*Sphagnum*	-606 ± 22	2004 AD	2002-2012 AD
HAR	SacA42509	6.9	*Sphagnum*	-677 ± 21	2002 AD	1999-2008 AD
HAR	SacA42510	9.1	*Sphagnum*	-788 ± 21	1999 AD	1996-2005 AD
HAR	SacA42511	11.3	*Sphagnum*	-838 ± 22	1998 AD	1994-2002 AD
HAR	SacA42512	13.6	*Sphagnum*	-914 ± 21	1996 AD	1991-1999 AD
HAR	SacA44490	15.8	*Sphagnum*	-1092 ± 22	1992 AD	1988-1996 AD
HAR	SacA44491	19.2	*Sphagnum*	-1333 ± 21	1988 AD	1984-1992 AD
HAR	SacA44492	21.3	*Sphagnum*	-1513 ± 20	1985 AD	1981-1989 AD

HAR	SacA44493	26.6	*Sphagnum*	-2186 ± 21	1979 AD	1974-1982 AD
HAR	SacA44494	31.7	*Sphagnum*	-2715 ± 20	1975 AD	1964-1976 AD
HAR	SacA44495	37.0	*Sphagnum*	-2462 ± 27	1964 AD	1930-1964 AD
HAR	SacA44496	43.5	*Sphagnum*	214 ± 23	1815 AD	1736-1885 AD
HAR	SacA44497	56.2	*Sphagnum*	407 ± 25	1608 AD	1518-1631 AD
HAR	SacA44498	90.7	*Sphagnum*	984 ± 24	1148 AD	1063-1216 AD

*****Data are from ref 28.

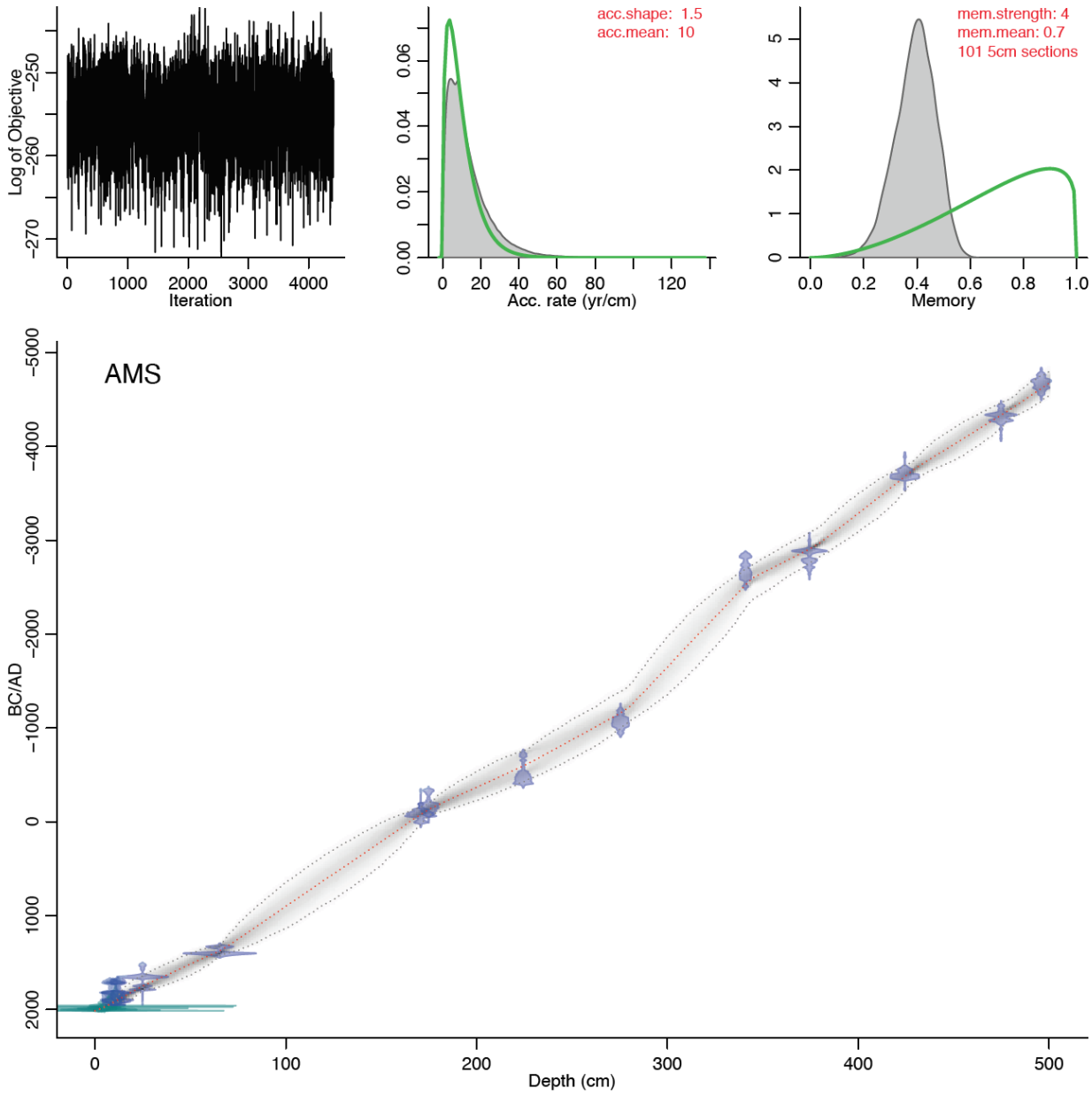
Log of Objective
−270
−260
−250
0
1000
2000
3000
4000
Iteration
acc.shape: 1.5
acc.mean: 10
0.00
0.02
0.04
0.06
0
20
40
60
80
120
Acc. rate (yr/cm)
mem.strength: 4
mem.mean: 0.7
101 5cm sections
0
1
2
3
4
5
0.0
0.2
0.4
0.6
0.8
1.0
Memory
AMS
BC/AD
−5000
−4000
−3000
−2000
−1000
0
1000
2000
0
100
200
300
400
500
Depth (cm)

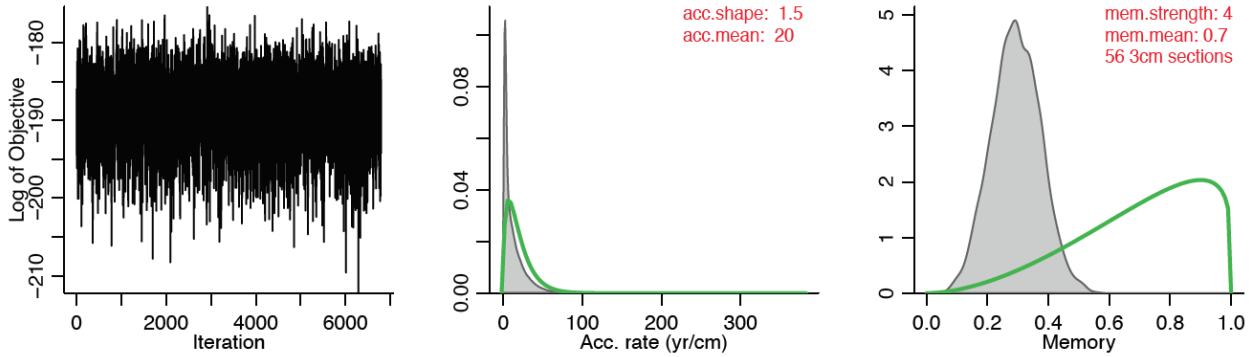
Log of Objective
−180
−190
−200
−210
0
2000
4000
6000
Iteration
acc.shape: 1.5
acc.mean: 20
0.08
0.04
0.00
0
100
200
300
Acc. rate (yr/cm)
mem.strength: 4
mem.mean: 0.7
56 3cm sections
5
4
3
2
1
0
0.0
0.2
0.4
0.6
0.8
1.0
Memory

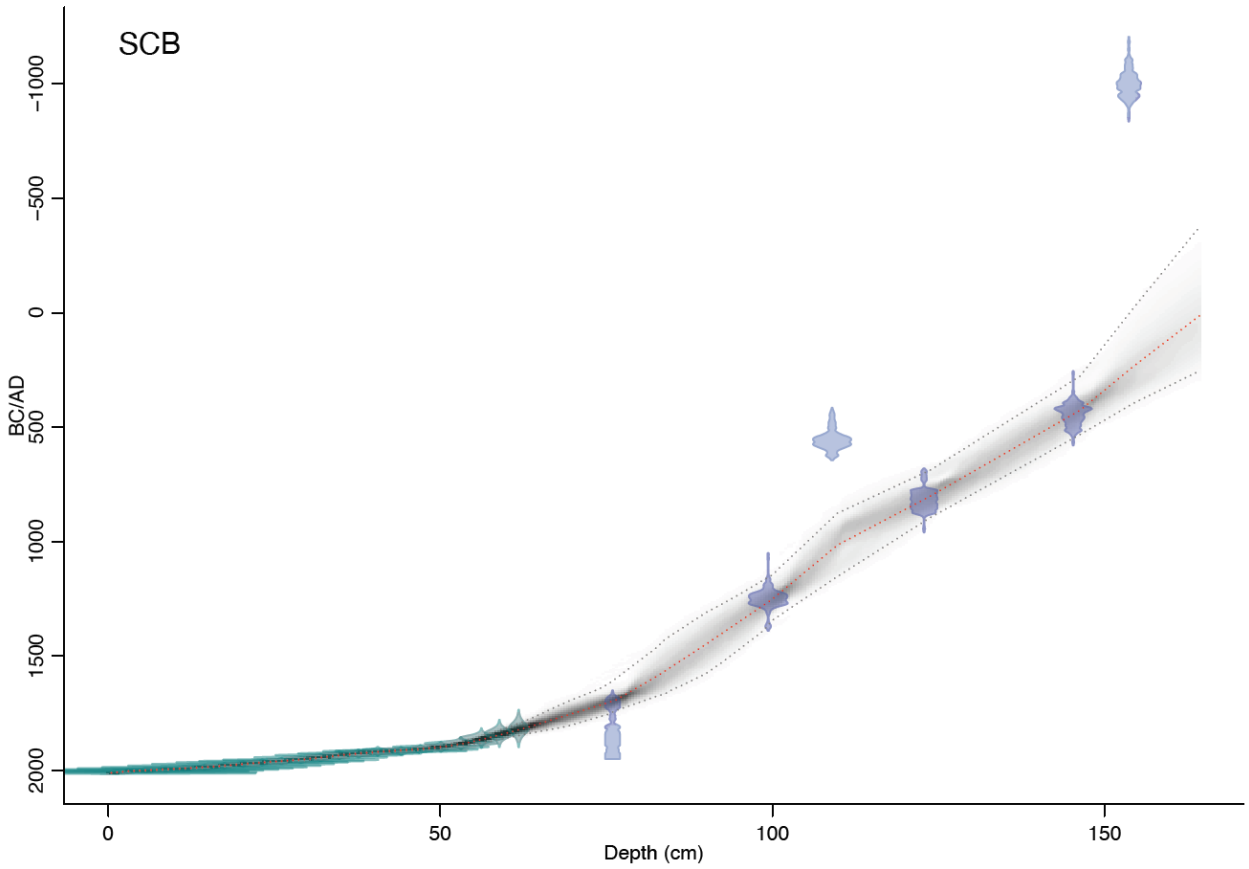
SCB
BC/AD
−1000
−500
0
500
1000
1500
2000
0
50
100
150
Depth (cm)

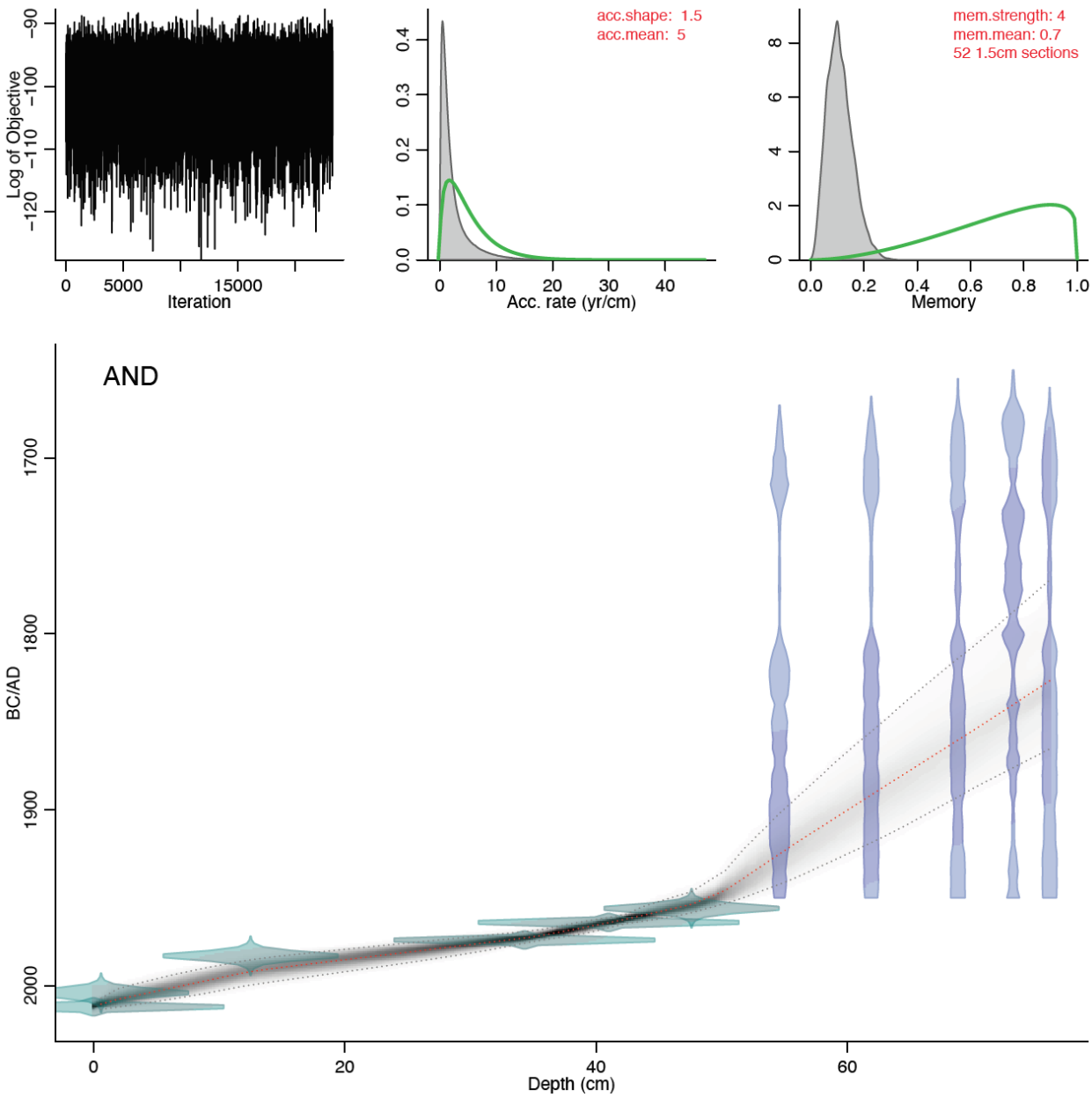
Log of Objective
−90
−100
−110
−120
0
5000
15000
Iteration
acc.shape: 1.5
acc.mean: 5
0.0
0.1
0.2
0.3
0.4
0
10
20
30
40
Acc. rate (yr/cm)
mem.strength: 4
mem.mean: 0.7
52 1.5cm sections
0
2
4
6
8
0.0
0.2
0.4
0.6
0.8
1.0
Memory
AND
BC/AD
1700
1800
1900
2000
0
20
40
60
Depth (cm)

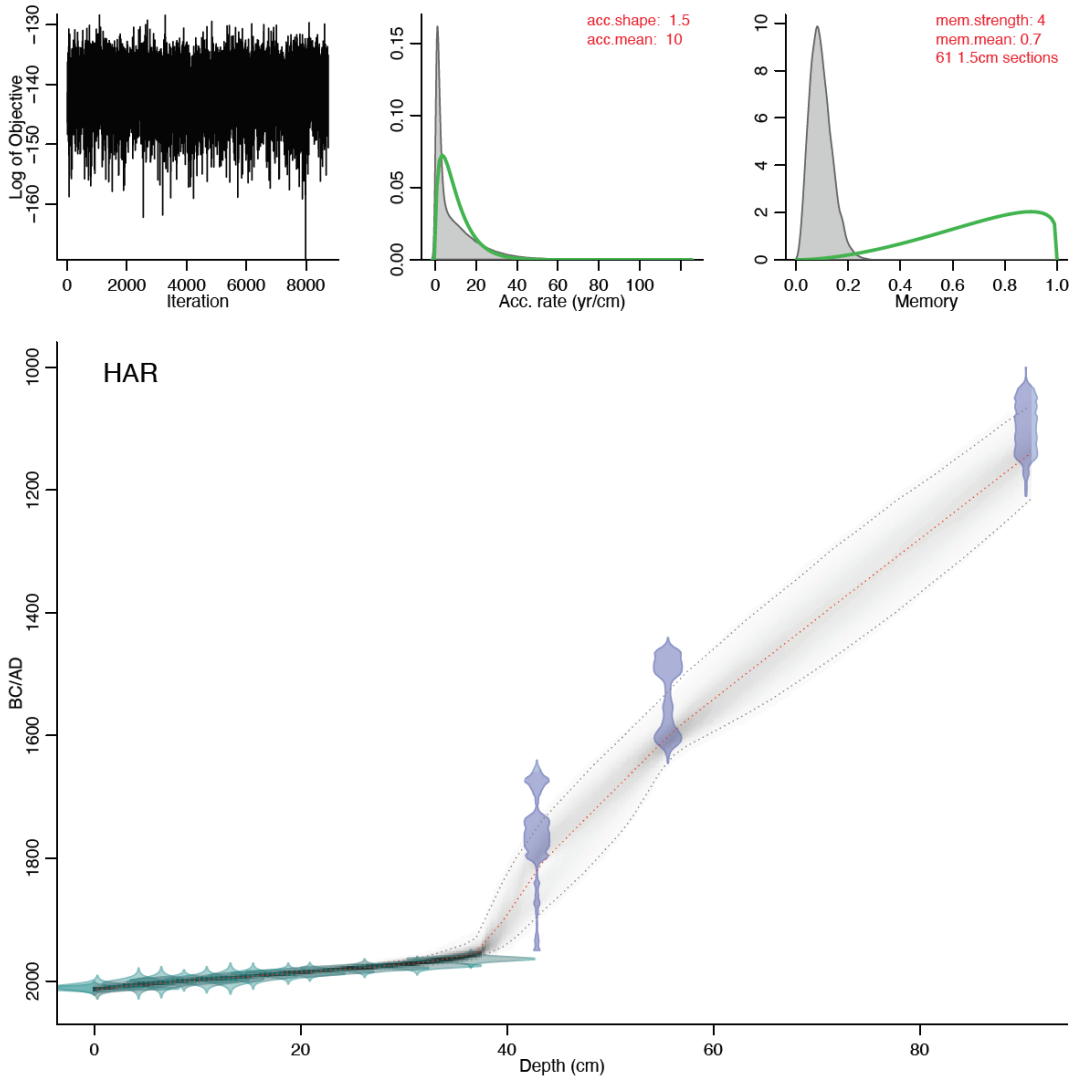

Figure S2. Age models of peat cores from AMS, SCB, AND and HAR using Bacon. Calibrated ^{14}C dates show in transparent blue and ^{210}Pb dates show in transparent green. Red curve indicates single best-fit model based on the weighted mean age for each depth. Darker greys represent more likely calendar ages with 95% confidence intervals shown by grey stippled lines. Diagnostic plots in upper left panels confirm appropriate performance of the models. Settings for accumulation rate and memory are shown in middle and right upper panels (green line–prior, grey shade–posterior distribution), along with thickness and number of sections used for modelling. Prior settings for accumulation rates described by gamma distribution with shape 1.5 and acc.mean 10 or 20 yr/cm, for memory the default beta distribution with parameters mem.strength=4 and mem.mean=0.7 was used.

Table S3 Summary of Hg measurements in standard reference materials.

SRM	materials	Measured value (mean ± 1σ, ng g^{-1})	Certified value (mean ± 2σ, ng g^{-1})
IPE 176	Reed/*Phragmites communis*	35.1 ± 6.3 (n=143)	37.9 ± 2.9
NIST 1632d	Coal	91.3 ± 7.0 (n=9)	92.8 ± 3.3
BCR 482	Lichen	481.3 ± 8.7 (n=5)	480 ± 20

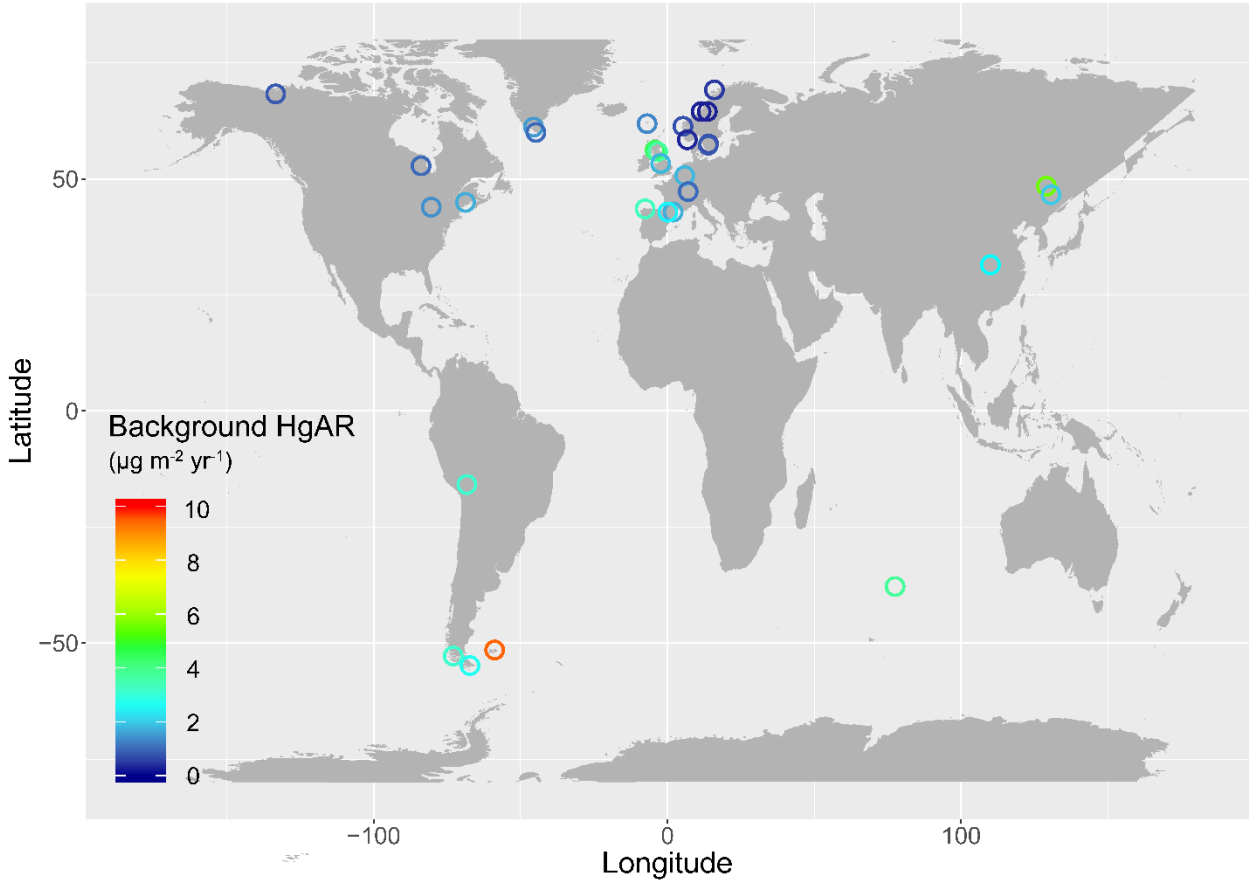

Figure S3. Natural background Hg accumulation rates (μg m^{-2} yr^{-1}) derived from natural peat archives. Details see Extended Data 2.

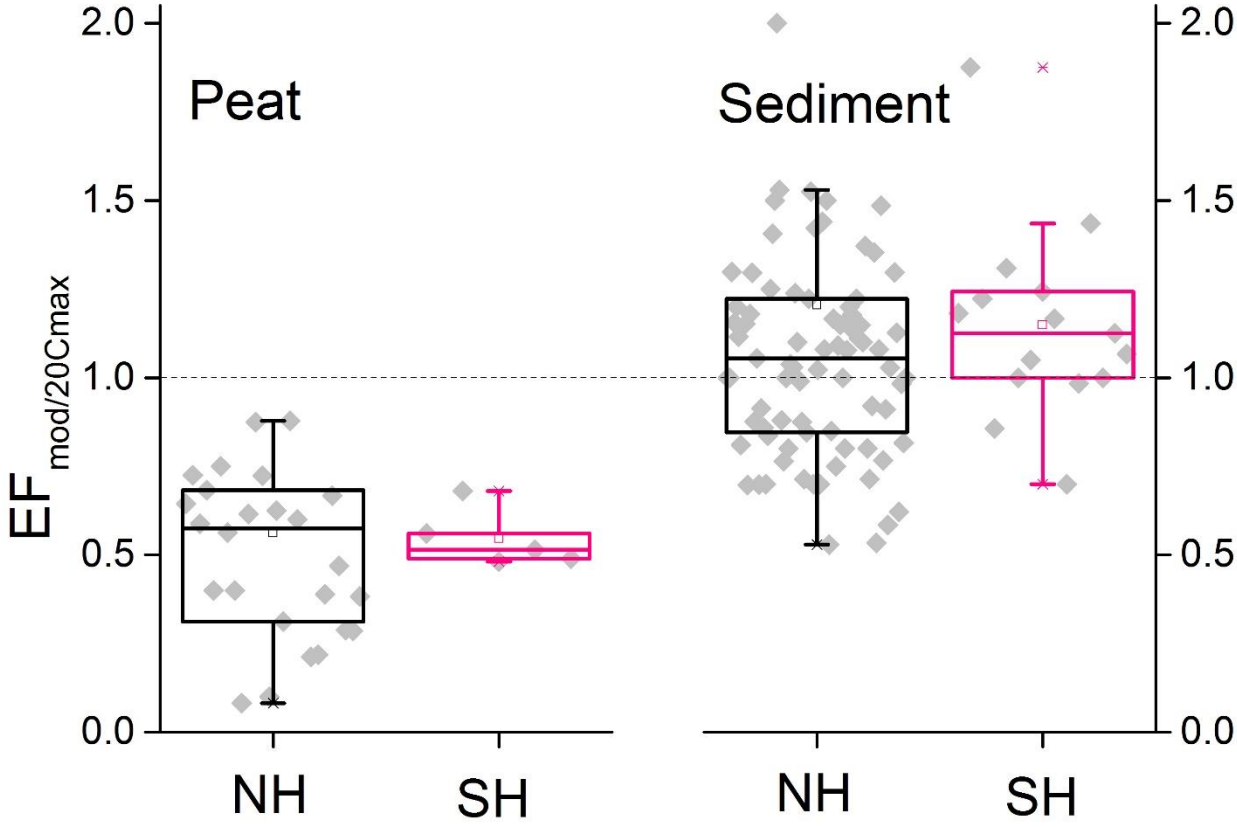

Figure S4. Profiles of HgAR enrichment factor of modern (post-1990) to extended 20th century maximum ($EF_{mod/20Cmax}$) from Northern Hemisphere (NH) and Southern Hemisphere (SH) peat and sediment records. Dashed line indicates EF=1.

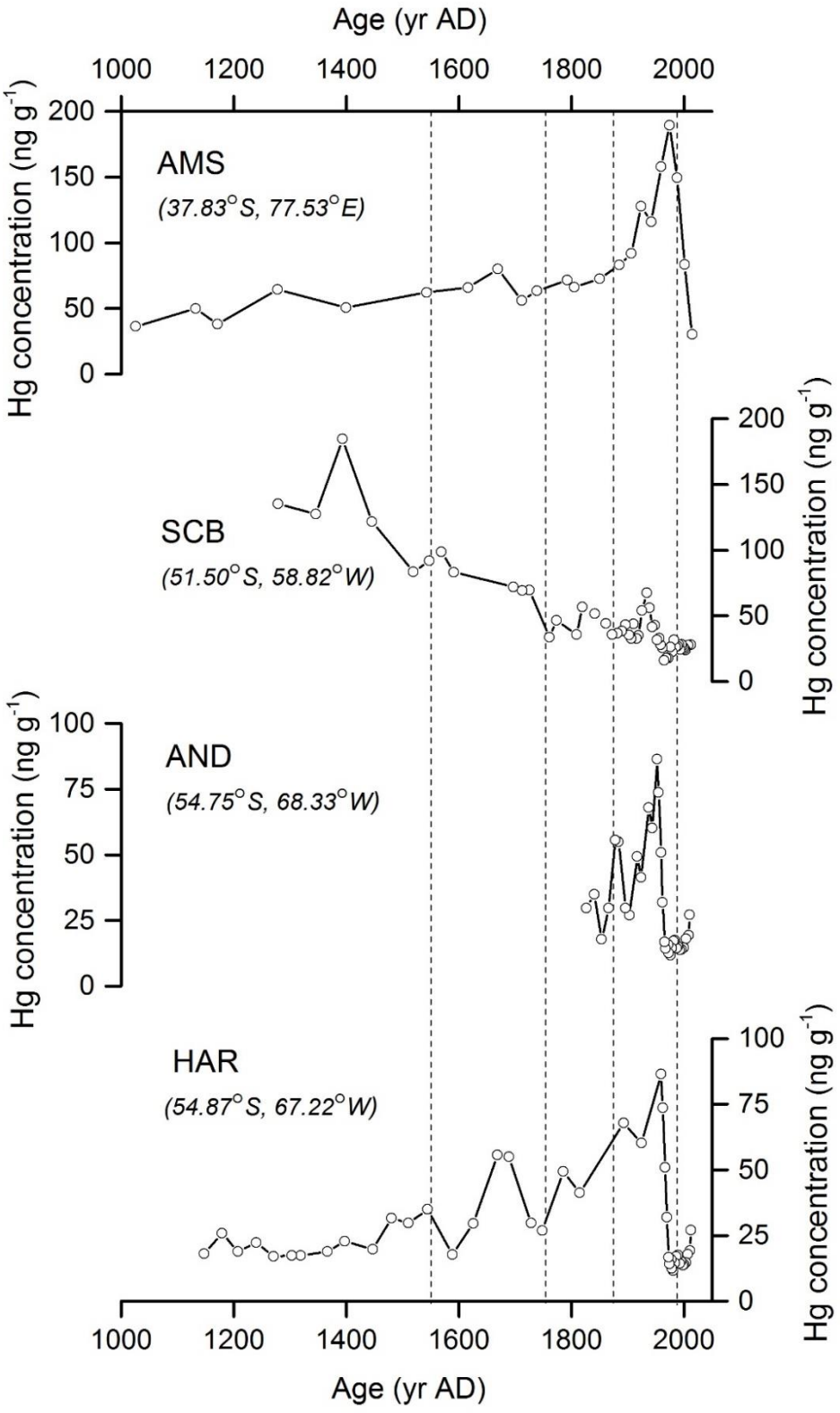

Figure S5. Profiles of Hg concentration (ng g^{-1}) in the peat cores from AMS, SCB, AND and HAR.

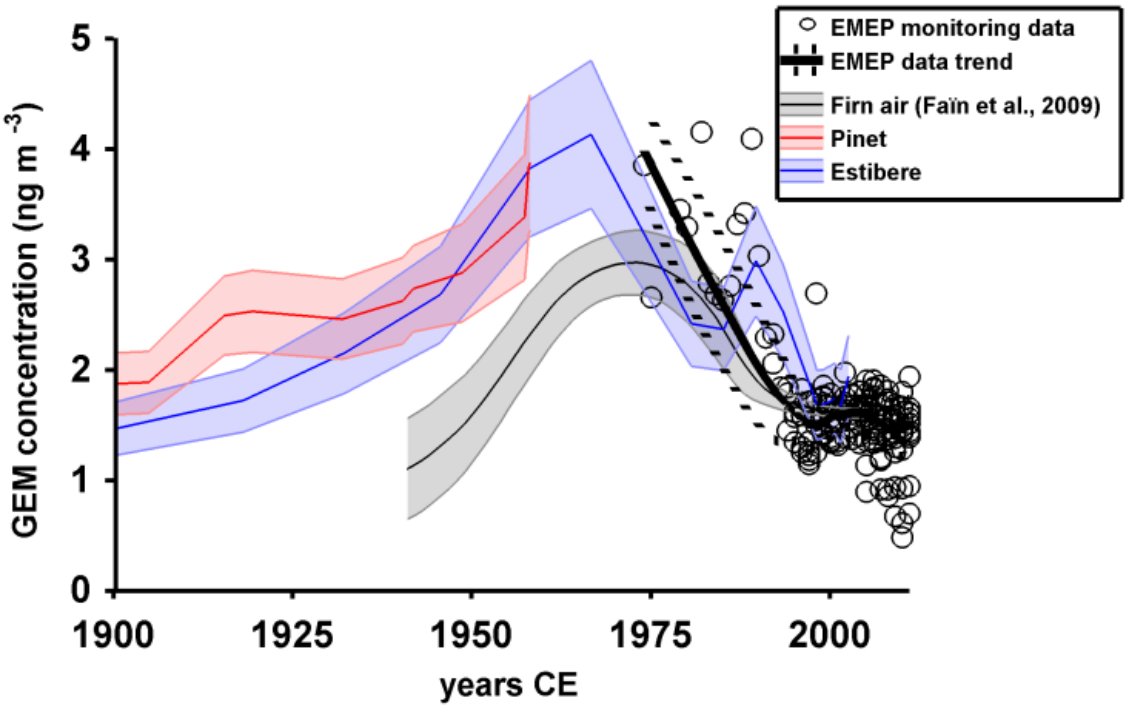

Figure S6. Historical atmospheric Hg monitoring observations and reconstructed Hg levels. Figure **r**eproduced from Enrico et al. 2017, ES&T with permission (9). Atmospheric gaseous elemental Hg^0 (GEM) monitoring data (circles) are from EMEP (10).

Supplementary references

1. Lebouvier, M. and Frenot, Y., 2007. Conservation and management in the French sub-Antarctic islands and surrounding seas. In *Papers and proceedings of the royal society of Tasmania* (Vol. 141, No. 1, pp. 23-28).
2. Li, C., Le Roux, G., Sonke, J., van Beek, P., Souhaut, M., Van der Putten, N. and De Vleeschouwer, F., 2017. Recent 210Pb, 137Cs and 241Am accumulation in an ombrotrophic peatland from Amsterdam Island (Southern Indian Ocean). *Journal of environmental radioactivity*, *175*, pp.164-169.
3. Moore, D.M., 1968. The vascular flora of the Falkland Islands. *The vascular flora of the Falkland Islands.*, (60).
4. Bokhorst, S., Convey, P., Huiskes, A. and Aerts, R., 2017. Dwarf shrub and grass vegetation resistant to long-term experimental warming while microarthropod abundance declines on the Falkland Islands. *Austral Ecology*, *42*(8), pp.984-994.
5. Belokopytov, I.E. and Beresnevich, V.V., 1955. Giktorf's peat borers. *Torfyanaya Promyshlennost*, *8*(9), p.10.
6. Wardenaar, E.C.P., 1987. A new hand tool for cutting soil monoliths. *Canadian journal of Soil science*, *67*(2), pp.405-407.
7. Mauquoy, D., Blaauw, M., van Geel, B., Borromei, A., Quattrocchio, M., Chambers, F.M. and Possnert, G., 2004. Late Holocene climatic changes in Tierra del Fuego based on multiproxy analyses of peat deposits. *Quaternary Research*, *61*(2), pp.148-158.
8. Vanneste, H., De Vleeschouwer, F., Martínez-Cortizas, A., Von Scheffer, C., Piotrowska, N., Coronato, A. and Le Roux, G., 2015. Late-glacial elevated dust deposition linked to westerly wind shifts in southern South America. *Scientific reports*, *5*, p.11670.
9. Enrico M., et al., Holocene Atmospheric Mercury Levels Reconstructed from Peat Bog Mercury Stable Isotopes. Environ. Sci. Technol. 51, 5899–5906 (2017).
10. European Monitoring and Evaluation Programme (2016). https://www.emep.int/

Supporting information 2

(See a separate excel file "Extended Data 2" as a complement to the thesis)

Conclusions and perspectives

A Paris Climate Agreement was adopted by 174 states during 2015-2016, aiming to hold "*the increase in the global average temperature to well below 2°C above pre-industrial levels and to pursue efforts to limit the temperature increase to 1.5°C above pre-industrial levels*" (UNFCCC, 2015). This climate goal represents the level of climate change that multi-governments would agree to prevent severe environmental consequences, finally leading to a sustainable food production and health economic developments (UNFCCC, 1992; Rogelj et al., 2016). National commitments on Paris climate agreement interact with other global environmental objectives, e.g., Minamata convention on mercury (Mulvaney et al., 2020). Minamata convention, ratified by 128 signatories in 2019, aims at lowering the release of highly toxic Mercury (Hg) to the environment. Minamata Convention attempts to "*address Hg thought its lifecycle from its mining to its management as waste*" (UNEP-MCM, 2018). The Objectives of Paris agreement and Minamata convention highlight both the anthropogenic perturbations since industrialization and the needs to better understand the pre-industrial environmental conditions for making accurate environmental assessments and subsequent proper policy.

Both past climate variability and current anthropogenic activities have been greatly investigated based on multi archives (e.g., sediment, peat and ice core) using numerous proxies (e.g., biology, geochemistry and geomorphology). Most of these human-climate-interaction studies have been conducted in the Northern Hemisphere (NH) due to predominant global anthropogenic emissions (e.g., gas, particles) taken place in boreal areas. Southern Hemisphere is, however, received less scrutiny, which precludes a thoughtful understanding of anthropogenic impact superimposed on the past environmental changes.

Southern Ocean south of 30°S, occupying 30% of global surface ocean areas, accounts for 43% of anthropogenic CO_2 uptake (Frolicher et al., 2014), which slows down the climate change we experience. Changes in Southern Hemisphere Westerly Wind (SWW) intensity is thought to affect whether Southern Ocean acts as a net source or sink of CO_2. This influences the CO_2 in the atmosphere and then global climate.

This study is designed to partially fill in the information gap of SWW and human impact in the SH in the Holocene, which is the main epoch involved with human activities. We focus on time-series variations of two representative forms of atmospheric proxies, dust and mercury (principally gaseous elemental Hg, Hg^0), both of which can derive from natural and

anthropogenic emissions. We use SH mid-latitude peat bog as historical recorders, which are exclusively fed by atmospheric input and therefore ideal atmospheric recorders.

1. Peat ^{210}Pb signatures and its function of recent age reconstruction

Aerosols have significant environmental impact by regulating atmospheric albedo, nutrient supply and nuclei formation. ^{222}Rn ($T_{1/2}$=3.8 d) is an inert gas emitting from continental curst and can decay to ^{210}Pb ($T_{1/2}$=22.3 yrs) in the atmosphere. As soon as ^{210}Pb is produced, it is attached rapidly to aerosols, which subsequently can travel over the planet. ^{222}Rn-^{210}Pb cycling has been used in global climate-aerosol models. Given the absence of historical ^{210}Pb data in the Southern Indian Ocean, Our ^{210}Pb values from an Amsterdam Island (AMS) peat profile has provided the first information (Chapter 1). An updated global ^{210}Pb data compilation allows us to discern relatively high ^{210}Pb flux at AMS relative to other Southern South American western coastal regions. Origins of continental air masses based on ^{222}Rn and high humidity at AMS are the processes responsible for high ^{210}Pb deposition at AMS. ^{210}Pb data and its deposition processes at AMS can add some values to the global climate-aerosol model projections.

The time-series recorders need accurate chronology to support the reconstruction of the past events at certain periods, especially for the past 150 years under intensive anthropogenic emissions of pollutants (e.g., Hg^0, dust). ^{210}Pb has been abundantly used in generating the recent age models (Appleby, 2001). Previous studies have doubted of the application of peat archives as industrial-impact recorder due to the potential of post-deposition of ^{210}Pb during peat mineralization, leading to inaccurate age model (e.g., Biester et al., 2007). The ^{210}Pb-based Constant Rate of Supply age model for AMS peat has been validated by independent chronomarkers, ^{137}Cs and ^{241}Am that related to nuclear weapon test mainly present in 1960s (Chapter 1). Coupled with the age constraint with 20 radiocarbon dating results, the whole age model profile in AMS core permits reliable reconstructions of climatic and anthropogenic signals (Chapter 2, Chapter 3 and Chapter 4).

2. Atmospheric dust and Hg isotopes: indicators of the Holocene SWW dynamics

The ^{210}Pb flux at AMS has illustrated the importance of continental aerosols deposited over this island. Previous works have suggested African continent and/or Madagascar as main origins of continental air mass/ chemical contributions to AMS by the source-sink studies on this island (Angot et al., 2014; Sciare et al., 2009; Baboukas et al., 2002; Gros et al., 1998; Miller et al., 1993; Moody et al., 1991; Balkanski and Jacob, 1990; Gaudichet et al., 1989; Polian et al., 1986; Gaudry et al., 1983). Southern South America (SSA) is overlooked as an important atmospheric

source to AMS by the studies mentioned above, probably due to long distance between AMS and SSA (> 10000 km). Our study has, however, confirmed SSA as a dominant atmospheric dust contributor (~45%) to AMS in the past 6600 yrs using chemical and isotopic binary mixing mass balance calculations (Chapter 2). Southern Africa (SAF) only consists of 15%, while the local source occupies the remaining 40% (Figure 1). Overall, the distal dust source contribution to AMS points out a counter-intuitive information that SSA overrides SAF as the predominant dust contributor to AMS. It indicates that substantial dust transported from SSA (e.g., Patagonia and Puna-Altiplano-plateau) and deposits over Indian Ocean.

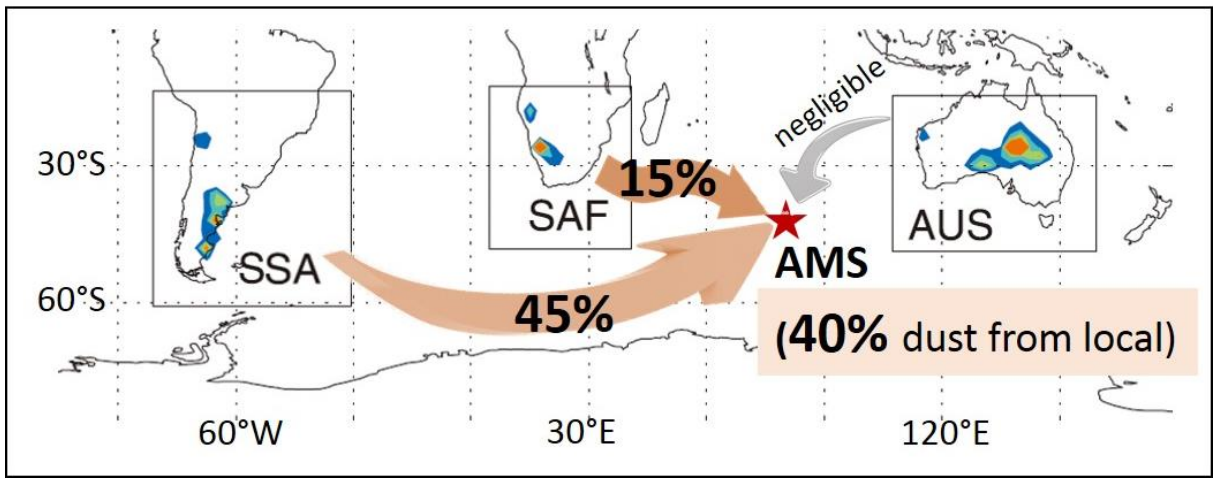

Figure 1. Dust contribution to Amsterdam Island (AMS) from potential dust sources (Southern South America, SSA; Southern Africa, SAF; Australia, AUS). In the past 6600 years (except the last 100 yrs), SSA consists of 45% of dust deposited at AMS peat profile, while SAF and local contributes 15% and 40%, respectively.

Distal dust deposited over AMS is mainly transported by SWW, which can in turn modulate the dust deposition pathways along the transport and at the targeted areas by changing wind speed and humidity. Dust composition is able to record the changes in SWW. Saunders et al., (2018) has suggested enhanced local/regional mineral input to lake sediment in Macquarie Island as a result of increase SWW intensity. However, dust variations in AMS peat and chemicals signal in precipitation in this island (Moody et al., 1991) show an opposite finding, arguing that strengthened / equatorward-shifted SWW lower both distal and local dust deposition to AMS (Chapter 2). These contradictory results can be explained by strengthened SWW, leading to both enhanced removal of distal dust enroute to AMS (Moody et al., 1991), and lower local AMS dust mobility under high humidity (Figure 2). We conclude that intensified SWW during periods of 6.2-4.9 cal. kyr BP and 3.9-2.7 cal. kyr BP can effectively

scavenge the long-range dust to Southern Indian Ocean, leading to enhanced dust deposition over the ocean and potentially to some extent increase oceanic primary productivity due to generally low atmospheric deposition in Southern Indian Ocean (Heimburger et al., 2013a; 2013b). SWW influence is, however, site-specific.

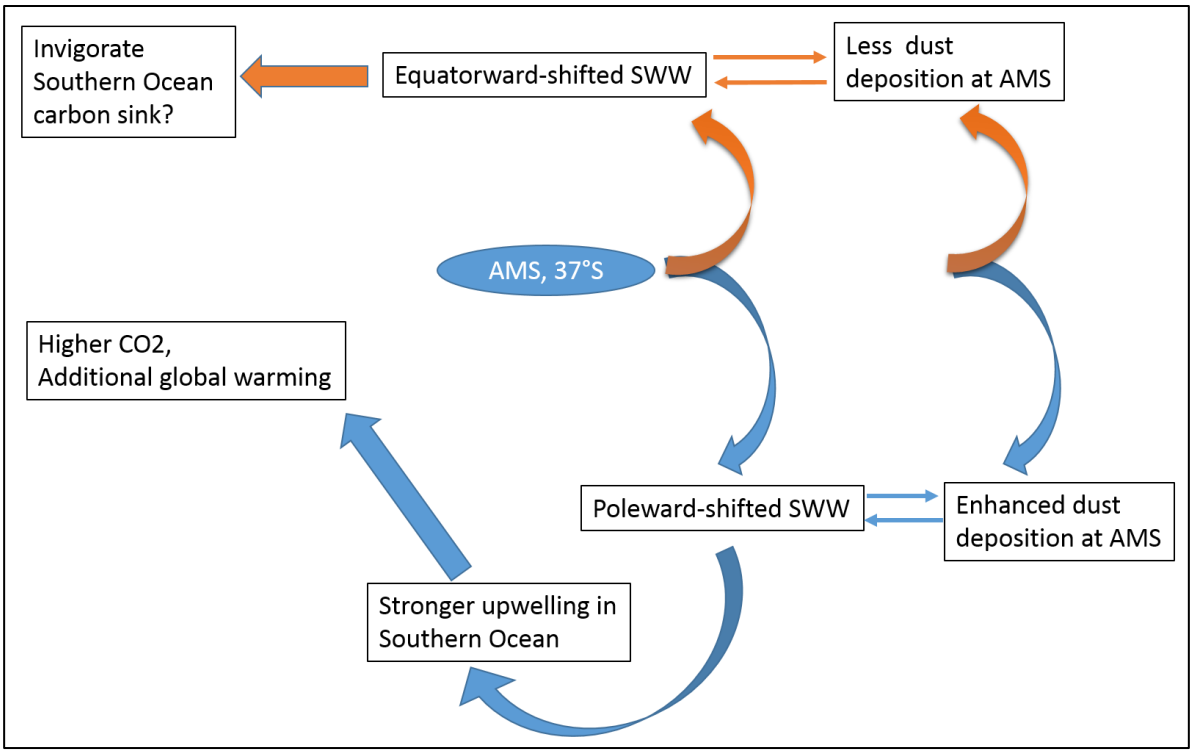

Figure 2. Conceptual diagram of the influences of SWW dynamics on atmospheric dust deposition and Southern Ocean carbon source-sink. SWW represent Southern Westerly Winds and AMS represents Amsterdam Island.

Multi methods have been used to investigate Hg biogeochemical cycle in the environment. The recent development of Hg isotopes have opened promising avenue to discern Hg source mixing and Hg transformation. Hg isotope dynamics have been abundantly investigated in the NH and by far, no time-series Hg isotope compositions related to SWW variability have been provided in the SH. Due to the conservative signature of Δ^{200}Hg and its distinct values between Hg^0 and rainfall (e.g., Enrico et al., 2016; Chen et al., 2012), AMS peat Δ^{200}Hg has been used to estimate Hg dry and wet deposition in the past 6600 yrs. Peat Hg isotope signatures, which are sensitive to rainfall inputs indicate that high dust, high mercury events correspond to less rainfall. The Hg-deposition-process-related SWW dynamics (Chapter 3) is in agreement with the dust based SWW variability (Chapter 2). We suggest that these events were caused by a poleward shift of the SWW at AMS. Our results, therefore, give the first insight to use Hg isotopes as SWW proxies.

3. Anthropogenic perturbations on atmospheric dust and Hg^0

How to distinguish between human-induced perturbations and ill-defined natural oscillations is a crucial question when considering issues like continental landscape degradation. Our study has clearly show a double increase in Southern African dust deposition to AMS in the last 100 years relative to the long past. Multi-evidences from other studies have shown the drier conditions with increased dust availability probably due to human-climate interaction (e.g., Nicholson et al., 2012; 2001; IPCC, 2007). SWW has shifted poleward in the past seven decades, which is in line with the increased dust input at AMS. We are, however, not able to quantify the influence between climate and anthropogenic on atmospheric dust deposited at AMS in the last 100 years.

Apart from recording the anthropogenic perturbation on atmospheric dust deposition, AMS peat has also shown a clear anthropogenic signal of a toxic chemical, Hg^0, with an x2 increase in its accumulation rate since the pre-industrial period (1450AD-1880AD). Peat, receiving Hg mainly by plant uptake of Hg^0 (Enrico et al., 2016), has been proven to be reliable Hg recorder (Amos et al., 2015). Most of data compilation in Amos et al., (2015) are from the NH and only 4 out of 88 cores are from the SH. Our four peat Hg profile from the SH have therefore contributed to the under-represented dataset. After reviewing 18 other SH cores and updating NH historical Hg database, we find that the NH all-time Hg increase (from pre-1450AD to 20th century) is x16 and SH is x4 (Figure 3). We attribute this difference to a combination of lower anthropogenic Hg emissions in the SH, and higher natural atmospheric SH Hg levels, supported by ×2 higher natural background Hg accumulation in SH peat (Chapter 4). Our findings suggest that background Hg levels in both hemispheres are different and should be taken into account in international Hg assessment reports and environmental policy objectives.

Overall, this thesis provides the information of 1/ Holocene SWW dynamics at their northern edge indicated by dust proxies (Chapter 1, 2), highlighting that poleward-shifted SWW can lead to more dust input coupled with less rainfall at AMS; 2/ the potential of Hg isotopes as a climate proxy (Chapter 3); and 3/ the anthropogenic perturbations on dust mobility and distinct Hg deposition in two hemispheres (Chapter 2, 4).

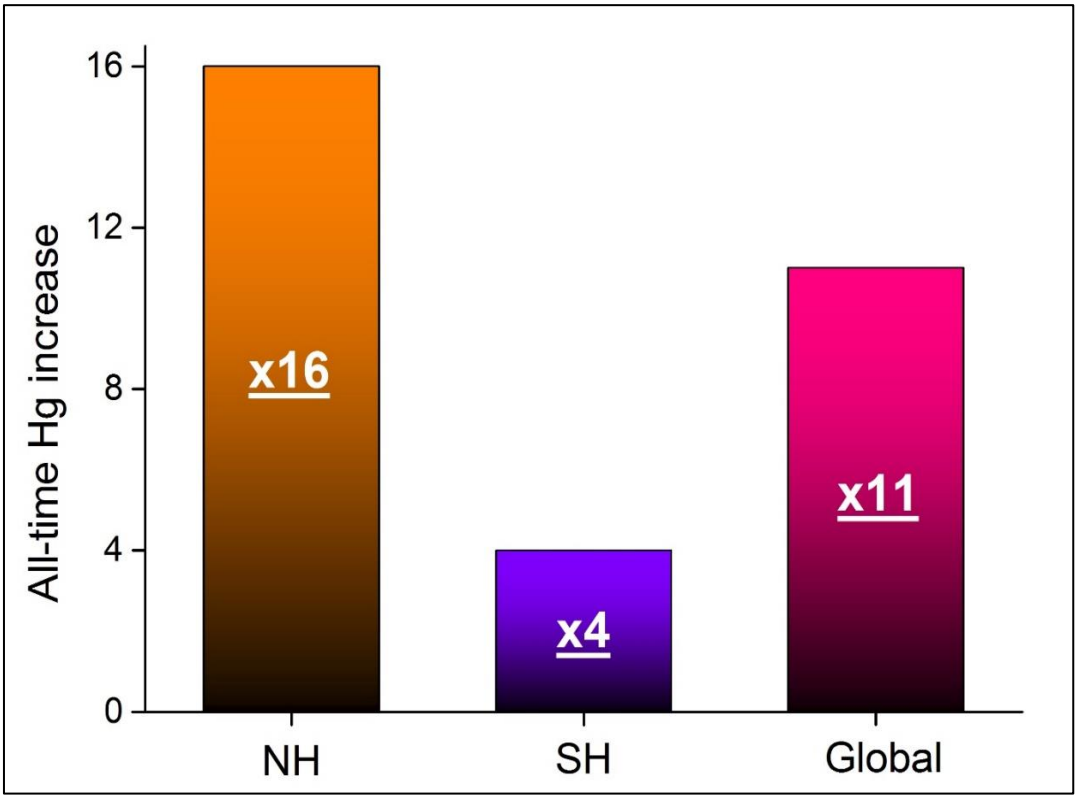

Figure 3. Difference of of all-time Hg increase in both hemispheres (since pre-1450AD).

4. Perspectives

4.1 Hg isotope signature in the SH Hg^0 and rainfall

Current investigations on Hg^0 and rainfall $\Delta^{200}Hg$ signatures are principally from NH. Even though it is assumed that $\Delta^{200}Hg$ signatures are similar in both hemispheres due to its conservative characteristic (Chen et al., 2012; Enrico et al., 2016). However, we should verify this hypothesis by investigating the Hg^0 and rainfall in the SH, especially from the local site where to sample the archive. All-year around Hg^0 and rainfall have been collected from AMS and shipped back to GET. Rainfall from Ushuaia, Tierra del Fuego, have been collected and ready to be transported back. Analysis of these samples will be the next step to unfold the actual Hg isotope composition in the SH Hg^0 and rainfall.

4.2 Botany-based climate information is needed to compare with the dust and Hg-based SWW dynamics

Dust compositions can reflect the SWW variations in a broad trend, while Hg isotopes can quantify SWW-based dry and wet deposition processes. For better developing Hg isotope proxies as climate indicators, one should also compare to classical botany-based environmental

change, even though botanical indicators maonly provide qualitative descriptions on climate variability. The macrofossil investigations in AMS peat profile will be completed by our colleagues. In the end, Hg isotope-based proxies, coupled with other geochemical and botanical indicators, enable us to have a solid reconstruction of the climate in the past (Figure 4), which is useful for better understanding the present and future climate change.

4.3 Climate simulations in the Holocene

SH climate variability during the entire Holocene is far less known than that in the last 150 years, mainly due to less observational data available. Climate modelling is good method to reconstruct the past and predict the future. Coupled Model Intercomparison Project Phase 5 (CMIP5) is a mature experimental framework for studying the output of coupled atmosphere-ocean general circulation models. In addition, one can also use other corresponding simulations for climatic output comparisons, for example, Atmospheric Model Intercomparison Project (AMIP) with prescribed Sea Surface Temperature and interactive continental surfaces. Linking the model output to the observationsal data will be allowed to explore the relationship between the observation-based quantified reconstructions of SWW strength, the overall structure of wind changes, and their mechanisms and drivers. Subsequently, one can improve the climate model with the observational data and then evaluate the impact of SWW on the Southern Ocean carbon sink in a long term.

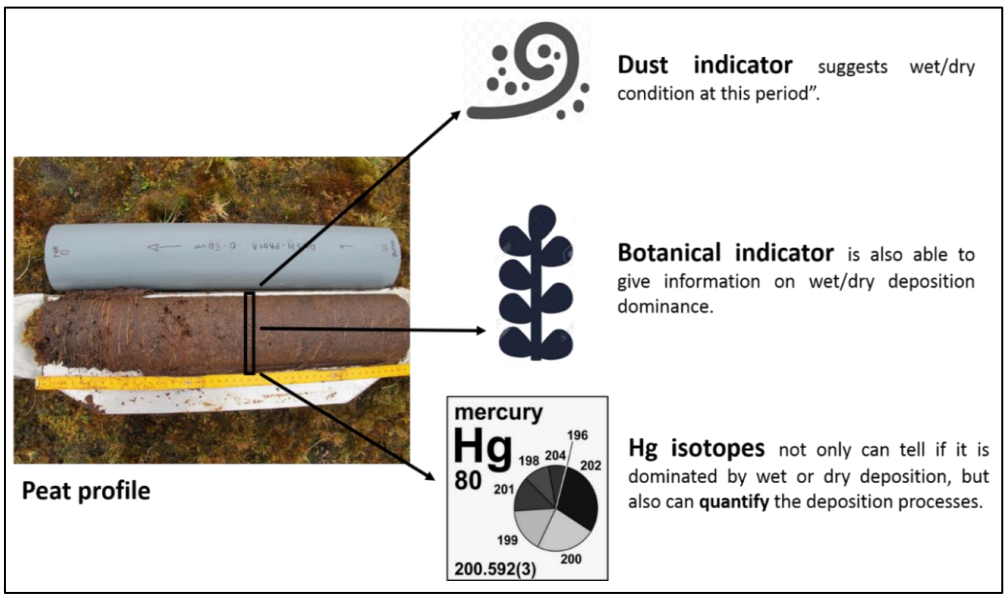

Figure 4. Conceptual diagram of dust, botanical and Hg isotopes as climatic proxies in peat archive.

References:

Amos, H.M., Sonke, J.E., Obrist, D., Robins, N., Hagan, N., Horowitz, H.M., Mason, R.P., Witt, M., Hedgecock, I.M., Corbitt, E.S. and Sunderland, E.M., 2015. Observational and modeling constraints on global anthropogenic enrichment of mercury. *Environmental science & technology*, *49*(7), pp.4036-4047.

Angot, H., Barret, M., Magand, O., Ramonet, M. and Dommergue, A. (2014) A 2-year record of atmospheric mercury species at a background Southern Hemisphere station on Amsterdam Island. Atmospheric Chemistry and Physics 14(20), 11461-11473.

Appleby, P. G. "Chronostratigraphic techniques in recent sediments. In 'Tracking environmental change using lake sediments. Volume 1: basin analysis, coring, and chronological techniques'.(Eds WM Last, JP Smol) pp. 171–203." (2001).

Baboukas, E., Sciare, J. and Mihalopoulos, N., 2002. Interannual variability of methanesulfonate in rainwater at Amsterdam Island (Southern Indian Ocean). *Atmospheric Environment*, *36*(33), pp.5131-5139.

Balkanski, Y.J. and Jacob, D.J., 1990. Transport of continental air to the subantarctic Indian Ocean. *Tellus B*, *42*(1), pp.62-75.

Biester, H., Bindler, R., Martinez-Cortizas, A. and Engstrom, D.R., 2007. Modeling the past atmospheric deposition of mercury using natural archives. *Environmental science & technology*, *41*(14), pp.4851-4860.

Carn, S.A., Fioletov, V.E., McLinden, C.A., Li, C. and Krotkov, N.A., 2017. A decade of global volcanic SO 2 emissions measured from space. *Scientific reports*, *7*, p.44095.

Gaudichet, A., Lefevre, R., Gaudry, A., Ardouin, B., Lambert, G. and Miller, J. (1989) Mineralogical composition of aerosols at Amsterdam Island. Tellus B 41(3), 344-352.

Gaudry, A., Ascencio, J.M. and Lambert, G., 1983. Preliminary study of CO2 variations at Amsterdam Island (Territoire des Terres Australes et Antarctiques Francaises). *Journal of Geophysical Research: Oceans*, *88*(C2), pp.1323-1329.

Gros, V., Poisson, N., Martin, D., Kanakidou, M. and Bonsang, B., 1998. Observations and modeling of the seasonal variation of surface ozone at Amsterdam Island: 1994–1996. *Journal of Geophysical Research: Atmospheres*, *103*(D21), pp.28103-28109.

Heimburger, A., Losno, R. and Triquet, S., 2013. Solubility of iron and other trace elements in rainwater collected on the Kerguelen Islands (South Indian Ocean). *Biogeosciences*, *10*(10), pp.6617-6628.

Heimburger, A., Losno, R., Triquet, S. and Nguyen, E.B., 2013. Atmospheric deposition fluxes of 26 elements over the Southern Indian Ocean: time series on Kerguelen and Crozet Islands. *Global Biogeochemical Cycles*, *27*(2), pp.440-449.

IPCC, 2007. Parry, et al., eds. Climate change 2007-impacts, adaptation and vulnerability: Working group II contribution to the fourth assessment report of the IPCC. Vol. 4. Cambridge University Press, 2007, pp435-460.

Miller, J.M., Moody, J.L., Harris, J.A. and Gaudry, A., 1993. A 10-year trajectory flow climatology for Amsterdam Island, 1980–1989. Atmospheric Environment. Part A. General Topics, 27(12), pp.1909-1916.

Moody, J.L., Pszenny, A.A.P., Gaudry, A., Keene, W.C., Galloway, J.N. and Polian, G., 1991. Precipitation composition and its variability in the southern Indian Ocean: Amsterdam Island, 1980–1987. *Journal of Geophysical Research: Atmospheres*, *96*(D11), pp.20769-20786.

Mulvaney, K., Selin, N.E., Giang, A., Muntean, M., Li, C.T., Zhang, D., Angot, H., Thackray, C.P. and Karplus, V., 2020. Mercury Benefits of Climate Policy in China: Addressing the Paris Agreement and the Minamata Convention Simultaneously. *Environmental Science & Technology*.

Nicholson, S.E., 2001. Climatic and environmental change in Africa during the last two centuries. *Climate research*, *17*(2), pp.123-144.

Nicholson, S.E., Dezfuli, A.K. and Klotter, D., 2012. A two-century precipitation dataset for the continent of Africa. *Bulletin of the American Meteorological Society*, *93*(8), pp.1219-1231.

Polian, G., Lambert, G., Ardouin, B. and Jegou, A. (1986) Long-range transport of continental radon in subantarctic and antarctic areas. Tellus B: Chemical and Physical Meteorology 38(3-4), 178-189.

Rogelj, J., Den Elzen, M., Höhne, N., Fransen, T., Fekete, H., Winkler, H., Schaeffer, R., Sha, F., Riahi, K. and Meinshausen, M., 2016. Paris Agreement climate proposals need a boost to keep warming well below 2 C. *Nature*, *534*(7609), p.631.

Saunders, K.M., Roberts, S.J., Perren, B., Butz, C., Sime, L., Davies, S., Van Nieuwenhuyze, W., Grosjean, M. and Hodgson, D.A., 2018. Holocene dynamics of the Southern Hemisphere westerly winds and possible links to CO2 outgassing. *Nature geoscience*, *11*, pp.650-655.

Sciare, J., Favez, O., Sarda-Estève, R., Oikonomou, K., Cachier, H. and Kazan, V., 2009. Long-term observations of carbonaceous aerosols in the Austral Ocean atmosphere: Evidence of a biogenic marine organic source. *Journal of Geophysical Research: Atmospheres*, *114*(D15).

Streets, D.G., Horowitz, H.M., Jacob, D.J., Lu, Z., Levin, L., Ter Schure, A.F. and Sunderland, E.M., 2017. Total mercury released to the environment by human activities. *Environmental science & technology*, *51*(11), pp.59695977.

UNEP-MCM, 2018. United Nations Environment programes- Minamata convention on mercury.

UNFCCC. *Adoption of the Paris Agreement*. Report No. FCCC/CP/2015/L.9/Rev.1, http://unfccc.int/resource/docs/2015/cop21/eng/l09r01.pdf (UNFCCC, 2015)

UNFCCC. *United Nations Framework Convention on Climate Change*. Report No. FCCC/INFORMAL/84, https://unfccc.int/resource/docs/convkp/conveng.pdf (UNFCCC, 1992)

Appendix

Appendix A for Chapter 1 (Table S3)

Table S3 Global ^{210}Pb data compilation

Source	Location	latitude	longtitude	Type of sample	^{210}Pb flux ± σ/ Bq m^{-2} y^{-1}
Peirson et al., 1966†	Indochina	1.3	103.8	Atmospheric deposition	142
Turekian et al., 1989†	Nothern Pacific	4	159	Atmospheric deposition	54
Peirson et al., 1966†	Nigeria	6.5	3.3	Atmospheric deposition	285
Turekian and Cochran, 1981†	Nothern Pacific	11.3	162.3	Atmospheric deposition	24
Joshi et al., 1969 *	India	11.4	76.7	Atmospheric deposition	87 ± 26.7
Joshi et al., 1969 *	India	13	77.5	Atmospheric deposition	82 ± 31.7
Joshi et al., 1969 *	India	19	72.9	Atmospheric deposition	250 ± 60
Turekian et al., 1989†	Nothern Pacific	21.3	158	Atmospheric deposition	45
Joshi et al., 1969 *	India	21.2	79.1	Atmospheric deposition	102 ± 35
Joshi et al., 1969 *	India	22.6	88.4	Atmospheric deposition	102 ± 48.3
Monaghan et al., 1986†	USA	25.8	81.2	Atmospheric deposition	42
Su et al., 2003	Taiwan	25	121	Atmospheric deposition	316.7
Su et al., 2003	Taiwan	25	121	Atmospheric deposition	183.3
Peirson et al., 1966*	Bahamas Islands	25	77.3	Atmospheric deposition	97
Tsunogai et al., 1985†	Japan	26.2	127.7	Atmospheric deposition	262
Tsunogai et al., 1985†	Nothern Pacific	27.1	142.2	Atmospheric deposition	166
Joshi et al., 1969 *	India	27.2	88.4	Atmospheric deposition	>230 ± 126.7
Turekian et al., 1989†	Nothern Pacific	28.2	177.4	Atmospheric deposition	36
Joshi et al., 1969 *	India	28.8	77.3	Atmospheric deposition	133 ± 43.3
Baskaran et al., 1993†	USA	29.3	94.8	Atmospheric deposition	171
Monaghan et al., 1986†	USA	30.6	96.4	Atmospheric deposition	93
Baskaran et al., 1993†	USA	30.6	96.4	Atmospheric deposition	176
Turekian et al., 1983†	Atlantic Ocean	32.2	64.7	Atmospheric deposition	115
Tsunogai et al., 1985†	Japan	32.7	129.9	Atmospheric deposition	359
Tsunogai et al., 1985†	Japan	33.1	139.8	Atmospheric deposition	327
Tsunogai et al., 1985†	Japan	33.7	135.4	Atmospheric deposition	202
Matsunami et al., 1975†	Japan	34.7	135.5	Atmospheric deposition	170
Fuller and Hammond, 1983†	USA	34	118.3	Atmospheric deposition	35

Fuller and Hammond, 1983†	USA	34 (ca.)	118 (ca.)	Atmospheric deposition	25 ± 1.7
Fuller and Hammond, 1983†	USA	34 (ca.)	118 (ca.)	Atmospheric deposition	35 ± 1.7
Joshi et al., 1969 *	India	34.1	74.9	Atmospheric deposition	182 ± 48.3
Tsunogai et al., 1985†	Japan	35.4	133.9	Atmospheric deposition	264
Shinagawa T., 1980 †	Japan	35.7	139.5	Atmospheric deposition	222
Shinagawa T., 1980 †	Japan	36.6	136.7	Atmospheric deposition	380
Gavini et al., 1974*	USA	36	94.2	Atmospheric deposition	96
Olsen et al., 1985†	USA	36	84.3	Atmospheric deposition	170
Fuller and Hammond, 1983†	USA	37.5	122.2	Atmospheric deposition	25
Olsen et al., 1985†	USA	37	76.3	Atmospheric deposition	144
Tsunogai et al., 1985†	Japan	38.2	140.9	Atmospheric deposition	196
CARVALHO F. P., 1990†	Portugal	38.8	9.1	Atmospheric deposition	56
Monaghan et al., 1986†	USA	38	122.3	Atmospheric deposition	32
Tsunogai et al., 1985†	Japan	39.7	140.1	Atmospheric deposition	262
Monaghan et al., 1986†	USA	40.8	111.8	Atmospheric deposition	78
Knuth et al., 1983†	USA	40.8	74.7	Atmospheric deposition	182
Turekian et al., 1983†	USA	41.3	72.9	Atmospheric deposition	200
Benninger L. K., 1976†	USA	41.3	72.9	Atmospheric deposition	170
Monaghan et al., 1986†	USA	41.3	72.9	Atmospheric deposition	107
Fukuda and Tsunogai, 1975†	Japan	41.7	140.7	Atmospheric deposition	256
Tsunogai et al., 1985†	Japan	41.7	140.7	Atmospheric deposition	257
Monaghan et al., 1986†	USA	41.8	87.7	Atmospheric deposition	132
Fukuda and Tsunogai, 1975†	Japan	41.9	140.1	Atmospheric deposition	290
Fukuda and Tsunogai, 1975†	Japan	41.9	140.3	Atmospheric deposition	443
Fukuda and Tsunogai, 1975†	Japan	41.9	140.4	Atmospheric deposition	465
Fukuda and Tsunogai, 1975 *	Japan	41.8	140.4	Atmospheric deposition	367 ± 100
McNeary and Baskaran, 2003	USA	42.4	83.0	Atmospheric deposition	235
Hussain et al., 1990†	France	43.5	4.6	Atmospheric deposition	82
Heyraud M., 1982†	France	43.8	7.4	Atmospheric deposition	110
Tsunogai et al., 1985†	Japan	43.8	143.9	Atmospheric deposition	217
Thomas A.J., 1988†	France	44.8	0.6	Atmospheric deposition	57
Preiss et al., 1996a†	France	45.1	6.1	Atmospheric deposition	113

Preiss et al., 1996a†	France	45.2	5.7	Atmospheric deposition	115
Peirson et al., 1966*	Canada	45.4	75.7	Atmospheric deposition	147
Dominik et al., 1987†	Italy	45.8	8.6	Atmospheric deposition	224
Preiss et al., 1996a†	France	45.9	6.9	Atmospheric deposition	109
Talbot and Andren, 1983†	USA	46.1	89.7	Atmospheric deposition	259
Dominik et al., 1987†	Switzerland	46	6.5	Atmospheric deposition	152
Preiss et al., 1996a†	France	46	7	Atmospheric deposition	51
Preiss et al., 1996a†	France	46	7	Atmospheric deposition	113
Preiss et al., 1996a†	France	46	7	Atmospheric deposition	56
Monaghan et al., 1986†	USA	47.2	122.5	Atmospheric deposition	58
Schuler et al., 1991†	Switzerland	47.4	8.6	Atmospheric deposition	140
Peirson et al., 1966*	Austria	47.5	13.5	Atmospheric deposition	128
Nevissi A. E., 1985†	USA	47.6	122.3	Atmospheric deposition	73
Winkler and Rosner, 2010	Germany	48.13	11.58	Atmospheric deposition	180
Peirson et al., 1966*	Austria	48.3	14.3	Atmospheric deposition	114
Thomas A.J., 1988†	France	48.8	2.3	Atmospheric deposition	109
Göbel et al., 1965†	Germany	49.3	7	Atmospheric deposition	104
Brunskill and Wilkinson, 1987†	Canada	49.7	93.8	Atmospheric deposition	76
Rulik et al., 1993†	Czech Republic	50.1	14.4	Atmospheric deposition	187
Clifton R. J., 1991†	UK	50.4	4.2	Atmospheric deposition	68
Peirson et al., 1966*	UK	51.7	5	Atmospheric deposition	85
Peirson et al., 1966 *	UK	51	5	Atmospheric deposition	85 ± 13.3
Zuo and Eisma, 1993†	Netherland	53.1	4.8	Atmospheric deposition	72
Beks et al., 1998	Netherlands	53.3	6.6	Atmospheric deposition	73
Eakins et al., 1984†	UK	54.5	3	Atmospheric deposition	147
Baranov and Vilenskii, 1965*	Russia	55.8	37.7	Atmospheric deposition	115 ± 10
Dibb and Jaffrezo, 1993†	Greenland	65.2	43.5	Atmospheric deposition	5.7
Peirson et al., 1966*	Norway	67.3	14.3	Atmospheric deposition	118
Peirson et al., 1966*	Norway	69.7	19	Atmospheric deposition	34
Dibb J. E., 1990b†	Greenland	72.2	38.8	Atmospheric deposition	6.6
Purchet et al., †	svalbard	77.2	15.8	Atmospheric deposition	77
Purchet et al., †	svalbard	77.4	15.4	Atmospheric deposition	61

Purchet et al., †	svalbard	77.7	17.3	Atmospheric deposition	150
Purchet et al., †	svalbard	78.7	13	Atmospheric deposition	47
Purchet et al., †	svalbard	79	13	Atmospheric deposition	30
Bonnyman and Molina-Ramo, 1971 *	Australia	12.4	130.7	Atmospheric deposition	95 ± 25
Preiss et al., 1996b†	Bolivia	16.4	68.1	Atmospheric deposition	75
Gregory L.P., 1975 *	Fiji	18.1	178.4	Atmospheric deposition	80 ± 16.7
Bonnyman and Molina-Ramo, 1971 *	Australia	19.2	146.8	Atmospheric deposition	38 ± 11.7
Bonnyman and Molina-Ramo, 1971 *	Australia	20.4	118.6	Atmospheric deposition	32 ± 10
Gregory L.P., 1975 *	Cook Island	21.3	159.8	Atmospheric deposition	51.7
Bonnyman and Molina-Ramo, 1971 *	Australia	23.7	133.9	Atmospheric deposition	52 ± 10
Bonnyman and Molina-Ramo, 1971 *	Australia	27.4	152.9	Atmospheric deposition	62 ± 11.7
Bonnyman and Molina-Ramo, 1971 *	Australia	27.5	153	Atmospheric deposition	65 ± 8.3
Bonnyman and Molina-Ramo, 1971 *	Australia	32.0	115.8	Atmospheric deposition	43 ± 11.7
Bonnyman and Molina-Ramo, 1971 *	Australia	33.1	115.9	Atmospheric deposition	47 ± 18.3
Bonnyman and Molina-Ramo, 1971 *	Australia	33.9	151.2	Atmospheric deposition	53 ± 15
Bonnyman and Molina-Ramo, 1971 *	Australia	34.8	150.7	Atmospheric deposition	70 ± 18.3
Bonnyman and Molina-Ramo, 1971 *	Australia	34.9	138.6	Atmospheric deposition	53 ± 11.7
Gregory L.P., 1975 *	New Zealand	35.1	173.3	Atmospheric deposition	62 ± 16.7
Bonnyman and Molina-Ramo, 1971 *	Australia	35.2	138.8	Atmospheric deposition	58 ± 13.3
Gregory L.P., 1975 *	New Zealand	36.9	174.8	Atmospheric deposition	50 ± 11.7
Peirson et al., 1966†	Australia	37.7	145	Atmospheric deposition	80
Bonnyman and Molina-Ramo, 1971 *	Australia	37.8	145	Atmospheric deposition	50 ± 11.7
Bonnyman and Molina-Ramo, 1971 *	Australia	38.2	146	Atmospheric deposition	67 ± 13.3
Gregory L.P., 1975 *	New Zealand	39.1	174.1	Atmospheric deposition	73 ± 15
Gregory L.P., 1975 *	New Zealand	39.7	176.9	Atmospheric deposition	30 ± 1.7
Bonnyman and Molina-Ramo, 1971 *	Australia	41.5	147.1	Atmospheric deposition	53 ± 8.3
Gregory L.P., 1975 *	New Zealand	42.5	171.2	Atmospheric deposition	125 ± 11.7
Bonnyman and Molina-Ramo, 1971 *	Australia	42.9	147.3	Atmospheric deposition	30 ± 3.3
Peirson et al., 1966†	Southern Island	43.6	172.7	Atmospheric deposition	23
Gregory L.P., 1975 *	New Zealand	43.6	172.7	Atmospheric deposition	23 ± 1.7
Gregory L.P., 1975 *	New Zealand	45.9	170.5	Atmospheric deposition	30 ± 8.3
Gregory L.P., 1975 *	New Zealand	46.4	168.4	Atmospheric deposition	35 ± 11.7

Peirson et al., 1966*	Atlantic Ocean	51.7	58	Atmospheric deposition	32
Pourchet et al., 1997†	Antartica	62.7	60.4	Atmospheric deposition	8
Peirson et al., 1966*	Atlantic Ocean	65	64	Atmospheric deposition	1.9
Olsen et al., 1985†	USA	19.5	75.6	Wetland	117
Fuller and Hammond, 1983†	USA	34 (ca.)	118 (ca.)	Wetland	23
Olsen et al., 1985†	USA	36.9	76	Wetland	212
Olsen et al., 1985†	USA	37.1	77.6	Wetland	＞188
Olsen et al., 1985†	USA	37.8	75.5	Wetland	120
McCaffrey and Thomson, 1974†	USA	41.5	73	Wetland	167
Armentano and Woodwell, 1975†	USA	41	72.5	Wetland	69
Armentano and Woodwell, 1975†	USA	41	72.5	Wetland	66
Mccaffrey and Thomson, 1980	USA	41.3	72.9	Wetland	178 ± 5
Olid et al., 2010	Iberian Peninsula	43.5	7.5	Wetland	183 ± 3
Olid et al., 2010	Iberian Peninsula	43.5	7.6	Wetland	169 ± 3
Olid et al., 2013	Spain	43.5	7.5	Wetland	155 ± 2
Olid et al., 2013	Spain	43.5	7.5	Wetland	131 ± 3
Olid et al., 2013	Spain	43.5	7.5	Wetland	122 ± 3
Begy et al., 2016	Romania	45.2	22.1	Wetland	277 ± 54
Pourchet et al., 1989†	France	45	6.3	Wetland	110
Begy et al., 2016	Romania	46.1	25.9	Wetland	172 ± 8
Begy et al., 2016	Romania	46.3	23.3	Wetland	113 ± 37
Appleby et al., 1997	Switzerland	46.8	7.2	Wetland	149 ± 4
Appleby et al., 1997	Switzerland	47.2	7.1	Wetland	121 ± 4
Appleby et al., 1997	Switzerland	47.2	7.1	Wetland	122 ± 4
Bao et al., 2010	China	47.4	120.7	Wetland	254 ± 50
Bao et al., 2010	China	47.4	120.7	Wetland	421 ± 17
Holynska et al., 1998	Poland	49.5	19.8	Wetland	74 ± 2
Mitchell et al., 1992†	Ireland	53.2	6.3	Wetland	46
Mitchell et al., 1992†	Ireland	53.2	6.3	Wetland	71
Mitchell et al., 1992†	Ireland	53.2	6.3	Wetland	79
Mitchell et al., 1992†	Ireland	54.2	9.5	Wetland	111
Mitchell et al., 1992†	Ireland	54.2	9.5	Wetland	107
Mitchell et al., 1992†	Ireland	54.3	7.7	Wetland	54
Gallagher et al., 2001	Irland	54 (ca.)	6 (ca.)	Wetland	202 ± 9.3
Gallagher et al., 2001	Irland	54 (ca.)	10 (ca.)	Wetland	165 ± 12.5
Pheiffer Madsen and Sørensen, 1979†	Denmark	55.5	8.3	Wetland	200
Pheiffer Madsen and Sørensen, 1979†	Denmark	55.5	8.3	Wetland	167
MacKenzie et al., 1998	Scotland	55	4	Wetland	106
MacKenzie et al., 1998	Scotland	55	4	Wetland	109
MacKenzie et al., 1997	Scotland	55	3	Wetland	73

Pheiffer Madsen and Sørensen, 1979†	Denmark	55	9	Wetland	123
MacKenzie et al., 1997	Scotland	56	4	Wetland	110
EL Daoushy Farid, 1986†	Sweden	57	14	Wetland	37 ± 14.8
EL Daoushy Farid, 1986†	Sweden	57	14	Wetland	74 ± 25.9
MacKenzie et al., 1997	Scotland	57	7	Wetland	153
Farmer et al., 2015	Scotland	57	3.8	Wetland	273
El-Daoushy and Tolonen, 1984†	Finland	61.7	25.3	Wetland	44
EL Daoushy Farid, 1986†	Finland	61	27	Wetland	44 ± 7.4
El-Daoushy and Tolonen, 1984†	Finland	62.1	30.2	Wetland	56
EL Daoushy Farid, 1986†	Finland	62	30	Wetland	56 ± 3.7
EL Daoushy Farid, 1986†	Sweden	64	15	Wetland	44 ± 14.8
Olid et al., 2014	Sweden	64.2	19.6	Wetland	64 ± 12.8
EL Daoushy Farid, 1986†	Sweden	65	18	Wetland	26 ± 11.1
EL Daoushy Farid, 1986†	Sweden	67	21	Wetland	15 ± 7.4
Pourchet et al., 1995†	Bolivia	16.2	68.3	Wetland	40
Pourchet et al., 1994†	Bolivia	16.2	68.3	Wetland	80
Pourchet et al., 1994†	Bolivia	18	65	Wetland	102
Humphires et al., 2010	South Africa	27.6	32.4	Wetland	135 ± 46.7
Humphires et al., 2010	South Africa	27.6	32.4	Wetland	192 ± 46.7
Kading et al., 2009	South Africa	32.8	18.2	Wetland	122.1
Ivanovich and Harmon, 1992	South Africa	33		Wetland	108.3
Windom H. L., 1969*	Mexico	19	97.3	Glacier	6.4
Windom H. L., 1969*	Mexico	19	98.6	Glacier	1.5
Bhandari et al., 1983†	India	28	88.7	Glacier	27
Purchet et al., †	China	28	102	Glacier	7.5
Gäggeler et al., 1983†	Switzerland	45.9	7.9	Glacier	25
Gäggeler et al., 1983†	Switzerland	45.9	7.9	Glacier	21
Gäggeler et al., 1983†	Switzerland	45.9	7.9	Glacier	22
Windom H. L., 1969*	USA	47.9	123.6	Glacier	26.7
Monaghan and Holdsworth, 1990†	Canada	60.6	140.5	Glacier	14.5
Windom H. L., 1969*	Canada	60.8	139.5	Glacier	6.5
Koide and Goldberg, 1977†	Greenland	63.5	44.6	Glacier	12
Nijampurkar and Clausen, 1990†	Greenland	65.2	43.5	Glacier	19.5
Dibb J. E., 1990†	Greenland	65	43.5	Glacier	5.9
Dibb J. E., 1990a†	Greenland	67	42	Glacier	8.3
Goldberg, E.D., 1963†	Greenland	71.1	37.3	Glacier	7.8
Dibb J. E., 1992†	Greenland	72.2	38.8	Glacier	4.1
Dibb J. E., 1992†	Greenland	72.2	38.8	Glacier	6.4
Dibb J. E., 1990b†	Greenland	72.3	38.8	Glacier	6.1
Dibb J. E., 1990b†	Greenland	72.3	38.8	Glacier	5.4
Dibb J. E., 1992†	Greenland	72.3	38.8	Glacier	7.2
Nijampurkar and Clausen, 1990†	Greenland	74.7	19.3	Glacier	6.4

Windom H. L., 1969*	Greenland	77	56.0	Glacier	18.33
Nijampurkar and Clausen, 1990†	Greenland	77.2	61.8	Glacier	10.8
Dibb J. E., 1990a†	Greenland	77	60	Glacier	8.4
Dibb J. E., 1990a†	Greenland	77	60	Glacier	8.8
Crozaz and Langway, 1966	Greenland	77.2	61.1	Glacier	15.17
Peters et al., 1997	Canada	80.8	72.9	Glacier	5.1 ± 2.4
Purchet et al., unpublished data†	Peru	13.9	70.8	Glacier	28
Baeza et al., 1996	Antarctica	62.7	60.4	Glacier	1.9 ± 0.4
Nezami et al., 1964†	Antartica	66.7	139.8	Glacier	3.33
Crozaz G., 1967†	Antartica	66.7	139.8	Glacier	3.8
Sanak J., 1983†	Antartica	66.7	140	Glacier	4.77
Sanak J., 1983†	Antartica	66.7	139	Glacier	5
Lambert et al., 1983†	Antartica	67.2	139	Glacier	6.63
Lambert et al., 1983†	Antartica	67.7	139	Glacier	2.69
Lambert et al., 1983†	Antartica	68.3	139	Glacier	4.76
Lambert et al., 1983†	Antartica	69.5	137	Glacier	2.49
Crozaz et al., 1964†	Antartica	70.5	24.3	Glacier	8.2
Lambert et al., 1983†	Antartica	70	136	Glacier	5.23
Nijampurkar et al., 2002	Antarctica	70.8	11.7	Glacier	4.3
Sanak J., 1983†	Antartica	71.5	133	Glacier	2.17
Sanak J., 1983†	Antartica	73	130	Glacier	1.33
Sanak J., 1983†	Antartica	74.2	95	Glacier	1.16
Pourchet et al., 1997†	Antartica	74.6	124	Glacier	1.07
Crozaz G., 1967†	Antartica	77.8	165	Glacier	6.9
Suzuki et al., 2004	Antarctic	77.4	39.6	Glacier	0.82
Crozaz G., 1967†	Antartica	80	120	Glacier	5.5
Windom H. L., 1969*	Antarctica	80	120	Glacier	0.83
Koide et al., 1979†	Antartica	82.3	170	Glacier	1.9
Crozaz G., 1967†	Antartica	82.9	18.2	Glacier	1.1
Picciotto et al., 1968*	Antarctica	82.1	55.1	Glacier	1
Crozaz G., 1967†	Antartica	85.2	1.6	Glacier	1.9
Crozaz G., 1967†	Antartica	85.8	8.7	Glacier	1.2
Crozaz G., 1967†	Antartica	86.6	30.6	Glacier	1.4
Coale and Bruland, 1986†	Antartica	90	0	Glacier	0.74
Picciotto et al., 1964†	Antartica	90	0	Glacier	1.8
Crozaz G., 1967†	Antartica	90	0	Glacier	1.89
Pourchet et al., 1997†	Antartica	90	0	Glacier	1.64
Giresse et al., 1994†	Cameroun	3.8	10	Sediment	95
Preiss et al., 1996b†	Cameroun	4.7	93	Sediment	278
Giresse et al., 1994†	Cameroun	4.7	9.3	Sediment	74
Giresse et al., 1994†	Cameroun	4.7	9.3	Sediment	251
Giresse et al., 1994†	Cameroun	5.5	10.5	Sediment	47
Giresse et al., 1994†	Cameroun	5.7	10.5	Sediment	140

Giresse et al., 1994†	Cameroun	5.7	10.5	Sediment	297
Giresse et al., 1994†	Cameroun	5.7	10.7	Sediment	177
Giresse et al., 1994†	Cameroun	5.8	10.2	Sediment	448
Giresse et al., 1994†	Cameroun	5.8	10.2	Sediment	263
Giresse et al., 1994†	Cameroun	5.8	10.2	Sediment	113
Giresse et al., 1994†	Cameroun	5.8	10.2	Sediment	193
Giresse et al., 1994†	Cameroun	6.2	10.5	Sediment	117
Giresse et al., 1994†	Cameroun	6.3	10	Sediment	67
Giresse et al., 1994†	Cameroun	6.3	10	Sediment	143
Giresse et al., 1994†	Cameroun	6.5	10	Sediment	36
Giresse et al., 1994†	Cameroun	7.2	13.7	Sediment	220
Giresse et al., 1994†	Cameroun	7.3	13.7	Sediment	12
Giresse et al., 1994†	Cameroun	7.3	13.7	Sediment	340
Giresse et al., 1994†	Cameroun	7.5	13.5	Sediment	447
Brenner M., 1999	Guatemala	15 (ca.)	90 (ca.)	Sediment	50
Brenner M., 1999	Guatemala	15 (ca.)	90 (ca.)	Sediment	31
Páez-Osuna and Mandelli, 1985†	Mexico	17	100.3	Sediment	212
Brenner M., 1999	Haiti	18 (ca.)	72 (ca.)	Sediment	33
Huh and Su, 2004	Taiwan	21.7	121	Sediment	103
Huh and Su, 2004	Taiwan	21.9	120.9	Sediment	209
Ming et al., 1983†	China	22.5	113.7	Sediment	3725
Ming et al., 1983†	China	22.5	113.7	Sediment	500
Ming et al., 1983†	China	22.5	113.7	Sediment	300
Huh and Su, 2004	Taiwan	22.1	120.8	Sediment	277
Huh and Su, 2004	Taiwan	23.8	120.9	Sediment	283 ± 9
Huh and Su, 2004	Taiwan	23.9	121	Sediment	206 ± 16
Huh and Su, 2004	Taiwan	24	121	Sediment	321
Huh and Su, 2004	Taiwan	24.6	121.4	Sediment	293 ± 12
Huh and Su, 2004	Taiwan	24.6	121.4	Sediment	177
Huh and Su, 2004	Taiwan	24.8	121.6	Sediment	262
Huh and Su, 2004	Taiwan	24.9	121.5	Sediment	364
Huh and Su, 2004	Taiwan	25	121.6	Sediment	392
Huh and Su, 2004	Taiwan	25.2	121.6	Sediment	2544 ± 22
Huh and Su, 2004	Taiwan	25.2	121.6	Sediment	1208
Huh and Su, 2004	Taiwan	25.3	121.5	Sediment	243
Huh and Su, 2004	Taiwan	25.3	121.5	Sediment	613
Huh and Su, 2004	Taiwan	25	121.7	Sediment	1053
Huh and Su, 2004	Taiwan	25.6	122.1	Sediment	1034 ± 25
Huh and Su, 2004	Taiwan	25.1	121.3	Sediment	336
Huh and Su, 2004	Taiwan	25.1	121.6	Sediment	1130
Huh and Su, 2004	Taiwan	25.1	121.4	Sediment	364
Huh and Su, 2004	Taiwan	25.2	121.5	Sediment	1059
Huh and Su, 2004	Taiwan	25.2	121.5	Sediment	554

Huh and Su, 2004	Taiwan	25.2	121.6	Sediment	1650
Preiss et al., 1996a†	Nepal	28.2	85.2	Sediment	284
Binford and Brenner,1986†	USA	28	82	Sediment	170
Schelske et al., 1994	USA	28.1	81.7	Sediment	1167
Xingfu, W et al., †	China	29.4	120.6	Sediment	330
Xingfu, W et al., †	China	29.4	125.6	Sediment	250
Xingfu, W et al., †	China	29.7	125	Sediment	285
Sanchez-Caberza et al., 2007	Spain	29	46	Sediment	64 ± 5
Xingfu, W et al., †	China	29	121.7	Sediment	355
Zheng et al., 2007	China	29.6	105.1	Sediment	588.6
Sanchez-Caberza et al., 2007	Spain	30	45	Sediment	81 ± 1.4
Xingfu, W et al., †	China	31.2	122.4	Sediment	150
Xingfu, W et al., †	China	31.3	123	Sediment	160
Xingfu, W et al., †	China	31.7	126	Sediment	230
Sanchez-Caberza et al., 2007	Spain	31	46	Sediment	98 ± 3
Sanchez-Caberza et al., 2007	Spain	31	46	Sediment	93 ± 5
Sanchez-Caberza et al., 2007	Spain	31	47	Sediment	186 ± 10
Sanchez-Caberza et al., 2007	Spain	31	47	Sediment	255 ± 8
Xingfu, W et al., †	China	31	122.5	Sediment	1630
Xingfu, W et al., †	China	31	123	Sediment	1120
Xingfu, W et al., †	China	31	123.2	Sediment	230
Xingfu, W et al., †	China	32.3	125.5	Sediment	200
Xingfu, W et al., †	China	32.5	126	Sediment	210
CARVALHO F.P., 1990†	Maderia Island	32.7	17	Sediment	50
CARVALHO F.P., 1990†	Maderia Island	32.7	17	Sediment	72
CARVALHO F.P., 1990†	Maderia Island	32.7	17	Sediment	106
CARVALHO F.P., 1990†	Maderia Island	32.7	17	Sediment	16
Flower et al., 1988†	Morocca	32.8	5.3	Sediment	215
Turekian and Cochran, 1981†	Israel	32.8	35.5	Sediment	30
Xingfu, W et al., †	China	32	124.8	Sediment	140
Flower et al., 1988†	Morocca	33.7	4.8	Sediment	200
Flower et al., 1988†	Morocca	33.8	6.2	Sediment	115
Wakiyama et al., 2010	Japan	33	132	Sediment	613.6
Sanchez-Caberza et al., 2007	Spain	33	46	Sediment	156 ± 8
Benmansour M., 2013	Morocco	33.8	6.7	Sediment	103 ± 31
Sanchez-Caberza et al., 2007	Spain	34	47	Sediment	205 ± 11
Fukuyama et al., 2008	Japan	34.4	136.4	Sediment	263.2
Graustein and Turekian, 1986†	USA	35.1	101.9	Sediment	144
Kurata and Tsunogai, 1986†	Japan	35.1	135.9	Sediment	250
Graustein and Turekian, 1986†	USA	35.2	87	Sediment	130
Matsumoto E., 1981†	Japan	35.3	136.2	Sediment	140
Graustein and Turekian, 1986†	USA	35.5	93.1	Sediment	187
Matsumoto E., 1981†	Japan	35.5	135.8	Sediment	580

Matsumoto E., 1981†	Japan	35.5	133.3	Sediment	650
Matsumoto E., 1981†	Japan	35.5	133	Sediment	160
Matsumoto E., 1981†	Japan	35.5	133	Sediment	250
Matsumoto E., 1981†	Japan	35.5	133	Sediment	360
Matsumoto E., 1981†	Japan	35.5	133	Sediment	310
Nosaki et al., 1978†	USA	35.7	106.3	Sediment	432
Nosaki et al., 1978†	USA	35.7	106.3	Sediment	217
Kurata and Tsunogai, 1986†	Japan	35.7	139.5	Sediment	180
Matsumoto E., 1975*	Japan	35	132	Sediment	150
Matsumoto E., 1975*	Japan	35	132	Sediment	300
Matsumoto E., 1975*	Japan	35	132	Sediment	366.7
Matsumoto E., 1975 *	Japan	35	132	Sediment	250
Sanchez-Caberza et al., 2007	Spain	35	47	Sediment	76 ± 9
Sanchez-Caberza et al., 2007	Spain	35	47	Sediment	91 ± 8
Sanchez-Caberza et al., 2007	Spain	35	47	Sediment	114 ± 7
Matsumoto E., 1981†	Japan	35	136	Sediment	40
Graustein and Turekian, 1986†	USA	36.4	81.6	Sediment	173
Graustein and Turekian, 1986†	USA	36.6	97.6	Sediment	156
Sanchez-Caberza et al., 2007	Spain	36	46	Sediment	58 ± 5
Sanchez-Caberza et al., 2007	Spain	36	47	Sediment	219 ± 7
Graustein and Turekian, 1986†	USA	36	79	Sediment	140
Garcia-Orellana et al., 2006	mediteranean	36.7	15.1	Sediment	56 ± 13
Garcia-Orellana et al., 2006	mediteranean	36.7	2.2	Sediment	34 ± 3
Garcia-Orellana et al., 2006	mediteranean	36.9	14.4	Sediment	58 ± 5
CARVALHO F.P., 1990†	Portugal	37.1	7.6	Sediment	31
CARVALHO F.P., 1990†	Portugal	37.3	7.5	Sediment	32
Graustein and Turekian, 1986†	USA	37.9	86.7	Sediment	163
Fisenne I. M., 1968*	USA	37	75	Sediment	200
O'Farrell et al., 2007	USA	37	122	Sediment	47.0
O'Farrell et al., 2007	USA	37	122	Sediment	59.3
Porto et al., 2014	Italy	37	14	Sediment	87.2
Sanchez-Caberza et al., 2007	Spain	37	46	Sediment	32 ± 3
Sanchez-Caberza et al., 2007	Spain	37	46	Sediment	35 ± 4
Helz et al., 1985†	USA	37	76	Sediment	168
Brush et al., 1982†	USA	38.2	76.8	Sediment	400
Brush et al., 1982†	USA	38.2	76.8	Sediment	470
Brush et al., 1982†	USA	38.3	76.8	Sediment	100
Brush et al., 1982†	USA	38.3	76.9	Sediment	1170
CARVALHO F.P., 1990†	Portugal	38.5	9	Sediment	73
Brush et al., 1982†	USA	38.5	77	Sediment	275
Brush et al., 1982†	USA	38.5	77.3	Sediment	575
Graustein and Turekian, 1986†	USA	38.8	75.3	Sediment	133

CARVALHO F.P., 1990†	Portugal	38.8	9.1	Sediment	54
CARVALHO F.P., 1990†	Portugal	38.8	9.1	Sediment	25
CARVALHO F.P., 1990†	Portugal	38.8	9.1	Sediment	46
Brush et al., 1982†	USA	38.8	77	Sediment	1860
Porto et al., 2012	Italy	38	15	Sediment	222 ± 7
Graustein and Turekian, 1986†	USA	38	80.3	Sediment	182
Graustein and Turekian, 1986†	USA	38	81	Sediment	102
CARVALHO F.P., 1990†	Portugal	38	7.9	Sediment	35
Helz et al., 1985†	USA	38	76	Sediment	177
Brush et al., 1982†	USA	38	76.3	Sediment	58
Monaghan M. C., 1989†	USA	39.3	123.8	Sediment	39
Monaghan M. C., 1989†	USA	39.3	123.8	Sediment	53
Graustein and Turekian, 1986†	USA	39.5	105	Sediment	100
Moore and Poet, 1976*	USA	39	105	Sediment	266.7
Porto et al., 2013	Italy	39	16	Sediment	339.4
Helz et al., 1985†	USA	39	76	Sediment	345
Porto et al., 2006	Italy	39.2	17.1	Sediment	164.0
Garcia-Orellana et al., 2006	mediteranean	39.9	4.3	Sediment	85 ± 9
Graustein and Turekian, 1986†	USA	40.2	89.1	Sediment	197
CARVALHO F.P., 1990†	Portugal	40.3	7.5	Sediment	58
CARVALHO F.P., 1990†	Portugal	40.3	8.5	Sediment	18
Monaghan M. C., 1989†	USA	40.7	122.3	Sediment	74
Monaghan M. C., 1989†	USA	40.7	122.3	Sediment	69
CARVALHO F.P., 1990†	Portugal	40.7	8.7	Sediment	7
Monaghan M. C., 1989†	USA	40	121	Sediment	102
Monaghan M. C., 1989†	USA	40	121	Sediment	140
Monaghan M. C., 1989†	USA	40	121	Sediment	122
Monaghan M. C., 1989†	USA	40	121	Sediment	153
Monaghan M. C., 1989†	USA	40	121	Sediment	116
Graustein and Turekian, 1986†	USA	40	82.3	Sediment	166
Schettler et al., 2006	China	40 (ca.)	130 (ca.)	Sediment	517
Garcia-Orellana et al., 2006	mediteranean	40	3.85	Sediment	82 ± 14
Garcia-Orellana et al., 2006	mediteranean	40.1	4.1	Sediment	84 ± 11
Graustein and Turekian, 1986†	USA	41.2	73.7	Sediment	130
McCall et al., 1984†	USA	41.2	81.3	Sediment	2800
McCaffrey and Thomson, 1980†	USA	41.3	72.8	Sediment	133
Benninger et al., 1975†	USA	41.3	72.9	Sediment	168
Benninger et al., 1975†	USA	41.3	72.9	Sediment	133
Nosaki et al., 1978†	USA	41.3	79.2	Sediment	199
Nosaki et al., 1978†	USA	41.5	78.2	Sediment	149
McCaffrey, 1977†	USA	41.5	73	Sediment	133

Kurata and Tsunogai, 1986†	Japan	41.7	140.7	Sediment	430
Graustein and Turekian, 1986†	USA	41.8	91.8	Sediment	162
Graustein and Turekian, 1986†	USA	41.8	75.9	Sediment	132
J Kada and M Heit, 1992†	USA	41.9	73.9	Sediment	177
Brugam B. R., 1975*	USA	41	72	Sediment	266.7
Brugam B. R., 1975*	USA	41	72	Sediment	383.3
Nosaki et al., 1978†	USA	41	77	Sediment	133
Graustein and Turekian, 1986†	USA	41	85.2	Sediment	125
Lewis M. Dale, 1977*	USA	41 (ca.)	79 (ca.)	Sediment	166.7
Giresse et al., 1994†	Bulgaria	42.1	23.5	Sediment	132
Giresse et al., 1994†	Bulgaria	42.1	23.5	Sediment	75
Giresse et al., 1994†	Bulgaria	42.1	23.5	Sediment	104
Giresse et al., 1994†	Bulgaria	42.1	23.5	Sediment	122
Purchet et al., †	Bulgaria	42.1	23.5	Sediment	286
Purchet et al., †	Bulgaria	42.1	23.5	Sediment	283
Purchet et al., †	Bulgaria	42.1	23.5	Sediment	370
Purchet et al., †	Bulgaria	42.1	23.5	Sediment	301
Robbins J. A., 1978†	Albania-Ex-Yougoslavia	42.2	19.3	Sediment	70
Benoit and Hemond, 1991†	USA	42.5	71.8	Sediment	133
Benoit and Hemond, 1991†	USA	42.5	71.8	Sediment	163
Graustein and Turekian, 1986†	USA	42.6	72.5	Sediment	126
DeConinck et al., 1983†	France	42.7	3	Sediment	310
DeConinck et al., 1983†	France	42.7	3	Sediment	120
Graustein and Turekian, 1986†	USA	42.8	100.3	Sediment	142
Robbins and Endington, 1974*	USA	42	87	Sediment	66.67
Robbins and Endington, 1974*	USA	42	86	Sediment	240
Robbins and Endington, 1974*	USA	42	86	Sediment	51.67
Gaspar et al., 2013	Spain	42	0.5	Sediment	61 ± 2.4
Garcia-Orellana et al., 2006	mediteranean	42.5	3.1	Sediment	61 ± 6
Garcia-Orellana et al., 2006	mediteranean	42.7	9.1	Sediment	59 ± 9
Garcia-Orellana et al., 2006	mediteranean	42.7	9.1	Sediment	62 ± 8
Garcia-Orellana et al., 2006	mediteranean	42.7	9.1	Sediment	61 ± 7
Kada and Heit, 1992†	USA	43.3	74.9	Sediment	40
Monna et al., 1997†	France	43.4	3.6	Sediment	193
Monna et al., 1997†	France	43.4	3.6	Sediment	133
Monna et al., 1997†	France	43.4	3.6	Sediment	130
Monna et al., 1997†	France	43.4	3.6	Sediment	178
Kada and Heit, 1992†	USA	43.8	74.8	Sediment	62
Kada and Heit, 1992†	USA	43.8	74.9	Sediment	236
Kada and Heit, 1992†	USA	43.9	75	Sediment	448

Kada and Heit, 1992†	USA	43.9	75	Sediment	74
Robbins and Endington, 1974*	USA	43	87	Sediment	100
Robbins and Endington, 1974*	USA	43	86	Sediment	63.33
Yang et al., 2011	China	43	125	Sediment	279 ± 11
Koide et al., 1972†	USA	43	89.2	Sediment	53
Garcia-Orellana et al., 2006	mediteranean	43.2	3.1	Sediment	83 ± 6
Garcia-Orellana et al., 2006	mediteranean	43.4	6.7	Sediment	121 ± 12
Olid et al., 2010	Iberian Peninsula	43.5	7.7	Sediment	181 ± 7
DURHAM and JOSHI, 1980a†	Canada	43.8	82.3	Sediment	56
DURHAM and JOSHI, 1980a†	Canada	43.8	82.1	Sediment	326
Graustein and Turekian, 1986†	USA	44.2	73.4	Sediment	122
Kada and Heit, 1992†	USA	44.2	74.8	Sediment	217
Graustein and Turekian, 1986†	USA	44.3	72.9	Sediment	306
Graustein and Turekian, 1986†	USA	44.4	74	Sediment	382
Kada and Heit, 1992†	USA	44.4	74.7	Sediment	230
Giresse et al., 1994†	France	44.7	6.9	Sediment	163
Robbins and Endington, 1974*	USA	44	86	Sediment	118.3
Graustein and Turekian, 1986†	USA	44	72	Sediment	126
Graustein and Turekian, 1986†	USA	44	71	Sediment	153
Davis et al., 1984†	USA	44	72	Sediment	128
Davis et al., 1984†	USA	44	71	Sediment	75
Davis et al., 1984†	USA	44	71	Sediment	73
Davis et al., 1984†	USA	44	71	Sediment	47
Von Damm et al., 1979†	USA	44	72	Sediment	583
DURHAM and JOSHI, 1980a†	Canada	44.2	83.0	Sediment	115
Durham and Joshi, 1984†	Canada	45.2	67.3	Sediment	195
Durham and Joshi, 1984†	Canada	45.4	81.8	Sediment	242
Durham and Joshi, 1984†	Canada	45.7	78.3	Sediment	37
Durham and Joshi, 1984†	Canada	45.7	81.8	Sediment	78
Durham and Joshi, 1984†	Canada	45.7	82	Sediment	19
Krishnaswamy et al., 1971*	France	45	2	Sediment	216.7
Robbins and Endington, 1974*	USA	45	86	Sediment	140
Durham and Joshi, 1984†	Canada	45	76.7	Sediment	53
Durham and Joshi, 1984†	Canada	45	76.8	Sediment	18
Davis et al., 1984†	USA	45	69	Sediment	410
Davis et al., 1984†	USA	45	69	Sediment	174
Davis et al., 1984†	USA	45	69	Sediment	154
Davis et al., 1984†	USA	45	69	Sediment	149
Davis et al., 1984†	USA	45	70	Sediment	142

Davis et al., 1984†	USA	45	70	Sediment	59
Davis et al., 1984†	USA	45	69	Sediment	51
Davis et al., 1984†	USA	45	69	Sediment	120
Davis et al., 1984†	USA	45	69	Sediment	88
Davis et al., 1984†	USA	45	69	Sediment	84
Pourchet et al., 1989†	France	45	6.3	Sediment	110
Pourchet et al., 1989†	France	45	6.3	Sediment	170
DURHAM and JOSHI, 1980a†	Canada	45.6	83.4	Sediment	185
Carpenter et al., 1981†	USA	46.4	124	Sediment	108
Carpenter et al., 1981†	USA	46.7	123.9	Sediment	114
Klump et al., 1989†	Laurentian Great Lakes	46.7	84.8	Sediment	329
Begy et al., 2016	Romania	46.8	25.8	Sediment	195 ± 12
Begy et al., 2016	Romania	46.8	25.8	Sediment	100 ± 10
Begy et al., 2016	Romania	46.8	25.8	Sediment	101 ± 9
Begy et al., 2016	Romania	46.8	25.8	Sediment	168 ± 8
Begy et al., 2016	Romania	46.8	25.8	Sediment	81 ± 4
Carpenter et al., 1981†	USA	46.8	124.1	Sediment	50
Klump et al., 1989†	Laurentian Great Lakes	46.9	86.6	Sediment	70
Klump et al., 1989†	Laurentian Great Lakes	46.9	84.5	Sediment	178
Krishnaswamy et al., 1971*	Switzerland	46	6	Sediment	71.67
Koide et al., 1972†	USA	46	89.4	Sediment	106
Viel M., 1983†	Switzerland	46	8.5	Sediment	104
Carpenter et al., 1981†	USA	47.1	124.1	Sediment	233
Klump et al., 1989†	Laurentian Great Lakes	47.1	87.6	Sediment	459
Klump et al., 1989†	Laurentian Great Lakes	47.2	86.1	Sediment	466
Von Gunten and Moser, 1993†	Switzerland	47.2	8.7	Sediment	213 ± 22
Von Gunten and Moser, 1993†	Switzerland	47.2	8.7	Sediment	193 ± 19
Von Gunten and Moser, 1993†	Switzerland	47.2	8.7	Sediment	227 ± 23
Von Gunten and Moser, 1993†	Switzerland	47.2	8.7	Sediment	320 ± 32
Von Gunten and Moser, 1993†	Switzerland	47.2	8.7	Sediment	375 ± 38
Von Gunten and Moser, 1993†	Switzerland	47.2	8.7	Sediment	400 ± 40
Von Gunten and Moser, 1993†	Switzerland	47.2	8.7	Sediment	305 ± 31
Erten et al., 1985†	Switzerland	47.2	8.7	Sediment	95 ± 10
Erten et al., 1985†	Switzerland	47.2	8.7	Sediment	85 ± 9
Carpenter et al., 1981†	USA	47.3	124.2	Sediment	127
Wan et al., 1987†	Switzerland	47.3	8.7	Sediment	55 ± 5
Carpenter et al., 1981†	USA	47.4	124.3	Sediment	114
Klump et al., 1989†	Laurentian Great Lakes	47.4	88.6	Sediment	81
Hemmerich R., 1980†	Germany	47.5	9.5	Sediment	100

Klump et al., 1989†	Laurentian Great Lakes	47.5	88.6	Sediment	111
Dominik et al., 1981†	Switzerland	47.5	9.5	Sediment	73
Dominik et al., 1981†	Switzerland	47.5	9.5	Sediment	82
Dominik et al., 1981†	Switzerland	47.5	9.5	Sediment	88
Dominik et al., 1981†	Switzerland	47.5	9.5	Sediment	205
Dominik et al., 1981†	Switzerland	47.5	9.5	Sediment	192
Dominik et al., 1981†	Switzerland	47.5	9.5	Sediment	63
Dominik et al., 1981†	Switzerland	47.5	9.5	Sediment	135
Von Gunten et al., 1987†	Switzerland	47.5	9.5	Sediment	175
Klump et al., 1989†	Laurentian Great Lakes	47.8	88.5	Sediment	241
Klump et al., 1989†	Laurentian Great Lakes	47.9	88.2	Sediment	588
Durham and Joshi, 1984†	Canada	47	84.3	Sediment	345
Durham and Joshi, 1984†	Canada	47	84.3	Sediment	229
Durham and Joshi, 1984†	Canada	47	84.3	Sediment	148
Klump et al., 1989†	Laurentian Great Lakes	47	86.1	Sediment	1125
Bloesch and Evans, 1982†	Switzerland	47	8.3	Sediment	100
Kato et al., 2010	Mongolia	47.2	108.7	Sediment	196.5
Kato et al., 2010	Mongolia	47.7	108.5	Sediment	200.1
Matsumoto and Wong, 1977†	Canada	48.5	123.5	Sediment	320
Smith and Ellis, 1982†	Canada	48.7	70.8	Sediment	3350
Smith and Walton, 1980†	Canada	48.7	-70.8	Sediment	425
Smith and Walton, 1980†	Canada	48.7	-70.8	Sediment	550
Smith and Walton, 1980†	Canada	48.7	-70.8	Sediment	360
Smith and Walton, 1980†	Canada	48.7	-70.8	Sediment	340
Smith and Walton, 1980†	Canada	48.7	-70.8	Sediment	340
Smith and Walton, 1980†	Canada	48.7	-70.8	Sediment	305
Smith and Walton, 1980†	Canada	48.7	-70.8	Sediment	155
Matsumoto and Wong, 1977†	Canada	48.7	123.5	Sediment	850
Durham and Joshi, 1984†	Canada	48.8	90.2	Sediment	25
Durham and Joshi, 1984†	Canada	48.8	90.3	Sediment	28
Durham and Joshi, 1981†	Laurentian Great Lakes	48.8	88.2	Sediment	106
Schelske et al., 1994	USA	48.5	114.4	Sediment	363.3
Durham and Joshi, 1980b†	Canada	49.8	77.5	Sediment	133
Dörr and Münnich, 1991	Germany	49 (ca.)	8.7 (ca.)	Sediment	90
Durham and Joshi, 1980b†	Canada	49	77	Sediment	18
Petit D., 1974*	Belgium	50	4	Sediment	158.3
Petit D., 1974*	Belgium	50	4	Sediment	130
Oldfield et al., 1980†	Belgium	50	5.3	Sediment	122
Oldfield et al., 1980†	Belgium	50	5.3	Sediment	115
Oldfield et al., 1980†	Belgium	50	5.3	Sediment	122
Edgington et al., 1991†	Russia	51.7	105.2	Sediment	40
Edgington et al., 1991†	Russia	51.8	104.5	Sediment	30

Edgington et al., 1991†	Russia	52.4	106	Sediment	97
Edgington et al., 1991†	Russia	52.4	106.2	Sediment	34
Edgington et al., 1991†	Russia	52.4	106.1	Sediment	44
Edgington et al., 1991†	Russia	52.9	107.9	Sediment	106
Appleby and Oldfield. 1983†	UK	52	1	Sediment	74
Appleby and Oldfield. 1983†	UK	52	1	Sediment	63
Appleby and Oldfield. 1983†	UK	52	1	Sediment	63
Elner and Happey, 1980†	UK	52	3.5	Sediment	450
Elner and Happey, 1980†	UK	52	3.5	Sediment	490
Oldfield and Appleby, 1984†	UK	52	3.5	Sediment	67
Oldfield and Appleby, 1984†	UK	52	3.5	Sediment	185
Edgington et al., 1991†	Russia	53.2	107.8	Sediment	134
Edgington et al., 1991†	Russia	53.5	108	Sediment	146
Edgington et al., 1991†	Russia	53.9	108.4	Sediment	159
Oldfield F., 1978†	Ireland	54.3	7.5	Sediment	170
Appleby et al., 1995†	UK	54.4	3	Sediment	115
Appleby et al., 1995†	UK	54.4	3.3	Sediment	175
Eakins et al., 1984†	UK	54.5	3	Sediment	162
Appleby et al., 1995†	UK	54.5	3	Sediment	149
Oldfield F., 1978†	Ireland	54.5	7.2	Sediment	150
Oldfield F., 1978†	Ireland	54.5	7.7	Sediment	240
Oldfield F., 1978†	Ireland	54.5	7.7	Sediment	220
Battarbee R. W., 1978†	Ireland	54.6	6.4	Sediment	118
Tylmann et al., 2016	Poland	54.1	22	Sediment	432 ± 8
Dearing et al., 1987†	Sweden	55.5	13.3	Sediment	130
Dearing et al., 1987†	Sweden	55.5	13.3	Sediment	133
Pheiffer Madsen and Sørensen, 1979†	Denmark	55.5	8.3	Sediment	530
EL Daoushy Farid, 1986†	Sweden	55	13	Sediment	189 ± 22
Hermanson et al., 1990	Arctic	56.2	79.3	Sediment	36.8
Hermanson et al., 1990	Arctic	56.2	79.3	Sediment	43.3
Hermanson et al., 1990	Arctic	56.2	79.3	Sediment	42.7
Hermanson et al., 1990†	Canada	56.2	79.3	Sediment	52
EL Daoushy Farid, 1986†	Sweden	56	15	Sediment	89 ± 7
EL Daoushy Farid, 1986†	Sweden	56	15	Sediment	122 ± 15
EL Daoushy Farid, 1986†	Sweden	57	12	Sediment	3.7
EL Daoushy Farid, 1986†	Scandinava	57	14	Sediment	96 ± 11
EL Daoushy Farid, 1986†	Scandinava	57	14	Sediment	33 ± 3.7
Farmer et al., 2015	Scotland	57.1	3.8	Sediment	322
EL Daoushy Farid, 1986†	Sweden	58	12	Sediment	59.2
EL Daoushy Farid, 1986†	Sweden	58	12	Sediment	144.3
EL Daoushy Farid, 1986†	Sweden	58	12	Sediment	96.2
EL Daoushy Farid, 1986†	Sweden	58	12	Sediment	222 ± 15
EL Daoushy Farid, 1986†	Sweden	58	12	Sediment	226 ± 11

EL Daoushy Farid, 1986†	Skagerrak	58	10	Sediment	204 ± 15
Davis et al., 1984†	Norway	58 (ca.)	8.7 (ca.)	Sediment	94
Monaghan and Holdsworth, 1990†	Canada	59.7	135.2	Sediment	20
EL Daoushy Farid, 1986†	Sweden	59	14	Sediment	59 ± 7.4
EL Daoushy Farid, 1986†	Norway	59	9	Sediment	185 ± 15
EL Daoushy Farid, 1986†	Norway	59	9	Sediment	259 ± 22
EL Daoushy Farid, 1986†	Sweden	59	18	Sediment	130 ± 11
Davis et al., 1984†	Norway	59 (ca.)	7.7 (ca.)	Sediment	125
Davis et al., 1984†	Norway	59 (ca.)	8.6 (ca.)	Sediment	112
Davis et al., 1984†	Norway	59 (ca.)	6.5 (ca.)	Sediment	111
Davis et al., 1984†	Norway	59 (ca.)	6.7 (ca.)	Sediment	92
Davis et al., 1984†	Norway	>60 (ca.)		Sediment	167
Davis et al., 1984†	Norway	>60 (ca.)		Sediment	129
Davis et al., 1984†	Norway	>60 (ca.)		Sediment	102
Davis et al., 1984†	Norway	>60 (ca.)		Sediment	82
Monaghan and Holdsworth, 1990†	Canada	60.7	134.8	Sediment	38
Monaghan and Holdsworth, 1990†	Canada	60.7	134.8	Sediment	30
EL Daoushy Farid, 1986†	Sweden	60	14	Sediment	22.2
Edgington et al., 1991†	Russia	60	107.8	Sediment	84
Davis et al., 1984†	Norway	60 (ca.)	6.5 (ca.)	Sediment	112
Appleby et al., 1979†	Finland	61.9	25.9	Sediment	233
EL Daoushy Farid, 1986†	Sweden	61	15	Sediment	137 ± 15
Monaghan and Holdsworth, 1990†	Canada	61	138.3	Sediment	21
Monaghan and Holdsworth, 1990†	Canada	61	138.3	Sediment	54
Monaghan and Holdsworth, 1990†	Canada	61	138.3	Sediment	30
Monaghan and Holdsworth, 1990†	Canada	61	138.3	Sediment	43
Appleby et al., 1979†	Finland	61	25.1	Sediment	280
Oldfield and Appleby, 1984†	Finland	61 (ca.)	24.9 (ca.)	Sediment	81
Davis et al., 1984†	Norway	61 (ca.)	8.9 (ca.)	Sediment	143
Davis et al., 1984†	Norway	61 (ca.)	7.3 (ca.)	Sediment	93
Persson B. R., 1970†	Sweden	62.3	12.3	Sediment	63
Appleby et al., 1979†	Finland	62.4	29.1	Sediment	240
EL Daoushy Farid, 1986†	Sweden	62	16	Sediment	78 ± 15
EL Daoushy Farid, 1986†	Sweden	62	15	Sediment	33 ± 3.7
EL Daoushy Farid, 1986†	Sweden	63	15	Sediment	63 ± 7.4
Davis et al., 1984†	Norway	63 (ca.)	8.7 (ca.)	Sediment	131
EL Daoushy Farid, 1986†	Sweden	64	16	Sediment	37 ± 3.7
Klaminder et al., 2006	Sweden	64.2	19.6	Sediment	77.85
EL Daoushy Farid, 1986†	Sweden	65	19	Sediment	96 ± 11

Bindler et al., 2001	Greenland	66.494	53.53	Sediment	61
Bindler et al., 2001	Greenland	66.965	49.802	Sediment	27
EL Daoushy Farid, 1986†	Sweden	66	19	Sediment	59 ± 7.4
EL Daoushy Farid, 1986†	Sweden	66	21	Sediment	44 ± 3.7
EL Daoushy Farid, 1986†	Sweden	67	21	Sediment	74 ± 7.4
EL Daoushy Farid, 1986†	Sweden	68	21	Sediment	30 ± 3.7
Fitzgerald et al., 2005	Arctic	68.5	149.7	Sediment	78
Fitzgerald et al., 2005	Arctic	68.5	149.7	Sediment	74
Fitzgerald et al., 2005	Arctic	68.5	149.7	Sediment	70
Cornwell et al., 1985	Arctic	68.6	149.6	Sediment	23 ± 8.3
Fitzgerald et al., 2005	Arctic	68.6	149.8	Sediment	37
Fitzgerald et al., 2005	Arctic	68.6	149.8	Sediment	33
Fitzgerald et al., 2005	Arctic	68.6	149.8	Sediment	52
Fitzgerald et al., 2005	Arctic	68.7	149.7	Sediment	56
Fitzgerald et al., 2005	Arctic	68.7	149.7	Sediment	67
Fitzgerald et al., 2005	Arctic	68.7	149.7	Sediment	30
Fitzgerald et al., 2005	Arctic	68.7	150.0	Sediment	44
Fitzgerald et al., 2005	Arctic	68.7	150.0	Sediment	30
Fitzgerald et al., 2005	Arctic	68.7	150.0	Sediment	63
Fitzgerald et al., 2005	Arctic	68.9	150.3	Sediment	78
Fitzgerald et al., 2005	Arctic	68.9	150.3	Sediment	56
Fitzgerald et al., 2005	Arctic	68.9	150.3	Sediment	37
Weiss and Naidu, 1986	Arctic	70	149	Sediment	216.3
Kipphut et al., 1978	Arctic	74.7		Sediment	45.5
Szczuciński et al., 2009	Svalbard	78.53	16.3	Sediment	140
Szczuciński et al., 2009	Svalbard	78.6	16.5	Sediment	176.7
Szczuciński et al., 2009	Svalbard	78.6	16.5	Sediment	171.7
Szczuciński et al., 2009	Svalbard	78.7	16.7	Sediment	213.3
Szczuciński et al., 2009	Svalbard	78.7	16.5	Sediment	100
Szczuciński et al., 2009	Svalbard	78.7	16.5	Sediment	95
Pourchet et al., 1994†	Bolivia	16.2	68.9	Sediment	11
Pourchet et al., 1994†	Bolivia	16.2	68.9	Sediment	55
Pourchet et al., 1994†	Bolivia	16.2	68.7	Sediment	73
Pourchet et al., 1994†	Bolivia	16.2	68.7	Sediment	69
Pourchet et al., 1995†	Bolivia	16.2	68.3	Sediment	162
Pourchet et al., 1995†	Bolivia	16.2	68.3	Sediment	147
Pourchet et al., 1994†	Bolivia	16.4	69	Sediment	9
Pourchet et al., 1994†	Bolivia	16.4	69	Sediment	62
Binford et al., 1991†	Bolivia	16.4	68.8	Sediment	47
Walling et al., 2003	Zambia	16.2	28	Sediment	83 ± 12.5
Brenner M., 1999	Bolivia	16.3	68.7	Sediment	31.7
Rabesiranana et al., 2016	Madagascar	18.9	47.8	Sediment	95.8 ± 12.5
Curran C.M., 1996	Australia	19	146	Sediment	44 ± 38.9

Humphires and Benitez-Nelson, 2013	South Africa	27.3	32.6	Sediment	78 ± 5.2
Humphires and Benitez-Nelson, 2013	South Africa	27.3	32.6	Sediment	51 ± 4.4
Nosaki et al., 1978†	South Africa	29.8	31	Sediment	108
Blake et al., 2009	Australia	34.2	150.5	Sediment	60 ± 5.3
Cisternas and Araneda, 2001	Chile	36.9	73.1	Sediment	23.6
Guevara et al., 2003	Argentina	40.5-(-41.2)	71.2-(-71.8)	Sediment	40 ± 1.8
Guevara et al., 2003	Argentina	40.5-(-41.2)	71.2-(-71.8)	Sediment	24 ± 1.5
Guevara et al., 2003	Argentina	40.5-(-41.2)	71.2-(-71.8)	Sediment	27 ± 1
Guevara et al., 2003	Argentina	40.5-(-41.2)	71.2-(-71.8)	Sediment	48 ± 1.3
Guevara et al., 2003	Argentina	40.6	71.4	Sediment	20.9 ± 0.4
Guevara et al., 2003	Argentina	41	71.5	Sediment	7.5 ± 0.7
Guevara et al., 2003	Argentina	41	71.5	Sediment	25.5 ± 1.1
Guevara et al., 2003	Argentina	41	71.5	Sediment	4.1 ± 1.2
Guevara et al., 2003	Argentina	41	71.5	Sediment	4 ± 0.6
Appleby et al., 1995†	Antartic regions	60.7	45.6	Sediment	32
Appleby et al., 1995†	Antartic regions	60.7	45.6	Sediment	137
Appleby et al., 1995†	Antartic regions	60.7	45.6	Sediment	40
Roos et al., 1994†	Antartic regions	60	60	Sediment	1.2
Roos et al., 1994†	Antartic regions	60	60	Sediment	8.7
Roos et al., 1994†	Antartic regions	62.6	60.5	Sediment	3.7

"*": Turekian, K. Y.; Nozaki, Y.; Benninger, L. K., Geochemistry of atmospheric radon and radon products. Annual Review of Earth and Planetary Sciences 1977, 5, 227.

"†": From Preiss, N. Etude du ^{210}Pb d'origine atmosphérique dans l'air, la neige, les sols et les sédiments: Mesures, inventaires et interprétation à l'échelle globale. 1997

"ca.": Approximately. No digit-records of Latitude and Longtitude in the paper

"^{210}Pb flux/ Bq m^{-2} yr^{-1}" Column: use "=" instead of ">" to make the compilation for Figure S2

Here are the best data compilation we can do.

Appendix B for Chapter 2 (Table S1-S6)

Table S1. REE concentration (given in µg g^{-1}) and neodymium isotopic signature of Southern African soil and dust samples.

Sample ID	Sample type	Sampling site	Latitude (S)	Longitude (E)	La	Ce	Pr	Nd	Sm	Eu	Gd	Tb	Dy	Ho	Er	Tm	Yb	Lu	$^{143}Nd/^{144}Nd$	±2σ
EP-AS-ON	aerosol	Etosha Pan	18° 53' 26.6"	15° 50' 35.5"	1.8	6.0	.9	0.5	0	.5	.9	.3	.5	.3	.8	.1	.8	.1	0.511512	0.000006
EP-AS-PR	aerosol	Etosha Pan	18° 57' 41.7"	15° 52' 06.3"	9.5	1.5	.3	4	5	.4	.5	.2	.2	.2	.6	.1	.7	.1	0.511493	0.000007
EP-AS-W	aerosol	Etosha Pan	19° 02' 53.3"	15° 53' 41.7"	7.0	1	1	6.4	1.1	0	1	0	0	0	0	0.1	0	0	0.511440	0.000033
EP-SS-ON	soil	Etosha Pan	18° 53' 26.6"	15° 50' 35.5"	2	4	5	2	4.	1	4	0	3	0	1	0.	1	0	0.511	0.00
					3.7	9.9	.7	1.5	3	.2	.0	.5	.1	.6	.6	2	.3	.2	543	0003
EP-SS-PR	soil	Etosha Pan	18° 57' 41.7"	15° 52' 06.3"	1	3	3	1	2.	0	2	0	2	0	1	0.	1	0	0.511	0.00
					5.5	6.7	.8	4.0	7	.7	.6	.3	.0	.4	.1	2	.1	.2	472	0009
EP-SS-W	soil	Etosha Pan	19° 02' 53.3"	15° 53' 41.7"	1	4	4	1	3.	0	3	0	2	0	1	0.	1	0	N/A	N/A
					9.4	8.5	.8	7.9	4	.9	.3	.4	.6	.5	.4	2	.4	.2		
SP-AS-SD157	aerosol	Sua Pan	20° 32' 54.2"	25° 59' 16.4"	1	2	3	1	2.	0	1	0	1	0	0	0.	0	0	0.511	0.00
					5.1	5.5	.3	1.9	0	.5	.9	.2	.3	.2	.6	1	.4	.1	308	0002
SP-AS-SD544	aerosol	Sua Pan	20° 34' 31.4"	25° 57' 32.4"	1	2	3	1	2.	0	2	0	1	0	0	0.	0	0	0.511	0.00
					7.5	8.0	.9	3.8	3	.7	.2	.3	.5	.3	.7	1	.5	.1	331	0008
SP-AS-SD608	aerosol	Sua Pan	20° 34' 31.4"	25° 57' 32.4"	1	2	3	1	2.	0	2	0	1	0	0	0.	0	0	0.511	0.00
					5.2	4.0	.3	1.8	1	.6	.0	.2	.3	.2	.6	1	.5	.1	341	0007
SP-SS-sua18	soil	Sua Pan	20° 33' 15.8"	25° 58' 8.4"	8.4	1	1	6.5	1.1	0	1	0	0	0	0	0.0	0	0	0.511	0.00
						4.4	.9			.4	.1	.1	.7	.1	.3		.3	.0	326	0007
SP-SS-sua33	soil	Sua Pan	20° 32' 21.1"	25° 57' 33.1"	1	2	2	1	1.	0	1	0	1	0	0	0.	0	0	0.511	0.00
					3.1	2.0	.9	0.2	7	.6	.7	.2	.1	.2	.5	1	.4	.1	312	0003
SP-SS-sua31	soil	Sua Pan	20° 32' 52.8"	25° 54' 40.3"	6.8	1.2	1	5.3	0.9	0	0	0	0	0	0	0.	0	0	0.511	0.00
						.2	.5			.3	.8	.1	.6	.1	.3	0	.3	.0	371	0009

Table S2. REE concentration (given in µg g^{-1}) and neodymium isotopic signature in surface sediment from desert of Northwest Australia

Sample ID	Sampling site	Latitude	Longitude	La	Ce	Pr	Nd	Sm	Eu	Gd	Tb	Dy	Ho	Er	Tm	Yb	Lu	$^{143}Nd/^{144}Nd$	±2σ
Dune #07	desert of Northwest Australia	22°39.476′	113°41.812′	1.8	3.3	0.4	1.8	0.4	0.1	0.5	0.1	0.5	0.1	0.3	0.0	0.3	0.0	0.511693	0.000008
Lyndon R #20	desert of Northwest Australia	23°32.414′	113°57.797′	3.2	6.1	0.7	2.8	0.5	0.2	0.6	0.1	0.5	0.1	0.3	0.0	0.2	0.0	0.511888	0.000016
Gascoyne R #23	desert of Northwest Australia	24°49.548′	113°46.295′	21.4	44.3	4.9	17.5	3.2	0.7	3.2	0.4	2.5	0.4	1.3	0.2	1.2	0.2	0.511695	0.000008
Dune #25	desert of Northwest Australia	23°06.932′	113°50.714′	14.2	26.9	3.2	11.7	2.2	0.5	2.0	0.3	1.8	0.3	0.8	0.1	0.7	0.1	0.511569	0.000008

Table S3. Protocol for soil digestion

1. Weight 50 mg sample into the savillex.
2. Add HNO3 into the savillex and put it in the ultrason for 30 min, then add 0.5ml HF. Heat it for 3 days at 130°C
3. Evaporate the soluton at 75°C.
4. Add 2 ml aqua regia (HNO3: HCl = 1:2), put it in the ultrason for 30 min. Heat it for 3 days at 130°C.
5. Evaporate the solutions at 75°C
6. Add 2 ml 6M HCl and put it in the ultrason for 30 min. Heat it for 1.5 days at 100°C.
7. Evaporer the solutions à 75°C.
8. Add 2 ml de 35% HNO3, put it in the ultrason for 30 min. Heat it at 90°C for 2 hours first, then continue at 50°C for one day.
9. Transfer the solution into the falcon tube and add MQ upto12 ml. Here you have the mother solution.

Dilution for ICP-MS:

Take 1 ml of mother solution and add 2% HNO3 upto 10ml (=9 ml 2% HNO3). Add 50 µl of In/Re inside the solution.

Table S4. Recovery and reproductivity from Certified Reference materials are reported (mean ± σ; µg g^{-1}), including SRM1515 (Apple leaves), SRM1547 (Peach leaves), NJV942 (sphagnum), NJV941(carex), WQB-1 (Great lakes sediment), and LKSD-3 (Canadian lake sediment). Informative provisional values are reported in italic and under brackets, respectively.

Elements	Instrument	SRM 1515 (n=4)		SRM 1947 (n=3)		NJV 942 (n=4)		NJV 941 (n=8)		WQB-1 (n=3)		LKSD-3 (n=4)	
		measured	certified	measured	certified	measured	certified	measured	certified	measured	certified	measured	certified
Al	ICP-OES	283±8.3	286±9	243±5	249±8	868±84	950±100	844±84	900±79				
K	ICP-OES	12713±4113	16100±200	22177±514	24300±300	203±18	*170±5*	140±10	*120±4*				
Ti	ICP-OES	13.0±0.5		22±6		59±2	*75±31*	31±3	*40±10*				
Mg	ICP-MS	2738±105	2710±80	4128±217	4320±80	1047±112	1100±110	717±76	770±89				
Ca	ICP-MS	15236±603	15260±150	14687±757	15600±200	1064±126	1200±110	7469±1011	10200±510				
Ga	ICP-MS	0.49±0.03		0.33±0.04		0.27±0.05		0.16±0.02					
Rb	ICP-MS	9.4±0.4	9	17.1±0.86	19.7±1.2	0.72±0.12		0.4±0.06					
Sr	ICP-MS	25±1	25±2	52±2	53±4	17±2		32±3.2					
Zr	ICP-MS	0.17±0.02		0.59±0.08		1.6±0.3		1.2±0.4					
Cs	ICP-MS	0.006±0.001		0.07±0.004		0.03±0.003		0.02±0.003					
La	ICP-MS	20.7±0.8	*20*	8.3±0.4	*9*	0.87±0.09		0.7±0.06		46±2	*37.9*	50±1	(52)
Ce	ICP-MS	3.0±0.1	*3*	9±0.4	*10*	1.65±0.17		1.49±0.13		96±2	*77.6*	99±3	(90)
Pr	ICP-MS	4.1±0.2	-	1.7±0.1		0.21±0.02		0.19±0.02		11±0.1		12±0.04	
Nd	ICP-MS	15.5±0.6	*17*	6.2±0.3	*7*	0.72±0.08		0.69±0.06		40±0.3		45±0.5	(44)
Sm	ICP-MS	2.8±0.1	*3*	0.99±0.06	*1*	0.13±0.01		0.13±0.01		7.5±0.05		7.9±0.1	(8)
Eu	ICP-MS	0.25±0.01	*0.2*	0.19±0.01	*0.17*	0.03±0.02		0.03±0.002		1.6±0.03		1.5±0.01	(1.5)
Gd	ICP-MS	2.94±0.09	*3*	0.97±0.05	*1*	0.12±0.01		0.13±0.01		7±0.2		7±0.1	
Tb	ICP-MS	0.37±0.02	*0.4*	0.11±0.007	*0.1*	0.02±0.02		0.02±0.002		0.95±0.02		0.9±0.01	(1)
Dy	ICP-MS	1.78±0.08		0.52±0.03		0.09±0.09		0.11±0.01		5.6±0.1		5.1±0.04	(4.9)
Ho	ICP-MS	0.27±0.01		0.08±0.004		0.02±0.02		0.02±0.002		1.01±0		0.93±0.008	
Er	ICP-MS	0.57±0.02		0.21±0.01		0.05±0.06		0.07±0.006		3±0.2		2.7±0.05	
Tm	ICP-MS	0.05±0.002		0.02±0.0004		0.01±0.005		0.01±0.001		0.42±0.02		0.38±0.01	
Yb	ICP-MS	0.19±0.01	*0.3*	0.12±0.004	*0.2*	0.05±0.05		0.06±0.006		2.8±0.1		2.5±0.03	(2.7)
Lu	ICP-MS	0.02±0.001		0.02±0.0001		0.007±0.0006		0.01±0.001		0.41±0.02		0.38±0.005	(0.4)
Hf	ICP-MS	0.027±0.001		0.06±0.02		0.11±0.02		0.09±0.03					
Pb	ICP-MS	0.43±0.008	0.47±0.024	0.74±0.01	0.87±0.03	9.16±0.13	10.1±0.82	1.85±0.19	2.4±0.29				
Th	ICP-MS	0.021±0.003	*0.03*	0.04±0.005	*0.05*	0.13±0.01		0.11±0.01					
U	ICP-MS	0.007±0.0002	*0.006*	0.015±0.004	*0.015*	0.05±0.005		0.03±0.004					

Table S5: Source mixing-line calculation. AMS represents for Amsterdam Island, while SAF and SSA are Southern Africa and Southern South America, respectively. Symbol of f() means percentage. Symbols of φem1 and φem2 represent for **the fraction of considered element in end-member 1 and end-member 2. RMSE is abbreviation of "Root mean square root".**

f(AMS)	f(SAF)	f(SSA)	φ_{em1}Eu*	φ_{em2}Eu*	(Eu/Eu*)mix	φ_{em1}Yb	φ_{em2}Yb	(La/Yb_N)mix	f(AMS)	f(SAF)	f(SSA)	φ_{em1}La	φ_{em2}La	(Eu/La_N)mix	φ_{em1}Nd	φ_{em2}Nd	$(^{143}Nd/^{144}Nd\text{-})$mix	εNd	**RMSE**
5%	95%	0%	0.09	0.91	1.10	0.14	0.86	0.84	5%	95%	0%	0.05	0.95	1.53	0.06	0.94	0.511504	-22.13	7.46
10%	90%	0%	0.18	0.82	1.12	0.26	0.74	0.76	10%	90%	0%	0.09	0.91	1.63	0.13	0.87	0.511593	-20.39	6.59
15%	85%	0%	0.26	0.74	1.13	0.36	0.64	0.70	15%	85%	0%	0.14	0.86	1.73	0.19	0.81	0.511679	-18.70	5.75
20%	80%	0%	0.33	0.67	1.14	0.44	0.56	0.64	20%	80%	0%	0.19	0.81	1.83	0.25	0.75	0.511763	-17.06	4.93
25%	75%	0%	0.40	0.60	1.16	0.52	0.48	0.60	25%	75%	0%	0.24	0.76	1.93	0.30	0.70	0.511845	-15.47	4.14
30%	70%	0%	0.46	0.54	1.17	0.58	0.42	0.55	30%	70%	0%	0.29	0.71	2.02	0.36	0.64	0.511924	-13.92	3.37
35%	65%	0%	0.51	0.49	1.18	0.63	0.37	0.52	35%	65%	0%	0.33	0.67	2.13	0.41	0.59	0.512001	-12.42	2.63
40%	60%	0%	0.57	0.43	1.19	0.68	0.32	0.49	40%	60%	0%	0.38	0.62	2.23	0.47	0.53	0.512076	-10.96	1.92
45%	55%	0%	0.62	0.38	1.20	0.72	0.28	0.46	45%	55%	0%	0.43	0.57	2.33	0.52	0.48	0.512149	-9.54	1.25
50%	50%	0%	0.66	0.34	1.20	0.76	0.24	0.43	50%	50%	0%	0.48	0.52	2.43	0.57	0.43	0.512220	-8.16	0.68
55%	45%	0%	0.71	0.29	1.21	0.80	0.20	0.41	55%	45%	0%	0.53	0.47	2.53	0.62	0.38	0.512289	-6.81	0.57
60%	40%	0%	0.75	0.25	1.22	0.83	0.17	0.39	60%	40%	0%	0.58	0.42	2.64	0.66	0.34	0.512356	-5.50	1.04
65%	35%	0%	0.78	0.22	1.22	0.86	0.14	0.37	65%	35%	0%	0.63	0.37	2.74	0.71	0.29	0.512422	-4.22	1.62
70%	30%	0%	0.82	0.18	1.23	0.88	0.12	0.35	70%	30%	0%	0.69	0.31	2.85	0.75	0.25	0.512485	-2.98	2.22
75%	25%	0%	0.85	0.15	1.24	0.91	0.09	0.34	75%	25%	0%	0.74	0.26	2.95	0.80	0.20	0.512548	-1.76	2.82
80%	20%	0%	0.89	0.11	1.24	0.93	0.07	0.32	80%	20%	0%	0.79	0.21	3.06	0.84	0.16	0.512608	-0.58	3.41
85%	15%	0%	0.92	0.08	1.25	0.95	0.05	0.31	85%	15%	0%	0.84	0.16	3.17	0.88	0.12	0.512667	0.57	3.98
90%	10%	0%	0.95	0.05	1.25	0.97	0.03	0.30	90%	10%	0%	0.89	0.11	3.28	0.92	0.08	0.512725	1.70	4.54
95%	5%	0%	0.97	0.03	1.26	0.98	0.02	0.29	95%	5%	0%	0.95	0.05	3.39	0.96	0.04	0.512781	2.80	5.09
5%	90%	5%	0.09	0.83	1.09	0.14	0.77	0.82	5%	90%	5%	0.05	0.88	1.52	0.06	0.86	0.511586	-20.52	6.66
10%	85%	5%	0.17	0.75	1.10	0.25	0.66	0.75	10%	85%	5%	0.09	0.83	1.61	0.12	0.80	0.511671	-18.86	5.83
15%	80%	5%	0.25	0.68	1.12	0.34	0.57	0.69	15%	80%	5%	0.14	0.78	1.71	0.18	0.74	0.511754	-17.25	5.03
20%	75%	5%	0.32	0.61	1.13	0.42	0.50	0.63	20%	75%	5%	0.18	0.74	1.80	0.24	0.68	0.511834	-15.68	4.24
25%	70%	5%	0.38	0.55	1.14	0.49	0.43	0.59	25%	70%	5%	0.23	0.69	1.90	0.29	0.63	0.511912	-14.16	3.49
30%	65%	5%	0.44	0.49	1.15	0.56	0.38	0.55	30%	65%	5%	0.28	0.64	1.99	0.35	0.58	0.511988	-12.68	2.75

35%	60%	5%	0.50	0.44	1.16	0.61	0.33	0.52	35%	60%	5%	0.32	0.60	2.09	0.40	0.52	0.512062	-11.24	2.04
40%	55%	5%	0.55	0.39	1.17	0.66	0.28	0.48	40%	55%	5%	0.37	0.55	2.19	0.45	0.47	0.512133	-9.84	1.37
45%	50%	5%	0.60	0.34	1.18	0.70	0.24	0.46	45%	50%	5%	0.42	0.50	2.29	0.50	0.43	0.512203	-8.48	0.76
50%	45%	5%	0.65	0.30	1.19	0.74	0.21	0.43	50%	45%	5%	0.47	0.45	2.39	0.55	0.38	0.512271	-7.15	0.46
55%	40%	5%	0.69	0.26	1.20	0.77	0.18	0.41	55%	40%	5%	0.52	0.40	2.49	0.60	0.33	0.512338	-5.86	0.85
60%	35%	5%	0.73	0.22	1.20	0.80	0.15	0.39	60%	35%	5%	0.57	0.35	2.59	0.64	0.29	0.512402	-4.60	1.42
65%	30%	5%	0.77	0.18	1.21	0.83	0.12	0.37	65%	30%	5%	0.62	0.30	2.69	0.69	0.24	0.512465	-3.37	2.01
70%	25%	5%	0.80	0.15	1.22	0.86	0.10	0.35	70%	25%	5%	0.66	0.25	2.79	0.73	0.20	0.512527	-2.17	2.60
75%	20%	5%	0.84	0.11	1.22	0.88	0.07	0.34	75%	20%	5%	0.71	0.20	2.90	0.78	0.16	0.512587	-1.00	3.18
80%	15%	5%	0.87	0.08	1.23	0.91	0.05	0.33	80%	15%	5%	0.76	0.15	3.00	0.82	0.12	0.512645	0.14	3.75
85%	10%	5%	0.90	0.05	1.23	0.93	0.03	0.31	85%	10%	5%	0.82	0.10	3.10	0.86	0.08	0.512702	1.26	4.31
90%	5%	5%	0.93	0.03	1.24	0.95	0.02	0.30	90%	5%	5%	0.87	0.05	3.21	0.90	0.04	0.512758	2.34	4.85
95%	0%	5%	0.96	0.00	1.25	0.96	0.00	0.29	95%	0%	5%	0.92	0.00	3.31	0.94	0.00	0.512813	3.41	5.38
0%	90%	10%	0.00	0.84	1.05	0.00	0.79	0.88	0%	90%	10%	0.00	0.85	1.41	0.00	0.84	0.511580	-20.65	6.72
5%	85%	10%	0.09	0.76	1.07	0.13	0.68	0.80	5%	85%	10%	0.04	0.80	1.50	0.06	0.78	0.511663	-19.02	5.91
10%	80%	10%	0.17	0.68	1.09	0.24	0.59	0.73	10%	80%	10%	0.09	0.76	1.59	0.12	0.73	0.511744	-17.43	5.12
15%	75%	10%	0.24	0.62	1.10	0.33	0.51	0.67	15%	75%	10%	0.13	0.71	1.69	0.18	0.67	0.511823	-15.89	4.35
20%	70%	10%	0.31	0.55	1.11	0.41	0.45	0.63	20%	70%	10%	0.18	0.67	1.78	0.23	0.62	0.511900	-14.39	3.60
25%	65%	10%	0.37	0.49	1.12	0.48	0.39	0.58	25%	65%	10%	0.22	0.62	1.87	0.29	0.57	0.511975	-12.94	2.87
30%	60%	10%	0.43	0.44	1.14	0.54	0.33	0.55	30%	60%	10%	0.27	0.58	1.97	0.34	0.52	0.512048	-11.52	2.17
35%	55%	10%	0.49	0.39	1.15	0.59	0.29	0.51	35%	55%	10%	0.32	0.53	2.06	0.39	0.47	0.512118	-10.14	1.50
40%	50%	10%	0.54	0.34	1.16	0.64	0.25	0.48	40%	50%	10%	0.36	0.48	2.16	0.44	0.42	0.512187	-8.79	0.86
45%	45%	10%	0.59	0.30	1.17	0.68	0.21	0.46	45%	45%	10%	0.41	0.44	2.25	0.49	0.37	0.512255	-7.48	0.42
50%	40%	10%	0.63	0.26	1.17	0.72	0.18	0.43	50%	40%	10%	0.45	0.39	2.35	0.53	0.33	0.512320	-6.20	0.67
55%	35%	10%	0.67	0.22	1.18	0.75	0.15	0.41	55%	35%	10%	0.50	0.34	2.44	0.58	0.28	0.512384	-4.96	1.23
60%	30%	10%	0.71	0.18	1.19	0.78	0.12	0.39	60%	30%	10%	0.55	0.29	2.54	0.63	0.24	0.512446	-3.74	1.81
65%	25%	10%	0.75	0.15	1.20	0.81	0.10	0.37	65%	25%	10%	0.60	0.25	2.64	0.67	0.20	0.512507	-2.56	2.40
70%	20%	10%	0.79	0.11	1.20	0.84	0.07	0.36	70%	20%	10%	0.64	0.20	2.74	0.71	0.16	0.512566	-1.40	2.97
75%	15%	10%	0.82	0.08	1.21	0.86	0.05	0.34	75%	15%	10%	0.69	0.15	2.84	0.75	0.12	0.512624	-0.27	3.53
80%	10%	10%	0.85	0.05	1.22	0.88	0.03	0.33	80%	10%	10%	0.74	0.10	2.94	0.80	0.08	0.512681	0.83	4.08
85%	5%	10%	0.88	0.03	1.22	0.91	0.02	0.31	85%	5%	10%	0.79	0.05	3.04	0.83	0.04	0.512736	1.91	4.62
90%	0%	10%	0.91	0.00	1.23	0.93	0.00	0.30	90%	0%	10%	0.84	0.00	3.14	0.87	0.00	0.512790	2.96	5.15
0%	85%	15%	0.00	0.76	1.04	0.00	0.71	0.85	0%	85%	15%	0.00	0.78	1.40	0.00	0.77	0.511655	-19.17	5.98

5%	80%	15%	0.08	0.69	1.06	0.12	0.61	0.78	5%	80%	15%	0.04	0.74	1.49	0.06	0.71	0.511735	-17.61	5.20
10%	75%	15%	0.16	0.62	1.07	0.23	0.53	0.72	10%	75%	15%	0.09	0.69	1.58	0.12	0.66	0.511813	-16.09	4.45
15%	70%	15%	0.23	0.56	1.08	0.31	0.46	0.66	15%	70%	15%	0.13	0.65	1.67	0.17	0.61	0.511889	-14.62	3.71
20%	65%	15%	0.30	0.50	1.10	0.39	0.40	0.62	20%	65%	15%	0.17	0.60	1.76	0.22	0.56	0.511962	-13.18	2.99
25%	60%	15%	0.36	0.44	1.11	0.46	0.34	0.58	25%	60%	15%	0.22	0.56	1.85	0.28	0.51	0.512034	-11.78	2.30
30%	55%	15%	0.42	0.39	1.12	0.52	0.30	0.54	30%	55%	15%	0.26	0.51	1.94	0.33	0.46	0.512104	-10.42	1.63
35%	50%	15%	0.47	0.34	1.13	0.57	0.25	0.51	35%	50%	15%	0.31	0.47	2.03	0.38	0.41	0.512172	-9.09	0.99
40%	45%	15%	0.52	0.30	1.14	0.62	0.22	0.48	40%	45%	15%	0.35	0.42	2.12	0.43	0.37	0.512238	-7.80	0.44
45%	40%	15%	0.57	0.26	1.15	0.66	0.18	0.46	45%	40%	15%	0.40	0.38	2.22	0.47	0.32	0.512303	-6.54	0.50
50%	35%	15%	0.62	0.22	1.16	0.70	0.15	0.43	50%	35%	15%	0.44	0.33	2.31	0.52	0.28	0.512366	-5.31	1.04
55%	30%	15%	0.66	0.18	1.17	0.73	0.12	0.41	55%	30%	15%	0.49	0.28	2.40	0.56	0.24	0.512427	-4.11	1.62
60%	25%	15%	0.70	0.15	1.18	0.76	0.10	0.39	60%	25%	15%	0.53	0.24	2.50	0.61	0.19	0.512488	-2.93	2.20
65%	20%	15%	0.73	0.12	1.18	0.79	0.08	0.37	65%	20%	15%	0.58	0.19	2.59	0.65	0.15	0.512546	-1.79	2.76
70%	15%	15%	0.77	0.08	1.19	0.82	0.05	0.36	70%	15%	15%	0.63	0.14	2.69	0.69	0.11	0.512603	-0.67	3.32
75%	10%	15%	0.80	0.05	1.20	0.84	0.04	0.34	75%	10%	15%	0.67	0.10	2.79	0.73	0.07	0.512659	0.42	3.87
80%	5%	15%	0.83	0.03	1.20	0.87	0.02	0.33	80%	5%	15%	0.72	0.05	2.88	0.77	0.04	0.512714	1.48	4.40
0%	80%	20%	0.00	0.70	1.02	0.00	0.63	0.83	0%	80%	20%	0.00	0.71	1.39	0.00	0.70	0.511727	-17.78	5.29
5%	75%	20%	0.08	0.63	1.04	0.12	0.55	0.76	5%	75%	20%	0.04	0.67	1.48	0.06	0.65	0.511803	-16.29	4.54
10%	70%	20%	0.16	0.56	1.06	0.22	0.47	0.70	10%	70%	20%	0.08	0.63	1.56	0.11	0.60	0.511878	-14.83	3.82
15%	65%	20%	0.23	0.50	1.07	0.30	0.41	0.65	15%	65%	20%	0.13	0.59	1.65	0.17	0.55	0.511950	-13.42	3.11
20%	60%	20%	0.29	0.45	1.08	0.38	0.35	0.61	20%	60%	20%	0.17	0.54	1.74	0.22	0.50	0.512021	-12.04	2.42
25%	55%	20%	0.35	0.40	1.10	0.44	0.30	0.57	25%	55%	20%	0.21	0.50	1.82	0.27	0.45	0.512090	-10.69	1.75
30%	50%	20%	0.41	0.35	1.11	0.50	0.26	0.54	30%	50%	20%	0.25	0.45	1.91	0.32	0.41	0.512157	-9.38	1.11
35%	45%	20%	0.46	0.30	1.12	0.55	0.22	0.51	35%	45%	20%	0.30	0.41	2.00	0.37	0.36	0.512222	-8.11	0.52
40%	40%	20%	0.51	0.26	1.13	0.60	0.19	0.48	40%	40%	20%	0.34	0.37	2.09	0.41	0.32	0.512286	-6.86	0.35
45%	35%	20%	0.56	0.22	1.14	0.64	0.16	0.45	45%	35%	20%	0.39	0.32	2.18	0.46	0.27	0.512349	-5.65	0.86
50%	30%	20%	0.60	0.18	1.15	0.68	0.13	0.43	50%	30%	20%	0.43	0.28	2.27	0.51	0.23	0.512409	-4.46	1.43
55%	25%	20%	0.64	0.15	1.16	0.71	0.10	0.41	55%	25%	20%	0.47	0.23	2.36	0.55	0.19	0.512469	-3.30	2.00
60%	20%	20%	0.68	0.12	1.16	0.74	0.08	0.39	60%	20%	20%	0.52	0.19	2.46	0.59	0.15	0.512527	-2.17	2.56
65%	15%	20%	0.72	0.08	1.17	0.77	0.06	0.38	65%	15%	20%	0.56	0.14	2.55	0.63	0.11	0.512583	-1.07	3.12
70%	10%	20%	0.75	0.05	1.18	0.80	0.04	0.36	70%	10%	20%	0.61	0.09	2.64	0.68	0.07	0.512639	0.01	3.66
75%	5%	20%	0.79	0.03	1.19	0.82	0.02	0.35	75%	5%	20%	0.65	0.05	2.74	0.72	0.04	0.512693	1.07	4.18

0%	75%	25%	0.00	0.63	1.01	0.00	0.56	0.81	0%	75%	25%	0.00	0.65	1.38	0.00	0.64	0.511794	-16.47	4.64
5%	70%	25%	0.08	0.57	1.03	0.11	0.49	0.75	5%	70%	25%	0.04	0.61	1.46	0.06	0.59	0.511867	-15.04	3.92
10%	65%	25%	0.15	0.51	1.04	0.21	0.42	0.69	10%	65%	25%	0.08	0.57	1.55	0.11	0.54	0.511938	-13.65	3.22
15%	60%	25%	0.22	0.45	1.06	0.29	0.36	0.64	15%	60%	25%	0.12	0.53	1.63	0.16	0.49	0.512008	-12.29	2.54
20%	55%	25%	0.28	0.40	1.07	0.36	0.31	0.60	20%	55%	25%	0.16	0.48	1.72	0.21	0.44	0.512076	-10.96	1.88
25%	50%	25%	0.34	0.35	1.08	0.42	0.27	0.57	25%	50%	25%	0.21	0.44	1.80	0.26	0.40	0.512142	-9.67	1.24
30%	45%	25%	0.40	0.30	1.10	0.48	0.23	0.53	30%	45%	25%	0.25	0.40	1.89	0.31	0.35	0.512207	-8.41	0.64
35%	40%	25%	0.45	0.26	1.11	0.53	0.19	0.50	35%	40%	25%	0.29	0.35	1.98	0.36	0.31	0.512270	-7.18	0.25
40%	35%	25%	0.50	0.22	1.12	0.58	0.16	0.48	40%	35%	25%	0.33	0.31	2.06	0.40	0.27	0.512332	-5.98	0.68
45%	30%	25%	0.54	0.19	1.13	0.62	0.13	0.45	45%	30%	25%	0.38	0.27	2.15	0.45	0.23	0.512392	-4.80	1.25
50%	25%	25%	0.59	0.15	1.14	0.66	0.10	0.43	50%	25%	25%	0.42	0.22	2.24	0.49	0.19	0.512450	-3.66	1.81
55%	20%	25%	0.63	0.12	1.14	0.69	0.08	0.41	55%	20%	25%	0.46	0.18	2.33	0.54	0.15	0.512508	-2.54	2.37
60%	15%	25%	0.67	0.08	1.15	0.72	0.06	0.39	60%	15%	25%	0.50	0.14	2.42	0.58	0.11	0.512564	-1.45	2.92
65%	10%	25%	0.70	0.06	1.16	0.75	0.04	0.38	65%	10%	25%	0.55	0.09	2.51	0.62	0.07	0.512619	-0.38	3.45
70%	5%	25%	0.74	0.03	1.17	0.78	0.02	0.36	70%	5%	25%	0.59	0.05	2.60	0.66	0.04	0.512672	0.67	3.98
0%	70%	30%	0.00	0.57	1.00	0.00	0.50	0.79	0%	70%	30%	0.00	0.59	1.37	0.00	0.58	0.511857	-15.24	4.02
5%	65%	30%	0.08	0.51	1.02	0.11	0.43	0.73	5%	65%	30%	0.04	0.55	1.45	0.05	0.53	0.511927	-13.87	3.33
10%	60%	30%	0.15	0.45	1.03	0.20	0.37	0.68	10%	60%	30%	0.08	0.51	1.53	0.11	0.48	0.511996	-12.53	2.66
15%	55%	30%	0.21	0.40	1.05	0.28	0.32	0.64	15%	55%	30%	0.12	0.47	1.62	0.16	0.44	0.512063	-11.22	2.01
20%	50%	30%	0.28	0.35	1.06	0.35	0.27	0.60	20%	50%	30%	0.16	0.43	1.70	0.21	0.39	0.512128	-9.94	1.37
25%	45%	30%	0.33	0.31	1.07	0.41	0.23	0.56	25%	45%	30%	0.20	0.39	1.78	0.25	0.35	0.512192	-8.70	0.76
30%	40%	30%	0.39	0.26	1.08	0.47	0.19	0.53	30%	40%	30%	0.24	0.34	1.87	0.30	0.31	0.512254	-7.48	0.24
35%	35%	30%	0.44	0.22	1.09	0.52	0.16	0.50	35%	35%	30%	0.28	0.30	1.95	0.35	0.27	0.512315	-6.29	0.51
40%	30%	30%	0.49	0.19	1.10	0.56	0.13	0.48	40%	30%	30%	0.32	0.26	2.04	0.39	0.22	0.512375	-5.14	1.07
45%	25%	30%	0.53	0.15	1.11	0.60	0.10	0.45	45%	25%	30%	0.37	0.22	2.12	0.44	0.19	0.512433	-4.00	1.63
50%	20%	30%	0.57	0.12	1.12	0.64	0.08	0.43	50%	20%	30%	0.41	0.17	2.21	0.48	0.15	0.512490	-2.90	2.18
55%	15%	30%	0.61	0.09	1.13	0.67	0.06	0.41	55%	15%	30%	0.45	0.13	2.29	0.52	0.11	0.512545	-1.82	2.73
60%	10%	30%	0.65	0.06	1.14	0.71	0.04	0.39	60%	10%	30%	0.49	0.09	2.38	0.56	0.07	0.512599	-0.76	3.25
65%	5%	30%	0.69	0.03	1.15	0.74	0.02	0.38	65%	5%	30%	0.53	0.04	2.47	0.60	0.04	0.512652	0.28	3.77
0%	65%	35%	0.00	0.51	0.99	0.00	0.44	0.78	0%	65%	35%	0.00	0.54	1.36	0.00	0.52	0.511916	-14.08	3.44
5%	60%	35%	0.07	0.46	1.00	0.10	0.38	0.72	5%	60%	35%	0.04	0.50	1.44	0.05	0.48	0.511984	-12.76	2.78
10%	55%	35%	0.14	0.40	1.02	0.19	0.33	0.67	10%	55%	35%	0.08	0.46	1.52	0.10	0.43	0.512050	-11.47	2.13

15%	50%	35%	0.21	0.36	1.03	0.27	0.28	0.63	15%	50%	35%	0.12	0.42	1.60	0.15	0.39	0.512115	-10.21	1.50
20%	45%	35%	0.27	0.31	1.05	0.34	0.24	0.59	20%	45%	35%	0.16	0.38	1.68	0.20	0.34	0.512178	-8.98	0.89
25%	40%	35%	0.33	0.27	1.06	0.40	0.20	0.56	25%	40%	35%	0.20	0.33	1.76	0.25	0.30	0.512239	-7.78	0.32
30%	35%	35%	0.38	0.23	1.07	0.45	0.16	0.53	30%	35%	35%	0.24	0.29	1.84	0.29	0.26	0.512299	-6.60	0.35
35%	30%	35%	0.43	0.19	1.08	0.50	0.13	0.50	35%	30%	35%	0.28	0.25	1.93	0.34	0.22	0.512358	-5.46	0.90
40%	25%	35%	0.48	0.15	1.09	0.55	0.11	0.47	40%	25%	35%	0.32	0.21	2.01	0.38	0.18	0.512416	-4.34	1.46
45%	20%	35%	0.52	0.12	1.10	0.59	0.08	0.45	45%	20%	35%	0.36	0.17	2.09	0.43	0.14	0.512472	-3.24	2.00
50%	15%	35%	0.56	0.09	1.11	0.62	0.06	0.43	50%	15%	35%	0.40	0.13	2.18	0.47	0.11	0.512527	-2.17	2.54
55%	10%	35%	0.60	0.06	1.12	0.66	0.04	0.41	55%	10%	35%	0.44	0.09	2.26	0.51	0.07	0.512580	-1.13	3.06
60%	5%	35%	0.64	0.03	1.13	0.69	0.02	0.40	60%	5%	35%	0.48	0.04	2.34	0.55	0.03	0.512633	-0.10	3.58
5%	55%	40%	0.07	0.41	0.99	0.10	0.34	0.71	5%	55%	40%	0.04	0.44	1.43	0.05	0.42	0.512038	-11.71	2.25
10%	50%	40%	0.14	0.36	1.01	0.18	0.29	0.66	10%	50%	40%	0.08	0.41	1.51	0.10	0.38	0.512101	-10.47	1.63
15%	45%	40%	0.20	0.31	1.02	0.26	0.24	0.62	15%	45%	40%	0.11	0.37	1.59	0.15	0.34	0.512164	-9.25	1.03
20%	40%	40%	0.26	0.27	1.04	0.32	0.20	0.59	20%	40%	40%	0.15	0.33	1.66	0.20	0.30	0.512225	-8.07	0.44
25%	35%	40%	0.32	0.23	1.05	0.38	0.17	0.55	25%	35%	40%	0.19	0.29	1.74	0.24	0.26	0.512284	-6.91	0.20
30%	30%	40%	0.37	0.19	1.06	0.44	0.14	0.52	30%	30%	40%	0.23	0.25	1.82	0.29	0.22	0.512342	-5.77	0.74
35%	25%	40%	0.42	0.15	1.07	0.49	0.11	0.50	35%	25%	40%	0.27	0.21	1.90	0.33	0.18	0.512399	-4.67	1.29
40%	20%	40%	0.47	0.12	1.08	0.53	0.08	0.47	40%	20%	40%	0.31	0.16	1.98	0.37	0.14	0.512454	-3.58	1.83
45%	15%	40%	0.51	0.09	1.09	0.57	0.06	0.45	45%	15%	40%	0.35	0.12	2.07	0.42	0.11	0.512509	-2.52	2.36
50%	10%	40%	0.55	0.06	1.10	0.61	0.04	0.43	50%	10%	40%	0.39	0.08	2.15	0.46	0.07	0.512562	-1.49	2.88
55%	5%	40%	0.59	0.03	1.11	0.64	0.02	0.41	55%	5%	40%	0.43	0.04	2.23	0.50	0.03	0.512614	-0.47	3.39
5%	50%	45%	0.07	0.36	0.98	0.09	0.29	0.70	5%	50%	45%	0.04	0.39	1.42	0.05	0.38	0.512089	-10.72	1.76
10%	45%	45%	0.14	0.31	1.00	0.18	0.25	0.65	10%	45%	45%	0.07	0.36	1.50	0.10	0.33	0.512150	-9.52	1.16
15%	40%	45%	0.20	0.27	1.01	0.25	0.21	0.61	15%	40%	45%	0.11	0.32	1.57	0.14	0.29	0.512210	-8.34	0.57
20%	35%	45%	0.26	0.23	1.03	0.31	0.17	0.58	20%	35%	45%	0.15	0.28	1.65	0.19	0.25	0.512269	-7.20	0.09
25%	30%	45%	0.31	0.19	1.04	0.37	0.14	0.55	25%	30%	45%	0.19	0.24	1.73	0.24	0.22	0.512326	-6.08	0.58
30%	25%	45%	0.36	0.15	1.05	0.43	0.11	0.52	30%	25%	45%	0.22	0.20	1.80	0.28	0.18	0.512383	-4.98	1.12
35%	20%	45%	0.41	0.12	1.06	0.47	0.08	0.50	35%	20%	45%	0.26	0.16	1.88	0.32	0.14	0.512438	-3.91	1.66
40%	15%	45%	0.46	0.09	1.07	0.52	0.06	0.47	40%	15%	45%	0.30	0.12	1.96	0.36	0.10	0.512491	-2.86	2.18
45%	10%	45%	0.50	0.06	1.08	0.56	0.04	0.45	45%	10%	45%	0.34	0.08	2.04	0.41	0.07	0.512544	-1.84	2.70
50%	5%	45%	0.54	0.03	1.09	0.59	0.02	0.43	50%	5%	45%	0.38	0.04	2.12	0.45	0.03	0.512595	-0.83	3.20
0%	50%	50%	0.00	0.36	0.96	0.00	0.30	0.73	0%	50%	50%	0.00	0.38	1.34	0.00	0.37	0.512076	-10.96	1.88
5%	45%	50%	0.07	0.32	0.97	0.09	0.25	0.69	5%	45%	50%	0.04	0.35	1.41	0.05	0.33	0.512137	-9.77	1.29
10%	40%	50%	0.13	0.27	0.99	0.17	0.21	0.65	10%	40%	50%	0.07	0.31	1.48	0.09	0.29	0.512196	-8.62	0.71
15%	35%	50%	0.19	0.23	1.00	0.24	0.18	0.61	15%	35%	50%	0.11	0.27	1.56	0.14	0.25	0.512254	-7.48	0.15
20%	30%	50%	0.25	0.19	1.02	0.30	0.14	0.58	20%	30%	50%	0.15	0.23	1.63	0.19	0.21	0.512311	-6.38	0.42

25%	25%	50%	0.30	0.15	1.03	0.36	0.11	0.55	25%	25%	50%	0.18	0.19	1.71	0.23	0.17	0.512367	-5.29	0.96
30%	20%	50%	0.35	0.12	1.04	0.41	0.09	0.52	30%	20%	50%	0.22	0.16	1.79	0.27	0.14	0.512421	-4.23	1.49
35%	15%	50%	0.40	0.09	1.05	0.46	0.06	0.49	35%	15%	50%	0.26	0.12	1.86	0.31	0.10	0.512474	-3.19	2.01
40%	10%	50%	0.45	0.06	1.06	0.50	0.04	0.47	40%	10%	50%	0.29	0.08	1.94	0.36	0.07	0.512526	-2.18	2.52
45%	5%	50%	0.49	0.03	1.07	0.54	0.02	0.45	45%	5%	50%	0.33	0.04	2.02	0.40	0.03	0.512577	-1.18	3.02
50%	0%	50%	0.53	0.00	1.08	0.58	0.00	0.43	50%	0%	50%	0.37	0.00	2.09	0.44	0.00	0.512627	-0.21	3.51
5%	40%	55%	0.07	0.27	0.96	0.09	0.22	0.68	5%	40%	55%	0.04	0.30	1.40	0.05	0.29	0.512183	-8.88	0.84
10%	35%	55%	0.13	0.23	0.98	0.16	0.18	0.64	10%	35%	55%	0.07	0.26	1.47	0.09	0.25	0.512240	-7.76	0.28
15%	30%	55%	0.19	0.19	0.99	0.23	0.15	0.60	15%	30%	55%	0.11	0.23	1.55	0.14	0.21	0.512296	-6.66	0.27
20%	25%	55%	0.24	0.16	1.01	0.29	0.12	0.57	20%	25%	55%	0.14	0.19	1.62	0.18	0.17	0.512351	-5.59	0.81
25%	20%	55%	0.30	0.12	1.02	0.35	0.09	0.54	25%	20%	55%	0.18	0.15	1.69	0.22	0.14	0.512405	-4.54	1.33
30%	15%	55%	0.35	0.09	1.03	0.40	0.06	0.52	30%	15%	55%	0.21	0.11	1.77	0.27	0.10	0.512458	-3.51	1.85
35%	10%	55%	0.39	0.06	1.04	0.45	0.04	0.49	35%	10%	55%	0.25	0.08	1.84	0.31	0.07	0.512509	-2.51	2.35
40%	5%	55%	0.44	0.03	1.05	0.49	0.02	0.47	40%	5%	55%	0.29	0.04	1.92	0.35	0.03	0.512560	-1.52	2.85
0%	40%	60%	0.00	0.28	0.94	0.00	0.22	0.71	0%	40%	60%	0.00	0.29	1.32	0.00	0.28	0.512170	-9.14	0.97
5%	35%	60%	0.07	0.23	0.95	0.08	0.18	0.67	5%	35%	60%	0.03	0.26	1.39	0.05	0.24	0.512226	-8.03	0.42
10%	30%	60%	0.13	0.19	0.97	0.16	0.15	0.63	10%	30%	60%	0.07	0.22	1.46	0.09	0.21	0.512282	-6.94	0.14
15%	25%	60%	0.18	0.16	0.98	0.23	0.12	0.60	15%	25%	60%	0.10	0.19	1.53	0.13	0.17	0.512336	-5.88	0.66
20%	20%	60%	0.24	0.12	1.00	0.29	0.09	0.57	20%	20%	60%	0.14	0.15	1.61	0.18	0.13	0.512390	-4.85	1.18
25%	15%	60%	0.29	0.09	1.01	0.34	0.06	0.54	25%	15%	60%	0.17	0.11	1.68	0.22	0.10	0.512442	-3.83	1.69
30%	10%	60%	0.34	0.06	1.02	0.39	0.04	0.51	30%	10%	60%	0.21	0.07	1.75	0.26	0.07	0.512493	-2.83	2.19
35%	5%	60%	0.38	0.03	1.03	0.44	0.02	0.49	35%	5%	60%	0.24	0.04	1.82	0.30	0.03	0.512543	-1.86	2.68
5%	30%	65%	0.06	0.20	0.95	0.08	0.15	0.66	5%	30%	65%	0.03	0.22	1.38	0.04	0.20	0.512268	-7.22	0.08
10%	25%	65%	0.12	0.16	0.96	0.15	0.12	0.62	10%	25%	65%	0.07	0.18	1.45	0.09	0.17	0.512322	-6.17	0.52
15%	20%	65%	0.18	0.12	0.97	0.22	0.09	0.59	15%	20%	65%	0.10	0.14	1.52	0.13	0.13	0.512374	-5.14	1.03
20%	15%	65%	0.23	0.09	0.99	0.28	0.07	0.56	20%	15%	65%	0.14	0.11	1.59	0.17	0.10	0.512426	-4.13	1.54
25%	10%	65%	0.28	0.06	1.00	0.33	0.04	0.54	25%	10%	65%	0.17	0.07	1.66	0.21	0.07	0.512477	-3.15	2.03
30%	5%	65%	0.33	0.03	1.01	0.38	0.02	0.51	30%	5%	65%	0.20	0.04	1.73	0.25	0.03	0.512526	-2.18	2.52
20%	10%	70%	0.23	0.06	0.98	0.27	0.04	0.56	20%	10%	70%	0.13	0.07	1.58	0.17	0.06	0.512461	-3.45	1.88
22%	8%	70%	0.25	0.05	0.98	0.29	0.03	0.55	22%	8%	70%	0.15	0.06	1.61	0.18	0.05	0.512481	-3.07	2.07
24%	6%	70%	0.27	0.03	0.99	0.31	0.02	0.54	24%	6%	70%	0.16	0.04	1.63	0.20	0.04	0.512500	-2.69	2.26
26%	4%	70%	0.29	0.02	0.99	0.33	0.02	0.53	26%	4%	70%	0.17	0.03	1.66	0.22	0.03	0.512520	-2.31	2.45
28%	2%	70%	0.31	0.01	1.00	0.35	0.01	0.52	28%	2%	70%	0.19	0.01	1.69	0.23	0.01	0.512539	-1.93	2.64
30%	0%	70%	0.32	0.00	1.00	0.37	0.00	0.51	30%	0%	70%	0.20	0.00	1.72	0.25	0.00	0.512558	-1.56	2.83
5%	20%	75%	0.06	0.12	0.93	0.08	0.10	0.65	5%	20%	75%	0.03	0.14	1.37	0.04	0.13	0.512345	-5.71	0.75
10%	15%	75%	0.12	0.09	0.94	0.14	0.07	0.61	10%	15%	75%	0.06	0.10	1.43	0.08	0.10	0.512396	-4.72	1.24
15%	10%	75%	0.17	0.06	0.96	0.21	0.04	0.58	15%	10%	75%	0.10	0.07	1.50	0.12	0.06	0.512446	-3.75	1.73
20%	5%	75%	0.22	0.03	0.97	0.26	0.02	0.55	20%	5%	75%	0.13	0.03	1.57	0.17	0.03	0.512494	-2.80	2.20
25%	0%	75%	0.27	0.00	0.98	0.31	0.00	0.53	25%	0%	75%	0.16	0.00	1.64	0.20	0.00	0.512542	-1.87	2.67

0%	20%	80%	0.00	0.12	0.91	0.00	0.10	0.68	0%	20%	80%	0.00	0.14	1.30	0.00	0.13	0.512331	-5.98	0.62
10%	10%	80%	0.12	0.06	0.94	0.14	0.04	0.61	10%	10%	80%	0.06	0.07	1.43	0.08	0.06	0.512431	-4.04	1.58
20%	0%	80%	0.22	0.00	0.96	0.26	0.00	0.55	20%	0%	80%	0.13	0.00	1.56	0.16	0.00	0.512526	-2.18	2.51
5%	15%	80%	0.06	0.09	0.92	0.07	0.07	0.64	5%	15%	80%	0.03	0.10	1.36	0.04	0.10	0.512382	-5.00	1.10
15%	5%	80%	0.17	0.03	0.95	0.20	0.02	0.58	15%	5%	80%	0.10	0.03	1.49	0.12	0.03	0.512479	-3.10	2.05
5%	10%	85%	0.06	0.06	0.91	0.07	0.04	0.63	5%	10%	85%	0.03	0.07	1.35	0.04	0.06	0.512416	-4.33	1.44
10%	5%	85%	0.11	0.03	0.93	0.14	0.02	0.60	10%	5%	85%	0.06	0.03	1.42	0.08	0.03	0.512464	-3.40	1.90
15%	0%	85%	0.16	0.00	0.94	0.20	0.00	0.57	15%	0%	85%	0.09	0.00	1.48	0.12	0.00	0.512511	-2.48	2.36
0%	10%	90%	0.00	0.06	0.89	0.00	0.05	0.66	0%	10%	90%	0.00	0.06	1.28	0.00	0.06	0.512402	-4.61	1.30
10%	0%	90%	0.11	0.00	0.92	0.13	0.00	0.60	10%	0%	90%	0.06	0.00	1.41	0.08	0.00	0.512496	-2.78	2.21
5%	5%	90%	0.06	0.03	0.91	0.07	0.02	0.63	5%	5%	90%	0.03	0.03	1.35	0.04	0.03	0.512449	-3.68	1.76
5%	0%	95%	0.06	0.00	0.90	0.07	0.00	0.62	5%	0%	95%	0.03	0.00	1.34	0.04	0.00	0.512481	-3.07	2.07
0%	0%	100%	0.00	0.00	0.88	0.00	0.00	0.65	0%	0%	100%	0.00	0.00	1.27	0.00	0.00	0.512466	-3.35	1.93

Table S6. Neodymium isotopic signature of AMS peat samples

Sample	ID	Mid-Point Depth (cm)	$^{143}Nd/^{144}Nd$	2σ	εNd	2σ
	AMS14-PB01A-1	1	0.512191	0.000011	-8.7	-0.2
	AMS14-PB01A-2	2	0.512146	0.000011	-9.6	-0.2
	AMS14-PB01A-3	3	0.512373	0.000073	-5.2	1.4
	AMS14-PB01A-4	5	0.512323	0.000015	-6.1	0.3
	AMS14-PB01A-5	6	0.512295	0.000007	-6.7	-0.1
	AMS14-PB01A-6	8	0.512252	0.000003	-7.5	0.1
	AMS14-PB01A-7	9	0.512301	0.000037	-6.6	0.7
	AMS14-PB01A-8	11	0.511833	0.000428	-4.8	-0.2
	AMS14-PB01A-10	13	0.512664	0.000020	0.5	0.4
	AMS14-PB01A-13	17	0.512522	0.000007	-2.3	-0.1
	AMS14-PB01A-16	21	0.512620	0.000005	-0.4	0.1
	AMS14-PB01A-21	28	0.512410	0.000010	-4.4	0.2
	AMS14-PB01A-30	39	0.512454	0.000015	-3.6	0.3
	AMS14-PB01A-56	73	0.512562	0.000012	-1.5	0.2
	AMS14-PB01A-62	81	0.512571	0.000008	-1.3	0.2

AMS14-PB01A-70	92	0.512516	0.000012	-2.4	0.2
AMS14-PB01A-87	114	0.512614	0.000008	-0.5	0.2
AMS14-PB01A-93	121	0.512632	0.000021	-0.1	0.4
AMS14-PB01A-104	136	0.512502	0.000020	-2.7	0.4
AMS14-PB01A-113	148	0.512578	0.000004	-1.2	0.1
AMS14-PB01A-129	169	0.512499	0.000003	-2.7	0.1
AMS14-PB01A-139	183	0.512516	0.000006	-2.4	0.1
AMS14-PB01A-150	198	0.512579	0.000007	-1.2	0.1
AMS14-PB01A-165	218	0.512493	0.000039	-2.8	0.8
AMS14-PB01A-211	278	0.512515	0.000018	-2.4	0.4
AMS14-PB01A-218	288	0.512545	0.000010	-1.8	-0.2
AMS14-PB01A-218	294	0.512517	0.000004	-2.4	-0.1
AMS14-PB01A-238	314	0.512506	0.000012	-2.6	0.2
AMS14-PB01A-243	321	0.512486	0.000017	-3.0	0.3
AMS14-PB01A-244	322	0.512506	0.000017	-2.6	0.3
AMS14-PB01A-249	329	0.512544	0.000012	-1.8	0.2
AMS14-PB01A-255	337	0.512570	0.000008	-1.3	0.2
AMS14-PB01A-282	372	0.512514	0.000016	-2.4	0.3
AMS14-PB01A-283	373	0.512559	0.000009	-1.5	0.2
AMS14-PB01A-291	384	0.512527	0.000004	-2.2	0.1
AMS14-PB01A-294	388	0.512410	0.000018	-4.4	0.4
AMS14-PB01A-314	415	0.512474	0.000013	-3.2	0.3
AMS14-PB01A-321	424	0.512428	0.000016	-4.1	0.3
AMS14-PB01A-365	483	0.512509	0.000017	-2.5	0.3
AMS14-PB01A-369	488	0.512528	0.000009	-2.1	0.2
AMS14-PB01A-376	497	0.512595	0.000010	-0.8	0.2

Appendix C for Chapter 4 (Extended data 1)

Extended data1. This data file contains Hg concentration (ng g^{-1}) and Hg flux (µg m^{-2} yr^{-1}) in four peat profiles from Amsterdam Island, Falkland Islands (Islas Malvinas), Andorra and Harberton. Peat mass accumulation rate from each core is also presented, which is calculated from density (g cm-3) and age interval (cm yr-1). Age interval is obtained based on age model results (yr, see Supplementary Information) and the thickness of the layer (cm).

Amsterdam Island (AMS)					Falkland Islands (SCB, Islas Malvinas)				
Mid-depth (cm)	Age (AD/BC)	Hg (ppb)	peat mass accumulation rate (g cm^{-2} yr^{-1})	Hg flux (µg m^{-2} yr^{-1})	Mid-depth (cm)	Age (AD/BC)	Hg (ppb)	peat mass accumulation rate (g cm^{-2} yr^{-1})	Hg flux (µg m^{-2} yr^{-1})
0.6	2014	30	0.013	3.8	0.5	2012	28	0.023	6.4
2.0	2001	83	0.006	5.2	2.0	2008	27	0.031	8.5
3.5	1988	149	0.008	12.5	3.4	2003	24	0.057	13.6
4.9	1975	189	0.010	19.8	4.8	2001	25	0.053	13.3
6.4	1960	158	0.009	13.8	6.3	1999	26	0.052	13.4
7.8	1942	116	0.010	12.1	7.7	1997	27	0.046	12.4
9.4	1924	128	0.010	12.9	9.3	1995	28	0.040	11.1
10.8	1906	92	0.017	15.8	10.7	1993	24	0.051	12.3
13.2	1885	83	0.016	13.0	12.1	1991	28	0.040	11.2
17.0	1850	72	0.009	6.7	13.6	1988	27	0.036	9.8
21.0	1805	66	0.013	8.7	15.0	1986	26	0.030	8.0
22.3	1793	72	0.014	10.2	16.5	1983	31	0.032	10.0
27.6	1739	63	0.013	8.5	18.0	1979	23	0.036	8.1
30.3	1712	56	0.014	7.9	19.4	1976	26	0.028	7.4
34.1	1669	80	0.015	11.7	20.8	1972	18	0.026	4.5
39.1	1617	66	0.010	6.7	22.3	1968	18	0.029	5.1
47.0	1543	62	0.016	10.0	23.7	1965	16	0.037	6.0
64.1	1399	51	0.016	8.2	25.2	1962	26	0.032	8.1
73.1	1278	64	0.012	7.9	26.6	1959	28	0.026	7.2
81.0	1171	38	0.007	2.8	28.1	1956	33	0.025	8.3
83.8	1133	50	0.009	4.7	29.6	1952	32	0.024	7.4
91.5	1026	36	0.011	3.8	31.1	1948	43	0.018	7.7
98.3	932	40	0.006	2.5	32.5	1943	41	0.029	11.9
113.6	711	50	0.008	4.0	33.8	1939	56	0.032	18.0
121.4	599	46	0.010	4.8	35.3	1934	67	0.026	17.6
123.7	566	37	0.008	2.8	38.2	1926	54	0.030	16.3
130.5	467	43	0.009	3.8	41.1	1919	35	0.031	10.9
135.9	398	39	0.008	3.2	42.5	1916	33	0.053	17.3
139.9	339	38	0.009	3.5	46.1	1910	44	0.029	12.6
145.4	256	38	0.009	3.4	47.7	1907	33	0.017	5.6
148.1	219	43	0.009	3.9	49.2	1902	35	0.013	4.4
162.4	24	31	0.008	2.4	50.7	1896	43	0.011	4.9

169.3	-61	25	0.010	2.5	52.3	1890	38	0.010	3.9
176.2	-139	39	0.011	4.3	53.8	1882	37	0.008	3.1
179.1	-166	25	0.015	3.6	55.4	1872	36	0.009	3.3
180.5	-179	26	0.012	3.2	56.8	1862	44	0.011	4.8
183.2	-203	36	0.016	5.6	59.6	1842	52	0.013	6.7
185.9	-225	33	0.011	3.8	62.4	1820	57	0.011	6.0
188.7	-250	34	0.012	4.0	63.8	1809	36	0.008	2.8
192.6	-283	52	0.013	6.5	68.2	1773	47	0.009	4.3
198.0	-331	37	0.009	3.3	69.6	1761	34	0.008	2.7
213.8	-472	41	0.015	6.2	73.7	1725	69	0.015	10.4
217.8	-505	29	0.017	5.0	75.2	1713	69	0.010	7.0
221.8	-536	35	0.015	5.3	76.5	1697	72	0.009	6.8
228.4	-600	19	0.010	2.0	82.7	1591	83	0.013	10.8
234.7	-685	19	0.010	1.9	83.8	1569	99	0.009	8.5
238.7	-728	12	0.009	1.1	85.0	1548	92	0.007	6.3
244.1	-794	12	0.006	0.7	86.3	1519	84	0.008	6.5
246.8	-826	8	0.011	0.9	90.0	1446	122	0.007	8.1
249.5	-857	13	0.007	0.9	92.5	1393	185	0.007	13.8
263.4	-1006	9	0.008	0.7	95.0	1346	128	0.008	9.9
268.7	-1069	11	0.011	1.1	98.6	1279	135	0.007	9.0
272.7	-1112	9	0.006	0.5					
277.8	-1182	8	0.007	0.6					
286.2	-1329	12	0.006	0.7					
287.5	-1359	13	0.004	0.5					
294.1	-1502	29	0.006	1.8					
295.4	-1529	40	0.006	2.6					
298.0	-1593	35	0.005	1.6					
314.0	-1953	60	0.008	4.8					
316.6	-2011	67	0.009	6.0					
320.5	-2095	54	0.007	3.9					
321.9	-2125	66	0.011	7.5					
327.5	-2247	49	0.007	3.4					
328.8	-2277	63	0.010	6.2					
337.0	-2457	39	0.008	3.2					
340.9	-2535	29	0.010	2.8					
344.8	-2600	18	0.005	0.9					
348.7	-2649	19	0.016	3.1					
364.0	-2801	9	0.010	1.0					
366.6	-2827	9	0.016	1.5					
369.1	-2853	14	0.020	2.8					
371.8	-2878	13	0.017	2.3					
373.1	-2889	15	0.020	3.0					
381.2	-2984	9	0.010	0.9					
383.9	-3029	8	0.009	0.7					
388.2	-3100	18	0.013	2.3					

392.3	-3170	9	0.007	0.6
395.1	-3218	10	0.012	1.2
412.6	-3504	6	0.006	0.4
415.2	-3548	7	0.009	0.6
421.8	-3647	15	0.014	2.0
424.4	-3685	8	0.011	0.9
427.1	-3718	10	0.007	0.7
429.9	-3757	13	0.010	1.3
431.3	-3779	13	0.013	1.8
433.8	-3810	11	0.012	1.3
437.8	-3860	13	0.013	1.7
439.2	-3877	7	0.010	0.7
447.4	-3982	9	0.012	1.1
464.5	-4203	7	0.013	1.0
467.1	-4235	24	0.015	3.6
469.6	-4267	12	0.015	1.8
477.4	-4363	17	0.017	2.9
482.8	-4432	21	0.016	3.4
486.6	-4483	14	0.012	1.6
487.9	-4502	15	0.014	2.0
491.8	-4554	13	0.012	1.6
495.9	-4613	16	0.012	2.0
497.3	-4630	22	0.013	2.8
499.1	-4650	30	0.008	2.5

Harberton (HAR)

Mid-depth (cm)	Age (AD/BC)	Hg (ppb)	peat mass accumulation rate (g cm^{-2} yr^{-1})	Hg flux (µg m^{-2} yr^{-1})
1.3	2013	27	0.050	13.5
2.4	2011	19	0.050	9.7
4.7	2007	18	0.068	12.3
6.9	2004	15	0.076	11.1
9.1	2000	14	0.058	8.0
11.3	1998	14	0.070	9.7
13.6	1995	15	0.077	11.7
15.8	1992	14	0.057	8.2
18.1	1989	18	0.069	12.1
20.3	1987	17	0.077	13.2
22.4	1984	15	0.084	12.2
24.6	1981	12	0.070	8.2
26.6	1979	13	0.069	8.6
27.6	1977	16	0.059	9.3
29.7	1974	14	0.075	10.7

Andorra (AND)

Mid-depth (cm)	Age (AD/BC)	Hg (ppb)	peat mass accumulation rate (g cm^{-2} yr^{-1})	Hg flux (µg m^{-2} yr^{-1})
1.9	2010	27	0.044	12.0
3.3	2008	19	0.037	7.2
6.2	2004	18	0.041	7.4
9.0	2000	15	0.045	6.5
11.7	1996	14	0.043	6.0
14.6	1992	14	0.067	9.2
17.5	1990	15	0.056	8.5
20.3	1987	14	0.063	9.0
23.2	1984	18	0.070	12.2
26.0	1981	17	0.066	11.2
28.9	1978	15	0.073	10.6
31.6	1976	12	0.064	7.4
34.3	1973	13	0.066	8.3
35.7	1972	16	0.040	6.3
38.4	1968	14	0.047	6.7

30.7	1973	17	0.072	12.0
32.8	1969	32	0.055	17.5
33.9	1967	51	0.056	28.4
35.9	1962	74	0.051	37.9
37.0	1959	86	0.023	20.1
39.6	1924	60	0.008	4.8
40.9	1893	68	0.005	3.3
43.5	1815	41	0.006	2.6
44.8	1785	49	0.008	4.0
47.3	1748	27	0.008	2.2
48.5	1728	30	0.007	2.0
51.0	1689	55	0.010	5.3
52.3	1668	56	0.013	7.2
54.9	1626	30	0.010	2.8
57.4	1589	18	0.008	1.5
60.8	1545	35	0.009	3.1
63.2	1510	30	0.013	3.7
65.6	1480	32	0.010	3.3
68.0	1447	20	0.010	2.0
71.8	1397	23	0.017	3.9
74.2	1367	19	0.010	2.0
77.8	1319	17	0.011	2.0
78.9	1303	17	0.009	1.6
81.3	1271	17	0.009	1.5
83.7	1240	22	0.011	2.4
86.1	1208	19	0.014	2.6
88.3	1179	26	0.015	3.8
90.7	1148	18	0.015	2.8

39.7	1966	17	0.050	8.3
42.4	1962	32	0.049	15.6
43.7	1960	51	0.039	20.0
46.4	1955	74	0.041	30.3
47.6	1952	86	0.036	31.2
50.3	1944	60	0.016	9.4
51.7	1937	68	0.015	10.2
54.6	1924	41	0.020	8.3
56.1	1917	49	0.019	9.3
59.0	1903	27	0.019	5.1
60.5	1896	30	0.018	5.5
63.2	1884	55	0.019	10.5
64.6	1878	56	0.018	9.9
67.3	1866	30	0.026	7.8
70.2	1854	18	0.015	2.7
73.2	1841	35	0.019	6.7
76.1	1827	30	0.017	4.9